UNIVERSITÀ
DEGLI STUDI
DI PADOVA

Sede Amministrativa: Università degli Studi di Padova

Dipartimento di Scienze Chimiche

Corso di dottorato di ricerca in Scienza ed Ingegneria dei Materiali e delle Nanostrutture
Ciclo XXXIV

Electrochemical scanning tunnelling microscopy on metal porphyrins: the shape of the active sites in the electrocatalysis of small molecules

Coordinatore: Ch.mo Prof. Giovanni Mattei
Supervisore: Prof. Christian Durante

Dottorando: Alessandro Facchin

Index

Abstract

Having the possibility of realising a thorough, systematic and extensive characterisation on a definite group of generic materials allows to understand a general trend in their chemical behaviour. In this work, several metal macrocyclic molecules were investigated from an electrochemical point of view, and information on the electrocatalytic process of oxygen reduction reaction (ORR) was gathered. In particular, two main characterisation techniques were employed, namely electrochemical scanning tunnelling microscopy (EC-STM) and cyclic voltammetry (CV). Cyclic voltammetry gave a macroscopic electrochemical knowledge of the investigated systems, allowing to discriminate whether a redox process concerned or not the metal centres and it provided also kinetic parameters for the ORR process or information about the bielectronic or tetraelectronic reduction of O_2 to H_2O_2 or to H_2O, respectively. Therefore, this work deals with molecular electrocatalysis of ORR, and the main characterisation technique herein employed is represented by electrochemical scanning tunnelling microscopy. STM itself is a powerful imaging tool to visualise matter at single molecular level, and in this case, it is coupled with a bipotentiostat to enable imaging in the electrochemical cell. The metal macrocycles deposited on a solid substrate (Au(111) and HOPG) when immersed in an electrolyte, realise an electrode surface, which is polarised as working electrode. At the same time, STM images can be recorded, providing a unique single molecule point of view under *in operando* condition. EC-STM allowed to investigate molecular behaviour in deaerated electrolyte, thereby succeeding in observing, for some metal-porphyrins, the redox reduction M(III)/M(II). Moreover, it enables O_2 adsorption visualisation onto the active catalytic centres, recognised in the central coordinated metal. The combination of EC-STM with CV brought to a large experimental data collection, which could be recombined into volcano-like correlations, where the half-peak current represents the kinetic parameter to be plotted versus the bumping arising from the STM topographic profile when O_2 binds onto the metal center, and that can be regarded as a measure of M-O_2 interaction.

A catalytic activity trend was established, and the redox behaviour of some metal centres was individuated as the true catalytic mechanism for ORR. For those metal-centred molecules exhibiting a redox couple, the ORR occurred within a redox-like catalysis, where the metal center mediates the reduction of the oxygen molecule, recovering its original oxidation state by reduction at the electrode. Conversely, molecules without a redox behaviour did result in worse performances, but a certain catalysis was still observed such for Pd or Cu octaethylporphyrins. In this case it was hypothesized that intermolecular charge transfer via non-covalent functionalization can impart ORR electrocatalytic activities to the exposed sites of the support or of the molecule where a partial positive charge can be induced. This is a curious effect since the support itself is not active, nor are the molecules, but the ensemble of both let arise new properties and new “cooperative” catalytic activity. Clearly, the capability to transfer charge density to the support or *vice versa* critically depends on the support itself, and this was clearly observed in non-redox-active system such as Pt-octaethylporphyrin when passing from HOPG to Au(111) electrode support.

Though representing purely molecular electrocatalysis, this work retains important links with fuel-cells, which are nowadays being explored as valuable alternatives to fossil fuels. Currently, these devices host Pt-based materials as main catalysts for the slow ORR, but platinum suffers from scarcity and high cost, and a valid alternative is represented by metal-nitrogen sites embedded in carbonaceous matrixes. Their performance is still not equal to Pt-based catalysts, but promising results are being obtained and in this regard EC-STM studies on molecular sites which mimic macroscopic materials can provide insightful considerations and correlations.

Riassunto

Avere a disposizione una caratterizzazione estesa e sistematica di un determinato gruppo di materiali consente di ricavare un andamento del loro comportamento chimico. In questo lavoro, un consistente numero di metallo-porfirine è stato valutato dal punto di vista elettrochimico, ricavandone informazioni circa il processo di reazione di riduzione di ossigeno (ORR). A tal scopo, sono state impiegate principalmente due tecniche di caratterizzazione. La tecnica di voltammetria ciclica (CV) ha restituito informazioni elettrochimiche di carattere macroscopico, permettendo di discriminare se i centri metallici fossero contraddistinti da un processo di ossidoriduzione o meno. Inoltre, essa ha potuto restituire importanti parametri cinetici circa la reazione ORR, così come informazioni circa bi- o tetra-elettronicità del processo di riduzione dell'ossigeno. Pertanto, il presente elaborato è volto alla trattazione di elettrocatalisi molecolare nell'ambito ORR, e la principale tecnica sperimentale di sperimentazione a tal fine è stata la microscopia a scansione di tunnelling in ambiente elettrochimico (EC-STM). La strumentazione STM si presenta come un potente mezzo di indagine, capace di visualizzare la materia a livello atomico, ed in questo risulta accoppiata con un bipotenziostato, consentendo la raccolta di immagini in ambiente elettrochimico. I sistemi metallo-macrociclici sono stati depositati su substrati solidi, quali Au(111) e HOPG, e quindi posti a contatto con elettrolita, realizzando in questa maniera di fatto una superficie elettrodica, operante con il ruolo di elettrodo di lavoro in una tradizionale cella a tre elettrodi. Nello stesso tempo, la strumentazione STM è in grado di scansionare il siffatto elettrodo di lavoro, caratterizzando pertanto il campione in condizioni *in operando*. Tramite EC-STM è stato investigato il comportamento molecolare in elettrolita privo di ossigeno, verificando che per alcune metallo-porfirine ha luogo una ossidoriduzione del tipo M(III)/M(II). Inoltre, è stato visualizzato il fenomeno di adsorbimento di ossigeno molecolare sui siti attivi catalitici, riconosciuti pertanto nei centri metallici coordinati da azoto. La combinazione tra EC-STM e CV ha quindi portato all'ottenimento di un vasto numero di dati, che sono stati inseriti in volcano-plots. Grandezze cinetiche quali la corrente a metà picco di riduzione ORR sono state correlate con la protrusione ricavata dai profili topografici delle immagini EC-STM, ottenendo anche una stima dell'iterazione metallo-ossigeno. È stato quindi individuato un andamento dell'attività catalitica. Inoltre, è stato riscontrato che soltanto i metalli dotati di un comportamento redox sono in grado di esercitare una catalisi mediata dal cambiamento di stato di ossidazione del centro metallico stesso. Al contrario, le porfine sprovviste di fenomeno redox comportano una peggiore attività catalitica di ORR. Tuttavia, è stato ipotizzato che meccanismo di trasferimento di carica possa comunque avvenire qualora venga indotta una parziale carica positiva. A tal proposito, l'effetto e il ruolo del substrato risultano determinanti, e ciò è stato evidenziato con il sistema di platino porfirina depositata su Au(111) e HOPG.

Pur focalizzandosi sull'aspetto della elettrocatalisi molecolare, questo lavoro mostra comunque una importante affinità con dispositivi elettrochimici avanzati quali le celle a combustibile. Allo stato attuale, l'impiego di materiali a base di platino garantisce le prestazioni migliori per la catalisi ORR, tuttavia permangono evidenti limitazioni al suo

uso a causa di un elevato costo e una bassa reperibilità a livello globale. Una valida alternativa è stata individuata nei materiali carboniosi opportunamente dopati con centri metallo-azoto, e le metallo-porfirine trattate in questo elaborato si qualificano come adeguati sistemi modello per migliorarne l'efficacia di ORR.

List of Abbreviations

CE	Counter Electrode
CV	Cyclic Voltammetry
DFT	Density Functional Theory
DMF	N,N-Dimethylformamide
DOS	Density of State
EC-STM	Electrochemical Scanning Tunnelling Microscopy
FCC	Face Centred Cubic
FeOEP	Iron octaethylporphyrin
FFT	Fast Fourier Transform
HCP	Hexagonal Close-Packed
HER	Hydrogen Evolution Reaction
HOPG	High-Oriented Pyrolytic Graphite
Non-PGM	non-Platinum group material
NPMCs	Non-Precious Metal Catalysts
OCP	Open Circuit Potential
OEP	Octaethylporphyrin
OER	Oxygen Evolution Reaction
ORR	Oxygen Reduction Reaction
PEMFC	Proton Exchange Membrane Fuel Cell
RE	Reference Electrode
RHE	Reversible Hydrogen Electrode
SAM	Self-Assembled Monolayer
SCE	Saturated Calomel Electrode
TE	Tip Electrode
UHV	Ultra-High Vacuum
WE	Working Electrode

Chapter 1

Introduction

To the eyes of a habitual operator of a scanning tunnelling microscope (STM), the outcoming STM pictures ordinarily appear easy to rationalise, with minimal variations of contrast being looked for justifying a certain phenomenon going on or happening. Indeed, recursive features are expected to manifest depending on the substrate, whose surface is studied. However, for the most part of physical chemists and even surface scientists who are not familiar or directly dealing with a scanning probe technique, interpretation of STM pictures at a glimpse is anything but easy. Actually, up to 1930s, microscopy was based on optical methods, which naturally present a lower limit of resolution in the order of micrometres due to diffraction. E. Ruska surpassed this limit upon using high energy electrons, with an associated shorter wavelength [1,2]. Electron microscopies later in 1940s and 1950s were developed, with transmission electron microscopy (TEM) being nowadays intensively exploited to look matter at the nanoscale. STM had a much later development, with Binnig and Rohrer being awarded with the Nobel prize for their STM "invention" in 1986, four years later than their first publications on this regard [3–7]. Nevertheless, a number of technical issues had to be overcome, like mechanical and vibrational insulation, poor tip quality, effective positioning of the tip on the sample, reduction of the sample roughness, and so on. Many different declinations of STM equipment are nowadays available, ranging from low-temperature UHV-STM to ambient pressure *in situ* / *in operando* setups. This means that scanning probe microscopies (STM and AFM) are currently widely employed, with a huge range of applications being involved.

Among these applications, catalysis retains a major role, being also at the basis of chemistry itself. In particular, surface science investigation of heterogeneous catalysis dates back to 1910s with the work of Langmuir about gas adsorption on solid surfaces, [8,9] but only many years later, for the first time ever, STM allowed to directly "watch" a reaction going on, with many examples being found elsewhere. For example, Murphy et al. experimentally demonstrated by UHV-STM oxygen adsorption and homolytic cleavage mediated by manganese porphyrins supported on Ag(111) [10]. Manganese tetraphenyl porphyrin chloride was functionalised on Ag(111), but chloride axial ligand was retained by Mn. In fact, STM images were exhibiting a dark hole or a bright spot in the centre depending on the applied bias voltage (negative sample bias led to dark spot, the opposite with positive sample bias). Only after proper annealing at 510 K, STM contrast changed, showing a dark spot both at positive and negative sample bias, indicating a complete loss of chloride ligands. At this point, O_2 was dosed in the UHV chamber, causing the gradual appearance of very bright spots, attributed to Mn-O_2 complex formation. It was found that MnTPP contrast changes from dark to bright spots, involving pairs of molecules. Namely, two dark contrast molecules turn bright in the same moment, indicating that O_2 actually dissociates in presence of two neighbouring Mn centres, bringing to MnOTPP complex formation.

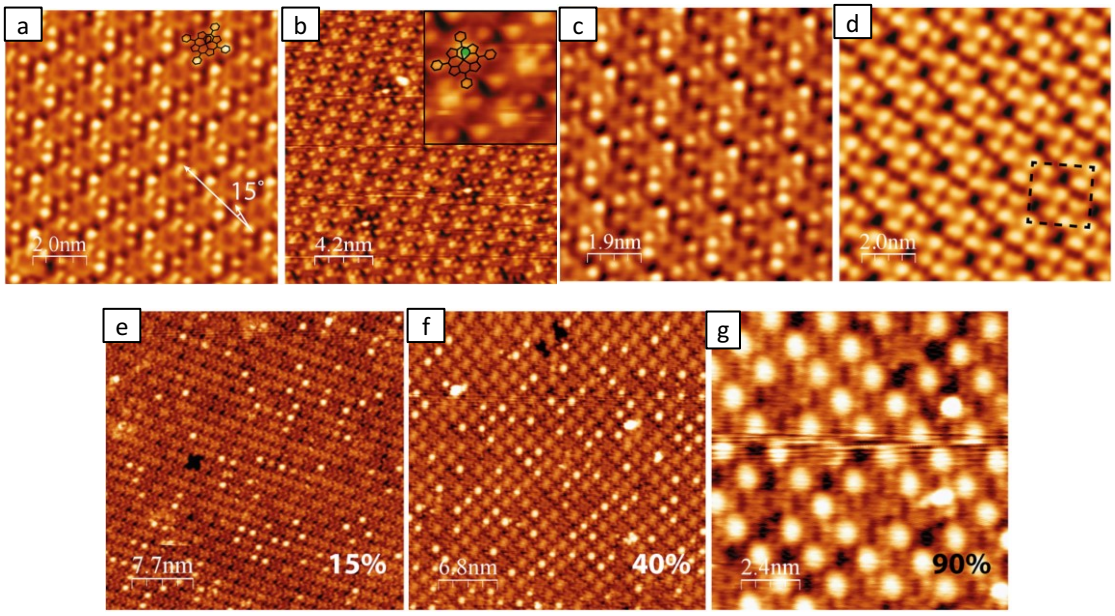

Figure 1.1 a) UHV-STM MnTPP adlayer on Ag(111) collected at negative sample bias. Dark spots are present at the molecular centres; b) UHV-STM MnTPP adlayer on Ag(111) collected at positive sample bias. Bright spots are present at the molecular centres. UHV-STM MnTPP adlayer on Ag(111) after 510 K annealing imaged at c) negative sample bias and d) positive sample bias: dark spots are present at the molecular centres for both bias cases. e-f) UHV-STM MnTPP adlayer on Ag(111) after O_2 dosage: bright spots gradually substitute dark ones. Oxidation proceeds via homolytic cleavage of O_2 and in fact bright spots appear in couples [10].

M. H. Chang et alii demonstrated that cobalt tetraphenylporphyrin can adsorb O_2, NO_2 and NH_3, leading to three different STM contrast shapes [11]. At this purpose, CoTPP molecules were deposited on Au(111) together with metal-free TPP. Square ring shape was observed for Co-O_2 complex, central bright spots for Co-NH_3 and rectangular ring shapes were visualised for Co-NO_2. The three experimental cases are reported in figure 1.2.a-c. Simulations of the STM contrast for the three complexes are shown in figures 1.2d-f and a remarkable correspondence can be found between experimental and theoretical images. The authors therefore succeeded in characterising small molecule adsorption onto selected metal single sites, an important first step towards imaging molecular catalysis.

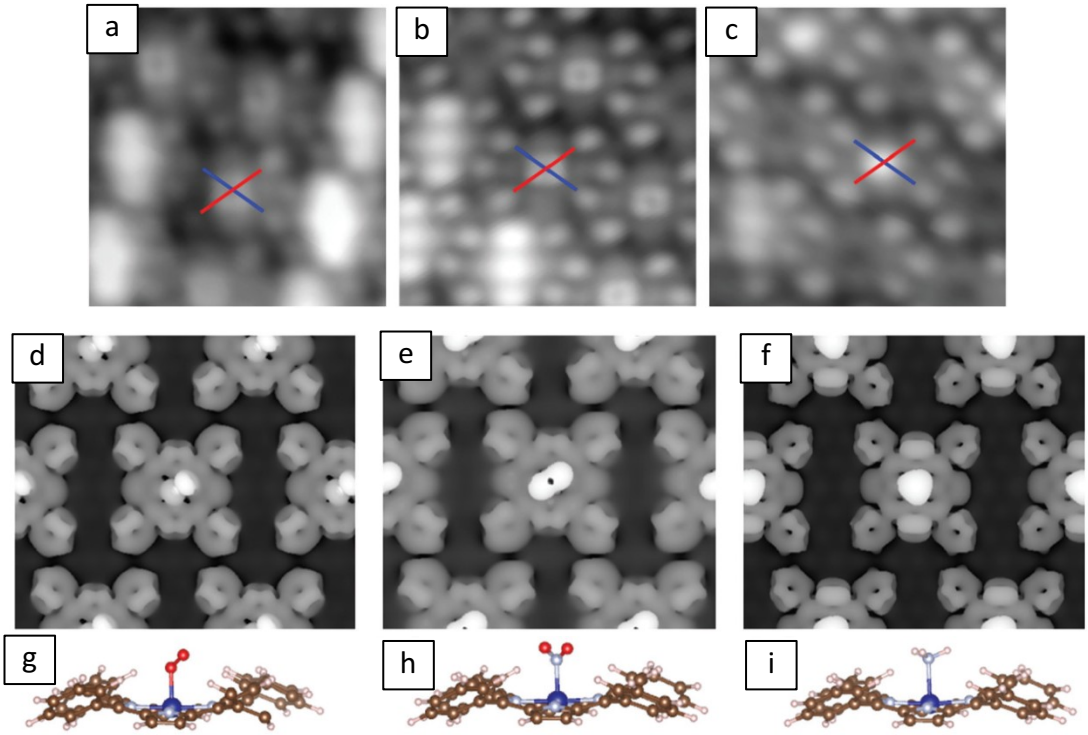

Figure 1.2. experimental UHV-STM images obtained for CoTPP in presence of a) O_2, b) NO_2 and c) NH_3. DFT simulation of STM contrast for CoTPP complexes is reported in d) for Co-O_2 complex, e) for Co-NO_2 complex and f) for Co-NH_3 complex. Stabilised atomic models for g) O_2 adsorption, h) NO_2 adsorption and i) NH_3 adsorption [11].

H. Kim et alii interestingly shown the switching and sensing of spin states with Co tetraphenyl porphyrin on Au(111) [12], and this gains a fundamental role in spintronic for molecular device applications. CoTPP was exposed to NO and this was experimentally observed by UHV-STM. The tree-lobed contrast of CoTPP switched to a ring shape within NO-CoTPP complex formation. Computational DFT calculations confirmed the experimental results. The obtained UHV-STM pictures are reported in figure 1.3.

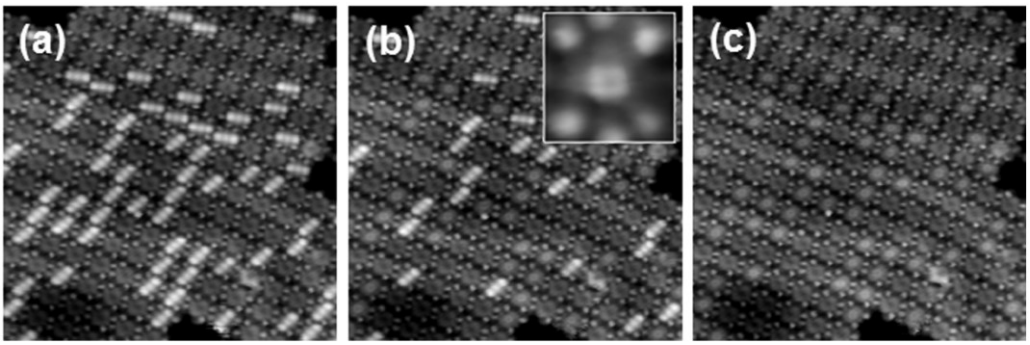

Figure 1.3. UHV-STM images of a mixed layer of CoTPP and free-base TPP deposited on Au(111). Image a) is obtained before NO exposure and shows the three-lobed uncoordinated CoTPP contrast. Image b) is obtained after 300 L exposure to NO, and ring-shaped molecules start to appear. Image c) is obtained after 900 L NO exposure and the number of ring-shaped molecules increase. In all images, H2TPP is not affected by NO exposure [12].

The study of the catalytic mechanism with STM technique has to be fairly downsized, because in all these cases, a common point was the employment of single crystals as metal substrates for the catalysis characterisation. Here arises one major issue of STM, namely the use of conductive single crystals as substrates. Apart of the obvious metallic character needed to enable electron tunnelling, the substrate is required to exhibit a rather atomically flat surface, with powders or other special forms of catalysts being completely discarded from this type of analysis. A large part of "real" catalysts should therefore be discarded, and the concept of catalysis studied within a STM approach (or, more specifically, a UHV-STM) should be better pinpointed as "model catalysis". Namely, making use of various metal single crystals, an adlayer of the desired material is deposited from gas phase, and the so obtained sample is probed by STM. Comparisons and dissimilarities are analysed with the corresponding macroscopic material and a deeper understanding of catalysis is achieved. Other tricks exist, like the "inverse catalysis". Instead of depositing a metal on an oxide surface, an oxide is grown on a metal with a limited thickness so that tunnelling is not inhibited [1,13,14]. For example, Schoiswohl et al. presented a number of UHV-STM characterisations of reactions on inverse model catalysts surfaces. Noble metal single crystal surfaces were decorated with oxide nanostructures, and UHV-STM was conducted to visualise surface processes with atomic level precision [15]. Thin films of vanadium oxides were grown on Pd(111), focussing in particular on the submonolayer oxide coverage regime. The sample was subjected to oxidation-reduction treatments, and morphological and structural changes were directly monitored by STM. Upon exposure to O_2, vanadium oxide passed from a (2x2) honeycomb structure to a (4x4) phase. Uncovered Pd(111) areas help the dissociation of molecular oxygen, acting therefore as reservoir of reactive oxygen species. Upon removing O_2 from the UHV chamber the (4x4) phase transformed into a zig-zag structure, but H_2 dosing was necessary to complete reduction and restore the initial oxide phase. Sequential STM images showing oxidation and reduction processes are shown in figure 1.4.

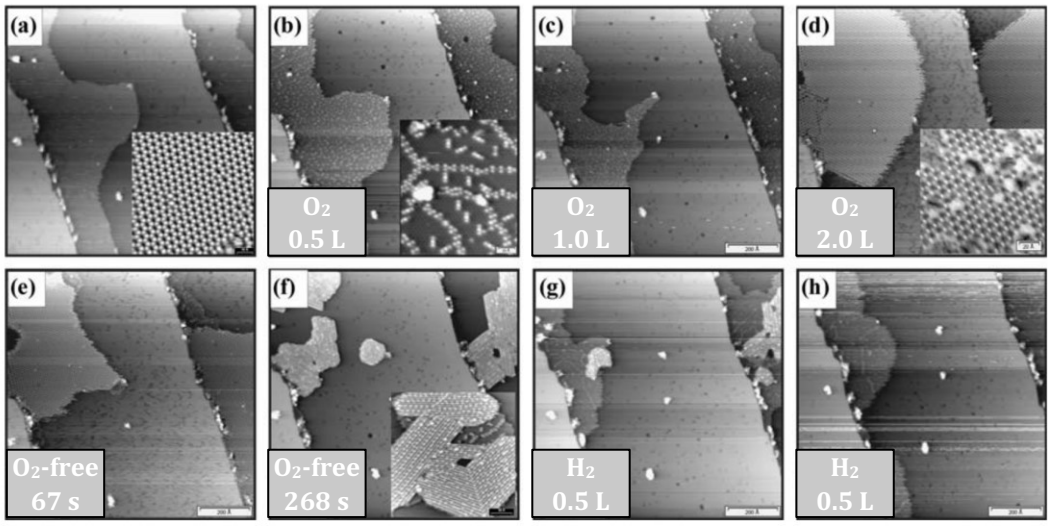

Figure 1.4. Sequential UHV-STM images showing a) vanadium oxide-modified Pd(111) immediately after the oxide deposition is covered to 40% by V_2O_3; image after b) 0.5 L, c) 1.0 L and d) 2.0L exposure to O_2. e) Image after pump-down of O_2 obtained after e) 67 seconds and f) 268 seconds. Images obtained after g) 0.5 L and h) 1.0 L exposure to H_2. [15]

A further step can be made with nanoparticulate surfaces, consisting of catalyst nanoparticles lying on an oxidic phase [8,13,14]. An example is represented by Au islands supported on an ultrathin MgO film, grown on Ag(001) [16,17]. The key-point is that a metal-insulator-metal interface is created, and it is experimentally proven that a negative charge is located on these Au islands, as shown in figure 1.5. Molecules like CO_2, CO and isophorone can reside on the rim of Au islands and electrons can be transferred for example to CO_2. A CO_2^- radical ion is formed and, basing on further characterisations and computational results, it further reacts to form oxalate.

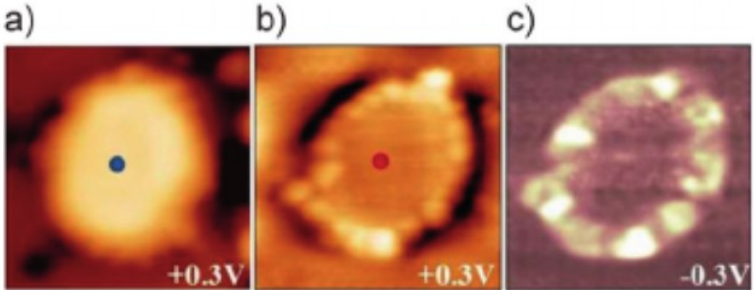

Figure 1.5. UHV-STM images of: a) pristine Au island on MgO|Ag(001); b) Au cluster after exposure to CO_2; c) dI/dV map showing high localisation of electronic density on the rim of Au island [17].

Despite the brilliant results, deriving from vivid and continuous efforts in surface science to come up with more and more advanced nano-systems, one major problem still holds, that is the UHV operating condition. Therefore, the so-called "pressure and material gaps" characterise UHV measurements [8]. The pressure gap is related to the vacuum pressure of $\approx$ 10-10 mbar at which STM experiments are conducted, while the material gap refers to the gap between the model catalysts probed by STM and its macroscopic counterpart. So, here lies the compromise between a perfectly controlled and controllable model system, but specific environmental conditions being realised.

Besides this, a link to the real world of catalysis does indeed exist, and it is classified in the category of *in situ* and *in operando* measurements. This means that a sample is characterised and at the same time it is exposed to real-world operating conditions, for example a solid substrate in contact with an electrolytic solution. When a standard electrochemical cell is coupled with a bipotentiostat and a STM, an electrochemical scanning tunnelling microscope is obtained (EC-STM). This instrument is able to collect STM images of a solid conductive substrate, which at the same time is immersed in an electrolytic solution together with reference and counter electrodes. This is a valid example of *in situ* measurement, because the probed surface stays at ambient pressure and in contact with a liquid, for which additional but hardly predictable interactions have to be taken into account. Moreover, the possibility to probe the sample surface, which at the same time is also polarised as working electrode, confers to the measurement the value of *in operando* characterisation.

A very recently published article is a clear example of the powerful capability of EC-STM to characterise an electrode surface *in operando*. Small-size controlled metallic palladium clusters were in situ generated under electrochemical control starting by a Pd(II) precursor [18]. Au(111) was employed as substrate. Thanks to EC-STM, it was

revealed that palladium electrochemical reduction occurs at much lower potential than for simple Pd salt solution, additionally resulting in monoatomic layer nanoparticles with narrow size distribution. In figure 1.6, EC-STM images of Au(111) in presence of Pd precursor are shown. In figure 1.6.a, no deposition is observed after 60 minutes of precursor exposure. A topographic profile was extracted by the red horizontal line, and it is shown in figure 1.6.g. This profile is coherent with a simple Au(111) step edge, indicating that deposition did not occur yet. When the applied potential was lowered to 0.2 V vs RHE, figure 1.6.e, palladium deposition started to occur, and the Au(111) is extensively covered by Pd islands at E_{app} = 0.1 V vs RHE, figure 1.6.f. the blue horizontal line corresponds to the topographic profile

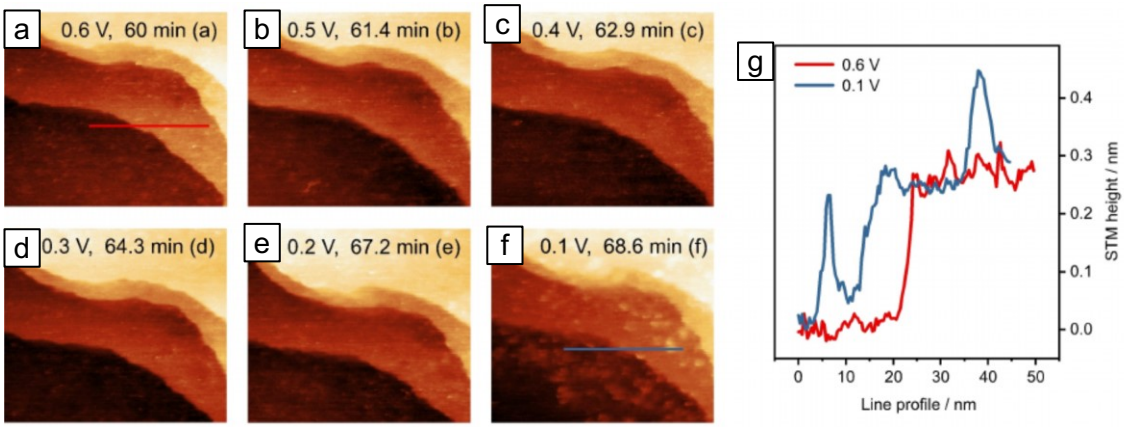

Figure 1.6. EC-STM images of Au(111) in contact with phosphate buffer containing the Pd precursor. a-d) After 60 minutes to precursor exposure, no deposition is observed due to the positive applied potential. e) At the applied potential of 0.2 V, Pd islands start to form; f) at the applied potential of 0.1 V the surface is covered by Pd islands. g) Topographic profiles of figure 1.6a (red line) and 1.6f (blue line) [18].

In other words, STM images are collected on a sample which at the same time is playing as an electrode, therefore it is under operating condition, providing so a photograph of its local density of states at a precisely applied working electrode potential. This retains a remarkable relevance in the terms of electrocatalysis, and even if the real catalytic processes occur at a much higher rate than STM imaging [8], it is interesting to photograph how the surface changed upon potential scanning, and how long does it take to recover from an electrochemical process. In particular, one can directly observe what occurs at the single atom level, identifying for example which are the real active sites of a molecule involved in a certain electrocatalysis mechanism.

This last remark actually constitutes the main topic of this thesis, in which macrocyclic metal complexes are analysed not only in their ability to self-assemble on the substrate surface, but especially to electrocatalyse O_2 reduction.

At this point, macrocyclic metal complexes deserve a dedicated paragraph in order to point out their relevance in terms of catalysis. Metal-phthalocyanines and -porphyrins are macrocyclic transition metal complexes already widely regarded as catalysts both for homogeneous and heterogeneous reactions [19]. If some conductive surfaces, e.g. metals, are functionalised with those compounds, an electrode surface is obtained and catalytic activity towards electrochemical reactions can arise. In this way, metal-phthalocyanines

were found to catalyse electro-oxidation of nitrogen-containing compounds, such as hydrazine and hydroxylamine [19]. Electrocatalytic effects were also discovered towards electrochemical reactions involving sulphur compounds, like mercaptoethanol, cysteine, gluthanione, as well as thionyl chloride and sulphuryl chloride. Other reactions of interest promoted by metal-N_4 macrocycles are the electroreduction of CO_2, NO_3^- and NO [19]. A vital reaction, on which life on earth is based, is the reduction of molecular oxygen through respiration. Food, i.e. glucose, is oxidised by an environmental oxidant, i.e. di-oxygen, to carbon dioxide and water, and the free energy produced by respiration is captured in the form of protons by enzymatic species like NADH and $FADH_2$. However, O_2 is kinetically inert at ambient conditions [20] due to low affinity for H^+ or electrophiles in general, and it possesses a triplet electronic ground state, which hinders reactions with most organic matter in a singlet ground state [20]. Energy metabolism of mammalians thus requires catalysis, which is ensured by enzymes. It is not surprising that these enzymes are based on *heme* groups, which actually feature FeN_4 sites in the form of iron-porphyrins [21]. Porphyrinato and phthalocyanato are tetradentate ligands and they are prone to coordinate a metal in their central cavity. The huge variety of metals that can be accommodated together with the high number of peripheral substituents make these molecules very versatile, in the sense that upon changing metal or substituents, one can instantly appreciate a change of physical chemical properties. Insertion of transition metals represents a valuable way to tune catalytic properties of porphyrins thanks to the redox behaviour exerted by the metal. The concept of redox catalysis is in fact well recognised, and it is at the basis of the above cited electroreduction reactions. The metal, possessing a low oxidation state, is able to donate one or more electrons to the analyte molecule, enabling its reduction. A simple but effective ORR scheme occurring on a generic nitrogen-coordinated site is reported, as follows, according to J. Zagal and M. Koper [19]:

$$[M^{III} - OH^-]_{ad} + H^+ + e^- \rightleftarrows [M^{II} - OH_2]_{ad} \quad 1.1$$

$$[M^{II} - OH_2]_{ad} + O_2 \rightarrow [M^{III} - O_2^-]_{ad} + H_2O \quad (rds) \quad 1.2$$

$$[M^{II} - OH_2]_{ad} + O_2 + e^- \rightarrow [M^{II} - O_2^-]_{ad} + H_2O \quad (rds) \quad 1.3$$

Turn-over of the catalyst is possible since the metal is stabilised by the surrounding nitrogen atoms of the ligand coordinating it. In this simple scheme of electrocatalysis, the first important passage is the molecule adsorption onto the metal centre. A complex is so formed, and electron transfer is then allowed, enabling the reduction reaction accomplishment. An example of molecular catalysis at an iron phthalocyanine functionalised Au(111) single crystal is now presented as an example of application of EC-STM to molecular catalysis [22]. In this case, iron phthalocyanine was first characterised in O_2-free electrolyte, so that the local density of states of the pure Fe phthalocyanine was imaged by STM, as shown in figure 1.7a. After that, O_2 saturation was performed in aqueous electrolyte, and molecules with a brighter central protrusion were imaged, as visible in figure 1.7b. Images under potential control were also recorded, figure 1.7c-f, showing that at sufficiently positive applied potentials O_2 is adsorbed on the Fe centres, while at reductive potentials the protrusion is lost due to continuous O_2 reduction turn-over.

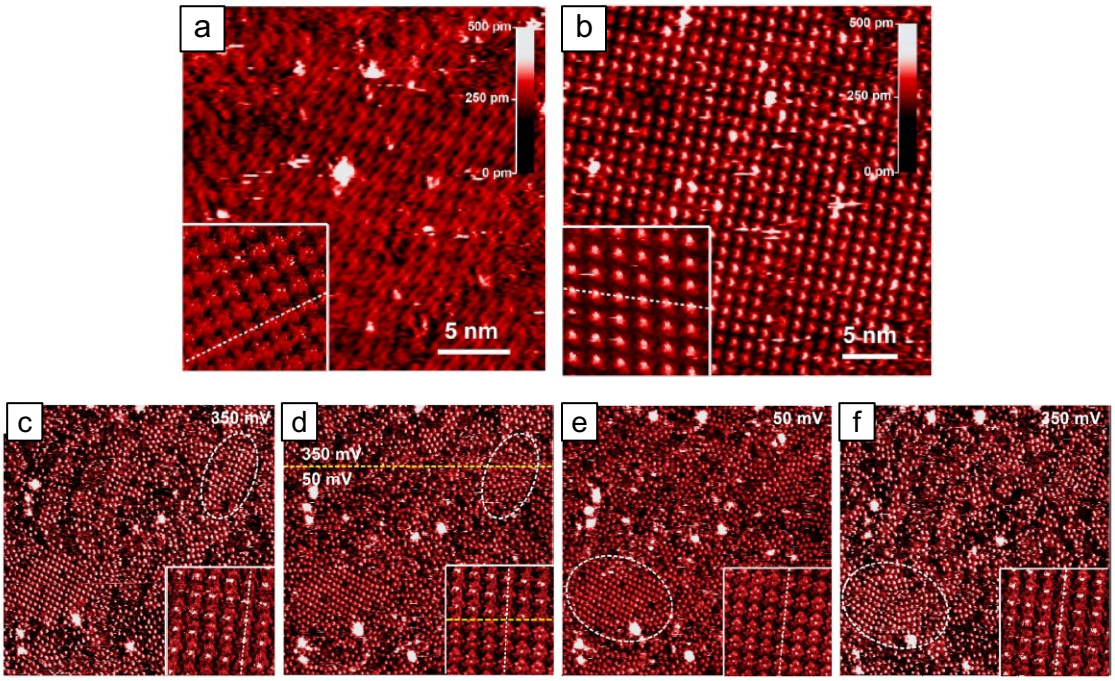

Figure 1.7. a) Fe phthalocyanine adlayer on Au(111) in contact with deaerated 0.1 M $HClO_4$. Molecules appear rather dark, and no bright spot was detected; b) Fe phthalocyanine adlayer on Au(111) in contact with O_2 saturated electrolyte. Molecules now exhibit a bright spot in the centre, indicating O_2 adsorption on Fe. Protrusions are maintained at positive potential (c), and when it is lowered to 50 mV they disappear (d,e). Upon returning to a more positive value, O_2 adsorption is restored [22].

Let us now delve into the main topic of this thesis, namely oxygen reduction reaction occurring on metal complexes. Nitrogen-coordinated metal sites are in fact known to efficiently catalyse the O_2 reduction reaction, emerging as valid alternatives to platinum and platinum-based catalyst materials (PGM). Although this work aims to characterise the fundamental aspects and mechanisms of electrocatalysis upon investigation at single molecular level, an ultimate relationship with real-world catalysts does exist, and it falls under the class of devices of fuel-cells, metal air batteries, electrochemical sensors and H_2O_2 electrolysers.

Much interest has been exerted on metal-air batteries and especially fuel cells, since they provide a consolidated technology for clean energy production and supply. Fuel-cells can be a valuable alternative to fossil fuel-based energy sources, since H_2 and O_2 are used as fuel and combustive, respectively, and the product of their combustion is H_2O, even if a real combustion does not take place. O_2 is entailed at the cathode of the cell, since it undergoes the reduction reaction, contrarily to H_2 which is subjected to oxidation. Actually, various types of fuel cells are nowadays a common reality, but each typology needs particular operating conditions to be fulfilled to deliver the best performances for which they have been projected.

In this regard, Proton Exchange Membrane Fuel Cell (PEMFCs) can be thought as an ideal final application of the present work, which aims to characterise macrocyclic molecules with FeN_4 centres deposited on an Au(111) electrode as model system for ORR

occurring at the cathode electrocatalyst surface. The half-cell reactions can be written as [23]:

$$Anode: H_2 \rightarrow 2H^+ + 2e^- \quad 1.4$$

$$Cathode: \frac{1}{2}O_2 + 2H^+ + 2e^- \rightarrow H_2O \quad 1.5$$

The global reaction is:

$$H_2 + \frac{1}{2}O_2 \rightarrow H_2O \quad 1.6$$

Therefore, protons (H^+) are generated by the hydrogen oxidation reaction (HOR) at the anode. Then, combined with molecular oxygen supplied at the cathode, they undergo oxygen reduction reaction (ORR) at the cathode. A PEMFC is mainly characterised by a quasi-solid electrolyte [19], namely a polymeric membrane frequently based on Nafion® polymer. The membrane is embedded between anode and cathode and allows migration of H^+ from anode to cathode, which mainly occurs via Grotthus mechanism [24–27]. H^+ jumps from one H_2O molecule to a new one thanks to linear chains of water molecules formed by hydrogen bonding.

PEMFCs operate at low temperature, generally < 100 °C, to avoid dehydration of the membrane, which represents an advantage in terms of cell fabrication and handling. However, the oxygen reduction reaction (ORR) is widely recognised as a low efficiency-process, especially at low temperatures like PEMFCs require, and a significant overpotential is needed for oxygen reduction to occur at a satisfactory rate. The overpotential request turns into loss of cell voltage: for this reason, the ORR needs to be catalysed. Pt-based electrodes exhibit the highest catalytic activity towards ORR [28]. Nonetheless, Pt and Pt-based materials suffer of scarcity and unequal distribution over the Earth's surface, and therefore imply high-costs, which hinder the widespread use of PEMFC. In any case, it is worth to briefly examine the reactivity of the Pt surface towards O_2 reduction. ORR at Pt surfaces is structure sensitive, so that the morphology can be conveniently used to tune the ORR activity. Since Pt possesses a face-centre cubic lattice, (111), (110) and (100) are the commonly exposed facets by bulk Pt crystals. The same holds for Pt crystals at the nanoscale, namely Pt nanoparticles. Actually, these low Miller index facets retain a lower activity compared to some high-index planes. Indeed, the latter have a higher number of defects, like kinks, step edges, which act as active sites for chemical bond breaking [29]. A computational study clarified the O_2 reduction reaction mechanism occurring on Pt(111) facet [30], recognising that more advanced Pt-based catalysts require additional aspects to be considered, but the aim is to point out the substantial difference of ORR mechanism with respect to the hereafter described M-N-C catalysts. First of all, physisorption in acid media was computed to be slightly energetically unfavourable by ca. 0.13 eV, so that chemisorption is preferred. O_2 chemisorbs with a end-on geometry, leading to formation of OOH species, and, thanks to H^+ presence, O or OH can be formed. These two further lead to H_2O formation by a series of protonation processes. ORR on Pt(111) is therefore described to proceed via two main routes, one featuring O_2 end-on adsorption onto Pt atoms (A) and the other accounting for OOH dissociation to form H_2O (B), as follows:

A

$$O_2 \rightarrow O_{2,ad} \quad 1.7$$

$$O_{2,ad} + H^+ + e^- \rightarrow O_{ad} + OH_{ad} \quad 1.8$$

$$O_{ad} + H^+ + e^- \rightarrow OH_{ad} \quad 1.9$$

$$2OH_{ad} + 2H^+ + 2e^- \rightarrow 2H_2O_{ad} \quad 1.10$$

B

$$O_2 + H^+ + e^- \leftrightarrow OOH_{ad} \quad 1.11$$

$$OOH_{ad} \rightarrow O_{ad} + OH_{ad} \quad 1.12$$

$$O_{ad} + H^+ + e^- \rightarrow OH_{ad} \quad 1.13$$

$$2OH_{ad} + 2H^+ + 2e^- \rightarrow 2H_2O_{ad} \quad 1.14$$

The rate determining step of ORR was computed to be protonation of O_{ad} to form OH. This explains why advanced materials like Pt_3Sc and Pt_3Y, which more weaky bind O_2, retain a higher ORR activity [30].

Non-Precious Metal Catalysts (NPMCs) are needed as alternative materials to Pt and it was found that metal coordinating nitrogen groups on mesoporous carbon material (M-N-MC) show a catalytic activity almost comparable to the most performing Pt catalysts [31]. Actually, the first encouraging results were conducted on cobalt phthalocyanine, for which Jasinski in 1964 discovered an electrocatalytic effects towards ORR in alkaline aqueous medium [32]. It was passing from the molecular catalyst to a pyrolysed one that a real breakthrough was achieved. The first approach was simply to heat at high temperature metal porphyrins and phthalocyanines, since they already are a source of MN_4 sites, and pyrolysis led to an improved final catalyst stability. Unfortunately, metal macrocycles are really expensive, and a large-scale catalyst production method would not represent a suitable and sustainable way of avoiding Pt-based materials. Therefore, another successful improvement was the preparation of M-N-C catalysts by pyrolysis of carbon, nitrogen and metal sources [33]. Within a decade, starting from 2009 up to nowadays the synthetic methods were intensively developed, understanding that not only the type of active sites is important, but also textural properties are essential to guarantee a maximised active sites exposure, as well as an efficient reactants supply and products removal.

In M-N-MC catalysts, a pyrolyzed mesoporous carbonaceous (MC) matrix embeds the active sites, represented by metal centres (M) coordinated by a various number of nitrogen atoms (N). At this level, a caveat must be made. The just described M-N-NC system can host a multitude of potentially active sites towards ORR: indeed, N-C, M@N-C and M-N_x sites are the three most probable categories of involved active sites during ORR. N-C sites refer to nitrogen heteroatom doping of a carbon plane. The main typologies of nitrogen-dopant species are pyridinic, pyrrolic and graphitic nitrogen, and they are shown with a simple sketch in figure 1.8.

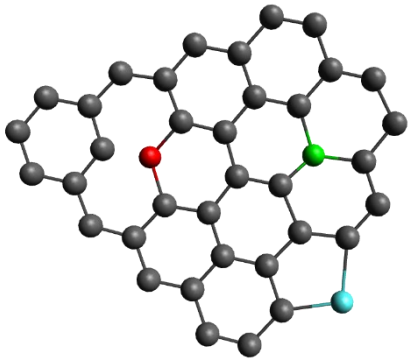

Figure 1.8 ball and sticks picture of graphitic (green), pyrrolic (light blue) and pyridinic (red) nitrogen-doped carbon sheet.

Basically, heteroatom doping acts by breaking the π-conjugation of the carbon plane, thus creating local modulations of electric charge, which can result in favourable O_2 binding sites for its reduction [35].

M@N-C stands for metal nanoparticles embedded in a nitrogen-doped carbonaceous matrix. Tylus et alii demonstrated the involvement of these sites in the ORR process, especially considering the case of acidic pH [34]. In particular, they investigated the behaviour of iron nanoparticles, and they found that metallic Fe nanoparticles are active as secondary active site sources, since they change the local charge distribution, thus promoting O_2 adsorption.

M-N_x active sites are regarded as the most active towards ORR compared to the previously presented ones. More specifically, the state-of-art results will now be presented for Fe-N_x based materials, due to the best results obtained in terms of final electrochemical performances. Actually, Fe-N_x accounts for a number of different active site forms, like Fe-N_4, Fe-N_{2+2}, N-Fe-N_{2+2}, Fe-N_{4+1} [35]. Fe-N_4 sites are characterised by four nitrogen atoms coordinating a central Fe atom, Fe-N_{2+2} stands for a bridging Fe between two nitrogen-doped carbon crystallites, N-Fe-N_{2+2} accounts for a bridging Fe centre between two nitrogen-doped carbon crystallites with N-graphitic in the plane underneath the Fe atom. Fe-N_{4+1} is associated to a Fe-N_4 site with an in-plane N-graphitic site underneath the Fe atom. Additionally, Fe-N_2 (nitrogen atoms at the crystallite edges) and Fe-N_3 (three out-of-plane nitrogen atoms) existence was also reported. All these types of Fe-N_x active sites are depicted in an illustrative picture, reported in figure 1.9.

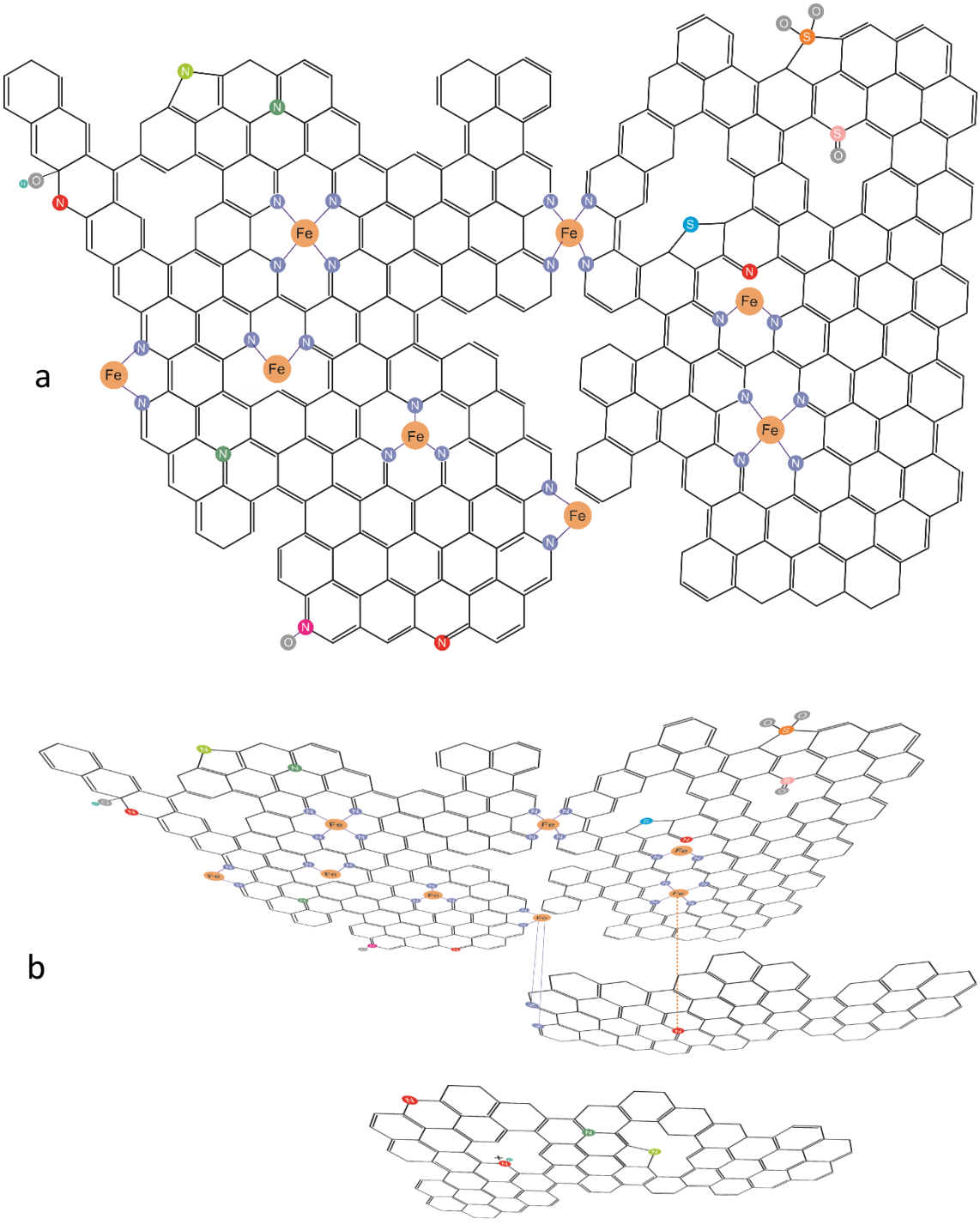

Figure 1.9. a) Ideal scheme containing the aforementioned active sites; b) perspective view of multiple carbonaceous sheets showing active sites distribution.

Various characterisation techniques were employed [35], starting from x-ray photoelectron spectroscopy (XPS). The different Fe coordination generates in fact slight modifications of the nitrogen chemical environment, thus leading to small variations of the revealed core electron binding energies, as shown in figure 1.10a. X-ray adsorption fine structure (EXAFS) conducted at the Fe K edge allowed to describe Fe coordination

number and its distance with the closer neighbours, as shown in figure 1.10b. Mössbauer spectroscopy also enables the assessment of the above cited Fe-containing moieties. Indeed, it can determine coordination environment, oxidation and spin stats of ^{57}Fe. The correlation of the identified Fe-containing species and the ORR activity identifies the dominating Fe-species on the ORR electrocatalysis. An example of Mössbauer spectroscopy is reported in figure 1.10c.

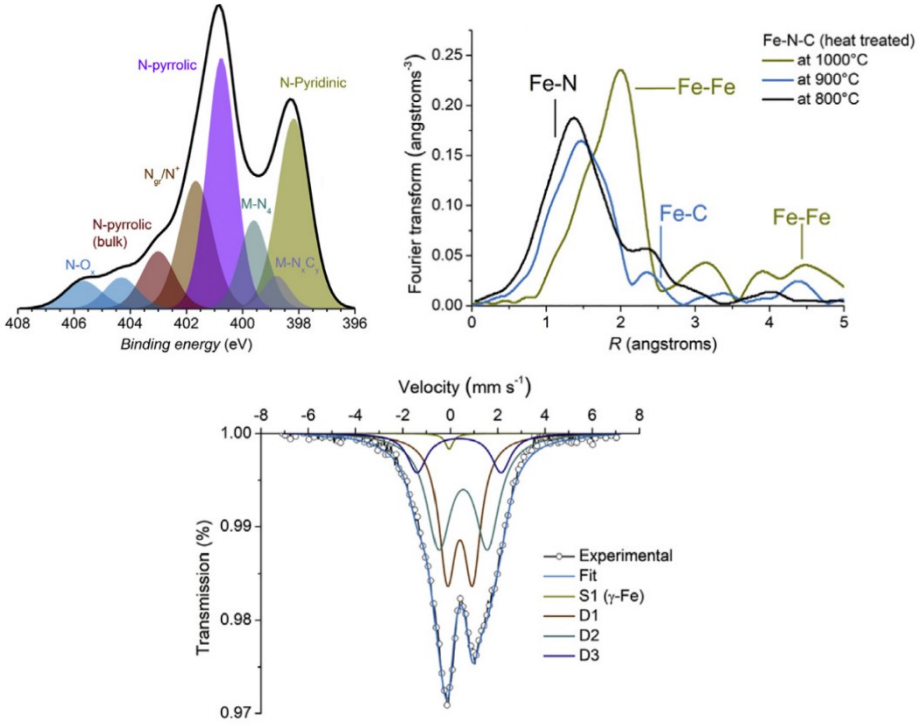

Figure 1.10. a) Example of XPS spectrum in the energy region of nitrogen-coordinating species; b) EXAFS characterisation showing characteristic Fe distances in a Fe-N-C material; c) Mössbauer spectrum of a F-N-C sample [35].

Although atomically dispersed M-N_x sites are generally considered the active centres of ORR electrocatalysis, synthetic paths for M-N-C are still linked to high temperature pyrolysis, which inevitably causes a high structural heterogeneity [33] An imaging tool with atomic precision would be useful to determine the active size distribution at the microscopic level. At this purpose, aberration corrected scanning transmission electron microscopy (AC-STEM) allows sub-angstrom scale image resolution achievement. In this way, Moiré fringes generated by graphene-like structures of carbon can be appreciated in figure 1.11a. Moreover, thanks to electron energy loss spectra, an iron atom surrounded by four nitrogen atoms could be resolved in the honeycomb lattice, obtaining an image of a Fe-N_4 site, reported in figure 1.11a. Low-temperature scanning tunnelling spectroscopy could also be successfully employed, arriving to image the electron density distribution of a Fe-N_4 site and its surroundings, as shown in figure 1.11b. The Fe centre appears as the brightest spot, and the coordinating nitrogen atoms also retain a bright contrast, indicating the enhanced local density of state produced by the FeN4 site [33].

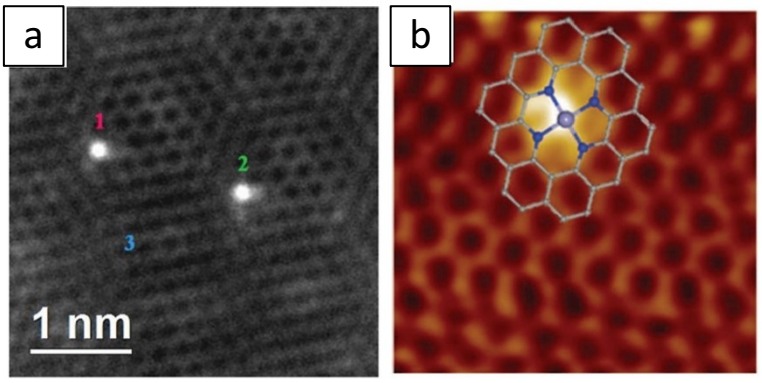

Figure 1.11 a) example of AC-STEM for a Fe-N-C sample; b) LT-STM showing a Fe-N4 site [33].

Despite all the above considerations, there is still a general lack of understanding on the main factors that govern electro-catalysis of ORR promoted by MN_x centres, and M-N-C synthesis are still often related to trial-and-error processes [33], always considering that heat treatments lead to high structural heterogeneity.

Gathering information about the Fe-N active site(s) holds a primary relevance in understanding the O_2 reduction reaction pathway, which is known to proceed according to two main mechanisms, recognised as "$2e^-$" or "$4e^-$ mechanism" [36]. Indeed, the $2e^-$ pathway involves two electrons in the electrocatalytic action, leading to hydrogen peroxide formation as the main reaction product. On the contrary, the $4e^-$ mechanism involves four electrons in the O_2 electroreduction, with water being produced as the main reaction product. The latter is then the most desirable reaction mechanism, since it makes the M-N-MC suitable for employment in possibly commercial PEMFCs, which would quickly worsen their performance due to hydrogen peroxide oxidising action onto the exchange membrane if the $2e^-$ pathway was followed. It is worth to examine a very recent demonstration of reaction mechanism assessment conducted on a macroscopic carbon-based catalyst. Venegas et alii realised the following experiment: iron (III) octaethylporphyrin chloride, cobalt (II) octaethylporphyrin and cobalt (II) tetraphenylporphyrin were separately mixed with carbon Vulcan XC-72 [37]. The resulting catalyst materials were either tested as produced or after pyrolysis at 800 °C for 2 hours. Resulting cyclic voltammograms are reported in figure 1.12. Black CVs refer to deaerated electrolyte case, while the red ones were collected in O_2 saturated electrolyte. The "HT" lettering recalls the heat treatment sample preparation step.
CVs of non-pyrolysed materials exhibit Fe(III)/Fe(II) and Co(III)/Co(II) redox processes, while for pyrolysed samples large faradaic contributions appear as consequence of reduction and oxidation of functional groups on the carbon matrix. In any case, an individual peak can still be detected, and it is situated at more positive potential than the corresponding non-pyrolysed material.

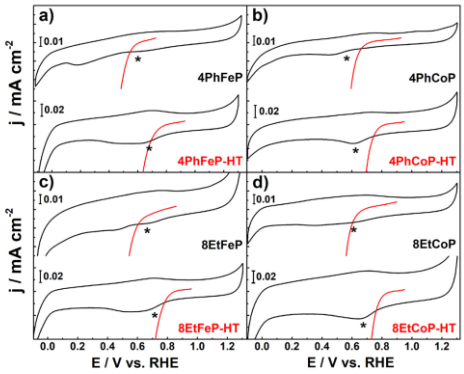

Figure 1.12 Cyclic voltammograms of a) iron tetraphenylporphyrin, b) cobalt tetraphenylporphyrin, c) iron octaethylporphyrin, d) cobalt octaethylporphyrin. Black lines refer to nitrogen saturation of 0.1 M H_2SO_4, while red curves refer to O_2 saturated electrolyte.

This indicates that the M(III)/M(II) redox potential is susceptible of the chemical environment. Pyrolysis alters the ligand around metal centres, in this case leading to a more electron-withdrawing one, which shifts redox potential to more positive values. Focussing on red CV, it is clear that in all cases the onset potential for ORR sits close to the M(III)/M(II) redox potential, indicating a central role of M(II) as main active site. Rotating ring and disk experiments were also conducted to experimentally detect the amount of produced H_2O_2 during ORR. Iron containing catalyst led to a preferential $4e^-$ mechanism, indicating that the main reaction pathways are the direct O_2 reduction to H_2O or two 2e-+2e consecutive reductions, the first producing H_2O_2 and the second further reducing the generated H_2O_2. Co catalysts preferentially led to a number of transferred electrons close to three, thereby meaning that a dual mechanism holds, with both H_2O_2 and H_2O being produced during ORR. Two reaction mechanisms are proposed. For low applied overpotential, the mechanism is:

$$[M^{3+} - OH^-]_{ad} + H_2O \rightleftarrows [M^{2+} - OH_2]_{ad} + OH^- \quad 1.15$$

$$[M^{2+} - OH_2]_{ad} + O_2 \rightarrow [M^{3+} - O_2]^-_{ad} + H_2O \rightleftarrows [M^{2+} - O_2]_{ad} + H_2O \quad 1.16$$

At high overpotential, the mechanism becomes:

$$[M^{2+} - OH_2]_{ad} + O_2 + e^- \rightarrow [M^{2+} - O_2]^-_{ad} + H_2O \quad 1.17$$

Up to now, experimental characterisation techniques were presented from a macroscopic point of view, except of electron microscopy techniques, which unfortunately suffer from the forementioned “pressure gap”, since they operate in UHV conditions. It is therefore clear that having the ability to study the ORR mechanism *in situ* at the single-site level would allow to discriminate different types of MN_x sites in terms of both the electrocatalytic activity towards ORR and of the preferential reaction pathway. On this regard, Metal-centred phthalocyanines and porphyrins are known to act as catalysts for ORR since 1960’s [32]. They are indeed good model systems for mimicking a specific class of MN_x sites, namely MN_4 [19,38–40].

Not only metal-porphyrins and -phthalocyanines are good examples of FeN_4 single sites, but the experimental conditions adopted in the present work try to mimic those of a PEMFC. Indeed, 0.1 M perchloric acid provides an acidic pH for the MN_4-based electrode, since for PEMFCs the polymeric membrane is designed for H^+ mobility and H^+ must be the product of HOR at the anode. The MN_4-based electrode is obtained by proper functionalisation of either a HOPG or Au(111) single crystals with MN_4 solutions. The MN_4/Au(111) and MN_4/HOPG electrodes are kept at room temperature, and PEMFCs require reasonably low temperature (generally 80-110 °C) to maintain a proper hydration level for the polymeric membrane. Of course, fuel cells do not deal with single crystals, nor with self-assembled monolayers of molecules adsorbed on it. Nonetheless, Au is almost inactive towards ORR [22,41–44], allowing to clearly evidence an eventual electrocatalytic effect of the functionalisation layer. In addition, dealing with a monolayer of well-defined MN_4 molecular species allows to distinctively determine the role of a single active centre.

Certainly, there are also differences between MN_4/Au and MN_4/HOPG electrodes and PEMFCs. The electrochemical environment modelled with an electrochemical cell cannot mimic the quasi-solid electrolytic membrane. Larger areas and higher electroactive material amounts characterise a standard fuel cell. Reactants are continuously supplied in gaseous phase with proper input flow systems, and the products are pulled out with adequate output flow systems, which allows recycling of non-reacted species.

In the present work, different MN_4-based molecular systems are examined in their ability to promote the O_2 reduction reaction. This task is accomplished by means of EC-STM, as well as by cyclic voltammetry (CV). Cyclic voltammetry provides a standard electrochemical characterisation of the MN_4 samples at macroscopic level. EC-STM allows to characterise each molecular system at the solid/electrolyte interface, furnishing a powerful tool to probe the structure of the MN_4-modified electrodes at single molecular level. This offers first of all the possibility to analyse the result of the substrate functionalisation, which will be represented by self-assembled monolayers. Moreover, EC-STM performs imaging under electrochemical conditioning of the FeN_4/Au electrode. This becomes an extraordinary relevant aspect, since EC-STM then provides a direct correlation between the macroscopic electrochemical response shown by the MN_4-based electrodes during a CV characterisation to its behaviour at the microscopic scale probed by means of STM. Indeed, the O_2 adsorption step is actually visualised, succeeding in some cases in distinguishing the *end-on* and/or the *side-on* adsorption geometry. Furthermore, *potentiodynamic imaging* demonstrates the O_2 disappearance from the metal sites at applied potentials close to the peak potential assigned to ORR process, therefore correlating the intense reductive current revealed at a definite applied potential to the system response at single sites.

The present works aims to provide an advanced understanding of the O_2 reduction reaction on specific FeN_4 sites by means of cyclic voltammetry and, above all, of EC-STM. In particular, the adsorption process and adsorption geometry are taken into account. Different molecular systems are compared to extract information about the effect of the chemical environment on the ORR electrocatalysis. They also serve as mean of evaluation for characterising the self-assembly process at the solid/liquid interface.

In chapter 2, theoretical concepts linked to STM tunnelling are outlined, trying to discriminate the general tunnelling theory developed for UHV with multiple approaches to the treatment of tunnelling at the solid/liquid interface. The basic STM working principles are enucleated. Theoretical concepts regarding the electrical double-layer and its modifications during a cyclic voltammetry experiment are also pointed out. In chapter 3, experimental setup and methods are elucidated, from glassware cleaning to Au preparation and functionalisation, as well as for CV experimental setting up. Chapter 4 describes the Au(111) and HOPG substrates employed in MN_4 functionalisation. The electrochemical response of the different MN_4/Au(111) electrodes is taken into exam in chapter 5. In chapter 6, extensive EC-STM analysis of the MN_4 systems is thoroughly described. Chapter 7 features an example of a different type of functionalised surface, namely graphene nanoribbons and their primitive structures. Actually, these samples are meant to represent the first stage towards the construction of an even more realistic model system for FeN_x-based materials. In chapter 8, data correlations are rationalized, pointing out the beneficial effect of the metal centre redox activity, when present, towards ORR.

References

[1] M. Bowker, Catalysis resolved using scanning tunnelling microscopy, Chemical Society Reviews. 36 (2007) 1656–1673.

[2] M. Knoll und E. Ruska, Das Elektronenmikroskop, Zeitschrift für Physik. Band 78, (1932) 318–339.

[3] G. Binnig, H. Rohrer, Ch. Gerber and E. Weibel (111) facets as the origin of reconstructed Au(110) surfaces, Surface science letters 131 (1983) 379–384.

[4] G. Binnig, H. Rohrer, Scanning tunnelling microscopy, Surface Science. 126 (1983) 236–244.

[5] G. Binnig, H. Rohrer, C. Gerber, E. Weibel, 7 × 7 Reconstruction on Si(111) Resolved in Real Space, Physical Review Letters. 50 (1983) 120–123.

[6] G. Binnig, H. Rohrer, C. Gerber, E. Weibel, Tunnelling through a controllable vacuum gap, Applied Physics Letters. 40 (1982) 178–180.

[7] G. Binnig, H. Rohrer, C. Gerber, E. Weibel, Surface studies by scanning tunnelling microscopy, Physical Review Letters. 49 (1982) 57–61.

[8] M. Bowker, P.R. Davies, Scanning Tunnelling Microscopy in Surface Science, Nanoscience and Catalysis, Wiley-VCH, 2010.

[9] I. Langmuir, The constitution and fundamental properties of solids and liquids. Part I. Solids., 2046 (1916) 2221–2294.

[10] B.E. Murphy, S.A. Krasnikov, N.N. Sergeeva, A.A. Cafolla, A.B. Preobrajenski, A.N. Chaika, O. Lübben, I. v. Shvets, Homolytic cleavage of molecular oxygen by manganese porphyrins supported on Ag(111), ACS Nano. 8 (2014) 5190–5198.

[11] M.H. Chang, N.Y. Kim, Y.H. Chang, Y. Lee, U.S. Jeon, H. Kim, Y.H. Kim, S.J. Kahng, O_2 , NO_2 and NH_3 coordination to Co-porphyrin studied with scanning tunnelling microscopy on Au(111), Nanoscale. 11 (2019) 8510–8517.

[12] H. Kim, Y.H. Chang, S.H. Lee, Y.H. Kim, S.J. Kahng, Switching and sensing spin states of Co-porphyrin in bimolecular reactions on Au(111) using scanning tunnelling microscopy, ACS Nano. 7 (2013) 9312–9317.

[13] H.J. Freund, M. Bäumer, H. Kuhlenbeck, Catalysis and surface science: What do we learn from studies of oxide-supported cluster model systems?, Advances in Catalysis. 45 (2000) 333–384.

[14] J. Libuda, H.J. Freund, Molecular beam experiments on model catalysts, Surface Science Reports. 57 (2005) 157–298.

[15] J. Schoiswohl, S. Surnev, F.P. Netzer, Reactions on inverse model catalyst surfaces: atomic views by STM, Topics in Catalysis. 36 (2005) 91–105.

[16] G. Pacchioni, H.J. Freund, Controlling the charge state of supported nanoparticles in catalysis: lessons from model systems, Chemical Society Reviews. 47 (2018) 8474–8502.

[17] F. Calaza, C. Stiehler, Y. Fujimori, M. Sterrer, S. Beeg, M. Ruiz-Oses, N. Nilius, M. Heyde, T. Parviainen, K. Honkala, H. Häkkinen, H.J. Freund, Carbon Dioxide Activation and Reaction Induced by Electron Transfer at an Oxide-Metal Interface, Angewandte Chemie - International Edition. 54 (2015) 12484–12487.

[18] N. Bock, A. de Clercq, L. Seidl, T. Kratky, T. Ma, S. Günther, U. Kortz, U. Heiz, F. Esch, Towards Size-Controlled Deposition of Palladium Nanoparticles from Polyoxometalate Precursors: An Electrochemical Scanning Tunnelling Microscopy Study, ChemElectroChem. 8 (2021) 1280–1288.

[19] J.H. Zagal, M.T.M. Koper, Reactivity Descriptors for the Activity of Molecular MN4 Catalysts for the Oxygen Reduction Reaction, Angewandte Chemie - International Edition. 55 (2016) 14510–14521.

[20] J.H. Zagal, F. Bedioui, J.P. Dodelet, N4-Macrocyclic Metal Complexes, Springer, 2006

[21] M. Shao, Electrocatalysis in Fuel Cells, Springer, 2015.

[22] J.Y. Gu, Z.F. Cai, D. Wang, L.J. Wan, Single-Molecule Imaging of Iron-Phthalocyanine-Catalyzed Oxygen Reduction Reaction by in Situ Scanning Tunnelling Microscopy, ACS Nano. 10 (2016) 8746–8750.

[23] J. Zhang, PEM Fuel Cell Electrocatalysts and Catalyst Layers Fundamentals and Applications, Springer, 2008.

[24] T. Okada, G. Xie, O. Gorseth, S. Kjelstrup, N. Nakamura, T. Arimura, Ion and water transport characteristics of Nafion membranes as electrolytes, Electrochimica Acta. 43 (1998) 3741–3747.

[25] D.N. Son, H. Kasai, Proton transport through aqueous Nafion membrane, European Physical Journal E. 29 (2009) 351–361.

[26] G.A. Ludueña, T.D. Kühne, D. Sebastiani, Mixed Grotthuss and vehicle transport mechanism in proton conducting polymers from Ab initio molecular dynamics simulations, Chemistry of Materials. 23 (2011) 1424–1429.

[27] www.lsbu.ac.ukwatergrotthuss.pdf

[28] Y. Nie, L. Li, Z. Wei, Recent advancements in Pt and Pt-free catalysts for oxygen reduction reaction, Chemical Society Reviews. 44 (2015) 2168–2201.

[29] S. Sui, X. Wang, X. Zhou, Y. Su, S. Riffat, C. Liu, A comprehensive review of Pt electrocatalysts for the oxygen reduction reaction: Nanostructure, activity, mechanism and carbon support in PEM fuel cells, Journal of Materials Chemistry A, 5 (2017) 1808–1825.

[30] L. Ou, S. Chen, Comparative study of oxygen reduction reaction mechanisms on the Pd(111) and Pt(111) surfaces in acid medium by DFT, Journal of Physical Chemistry C. 117 (2013) 1342–1349.

[31] G. Wu, K.L. More, C.M. Johnston, P. Zelenay, High-Performance Electrocatalysts for Oxygen Reduction Derived from Polyaniline, Iron, and Cobalt, Science. 332 (2011) 443–448.

[32] R. Jasinski, A New Fuel Cell Cathode Catalyst, Nature. 201 (1964) 1212–1213.

[33] M.X. Chen, L. Tong, H.W. Liang, Understanding the Catalytic Sites of Metal–Nitrogen–Carbon Oxygen Reduction Electrocatalysts, Chemistry - A European Journal. 27 (2021) 145–157.

[34] U. Tylus, Q. Jia, K. Strickland, N. Ramaswamy, A. Serov, P. Atanassov, S. Mukerjee, Elucidating oxygen reduction active sites in pyrolyzed metal-nitrogen coordinated non-precious-metal electrocatalyst systems, Journal of Physical Chemistry C. 118 (2014) 8999–9008.

[35] T. Asset, P. Atanassov, Iron-Nitrogen-Carbon Catalysts for Proton Exchange Membrane Fuel Cells, Joule. 4 (2020) 33–44.

[36] S. Kattel, P. Atanassov, B. Kiefer, A density functional theory study of oxygen reduction reaction on non-PGM Fe-Nx-C electrocatalysts, Physical Chemistry Chemical Physics. 16 (2014) 13800–13806.

[37] R. Venegas, K. Muñoz-Becerra, C. Candia-Onfray, J.F. Marco, J.H. Zagal, F.J. Recio, Experimental reactivity descriptors of M-N-C catalysts for the oxygen reduction reaction, Electrochimica Acta. 332 (2020), 135340.

[38] J.H. Zagal, Metallophthalocyanines as catalysts in electrochemical reactions, Coordination Chemistry Reviews. 119 (1992) 89–136.

[39] J.H. Zagal, M.A. Paez, A.A. Tanaka, J.R.Jr. dos Santos, C.A. Linkous, Electrocatalytic activity of metal phthalocyanines for oxygen reduction, Journal of Electroanalytical Chemistry. 339 (1992) 13–30.

[40] J.H. Zagal, S. Griveau, J.F. Silva, T. Nyokong, F. Bedioui, Metallophthalocyanine-based molecular materials as catalysts for electrochemical reactions, Coordination Chemistry Reviews. 254 (2010) 2755–2791.

[41] P. Quaino, N.B. Luque, R. Nazmutdinov, E. Santos, W. Schmickler, Why is gold such a good catalyst for oxygen reduction in alkaline media?, Angewandte Chemie - International Edition. 51 (2012) 12997–13000.

[42] P. Rodriguez, M.T.M. Koper, Electrocatalysis on gold, Physical Chemistry Chemical Physics. 16 (2014) 13583–13594.

[43] S. Yoshimoto, A. Tada, K. Suto, K. Itaya, Adlayer structures and electrocatalytic activity for O2 of metallophthalocyanines on Au(111): In situ scanning tunnelling microscopy study, Journal of Physical Chemistry B. 107 (2003) 5836–5843.

[44] S. Yoshimoto, A. Tada, K. Itaya, In Situ Scanning Tunnelling Microscopy Study of the Effect of Iron Octaethylporphyrin Adlayer on the Electrocatalytic Reduction of O2 on Au(111), Journal of Physical Chemistry B. 108 (2004) 5171–5174.

Chapter 2

Scanning Tunnelling Microscopy: Theory and Applications

In the early 1980s, the Scanning Tunnelling Microscope (STM) made his first appearance as a fundamental tool for studying surface structures and electronic properties of molecules. The invention owes to Gerd Binning and Heinrich Rohrer from IBM research laboratory in Zürich [1,2]. Further implementation led G. Binning, H. Rohrer, C. Gerber and E. Weibel to the successful imaging of 7x7 reconstructed Si(111) crystals and of Au(110) crystals [3]. In the 1959 speech entitled "There's Plenty of Room at the Bottom", Richard Feynman challenged scientists to see individual atoms distinctively, and to arrange them in a controlled way [4]. In 1986 Binning and Rohrer won the Nobel Prize in physics, with an invention that still nowadays represents a powerful tool able not only to merely observe a surface, but also to modify and manipulate it in the way we desire.

Scanning tunnelling microscopy is based on the quantum-mechanical phenomenon of electron tunnelling through a finite potential barrier between two conducting materials, which is possible thanks to the application of a bias voltage. To achieve high vertical and lateral resolution, one conductive material is shaped into a sharp tip, and it is scanned over a sample surface with a highly precise piezoelectric system. The tunnelling current is the collected signal, [5] and an advanced electronic system directly correlates it to the topography of the surface, resulting in a colour-mapped 2D or 3D image. The careful inspection and interpretation of the final STM pictures provides information of the surface structure, reactivity, modification, and many other different phenomena at the microscopic scale of matter depending on the measuring conditions.

A major improvement of STM was its extension from UHV to liquid environment, opening to the possibility of studying all the correlated processes to this special interface. Indeed, Sonnenfeld and Hansma managed to atomically resolve the surface structure of HOPG samples at the solid/water interface [6], unveiling the potentialities of imaging in a liquid, thus mimicking the conditions for important biological processes (DNA replication, enzymatic catalysis, membrane transport) [6]. Not only biological processes, but also corrosion of metals, etching of semiconductors, electrodeposition and dissolution of minerals can be potentially studied as solid/liquid interface phenomena [7].

An even more peculiar case arises when the liquid is represented by an electrolytic solution. The concept is to perform STM directly in an electrochemical environment (EC-STM), therefore under potential control of the sample, which acts at the same time as a working electrode of a "Four-Electrode Setup". This enables the investigation of a system at the solid/electrolyte interface, offering in addition the ability to tune its behaviour upon proper polarisation of the sample, being at the same time the working electrode. In this way, essential information can be obtained for the electrode/electrolyte interface, and electrochemical processes can be controlled, induced or inhibited.

In this work, the process of oxygen reduction reaction (ORR) on metal porphyrin-modified substrates will be examined by means of EC-STM, studying the influence that these metal-centred macrocycles exert on ORR as models of some of the most performing non-PGM ORR electrocatalysts. Additional information will come from complementary electrochemical characterisations, enriching and corroborating the EC-STM experimental observations.

2.1 Basic concepts of UHV-STM

Considering that STM was originally developed to work in in Ultra High Vacuum (UHV) environment, the first subjects of study were typically represented by single crystal surfaces. Therefore, it is worth reporting here under a simple calculation for the contamination rate of a surface [8]. The incident flux of gas molecules is proportional to the gas density and the average molecular velocity:

$$F = \frac{1}{4}\rho v \qquad 2.1$$

ρ can be calculated by the ideal gas law, being the number of molecules per volume: $pV = Nk_BT$, leads to $\frac{N}{V} = \rho = \frac{p}{k_BT}$. The mean velocity is given by Maxwell speed distribution, as: $v = \sqrt{\frac{8k_BT}{\pi m}}$. Therefore, the flux of incident molecules becomes:

$$F = \frac{1}{4}\rho v = \frac{1}{4}\left(\frac{p}{k_BT}\right)\left(\sqrt{\frac{8k_BT}{m\pi}}\right) = \frac{p}{\sqrt{2\pi m k_BT}} \qquad 2.2$$

The result is a number of molecules impacting the surface per square meter per second. A flux of $10^{27}\,\frac{molecules}{m^2 s}$ is attainable at environmental pressure (~760 Torr), while a flux of $10^{15}\,\frac{molecules}{m^2 s}$ is obtained at $\sim 10^{-9}\ Torr\ (\sim 10^{-9} mbar, UHV)$.

A lower time limit for surface contamination (i.e. formation of a monolayer of adsorbed species) can be calculated in the simple case of unitary sticking coefficient. The sticking coefficient S is a measure of the tendency of a species to adsorb (stick) onto a surface, and it is defined as the ratio of molecules impacting on the surface versus the number of molecules that stick on it. Sticking coefficients therefore vary from 0 (no adsorption) to 1 (maximum adsorption). Since the surface concentration is typically in the order of $10^{15}\,\frac{atoms}{cm^2}$, and upon assuming S=1, for a pressure of 760 Torr the corresponding time for monolayer contamination is $3.44\ 10^{-9}\ s$. For a pressure of $10^{-9}\ Torr\ (\sim 10^{-9} mbar)$, the monolayer formation time is $2.61\ 10^{3}\ s$. It is therefore clear that working at ambient pressure, in a "relatively low safe environment" poses serious concern about the capability of dispose of a clean substrate. Furthermore, the sticking coefficient is strongly dependent on other factors, such as temperature, surface coverage,

exposed crystallographic face and of course it changes on the basis of the adsorbing molecule. However, in the present research project, HOPG and Au(111) single crystals were the only substrate used, and this minimizes the problem of contamination since Au(111) is known to exhibit a low tendency to contamination [9].
The physical phenomenon at the basis of STM is the tunnelling of electrons through a potential barrier, even if the electrons should not possess enough energy to overcome that barrier. However, if the separation between the two conductive materials is made considerably small (few Angstrom), then the wave functions describing tip and sample can superimpose, allowing the tunnelling of electrons through the tip-sample gap. A general and elementary theory for electron tunnelling through a one-dimensional potential barrier is now presented, followed by more detailed theoretical descriptions. Figure 1.1 conveniently depicts the hereafter presented mathematical treatment of tunnelling.

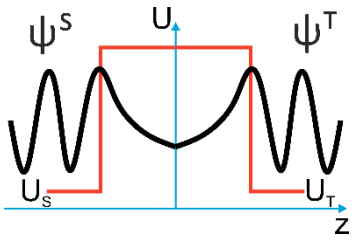

Figure 1.1 Schematic representation of a finite potential barrier which is penetrated by electron wavefunctions of sample and tip.

From a classical point of view, for a finite potential barrier with energy *U*, if an electron possesses an energy *E<U*, then it is unable to overcome the barrier. Considering quantum mechanics, the electron feeling a one-dimensional potential barrier *U(z)* is described by a wavefunction ψ(z), which must satisfy the Schrödinger equation:

$$-\frac{\hbar^2}{2m}\frac{d^2}{dz^2}\psi(z) + U(z)\psi(z) = E\psi(z) \qquad 2.3$$

The sample surface is located at *z=0*, while the tip is found at *z=s*.
Considering $U_s=U_t=-U$, when E>U, solutions to Schrödinger equation are:

$$\psi(z) = \psi(0)e^{\pm ikz} \qquad 2.4$$

Within the barrier, the solution is:

$$\psi(z) = \psi(0)e^{-\chi z} \qquad 2.5$$

since the electron penetrates through the barrier along the *z* direction. The probability density of finding the electron at a point *z* is the square modulus of the solution: $|\psi(z)|^2 = |\psi(0)|^2 e^{-2\chi z}$.
Propagation is possible also in the opposite direction, namely *-z*, and tunnelling is then bidirectional.

The incident current density is:

$$J_{inc} = -i\frac{\hbar}{2m}\left(\psi_1^*(z)\frac{d\psi_1(z)}{dz} - \psi_1(z)\frac{d\psi_1(z)}{dz}\right) \quad 2.6$$

while the transmitted one is:

$$J_{tr} = -i\frac{\hbar}{2m}\left(\psi_3^*(z)\frac{d\psi_3(z)}{dz} - \psi_3(z)\frac{d\psi_3(z)}{dz}\right) \quad 2.7$$

The ratio between transmitted and incident current density is:

$$T = \frac{J_{tr}}{J_{inc}} = \frac{1}{1 + \frac{(k^2+\chi^2)^2}{4k^2\chi^2}(\chi s)} \quad 2.8$$

In the limit of a strong attenuating barrier (U>>E), $\chi = \frac{\sqrt{2m(|U|-E)}}{\hbar}$ and $k = \frac{\sqrt{2m(E-|U|)}}{\hbar}$, the expression becomes:

$$T \approx \frac{16k^2\chi^2}{(k^2+\chi^2)^2} \cdot e^{-2\chi s} \quad 2.9$$

From this basic quantum mechanical treatment, a basic explanation of the tunnelling phenomenon was figured out. Note that the decay constant magnitude is dictated by the materials work functions (ϕ_S and ϕ_T), defined as the minimum energy necessary to remove an electron from the bulk to the vacuum level. U_s and U_t can be replaced with the work functions of sample and tip, respectively. The decay constant becomes: $\chi = \sqrt{\frac{2m\phi}{\hbar}} \backsim 1$ Å. This explains the high vertical resolution reached by STM, since for small variations in the sample topography produce large variations in the measured tunnelling current. A high lateral resolution can also be attained, provided that the tip-sample distance ΔZ is much smaller than the tip radius. Indeed, the distance to the sample surface varies as $\Delta Z \backsim \frac{\Delta x^2}{2R}$, where Δx is a point on the tip and R is the tip radius of curvature. Considering the tunnelling current equation derived for the one-dimensional potential barrier case (equation 2.7), then the lateral current distribution becomes:

$$I(\Delta x) \backsim e^{-2\chi\frac{\Delta x^2}{2R}} \quad 2.10$$

For $R = 10$ Å and $\Delta x \backsim 4.5$ Å, the lateral current distribution becomes $I(\Delta x) \backsim e^{-2}$. Therefore, a current column of $\backsim 9$ Å represents the lateral resolution limit. Disregarding the precise value, the order of magnitude indicates high lateral resolution, as well.

A more detailed mathematical and quantum mechanical description of the tunnelling phenomenon is provided by Bardeen and it is called the transfer Hamiltonian method [10].

The main assumptions are now presented, together with the main results, avoiding an excessive mathematical notation for the sake of conciseness and simplicity. In this model, electron tunnelling is treated as a one-particle process, neglecting interactions among electrons. The direct interaction of tip and sample state resulting in the formation of coupled electronic states is neglected [11]. Inelastic tunnelling is disregarded for the sake of simplicity, considering no energy loss for the tunnelling electrons.
When the distance between tip and sample is made sufficiently small, the time-dependent Schrödinger equation containing the sum of tip and sample potential functions governs the tip-sample system. It can be written as:

$$i\hbar\frac{\partial\psi}{\partial t} = \left(-\frac{\hbar^2}{2m}\frac{\partial^2}{\partial z^2} + U_S + U_T\right)\psi \qquad 2.11$$

The state ψ of the system can be written as a linear combination of sample and tip eigenfunctions, which should form an orthogonal basis set:

$$\psi = a_\mu(t)\psi_\mu^S e^{-iE_\mu^S t/\hbar} + \sum_{\nu=1}^{\infty} c_\nu(t)\psi_\nu^T e^{-iE_\nu^T t/\hbar} \qquad 2.12$$

At the first-order time dependent perturbation theory, substituting (2.12) into Schrödinger equation (2.11), the result is:

$$i\hbar\frac{dc_\nu(t)}{dt} = \langle\psi_\mu^S\rangle\, e^{-i\left(E_\mu^S - E_\nu^T + i\eta\right)t/\hbar} \qquad 2.13$$

$\langle\psi_\mu^S\rangle$ is the tunnelling matrix element ($\langle\psi_\mu^S\rangle = M_{\mu\nu}$) and it describes the projection of the initial state ψ_μ^S perturbed by the tip potential U_T onto the final state ψ_ν^T. Finally, integrating equation 13 over time, the expression for $c_\nu(t)$ becomes:

$$c_\nu(t) = \frac{1}{E_\mu - E_\nu + i\eta} M_{\mu\nu}\, e^{-i\left(E_\mu^S - E_\nu^T + i\eta\right)t/\hbar} \qquad 2.14$$

The square modulus of $c_\nu(t)$ stands for the probability that an electron, described by a state ψ_μ^S at $t = -\infty$, populates a state ψ_ν^T at time *t*. Finally, the tunnelling probability per unit time is:

$$P_{\mu\nu}(t) = \frac{d}{dt}|c_\nu(t)|^2 = \frac{2\eta}{\left(E_\mu^S - E_\nu^T\right)^2 + \eta^2} e^{2\eta t/\hbar}\frac{1}{\hbar}\left|M_{\mu\nu}\right|^2 \qquad 2.15$$

In the limit $\eta \to 0$, the Fermi's Golden rule is obtained:

$$P_{\mu\nu}(t) = \frac{2\pi}{\hbar}\delta\left(E_\mu^S - E_\nu^T\right)\left|M_{\mu\nu}\right|^2 \qquad 2.16$$

Where δ represent the Delta function, which guarantees elastic tunnelling, and the tunnelling current is proportional to $eP_{\mu\nu}$.
So far, the tunnelling process was considered to occur from a single state of the sample μ to a single state of the tip ν, but tip and substrate should be described with a continuous

spectrum of states, whose occupation is dictated by Fermi-Dirac distribution. Considering an applied bias voltage *V*, the expressions for the tunnelling current from sample to tip and from tip to sample can be written as, respectively:

$$I_{S\to T} = \frac{4\pi e}{\hbar}\sum_{\mu\nu} f\left(E_\mu^S - E_F^S\right)\left[1 - f(E_\nu^S - E_F^T)\right]\left|M_{\mu\nu}\right|^2 \delta\left(E_\nu^T - E_\mu^S - eV\right) \quad 2.17$$

$$I_{T\to S} = \frac{4\pi e}{\hbar}\sum_{\mu\nu} f\left(E_\mu^T - E_F^T\right)\left[1 - f(E_\nu^S - E_F^S)\right]\left|M_{\mu\nu}\right|^2 \delta\left(E_\nu^T - E_\mu^S - eV\right) \quad 2.18$$

The net tunnelling current is given by the difference with the above expressions 2.17 and 2.18, and is:

$$I = \frac{4\pi e}{\hbar}\sum_{\mu\nu}\left[f\left(E_\mu^S - E_F^S\right) - f\left(E_\mu^T - E_F^T\right)\right]\left|M_{\mu\nu}\right|^2 \delta\left(E_\nu^T - E_\mu^S - eV\right) \quad 2.19$$

Discrete states can be replaced with the corresponding density of states, n^S and n^T. The net tunnelling current is then:

$$I = \frac{4\pi e}{\hbar}\int_0^{eV} d\epsilon\, n^T(E_F^T - eV + \epsilon) n^S(E_F^S + \epsilon)|M|^2 \quad 2.20$$

In the limit of small bias voltage:

$$I = \frac{4\pi e}{\hbar} V n^T(E_F^T) n^S(E_F^S)|M|^2 \quad 2.21$$

It is worth calculating the differential conductivity, namely the first derivative of the current versus the voltage, given by:

$$\frac{dI}{dV} = \frac{4\pi e}{\hbar} n^T(E_F^T) n^S(E_F^S + eV)|M(E_F^S + eV, E_F^T)|^2 \quad 2.22$$

for which a change of the sign of the voltage bias *V* allows access to occupied or unoccupied states of the sample, alternatively.

The measured sample could be characterised by the presence of molecules, which often present vibrational modes or spin excitation modes. The tunnelling current can trigger these excitation mechanisms, and consequently the tunnelling electrons lose part of their energy. In these cases, an additional term can be added to the expression of the tunnelling current (equation 21) in order to account for the inelastic tunnelling phenomena [5,12–15]. Further development to the Bardeen's tunnelling theory was brought forth by Tersoff and Hamann. The difficult access to the tip states is herein overcome by representing the tip with potential and wave functions arbitrarily localized (modelled as a geometrical point). Therefore, the STM tip measures properties of unperturbed surfaces, rather than a convolution of tip and sample states. The Tersoff-Hamann model is quite effective to describe superstructures with sizes > 10 Å, while for smaller sizes at the molecular or

atomic scale it lacks information coming from the convolution of tip and sample electronic states [5].

2.2 Tunnelling through an electrolyte

Translating the concepts of electron tunnelling from UHV to the solid-liquid interface is not straightforward, because additional phenomena must be taken into account. A unique tunnelling theory has not been developed yet. Anyway, some quantitative results have been experienced, providing at least some guidelines to more detailed theoretical studies. An unambiguous point is that water exerts an effect on the tunnelling phenomenon, and variations of the tunnelling current can be detected [16]. This means that the effective barrier height for electron tunnelling has changed. Moreover, tunnelling at the solid/liquid interface causes the tip to certainly deal with an easier contamination, since high electric fields applied in a confined space between tip and sample can attract and accumulate impurities [16,17].
Schmickler and Henderson described the flat metal electrode surface as a jellium, i.e. they represent the metal as a homogeneous electron gas with a uniform positively charged background. The tip is considered as a jellium sphere, and water as a dielectric mean. The outcome is a reduced effective barrier height than the corresponding barrier heights detected in vacuum [16,18].
Sass and Gimzewski [19] pointed out the ionicity character carried by the apex atom of the tip, which is expected to give rise to a stronger interaction with the solvent molecules, forming a partial hydration shell around it [19]. Another aspect is the ability of water molecules to form localised regions of electrostatic attractive potential, which can be attained within two main mechanisms. The first is connected to the librations of the hydrogen-bonded water network, which can lower the tunnelling barrier, favouring electron transfer through the gap. The second concerns the solvent polarization due to the leakage of electronic charge by the tip, which again results in a lowering of the tunnelling barrier [19].

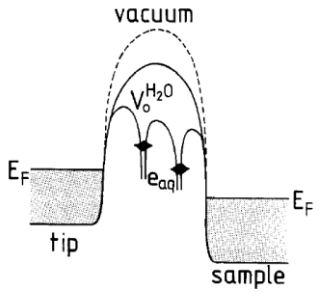

Figure 1.2. Lowering of the tunnelling barrier as consequence of solvent polarisation. Figure from [19].

That of Sass [19] was a forethought of the theory of tunnelling via intermediate states, meaning that electrons can tunnel from tip to sample (or vice versa) by passing through one or more intermediate states. Intermediate states are represented by hydrated electrons or dipole resonances [16,19,20]. The theory of intermediate states was developed by Halbritter [20]. He performed systematic Distance Tunnelling Spectroscopy and Voltage

Tunnelling Spectroscopy to modelise electron tunnelling in presence of a solid/electrolyte interface, assigning a primary role to intermediate states localised in the tunnelling gap. Their origin is connected with dipole resonances of ordered water molecules within the tunnelling gap. Assuming an exponential decay of the tunnelling current with respect to the tunnelling gap *d* of the type:

$$I_T(d) \propto e^{-2kd} \tag{2.23}$$

If one intermediate state is located in the tunnelling barrier, a "resonance" can occur, and the electron travels from the tip to the sample (or vice versa) passing through the intermediate state, and so a new expression of the tunnelling current can be written as:

$$I_{T,1}(d) \propto \rho_{l,0}\, e^{-\frac{2kd}{2}} \tag{2.24}$$

Where $\rho_{l,0}$ stands for the uniform distribution of localised states. *k* is the inverse decay length and it depends on the effective tunnelling barrier ϕ_{eff}:

$$k \propto \left(\phi_{eff}\right)^{1/2} \tag{2.25}$$

$I_{T,1}$ has a slower decay with *d*, namely a weaker distance dependence than I_T, which would be further weakened if *n* intermediate states are present in the gap, leading to a reduced effective tunnelling distance *d*:

$$d_{eff} = \frac{d}{n+1} \tag{2.26}$$

The tunnelling barrier becomes:

$$\phi_{eff} = \frac{\phi_0}{(n+1)^2} \tag{2.27}$$

Notice that, the higher the number of intermediate states, the lower is the effective tunnelling barrier, thus the higher should be the measured tunnelling current.
Intermediate states are herein interpreted as dipole resonances related to water molecules, which form layers uniformly covering the tip and the working electrode surface. The orientation of the molecules and the thickness of the resulting layers can be influenced by the chemical nature of the electrolyte, crystallographic orientation of the sample, and the presence of adsorbed species. Tunnelling through localised states is generally associated to a low number of intermediate states (1 to 3), since higher numbers would be affected by a bad signal/noise ratio.
Pan et alii [21] measured the energy barriers for electron tunnelling between a Pt-Ir tip and a gold sample under potential control, observing a strong dependence on the applied bias between tip and sample. A sharp dip was noticed at zero bias, attributing this effect to the induced polarization of the tunnelling gap.
Vaught et alii [22] found that, in water, rapid changes of the inverse decay length for tunnelling occur at tunnelling gaps where there are as many as three water molecules spanning in the gap. This was mainly explained as a changeling water structuration at the

solid-liquid interface, also considering a possible quantum mechanical effect when water cluster-size is below 100 molecules.
Mosyak et alii performed numerical simulations of electron tunnelling in water, finding an effective barrier lowering with respect to UHV [23]. However, additional effects were considered, finding out for example that a reduction in the tunnelling is caused by multiple scattering events of the electrons impacting with hard oxygen cores of water in the gap. Moreover, multiple scattering with oxygen atoms distorts and diffuses the tunnelling current, provoking loss of resolution, especially if the gap is large enough to accommodate water molecules.
Finally, the Hugelmann and Schindler study is reported [17,24]. Herein, the effect of the presence of water molecules in the tunnelling gap is analysed. A non-exponential decay of the tunnelling current with respect to the tunnelling gap *d* is revealed. An oscillatory tunnelling probability, with a period of 0.35 nm, was observed. This oscillation period is close to the predicted distance of water molecules in the Helmholtz layer of the solid/liquid interface. In fact, after the jump to contact of the tunnelling current at *z=0* (the sample surface), the tunnelling phenomenon initially behaves like in UHV, since the gap is still too small to accommodate any water molecule. In other words, the barrier increases with increasing gap width. When a gap of *z=0.15 nm* is reached, the barrier starts to decrease, because water molecules start to accommodate in the gap. When a gap width of 0.35 nm is realised, a complete layer of molecules is formed, and the tunnelling barrier height experiences a minimum. Then, it starts to increase up to *z=0.55*, distance at which new water molecules can accommodate in the gap. This brings to *z=0.70 nm*, where a full second layer of water molecules is formed, and the tunnelling barrier shows, as expected, a minimum. Therefore, tunnelling barrier minima occur each time a new water layer is completed within the tunnelling gap.

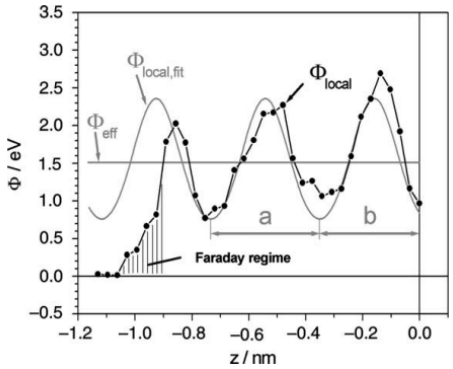

Figure 1.3. Oscillatory trend of the tunnelling probability with a period *a = 0.35 nm*. Figure from [18].

2.3 Operating modes for an STM

A scanning tunnelling microscope can basically work with two distinct operating modes. In most cases, like for this work, images are collected within the *constant current* mode. This means that the tunnelling current that flows between tip and sample is held constant. Since tunnelling current and tip-sample distance are exponentially linked (section 2.1), fixing the tunnelling current requires the tip-sample distance to be also kept constant.

However, each sample would have a certain surface roughness, and the tip-sample distance should be almost continuously varied during the scan. This can be accomplished thanks to the electronic circuit, whose core is constituted by operational amplifiers. These amplifiers, in fact, are part of a feedback loop circuit. The measured signal is recorded but at the same time it is used as feedback for the following scans. Namely, if the feedback loop detects an increase of the current (for example, due to a protrusion or to a different LDOS), a voltage response is sent to the piezoelectric scanner, which eventually would slightly withdraw to maintain the current constant. As a result, the vertical movement of the tip, coupled with its lateral displacement during the scan, generates a topographic profile. Combining all the recorded topographic profiles during the collection for one image, and assigning a colour hue to each height value, the final STM picture is obtained. STM images are then 2D projection of consecutive topographic profiles.
STM can also operate in *constant height mode*. In this case, the tip is scanned across the sample surface without electronically adjusting its height value, which is therefore constant. Image acquisition can be rather fast, but it accounts for a higher risk of blunting the tip due to surface roughness. This operating mode should in fact be employed only for very flat and defect-free surfaces.
Constant current mode is therefore preferentially chosen, being a slower but safer image acquisition technique, which can be employed for samples with a certain roughness to minimise tip blunting. It is also suitable for samples with unknown topography, or for samples whose topography may vary during scanning, due to for example a varying applied working electrode potential.

2.4 From theory to practical considerations (the role of the applied bias voltage)

The final STM image strongly depends on sign and magnitude of the applied voltage bias between tip and sample [25–27]. The hereby employed EC-STM instrumentation actually performs the polarisation on the tip, being the sample electrically grounded [5,28,29]. Therefore, for a negative bias voltage value, the Fermi level of the tip is raised, and electrons can "flow" from the tip to the unoccupied states of the sample, namely its LUMO. Contrary, when the bias voltage is positive, the tip Fermi level is reduced, and electrons can flow from the sample (HOMO) to the tip [30].

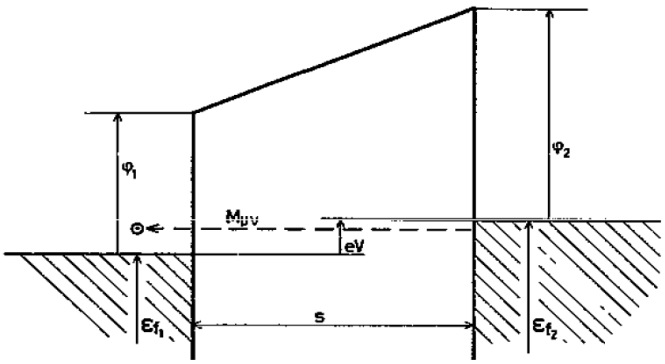

Figure 1.4. The Fermi level of the tip (right part) is raised and electrons flow to the HOMO of the sample (left part) [28].

From these considerations, one can understand that nearly every STM image is the result of a convolution between physical geometry and local density of states (LDOS) of the sample (note that also geometry and density of states of the tip should be considered, according to section 2.1).
Let us now describe more in detail how the LDOS can affect the final STM image. A simple metal-insulator-metal junction can be taken into account as a tip-UHV-sample model. The sample is not charged and electrons populate its bands up to the Fermi level. If nothing is present in the tunnelling gap (UHV), then the tunnelling current is proportional to the voltage bias and to the negative exponential of the tunnelling gap and of the work function, as shown in section 2.1. This is the case of the elastic tunnelling, because the electrons transmitted from the tip to the sample (or viceversa), passing from the UHV, lose no energy. Inelastic tunnelling arises when molecules are present in the gap between tip and electrode. In this condition, the tunnelling electrons can interact with time-varying molecular dipoles and cause an electronic or vibrational excitation of the molecule. For a vibrational motion with associated energy equal to $h\nu$, the inelastic tunnelling channel is open at $V_{bias}=\frac{h\nu}{e}$. A further increase of V_{bias} results in an increase of the final tunnelling current, and this opens the path to IETS (inelastic electron tunnelling spectroscopy) [25]. Additionally, new and more intense signals could be systematically observed but not explained with traditional IET. It is the case of OMT (orbital mediated tunnelling). This happens when the energy of the tunnelling electrons matches the one of a molecular state. The OMT mechanisms can be different. One possibility is the true resonance, when the residence time of the tunnelling electron is neglectable compared to nuclear motion. Another option is the oxidation or reduction of the molecule with a thermally induced return to the initial state. Finally, a redox reaction can occur too rapidly for thermal relaxation [25]. Within OMT, the voltage bias assumes a major role. We first remember that, when $V_{bias}<0$, the tip is negatively polarised in our instrumentation, meaning that empty states of the sample are probed (LUMO). Conversely, when $V_{bias}>0$, filled states are imaged (HOMO). Additionally, if the voltage bias equals the energy value of either the LUMO or the HOMO, then a OMT path is opened, and tunnelling is somewhat enhanced, registering therefore an increase in the measured tunnelling current. This would be well visualised in the form of peaks in a scanning tunnelling spectrum, where the differential tunnelling current $\frac{di_T}{dV}$ is plotted versus V_{bias} [25]. Nevertheless, an effect can be seen also in regular STM images. An example is hereafter reported. In figure 1.5, a mixed layer of NiTPP and CoTPP is displayed at different voltage bias values. At V_{bias}=-1.4 V, the two components can barely be distinguished, but at V_{bias}=-1.0 V some molecules appear rather bright, together with other molecules which did not change contrast [25,31]. This can be explained with OMT, since at V_{bias}=-1.0 V a fraction of tunnelling current is mediated by the Co(II) frontier orbitals [25,31].

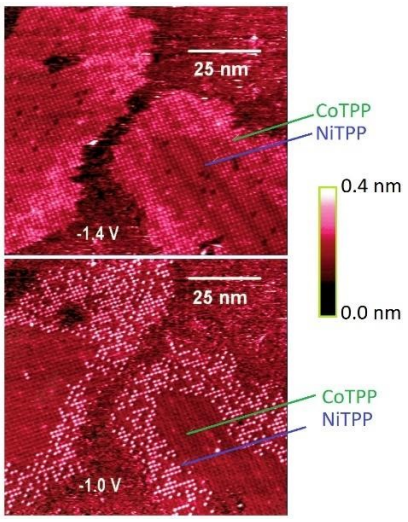

Figure 1.5. STM images of mixed composition islands of NiTPP and CoTPP at different bias voltages. At U_b = -1.4 V the two components are almost undistinguishable, whilst at U_b = -1.0 V CoTPP units display a sharp bright spot as consequence of orbital mediated tunnelling. Figure adapted from [31].

2.5 Beyond instrumental features

Some physical concepts are now presented for what concerns mere instrumental features, in particular tip positioning, tip shape and the vibration isolation issue. Although appearing simple or obvious, these aspects have a huge impact on the successful result of EC-STM measurements.

2.5.1 The physics of tip positioning

The tip is scanned onto the sample thanks to two positioners. A coarse positioner controls the coarse approach (or retraction) of the tip with respect to the sample, allowing the tip to quickly cover large distances (0.3 mm). A coarse positioner can be distinguished basically in three types: Mechanical, Louse or Beetle. The STM unit herein described features a Beetle-type coarse positioner, also known as Besocke positioner, as it was firstly introduced by K. Besocke in 1987 [32]**.** It consists of three piezoelectric tubes (Piezolegs) mounted on a fixed plate, together with the holder containing the PEEK cell with the sample. A depiction of the piezoleg system is shown in figure 1.6.

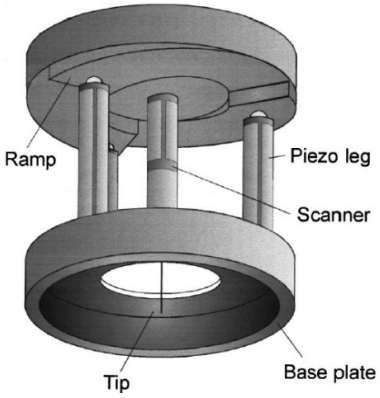

Figure 1.6. Draw of the piezoleg system for a Besocke positioner [33].
The tip is mounted on a cylindrical ramp, which is leaned onto the three piezolegs. Each piezoleg terminates with a 2 mm radius stainless steel sphere, which is glued to the piezoelectric tube in order to provide electrical isolation. Upon application of a proper voltage, the piezoelectric tubes oscillate, and the cylindrical ramps start rotating, thus pulling the tip forward (or backward). The voltage is then quickly reduced and the balls return to their original positions. Due to inertia of the ramp, the balls slip on it when returning to their original position, being now ready to a new voltage application. This "stick-and-slip" procedure is repeated until the feedback loop reaches a set-point tunnelling current. From there on, the approaching must be manually accomplished by forcing the stick-and-slip mechanism up to a tunnelling current value in the range [-300; +300] arbitrary units. The arbitrary units derive from instrumental calibration and a value belonging to the [-300; +300] a.u. range guarantees stable tunnelling conditions.
A fine positioner is made out of a piezoceramic tube, also called piezo-tube. This material exhibits piezoelectric effect, which means that if a mechanical stress is applied to the piezoceramic material, an electric field is generated. The corresponding electric polarisation is given by:

$$P_i = d_{ijk}\,\sigma_{jk} \tag{2.28}$$

The stress σ_{jk} is a second rank tensor, while the piezoelectric modulus d_{ijk} is a third rank tensor, but it is symmetric in the last two indexes (i.e.: $d_{ijk} = d_{ikj}$).
Alternatively, if an electric field is applied, the piezoceramic material undergoes a mechanical strain (inverse piezoelectric effect):

$$\varepsilon_{jk} = d_{ijk}E_i \tag{2.29}$$

Symmetry properties of crystals play a major role in determining piezoelectricity [34]**.** The piezoelectric tensor should in fact vanish in centre-symmetric crystals. Of the remaining 21 non-centre-symmetric crystallographic classes, 20 are compatible with piezoelectricity: despite being non-centre-symmetric, the 432 crystallographic class does not exhibit piezoelectricity due to annihilation of charges along the <111> polar axes.
To further elucidate piezoelectric properties, the following figure 1.7 is taken into exam.

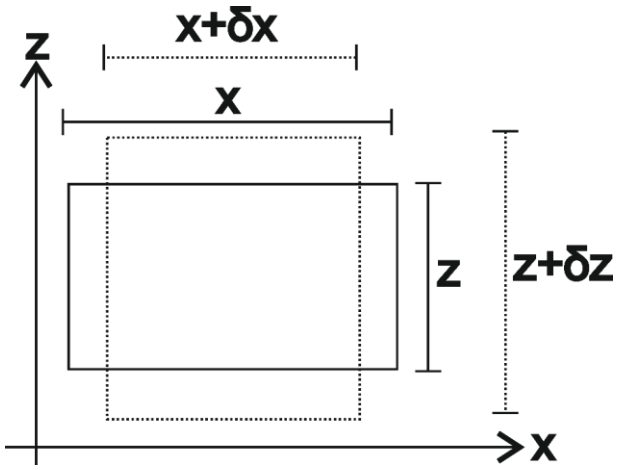

Figure 1.7. Scheme of a two-dimensional piezoelectric slab.

For the sake of convenience, a two-dimensional system is taken into account, with only *x* and *z* directions. If a voltage V is applied to a piezoelectric slab of thickness *z*, the corresponding uniform and stationary electric field will be defined as $E_z = \frac{V}{z}$. As a result, a strain in the *xz* plane is generated: $\varepsilon_x = \frac{\delta x}{x}$, $\varepsilon_z = \frac{\delta z}{z}$.

Typical values for piezoelectric coefficients are meters/Volts. These materials are therefore extremely sensitive, since a 1 V change in the applied voltage can turn into tens of nanometres difference in the tube length. Hence, these materials are suitable for STM imaging, which requires precise movements of the scanning tip with an accuracy of less than 0.1 Å.

Focusing on the experimental setup, the case of a piezoelectric tube must now be considered, since the tip is fitted into a piezoelectric tube, namely a tube made out of piezoelectric material. In particular, the inverse piezoelectric effect is exploited, obtaining a tube able to deform upon electric field application. For this purpose, four electrodes are realised on the external side of the tube and one contact is realised inside the tube itself. The four outer electrodes allow displacements of the tip in a parallel plane with respect to the sample surface. In this way, the tip can be swept over the surface sample, covering areas from 1 x 1 nm up to 1000 x 1000 nm. The inner electrode enables tip extension/retraction of ±100 nm along the perpendicular direction with respect to the sample surface.

Displacements in the *xy* plane are achieved by voltage application to two opposite electrodes. For example, a lateral displacement Δx along *x* direction is given by applying voltages of $-U_x$ and $+U_x$, respectively, to the two opposite electrodes placed along *x* direction: $\Delta x = \frac{2\sqrt{2}d_{xz}l^2U_x}{\pi Dh}$, with *l* length of the tube, *h* wall thickness, *D* the diameter of the tube.

A displacement in the vertical direction Z is accomplished by applying a voltage between the inner electrode and the four outer electrodes. The vertical displacement is then: $\Delta z = \frac{d_{xz}lU_z}{h}$ [35].

2.5.2 Tip shape

The tunnelling tip has a major role in determining the resolution capability of the STM unit. Indeed, if the tip is properly prepared, atomic resolution is readily achievable [36]. As already described, there exists an exponential dependency of the tunnelling current with respect to the tip-sample distance. For this reason, an ideal tip should terminate with a single atom in order to determine a precise tunnelling condition. However, real tips may more often present more than one atom at the very end of the tip, thus causing a general worsening of the tunnelling events. As a result, atomically sharp tips will properly follow surface protrusions, trenches and pits, thus providing an accurate representation of the sample topography. Conversely, a pyramidal-shaped or blunt tip will only approximately follow the surface roughness, hence providing a poor representation of the sample topography. If the tip has a particularly large termination, the sample itself can act as an imaging

probe, thus leading to an effective imaging of the tip. These concepts are depicted in figure 1.8.

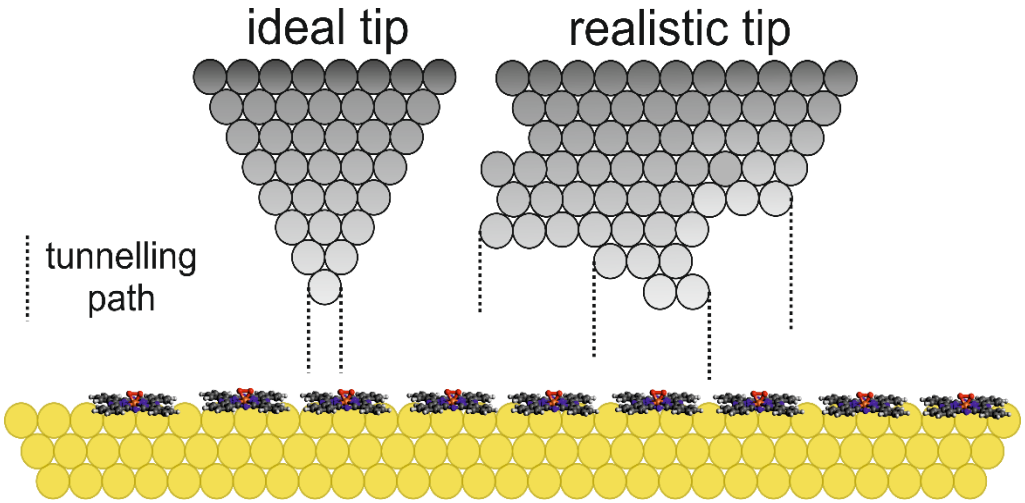

Figure 1.8. Visual representation of an ideal (left) and a realistic (right) tip.

Obtaining a small radius-of-curvature tip is therefore essential. Tips can be fabricated by mechanical grinding or cutting of metal wires, but usually these procedures lead to large radius-of-curvature tips, double tips, or blunt tips. The most common and reliable method for obtaining sharp tips is electrochemical etching. This procedure is further described in section 3.2.2.

2.5.3 Vibration isolation

Topographic profiles measured in constant-current mode are usually in the range of 10^1 - 10^2 pm. This means that the instrumentation must be extremely sensitive and accurate, and that small vibrations of even few μm, not detectable by eye, would be deleterious for STM imaging. Therefore, every source of vibration must be eliminated, or at least reduced down to 0.001 pm (two orders of magnitude less than operation range of STM). The two major issues are external vibrations, not related to the STM instrumentation, and inner vibrations, caused indeed by the instrumentation itself. Vibrations commonly found in the laboratory environment span from 1 to 100 Hz. It is the case of ventilation ducts, transformers and motors (6-65 Hz), or simply walking and working (1-3 Hz) nearby the instrumentation. Conversely, inner vibrations usually possess higher frequencies, from 1 to 100 kHz, and are often associated to the internal resonance frequency of the particular STM unit.
Various strategies are adopted to reduce, at the same time, inner and external vibrations, like suspension springs, rubber feet, heavy platforms. One of the most significant mean of vibration minimisation is represented by suspension springs and a noteworthy mode of operation description is provided herein. The suspension spring system consists in the combination of four steel springs coupled with a heavy granite plate, on which the STM unit is fixed. The resonance frequencies for vertical and lateral motion are, respectively:

$$f_{vertical} = \frac{1}{2\pi}\sqrt{\frac{k}{m}}\ ;\ f_{lateral} = \frac{1}{2\pi}\sqrt{\frac{g}{L}} \qquad 2.30$$

For vertical motion, the simple motion of a mass *m* attached to a spring with *k* spring constant is considered. For lateral motion, the case of a simple pendulum is considered: it is the case of a point mass suspended to a wire of negligible mass and length equal to L, which undergoes small amplitude oscillations.

2.6 Electrochemistry

Some theoretical concepts concerning electrochemistry are now presented. They are devoted to describing the main features regarding electrode interface as fundamental aspects related to STM and a brief description of hydrodynamic methods is also provided in view of experimental results presented in chapter 5.

2.6.1 Potential Differences

When a metal and an electrolyte are put to contact, microscopic changes take place at the interface. These phenomena are better described further on section 2.6.2. A charge q^M resides on the surface of the metal and it therefore originates an opposite charge in the liquid phase, $-q^S$. The two charges exactly compensate: $q^S = -q^M$
In this case, the charge on the metal surface is assumed to have a negative value. The potential profile is depicted in figure 1.9.

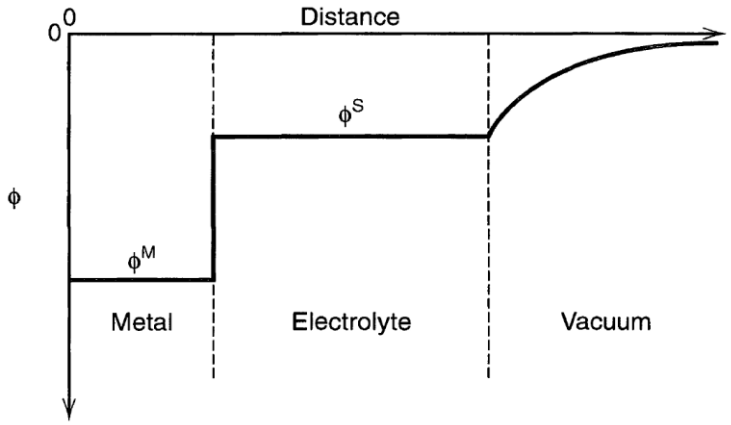

Figure 1.9. Potential profile through the system metal-electrolyte-vacuum [37].

Since a positive q^S charge appears at the interface, a negative charge $-q^M$ must reside at the outer surface of the electrolyte. If a positive test charge is now brought from an infinite distance to a definite distance, it will be attracted by the charge $-q^M$ on the outer surface of the electrolyte. A negative work is required for the test charge to cross any distance towards the electrolyte coming from the vacuum environment.
It is useful to recall the definition of potential difference between the point (x', y', z') and (x, y, z):

$$\phi(x', y', z') - \phi(x, y, z) = \int_{x,y,z}^{x',y',z'} -\epsilon \cdot dl \qquad 2.31$$

where ϵ is the electric field vector, whereas dl is the infinitesimal path tangent to the direction of movement. Within the electrolyte, no electric field arises, and the potential is constant. This constant value is generally termed ϕ^S. At the metal/solution interface, negative work is done to take the test charge through it, resulting in a sharp change in potential from ϕ^S to ϕ^M. The potential then remains constant at ϕ^M within the metal, since no electric field appears. The difference $\Delta\phi = \phi^M - \phi^S$ is called interfacial potential difference and it depends on the charge density at the interface. However, $\Delta\phi$ cannot be measured for a single interface, since sampling electrical properties of the solution would introduce at least one more interface. Nevertheless, electrochemical potentials can conveniently be defined:

$$\mu_i^\alpha = \mu_i^\alpha + z_i F \phi^\alpha \qquad 2.32$$

μ_i^α is the chemical potential, as shown in eq. 2.32, while z_i is the charge of the i-th species in phase α.

$$\mu_i^\alpha = \left(\frac{\partial G}{\partial n_i}\right)_T, p, n_{i \neq i} \qquad 2.33$$

n_i is the number of moles of *I* in phase α.
Let us consider the following cell:

$$Cu|Zn|ZnCl_2|AgCl|Ag|Cu' \qquad 2.34$$

The corresponding cell reaction is:

$$Zn + 2AgCl + 2e^-(Cu) \rightleftarrows Zn^{2+} + 2Ag + 2Cl^- + 2e^-(Cu') \qquad 2.35$$

At equilibrium, making use of electrochemical potential definition, eq. 2.35 becomes:

$$\mu_{Zn} + 2\mu_{AgCl} + 2\mu_e^{Cu'} = \mu^S_{Zn^{2+}} + 2\mu_{Ag} + 2\mu^S_{Cl^-} + 2\mu_e^{Cu} \qquad 2.36$$

Since $\Delta G = -nFE$, upon proper rearrangement of eq. 2.36, the result is:

$$E = E^0 - \frac{RT}{2F} ln \left(a^S_{Zn^{2+}}\right)(a^S_{Cl^-})^2 \qquad 2.37$$

Nernst equation for the cell (eq. 2.34) has been obtained. This shows the utility for treating interfacial regions with electrochemical potentials, rather than with interfacial potentials. A basic but quantitative approach is herein developed to describe the current-time response of a planar electrode used as working electrode in an unstirred electrolytic solution. The reaction $O + ne^- \rightarrow R$ is considered. If no stirring is performed on the solution, a variation of the concentration profile will occur, causing the current to depend upon this concentration variation:

$$C = C(x,t) \qquad i_d = C(E,t) \qquad 2.38$$

The current is therefore governed by diffusion, and will be termed as diffusion-limited current, $i_d(t)$. The calculation of $i_d(t)$ and $C_O(x,t)$ requires the solution of 2nd Fick's law (linear diffusion equation):

$$\frac{\partial C_O(x,t)}{\partial t} = D_O \frac{\partial^2 C_O(x,t)}{\partial x^2} \quad 2.39$$

Proper initial and boundary conditions are required to solve equation 2.39:

$$C_O(x,0) = C_O^* \quad 2.40$$

$$C_O(x,t) = C_O^* \quad 2.41$$

$$C_O(0,t) = f(E) = 0 \quad 2.42$$

Eq. 2.40 expresses the homogeneity of the solution at *t=0*; eq. 2.41 defines the semi-infinite nature of diffusion, i.e. regions far from electrode surface are unperturbed by reactions at the electrode surface; eq. 2.42 expresses the dependence of the concentration at the electrode surface on the applied potential, which for the reversible case will be provided by Nerst equation. In this case, the applied potential is assumed to be $E_f \ll E^\circ$, thus realising a surface concentration equal to 0 if a large time span is considered. Finally, flux balance for mass conservation holds:

$$D_O \left(\frac{\partial C_O(x,t)}{\partial x}\right)_{x=0} + D_R \left(\frac{\partial C_R(x,t)}{\partial x}\right)_{x=0} = 0 \quad 2.43$$

The partial differential equation dictated by eq. 2.39 can be solved upon Laplace transformation and its subsequent solution in Laplace space needs to undergo an inverse Laplace transformation, leading to the ultimate expression for $C(x,t)$.
By applying Laplace transformation, the following ordinary differential equation is obtained:

$$\frac{d^2 C_O(x,s)}{dx^2} - \frac{s}{D_O} C_O(x,s) + \frac{C_O^*}{D_O} = 0 \quad 2.44$$

Its solution yields:

$$C_O(x,s) = \frac{C_O^*}{s} + A(s) e^{-\sqrt{\frac{s}{D_O}}x} + D(s) e^{\sqrt{\frac{s}{D_O}}x} \quad 2.45$$

Boundary conditions derive from 2.42 and 2.43 and are:

$$C_O(0,s) = 0 \quad 2.46$$

$$C_O(x,s) = \frac{C_O^*}{s} \quad 2.47$$

Hence,

$$C_O(x,s) = \frac{C_O^*}{s} - \frac{C_O^*}{s} e^{-\sqrt{\frac{s}{D_O}}x} \quad 2.48$$

By using similar calculations and upon application of flux balance, the following expression for *R* species is obtained:

$$C_R(x,s) = \frac{C_O^*}{s} e^{-\sqrt{\frac{s}{D_R}}x} \quad 2.49$$

The inverse Laplace transform can now be successfully applied, as follows:

$$C_O(x,t) = L^{-1}\{C_O(x,s)\} = C_O^* \left(1 - erfc\left[\frac{x}{2\sqrt{D_O t}}\right]\right) \quad 2.50$$

$$C_R(x,t) = L^{-1}\{C_R(x,s)\} = C_O^* \frac{D_O}{D_R}\, erfc\left[\frac{x}{2\sqrt{D_R t}}\right] \quad 2.51$$

The error function rapidly reaches its asymptote, which corresponds to the bulk values of the corresponding O and R species. Namely, $C_O(x,t) \to C_O^*$, while $C_R(x,t) \to 0$, since the reaction $O + ne^- \to R$ was previously considered.
The flux at the electrode is proportional to the current (if *O* and *R* are transported to or from the electrode purely by diffusion):

$$\frac{i(t)}{nFA} = J_O(0,t) = -D_O \left(\frac{\partial C_O(x,t)}{\partial x}\right)_{x=0} \quad 2.52$$

If Laplace transform is applied to eq. 2.52, expression 2.53 is obtained:

$$i(s) = -nFAD_O \left(\frac{\partial C_O(x,s)}{\partial x}\right)_{x=0} \quad 2.53$$

Substituting eq. 2.48 into eq. 2.53, after proper differentiation, the result is:

$$i(s) = -nFAD_O \left\{\frac{C_O^*}{s}\sqrt{\frac{s}{D_O}} e^{-\sqrt{\frac{s}{D_O}}x}\right\}_{x=0} \quad 2.54$$

Inverse Laplace transform can now be applied, returning:

$$i(t) = L^{-1}\{i(s)\} = -\frac{nFAD_O^{\frac{1}{2}} C_O^*}{\pi^{\frac{1}{2}} t^{\frac{1}{2}}} = i_d(t) \quad 2.55$$

Eq. 2.53 is also known as the Cottrel equation, and it expresses the effect of electroactive species depletion near the surface with a characteristic $t^{-1/2}$ dependence, which is a distinctive mark of diffusion control rather than electron transfer kinetics.

A more general case occurs when the applied potential E_f is changed to any value on the cathodic wave of the reaction $O + ne^- \rightarrow R$, without the limitation of highly negative potentials as did before. Nerst equation, as well as eq. 2.31, 2.41 and 2.43 still hold. Nernst equation can be conveniently rewritten as:

$$\theta = \frac{C_O(0,t)}{C_R(0,t)} = e^{\frac{nF(E-E^{\circ\prime})}{RT}} \qquad 2.56$$

By applying boundary conditions to Laplace transforms, calculated with the same methods before employed, the following equations for concentration profiles in Laplace space are obtained:

$$C_O(x,s) = \frac{C_O^*}{s} - \frac{C_O^*}{(1+\theta\xi)} e^{-\sqrt{\frac{s}{D_O}}x} \qquad 2.57$$

$$C_R(x,s) = \frac{C_O^*\xi}{(1+\theta\xi)} e^{-\sqrt{\frac{s}{D_R}}x} \qquad 2.58$$

where $\xi = \sqrt{\frac{D_O}{D_R}}$.

If the same calculations before employed are now used, a more general Cottrell-like equation is achieved:

$$i(t) = -\frac{nFAD_O^{1/2}C_O^*}{(1+\xi\theta)\pi^{1/2}t^{1/2}} \qquad 2.59$$

Eq.2.59 is valid for whichever step experiment in a reversible system.
If the applied potential *E* is made vary with time with a definite scan rate, a variation of the flux with time will occur. For the sake of simplicity, a linear variation of potential with time is considered (eq. 2.60). Assuming a rapid electron transfer at the electrode surface, the Nerst equation holds, but it requires proper substitution with the new time-dependent potential *E*(*t*):

$$E(t) = E_i - vt \qquad 2.60$$

$$\frac{C_O(0,t)}{C_R(0,t)} = e^{\frac{nF(E_i-vt-E^{\circ\prime})}{RT}} \qquad 2.61$$

v is the scan rate expressed in V/s.
Eq. 2.61 can be rewritten as:

$$\frac{C_O(0,t)}{C_R(0,t)} = \theta S(t) \qquad 2.62$$

where $\theta = e^{\frac{nF}{RT}(E_i-E^{\circ\prime})}$ and $S(t) = e^{-\sigma t}$, with $\sigma = \frac{nF}{RT}v$.

Eq. 2.45 and 2.52 are still valid, and combining them together and making use of convolution theorem the result is:

$$C_O(0,t) = C_O^* - \frac{1}{nFAD_O^{1/2}\pi^{1/2}} \int_0^t (t-\tau)^{-1/2} \cdot i(\tau) d\tau \qquad 2.63$$

Similarly,

$$C_R(0,t) = \frac{1}{nFA\pi^{1/2}D_R^{1/2}} \int_0^t (t-\tau)^{-1/2} \cdot i(\tau) d\tau \qquad 2.64$$

By exploiting eq. 2.62, the integral contained in eq. 2.63 and eq. 2.64 becomes:

$$\int_0^t (t-\tau)^{-1/2} \cdot i(\tau) d\tau = \frac{nFA\pi^{1/2}D_O^{1/2}C_O^*}{(1+\theta S(t)\xi)} \qquad 2.65$$

However, a closed form of eq. 2.65 can only be numerically computed. Moreover, it is convenient to change the *i(t)* form to the *i(E)* one and to rewrite eq. 2.65 in a dimensionless form to simplify its numerical solution. This last point can be fulfilled by proper substitution, as follows:

$$\sigma t = \frac{nF}{RT} vt = \frac{nF}{RT}(E_i - E) \qquad 2.66$$

$$i(\tau) = g(z) \qquad 2.67$$

with $z = \sigma\tau$.
Eq. 2.65 then becomes:

$$\int_0^t (t-\tau)^{-1/2} \cdot i(\tau) d\tau = \int_0^z (\sigma t - z)^{-1/2} \sigma^{-1/2} \cdot g(z)\, dz = \frac{C_O^*(\pi D_O)^{1/2}}{1+S(\sigma t)\theta\xi} \qquad 2.68$$

Hence,

$$\int_0^t (t-\tau)^{-1/2} \cdot i(\tau) d\tau = \int_0^z (\sigma t - z)^{-1/2} \chi(z)\, dz = \frac{1}{1+S(\sigma t)\theta\xi} \qquad 2.69$$

with $\chi(z) = \frac{g(z)}{C_O^*(\pi D_O \sigma)^{1/2}}$.
Finally,

$$i = nFAC_O^*(\pi D_O \sigma)^{1/2}\chi(\sigma t) \qquad 2.70$$

$\chi(\sigma t)$ is a pure number and it is the result of numerical solutions found for eq. 2.69. In particular, the quantity $\pi^{\frac{1}{2}}\chi(\sigma t)$ reaches its maximum at a value of 0.4463, allowing to express the corresponding peak current as:

$$i_p = 0{,}4463nFAC_O^* D_o^{1/2} \left(\frac{nF}{RT}\right)^{1/2} v^{1/2} \qquad 2.71$$

which is known as the Randles-Sevcik equation.
The corresponding (cathodic) peak potential is given by:

$$E_p = E_{1/2} - 1{,}109\frac{RT}{nF} = -\frac{28{,}5}{n}\ mV \qquad 2.72$$

$E_{1/2}$ is the half-wave potential and it is given by:

$$E_{1/2} = E° - \frac{RT}{nF}\,ln\left(\frac{D_O}{D_R}\right)^{1/2} \qquad 2.73$$

2.6.2 Cyclic voltammetry technique

Cyclic voltammetry is now taken into exam. The applied potential is given by:

$$E(t) = E_i - \nu t, \text{for } 0 < t \leq \lambda \qquad 2.74$$

$$E(t) = E_i - 2\nu\lambda + \nu t, \text{for } t > \lambda \qquad 2.75$$

At time $t=\lambda$ the direction of scan is inverted: the corresponding potential E_λ is called switching potential. For equation 2.74, the mathematical treatment is the same of a linear scan voltammetry. For equation 2.75, similar arguments can be used in the mathematical description. For a Nerstian system, the following expression holds:

$$\frac{C_O(0,t)}{C_R(0,t)} = e^{\frac{nF(E_i - 2\nu\lambda + \nu t - E°)}{RT}} = \theta S(\sigma t) \qquad 2.76$$

where $\theta = e^{\frac{nF(E_i - E°)}{RT}}$ and $S(\sigma t) = e^{(\sigma t - 2\sigma\lambda)}$.
Nonetheless, the results are similar as already derived for a LSV experiment. A caveat concerns the switching potential E_λ, on which there exists a dependence for the curve if the cathodic peak is less than 35 mV to E_λ.

2.6.3 Linear sweep voltammetry with RDE

Hydrodynamic methods are now described, being fast and highly precise methods, which also provide a quick reaction steady state attainment. Moreover, at steady state, double-layer charging effects do not alter the measurement. In the end, hydrodynamic electrodes provide known and reproducible mass-transfer conditions, but the theoretical treatment requires solving the hydrodynamic problem, namely the determination of flow velocity profiles as functions of rotation speed, solution viscosity and density.
The simplest treatment is based on the diffusion layer approach, for which mass transfer occurs by diffusion in the layer defined by $0 < x < \delta$. A general equation for the flux of species is given by:

$$J_j = -D_j \nabla C_j - \frac{z_j F}{RT}\,D_j C_j \nabla \emptyset + C_j v \qquad 2.77$$

The first term refers to diffusion, represented by *D*, the diffusion coefficient, and by the concentration gradient of the *j-th* species; the second term represents migration, the last term expresses the convection, and ***v*** is the velocity vector.

The velocity profile is given by the expression of von Karman and Cochran, but it is convenient to transform it to cylindrical coordinates. The convective-diffusion equation can also be re-written in terms of cylindrical coordinates, and upon mathematical treatment the expression becomes:

$$i = nFAD_o\left(\frac{\partial C_o}{\partial y}\right)_{y=0} \quad 2.78$$

At the limiting current $i = i_{L,c}$, the Levich equation is obtained:

$$i = 0.62nFAD_o^{2/3}\omega^{1/2}v^{-1/6}C_o^* \quad 2.79$$

A deviation from linearity can arise in the plot of i vs $\omega^{1/2}$, indicating that a kinetic limitation is present due to charge transfer. Knowing that $k_c(E) = k^0 e^{\left[\frac{-\alpha nF(E-E^0}{RT}\right]}$ and $\frac{C_0(0,t)}{C_0^*} = \frac{i_{L,c}-i}{i_{L,c}}$, one obtains:

$$i = i_k\left(\frac{i_{L,c}-i}{i_{L,c}}\right) \quad 2.80$$

Where $i_k = nFAk_c(E)C_0^*$, which becomes:

$$\frac{1}{i} = \frac{1}{i_k} + \frac{1}{i_{L,c}} \quad 2.81$$

which is known as the Koutecky-Levich equation.

2.6.4 Linear sweep voltammetry with RRDE

The addition of an independent ring electrode surrounding the disk electrode provides additional information on the processes occurring at the disk surface. For example, if the disk electrode potential is cathodically swept and a species R is produced, the ring can conveniently be positively polarised, so that the R species can be oxidised to O.
The ring current profile can be derived with similar considerations of the disk electrode already discussed above, achieving the following expression:

$$i_{R,l,c} = 0.62nF\pi(r_3^3 - r_2)^{2/3}D_o^{2/3}\omega^{1/2}v^{-1/6}C_o^* \quad 2.82$$

Ring and disk current are correlated by:

$$\frac{i_R}{i_D} = \left(\frac{r_3^3}{r_1^3} - \frac{r_2^3}{r_1^3}\right)^{2/3} \quad 2.83$$

Where r1, r2 and r3 are geometrical entities, describing the radius of the disk, of the disk and the insulator, and of the disk, insulator and ring.

The employed rotating ring disk electrode (RRDE) is made of a glassy carbon disk (5 mm) and a Pt ring, which are separated by a PEEK spacing: figure 1.10.a and 1.10.b show the front and lateral view of the electrode.

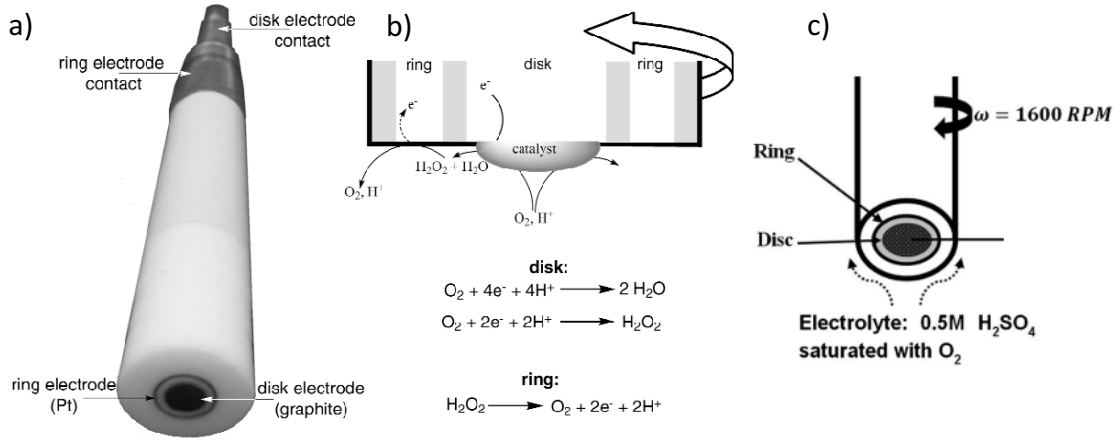

Figure 1.10. a) Structure of a rotating ring disk electrode (RRDE): the disk is made of glassy carbon, while the ring material is platinum; b) graphical representation of how the oxygen comes in contact the disk and how the hydrogen peroxide is detected by ring.

To sum up, RRDE operation is similar to RDE; the electroactive species is first put in contact with the central disk, where it can be oxidised or reduced. Reaction products, thanks to the rotation, are pushed towards the ring to be reduced or oxidised. The ring-disk geometry is determined by:

- transient time, which is the time required to be detected by ring
- the efficiency (N), which is the maximum amount of species revealed at the ring. It is connected to a geometrical quantity, thus it can be calculated knowing the disk radius, the ring radius, the insulator radius. Note that a previous calibration is needed, usually with a known redox couple standard, as $[Fe^3(CN)_6]^{3-} \rightarrow [Fe^2(CN)_6]^{2+}$. The used RRDE tip has a collection efficiency of 0.25.

RRDE can be used to detect peroxide (H_2O_2) produced during oxygen reduction, which is re-oxidised by the ring, as described in Figure 1.10.b. A linear potential scan is applied on the disk promoting ORR, while the ring is polarized at the constant oxidative potential for peroxide, if it is produced at the disk; in figure 1.11 an example of current vs potential for disk and ring is reported. Using RRDE technique, the number of electrons involved on ORR (n) and the peroxide yield (χ_{H2O2}) can be calculated applying equations 2.84 and 2.85, where i_d and i_r are disk and ring current, respectively and N is the collection efficiency.

$$n = \frac{4i_D}{i_D + {i_R}/{N}} \qquad 2.84$$

$$\chi_{H_2O_2} = 100\,\frac{2i_R}{Ni_D + i_R} \qquad 2.85$$

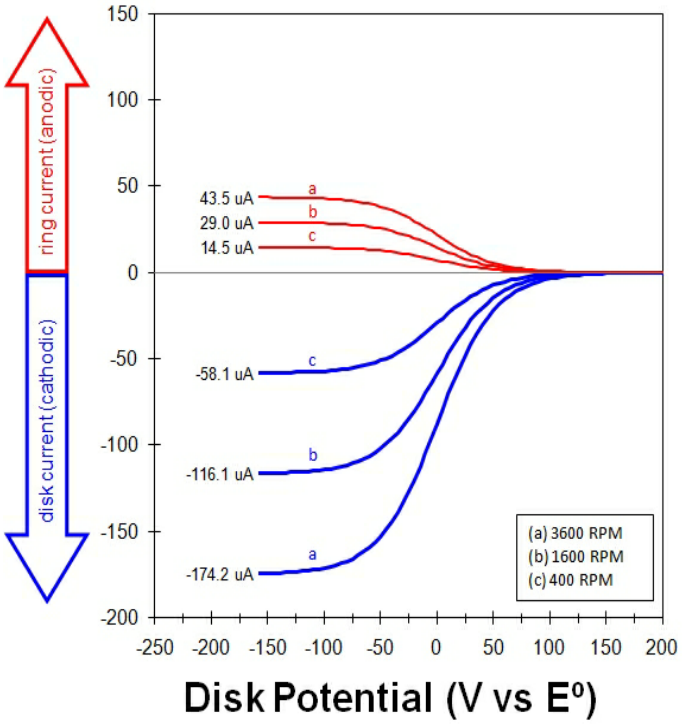

Figure 1.11. An example of linear sweep voltammetries (LSV) showing the current vs potential of disc (blue) and ring (red) at three different rotation speeds.

2.6.5 Models for double-layer

Helmholtz Model

If a metallic electrode is considered, then its metallic nature dictates that any excess charge should reside at its surface, since no electric fields can develop within itself at equilibrium. Helmholtz proposed that two sheets of charges exist, one due to excess charge of the metal at its surface, the other one formed by counterions from the liquid phase in contact with the electrode. From this concept arises the name of *double layer*. This configuration resembles a parallel plate capacitor, with charge density σ and voltage drop between the plates V linked together by:

$$\sigma = \frac{\varepsilon\varepsilon_0}{d}V \qquad 2.86$$

where ε is the dielectric constant of the medium, ε_0 is the permittivity of free space, d is the gap within the plates. A differential capacitance can be defined as:

$$C_d = \frac{\partial\sigma}{\partial V} = \frac{\varepsilon\varepsilon_0}{d} \qquad 2.87$$

This model predicts a constant differential capacitance, which is however different from what is experimentally observed. Namely, ε and/or d should depend on potential and concentration, and C_d also should.

Gouy-Chapman Theory

Charge carrier density can be small, especially if low electrolyte concentrations are realised. This causes the counter-charges to accumulate in a layer with definite thickness. As a result, a diffuse layer of charges in solution has formed to counterbalance the surface charge at the electrode surface. Greatest concentration of charges will be found near the electrode surface, since electrostatic forces are most able to overcome thermal processes, while progressively lesser concentrations will be found farther from the electrode. Therefore, the average distance *d* of charge separation should show dependencies on both potential and electrolyte concentration. Ions are considered as point charges, and for this reason the diffuse layer starts from the electrode surface.

Double-layer structure can be mathematically described by non-linear differential equation of Poisson-Boltzmann, which provides a link between electric potential, charge density and ion concentration:

$$\frac{d^2\phi}{dx^2} = -\frac{zen_0}{\varepsilon\varepsilon_0}\left(e^{-\frac{zen_0\phi(x)}{kT}} - e^{\frac{zex}{kT}}\right) \qquad 2.88$$

where n_0 is the bulk concentration of ions with charge *z*.

Upon solving Poisson-Boltzmann equation, the resulting differential capacitance is:

$$C_d = \frac{d\sigma_M}{d\phi_0} = \left(\frac{2z^2e^2\varepsilon\varepsilon_0 n_0}{kT}\right)^{1/2} cosh\ cosh\ \left(\frac{ze\phi_0}{2kT}\right) \qquad 2.89$$

Gouy-Chapman theory predicts a dependence of C_d on potential, concentration and temperature. However, experimental capacitance values are usually lower than predicted ones. The major limit of Gouy-Chapman model is related to the finite size of ions in the electrolyte.

Stern's Modification

Ions do possess finite size and cannot approach the electrode surface any closer than their ionic radius. If they are solvated, an extra thickness must be added to that radius. Moreover, a plane of closest approach is considered, namely a layer of anions that covers the electrode surface. Two main regions are therefore defined: Inner Helmholtz Plane (IHP) and Outer Helmholtz Plane (OHP). At IHP, the adsorption of species without hydration sphere is observed. At OHP, ions with hydration sphere are encountered. Ions in direct contact with the electrode surface are said to be specifically adsorbed on it (see *Specific adsorption* hereafter). The differential capacitance is conveniently expressed by two terms: Helmholtz Capacitance (C_H) and Diffuse Layer Capacitance (C_{DL}). The differential capacitance is then given by:

$$\frac{1}{C_d} = \frac{1}{C_H} + \frac{1}{C_{DL}} \qquad 2.90$$

C_H contributes to C_d with charges held at the OHP, while C_{DL} is the capacitance of truly diffuse charge. C_d is governed by the smaller of the contributions: at large electrolyte

concentrations, and/or at large polarisations in diluted medium, C_{DL} becomes very large and therefore $\frac{1}{C_{DL}}$ becomes neglectable.

The following figure 1.12 displays a visual representation of the three double-layer model.

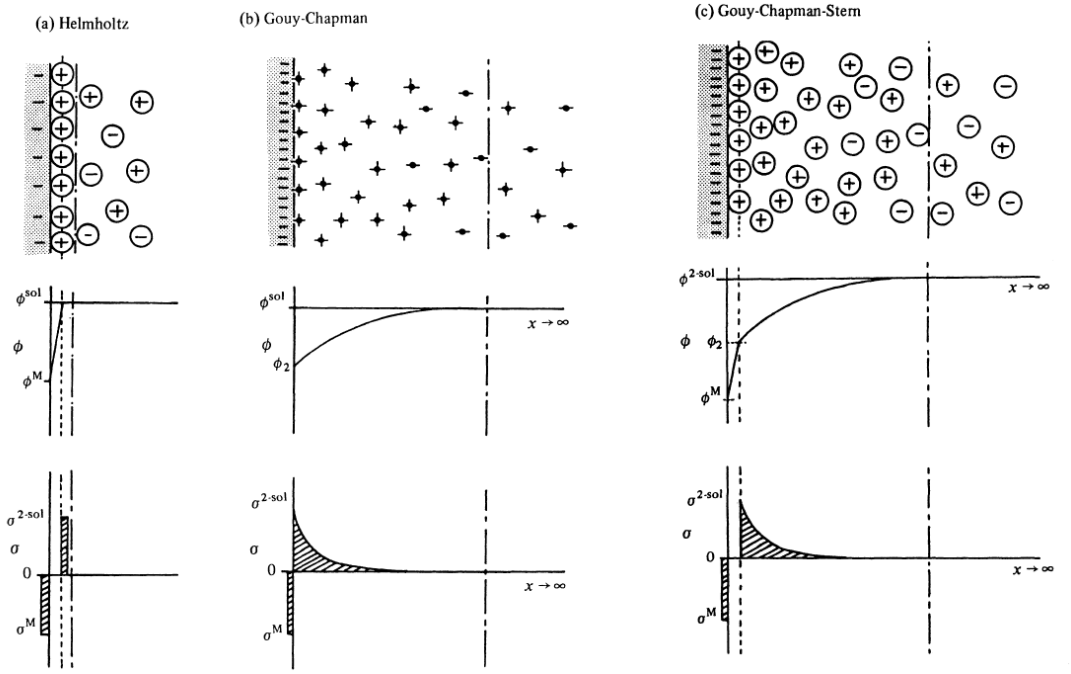

Figure 1.12. Schematic models of the ion, potential (**ϕ**) and charge (**σ**) distribution in a direction perpendicular to the plane of the electrode as described by (a) Helmholtz, (b) Gouy Chapman, and (c) Stern [38].

Specific Adsorption

Specifically, adsorbed ions are tightly bound to the electrode surface and therefore in direct contact with it. Hence, specific adsorption phenomena occur at IHP. SO_4^-, Cl^-, Br^-, I^- have weakly bound solvation water and they are prone to specific adsorb on clean electrode surfaces [39].

The amount of adsorbed species depends on its size and on its orientation on the electrode surface. Ions can in fact adsorb on sites in exact correspondence with surface atoms, giving a commensurate adsorption. Generally, ionic or molecular dimensions are too large to give this kind of adsorption, and an energetically more favourable packing occurs for higher spacings. If the required spacings prevent a fitting into vacant sites, rotations of the adsorbate unit cell can occur.

Self-Assembly at the solid/liquid interface

Self-Assembly deals with the process of spontaneous association of atomic or molecular entities, which under thermodynamic equilibrium conditions organise themselves into stable and well-defined structures joined by non-covalent bonds [40] [41] [38]. Despite this self-organisation process based on weak interactions of single molecular units, it results in well-defined hierarchical macroscopic structures. It is worth to mention that the generated self-assembled structures occupy a thermodynamic minimum [42]**.** There exist

examples of monolayers based on covalent bonds: thiolated groups easily form Self-Assembled Monolayers (SAM) on gold surfaces [38]. Nevertheless, the most riveting aspect of SAM formation lies in the ability to discard covalent bonds in favour of non-covalent interactions, which are notoriously weaker and less directional. It is the case of electrostatic interactions (involving ions and/or dipoles), hydrogen bonds, hydrophobic interactions, π stacking and Van der Waals interactions [43]**.** An individual non-covalent interaction is weak, i.e. its binding energy is $\sim 0.1 - 5\ \frac{kcal}{mol}$. It is comparable to thermal energy: at $T = 300\ K$, the associated thermal energy is $kT \sim 0.6 \frac{kcal}{mol}$. However, if an ensemble of units is attained, then a summation of weak interactions occurs, possibly leading to a system with sufficient stability, namely a self-assembled monolayer. Adverse phenomena must not be neglected. Indeed, competing interactions with solvent molecules can arise, preventing the desired species to interact among themselves. Moreover, entropy gained by eventual SAM disruption must be overwhelmed, since SAM formation is regarded as an energetically favourable process. A simple calculation can be provided: if two particles are brought together, the entropic contribution will be: $-T\Delta S \approx +5.5\ \frac{kcal}{mol}$. In addition, a conformational contribution must be considered, since freely rotating bonds are freezed when molecules are packed together: $-T\Delta S \cong +0.7\ \frac{kcal}{mol}$.
The self-assembly should result in a globally negative Gibbs free energy variation, meaning that good intermolecular contact (i.e. multipoint contact) must be fulfilled, and the assembling units should be sufficiently rigid to enforce intermolecular interactions.
In the present work, extensive Self-Assembled Monolayers are successfully obtained for a series of metalated Octaethylporphyrins Fe(II)-Phthalocyanine and Fe(III)-tetramethoxyphenyl porphyrin chloride. An organised layer is also desirable for STM, since single molecules are often too mobile to be properly imaged [43]**.** The tunnelling tip can in fact perturbate molecular adsorption, causing removal or displacement of the molecule. The resolution may also worsen. Conversely, if molecules are packed in ordered domains, their mobility is reduced, and imaging is more efficient [44]**.**

2.6.6 Reference Electrode

The reference electrode has the role to provide a fixed and constant potential, that does not vary during electrochemical characterisation. A reference electrode should in principle behave as an ideal non-polarisable electrode. Non-polarisable interface refers to an electrode surface, at which electron transfer is extremely fast. As a consequence, its potential should not change even if a current flows through it [37]. Since electron transfer process is fast, the electrode potential is calculated with Nernst equation. For this purpose, a special class of reference electrodes is considered, namely Hydrogen electrodes. These electrodes are based on platinised platinum foils, meshes or wires as active material able to exchange electrons in the redox process, on which hydrogen electrodes rely:

$$2H^+ + 2e^- \rightleftarrows H_2 \qquad 2.91$$

with an associated potential, by convention, of: $E°_{H^+/H_2} = 0\ V$ at all temperatures. This is strictly valid only if H_2 pressure is equal to 1 atm and if the solution contacting the Pt material possesses unitary activity, and the corresponding electrode is known as Normal Hydrogen Electrode (NHE) or Standard Hydrogen Electrode (SHE). However, such conditions are not often attainable, but a convenient alternative can be employed, namely the Reversible Hydrogen Electrode (RHE). The glass electrode containing the Pt material is filled with the same electrolyte contained in the electrochemical cell and it is negatively polarised with respect to a counter-electrode, usually of Pt material. The negative polarisation enables Hydrogen Evolution Reaction at the RHE Pt surface, and gaseous H_2 accumulates in a bubble, which is trapped in the glass electrode. Therefore, the Pt mesh (or wire or foil) is in contact with both gaseous H_2 and hydronium ions (in liquid phase), satisfying the equilibrium reaction (86). Of course, proper calculations need to be applied since deviations from Normal condition are introduced. This can be accomplished by the equation:

$$E_{H_2,H^+} = E°_{H_2,H^+} + \frac{RT}{F}\ln\frac{a_{H^+}}{\sqrt{p_{H_2}}} \qquad 2.92$$

Nonetheless, the RHE represents an actual practical advantage. The electrode is in fact filled with the same solution of the cell, and H_2 is generated *in situ*, with no need of an external hydrogen generator.

2.6.7 Working Electrode

The working electrode defines the interface under study [37]**.** Many classes of working electrodes have been used, but the present work only deals with a single-crystal electrode, namely a gold electrode exposing its (111) crystallographic face and HOPG. Working electrode substrates should possess an even current and potential distribution and it should not chemically react with the electrolytic solution. Solid substrates can contaminate, oxidise and change in surface morphology with time, therefore they usually undergo pre-treatments before being mounted in the electrochemical cell. Pre-treatments can concern exfoliation, mechanical polishing or electropolishing techniques, chemical treatments with etching solutions or thermal annealing. This last procedure was largely employed in this work through a flame-annealing procedure in inert Ar atmosphere, as further described in section 3.2.3.

2.6.8 Counter Electrode

The counter-electrode has the unique role to maintain the current required by the working electrode, without causing any limitation in the measured response of the cell [37]. Its potential is not matter of interest, and the only demanded feature is the ability to sustain the current developed at the working electrode. Oxidation/reduction reactions will occur at the counter-electrode surface when reduction/oxidation processes occur at the working electrode surface. Therefore, reaction products developed at the counter-electrode should always be considered, aiming at the counter-electrode that introduces less contaminations

of the electrolytic environment as possible, in order not to interfere in the electrochemical response of the working electrode.

References

[1] G. Binnig, H. Rohrer, Scanning tunnelling microscopy, Surface Science. 126 (1983) 236–244.

[2] G. Binnig, H. Rohrer, C. Gerber, E. Weibel, Surface studies by scanning tunnelling microscopy, Physical Review Letters. 49 (1982) 57–61.

[3] G. Binnig, H. Rohrer, C. Gerber, E. Weibel, 7 × 7 Reconstruction on Si(111) Resolved in Real Space, Physical Review Letters. 50 (1983) 120–123.

[4] R.P. Feynman, There's Plenty of Room at the Bottom, Engineering and Science. (1960) 22–36.

[5] S. Lounis, Theory of Scanning Tunnelling Microscopy, in: Computing Solids - Models, Ab Initio Methods and SupercomPuting, 2014: p. 38.

[6] R. Sonnenfeld, P.K. Hansma, Atomic-resolution microscopy in water, Science. 232 (1986) 211–213.

[7] A.J. Bard, F.-R. Fan, Studies of the Liquid/Solid Interface by Scanning Tunnelling Microscopy and Scanning Electrochemical Microscopy, Faraday Discuss. 94 (1992) 1–22.

[8] Why is UHV required for surface studies? https://chem.libretexts.org/@go/page/25379

[9] M.A. Lazaga, D.T. Wickham, D.H. Parker, G.N. Kastanas, B.E. Koel, Reactivity of Oxygen Adatoms on the Au(111) Surface, Acs Symposium Series. 523 (1993) 90–109.

[10] J. Bardeen, Tunnelling from a many-particle point of view, Physical Review Letters. 6 (1960) 57–59.

[11] G. Teobaldi, E. Inami, J. Kanasaki, K. Tanimura, A.L. Shluger, Role of applied bias and tip electronic structure in the scanning tunnelling microscopy imaging of highly oriented pyrolytic graphite, Physical Review B - Condensed Matter and Materials Physics. 85 (2012) 1–15.

[12] N. Lorente, J.P. Gauyacq, Efficient spin transitions in inelastic electron tunnelling spectroscopy, Physical Review Letters. 103 (2009) 1–4.

[13] J. Fransson, Spin inelastic electron tunnelling spectroscopy on local spin adsorbed on surface, Nano Letters. 9 (2009) 2414–2417.

[14] J. Fernández-Rossier, Theory of single-spin inelastic tunnelling spectroscopy, Physical Review Letters. 102 (2009) 1–4.

[15] M. Persson, Theory of inelastic electron tunnelling from a localized spin in the impulsive approximation, Physical Review Letters. 103 (2009) 1–4.

[16] W. Schmickler, Electronic Effects in the Electric Double Layer, Chemical Reviews. 96 (1996) 3177–3200.

[17] M. Hugelmann, W. Schindler, Tunnel barrier height oscillations at the solid/liquid interface, Surface Science. 541 (2003) L643–L648.

[18] W. Schmickler, D. Henderson, A model for the scanning tunnelling microscope operating in an electrolyte solution, J. Ele. 290 (1990) 283–291.

[19] J.K. Sass, J.K. Gimzewski, Solvent dynamical effects in STM with a polar liquid in the gap, Journal of Electroanalytical Chemistry. 308 (1991) 333–337.

[20] J. Halbritter, G. Repphun, S. Vinzelberg, G. Staikov, W.J. Lorenz, Tunnelling Mechanisms in Electrochemical STM - Distance and Voltage Tunnelling Spectroscopy, Electrochimica Acta. 40 (1995) 1385–1394.

[21] J. Pan, T.W. Jing, S.M. Lindsay, Tunnelling barriers in electrochemical scanning tunnelling microscopy, Journal of Physical Chemistry. 98 (1994) 4205–4208.

[22] A. Vaught, T.W. Jing, S.M. Lindsay, Non-exponential tunnelling in water near an electrode, Chemical Physics Letters. 236 (1995) 306–310.

[23] A. Mosyak, A. Nitzan, R. Kosloff, Numerical simulations of electron tunnelling in water, Journal of Chemical Physics. 104 (1996) 1549–1559.

[24] M. Hugelmann, W. Schindler, In Situ Distance Tunnelling Spectroscopy at Au(111)/0.02 M HClO4: From Faradaic Regime to Quantized Conductance Channels, Journal of The Electrochemical Society. 151 (2004) E97–E101.

[25] K.W. Hipps, Scanning Tunnelling Spectroscopy (STS), in: Handbook of Applied Solid State Spectroscopy, 2006: pp. 305–350.

[26] R.J. Hamers, Atomic Resolution Surface Spectroscopy with the Scanning Tunnelling Microscope, Ann. Rev. Phys. Chem. 40 (1989) 531–559.

[27] K.W. Hipps, U. Mazur, Inelastic electron tunnelling: An alternative molecular spectroscopy, Journal of Physical Chemistry. 97 (1993) 7803–7814.

[28] L.E.C. van de Leemput, H. van Kempen, Scanning tunnelling microscopy, Reports on Progress in Physics. 55 (1992) 1165–1240.

[29] A.A. Gewirth, H. Siegenthaler, eds., Nanoscale Probes of the Solid/Liquid Interface, Series E: Applied Sciences – Vol. 288.

[30] K. Besocke, An Easily Operable Scanning Tunnelling Microscope, Surface Science. 181 (1987) 145–153.

[31] L. Scudiero, D.E. Barlow, K.W. Hipps, Physical Properties and Metal Ion Specific Scanning Tunnelling Microscopy Images of Metal(II) Tetraphenylporphyrins Deposited from Vapor onto Gold (111), Journal of Physical Chemistry B. 104 (2000) 11899–11905.

[32] M. Wilms, M. Kruft, G. Bermes, K. Wandelt, A new and sophisticated electrochemical scanning tunnelling microscope design for the investigation of potentiodynamic processes, Review of Scientific Instruments. 70 (1999) 3641–3650.

[33] A.L. Kholkin, N.A. Pertsev, A. V. Goltsev, Piezoelectricity and Crystal Symmetry, chapter 2, 2008.

[34] http://www.pi-usa.us/tutorial/4_39.html.

[35] M. Wilms, P. Broekmann, C. Stuhlmann, K. Wandelt, In-situ STM investigation of adsorbate structures on Cu (111) in sulfuric acid electrolyte, Surface Science. 416 (1998) 121–140.

[36] A.J. Bard, L.R. Faulkner, Electrochemical Methods: Fundamentals and Applications, 2nd Edition, Wiley, New York, 2001.
[37] D. Pletcher, R. Greff, R. Peat, L.M. Peter, J. Robinson, Instrumental Methods in Electrochemistry, 1985.
[38] G.M. Whitesides, J.P. Mathias, C.T. Seto, Molecular Self-Assembly and Nanochemistry : A Chemical Strategy for the Synthesis of Nanostructures, Science. 254 (1991) 1312–1319.
[39] O.M. Magnussen, Ordered anion adlayers on metal electrode surfaces, Chemical Reviews. 102 (2002) 679–725.
[40] S. Zhang, Molecular Self-Assembly, Elsevier Science, 2001.
[41] L. Jean-Marie, Supramolecular Chemistry, Science. 260 (1993) 1762–1763.
[42] C. Vericat, M.E. Vela, G. Benitez, P. Carro, R.C. Salvarezza, Self-assembled monolayers of thiols and dithiols on gold: New challenges for a well-known system, Chemical Society Reviews. 39 (2010) 1805–1834.
[43] A.J. Bard, L.R. Faulkner, Electrochemical Methods, Fundamentals and Applications, John Wiley & Sons, inc., 2001.
[44] C.G. Zoski, Handbook of Electrochemistry, Elsevier, 2007.

Chapter 3

Experimental

The experimental setups and the techniques used in this work are herein presented, detailing, with a special attention, the sequences of passages required for obtaining reproducible experiments and the theory and operational conditions of the employed instrumentations. First of all, cyclic voltammetry (CV) will be described as an integrated part of the EC-STM technique, because it provides information that mainly has a supporting character. In fact, from a mere experimental point of view, CV affords experimental features, on which EC-STM is also primarily based. Paramount relevance for EC-STM is possessed by the STM unit, since the results of an EC-STM measurement session actually are STM images at a defined electrochemical potential. Therefore, EC-STM can roughly be thought of as an investigation technique that combines the imaging capability at the microscopic scale of STM to the macroscopic electrochemical knowledge provided by CV. Finally, a brief description of the rotating ring and disk (RRDE) is provided as a complementary technique in assessing oxygen reduction reaction mechanism, even if its employment was restricted to few molecular systems.

3.1 Cyclic Voltammetry "Ex-Situ" experimental setup

The cyclic voltammetry experiments were carried out both in a standard five necked glass reactor or in a special designed cell suitable also for EC-STM experiments. The required experimental setup is called "three-electrodes setup", because three electrodes are mounted. In a CV experiment, a potential difference is generated by mean of a potentiostat between a Working Electrode (WE) and the Reference Electrode (RE), that allows to trigger an electrochemical effect or process that is evidenced by the flowing of a current between the WE and the Counter Electrode (CE). The RE provides a constant potential, which in fact is used as a reference, for determining and/or intentionally varying (i.e.: polarising) the WE potential.

In the present work, a reversible hydrogen electrode (RHE) was employed and consists of a platinum wire supported inside a glass capillary, as shown in figure 3.1. The capillary is sealed from one side where only a small portion of Pt wire protrudes for assuring the electric contact, whereas the other side is open, and the dangling Pt wire is half-immersed in the electrolyte solution in equilibrium with an electrogenerated H_2 bubble. The RHE system involves the overall equilibrium reaction: $2H^+ + 2e^- \rightleftarrows H_2$.

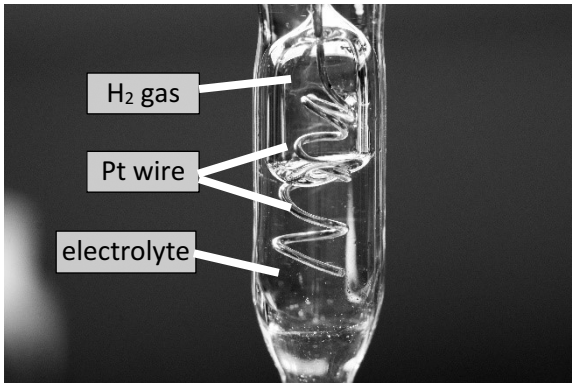

Figure 3.1. image of the RHE electrode used for EC-STM and cyclic voltammetry experiments.

In the RHE, H_2 is not supplied but it is generated directly *in-situ*. For this purpose, the Pt wire must be rinsed with MilliQ water and sonicated for 15 minutes, repeating the procedure for 5 times, then the capillary is filled with an Ar-purged 0.1 M $HClO_4$ solution, which is the same electrolyte used for STM measurements, as well as for CV. H_2 is generated in a two-electrodes circuit where RHE is polarized at negative potential, while a common Pt electrode acts as anode. In details: before electrolysis, the Pt wire is sonicated many times for 15 min inside a test tube filled with MilliQ and immersed for at least 10 hours in Piranha solution, repeating the procedure 2 times. The two extensively cleaned electrodes are connected to a power supply: RHE and the Pt-wire as the negative and the positive pole, respectively. Being negatively polarised, the aqueous solution contacting the Pt wire undergoes electrolysis, which affords the reduction of hydrogen ions to molecular hydrogen (hydrogen evolution reaction, HER). On the anode side, the aqueous solution contacting the Pt counter electrode undergoes oxidation, where H_2O is oxidized to molecular oxygen (oxygen evolution reaction, OER). The optimal current density found for allowing HER to occur at the Pt-wire surface was $j = 10\ mA\ cm^{-2}$. At this value a sufficiently large H_2 bubble can form in a few minutes (< 10 min). The corresponding potential that allowed to maintain such a current was found to oscillate around 15 V. According to this procedure and because the system is in equilibrium with the external environmental pressure, the H_2 bubble pressure is close to 1 atm. The so generated $H_2|H_3O^+$ interface will afford a constant potential value as long as the H_2 reservoir remains disposable during electrochemical measurements. Once the potentiostat is switched off, the RHE is taken out from the beaker and quickly immersed in 0.1 M $HClO_4$ filled glass container end capped with a glass septum, which avoids any contaminants to be exchanged with the main cell compartment. The glass container is in turn inserted in a glass holder with two capillary tubes at the bottom. These two capillary tubes allow the electrolyte to flow inside and outside, by keeping continuously immersed the RHE within the electrolyte and connected with the electrochemical system.

It is worth noting that an activation procedure was required because previous trials directly with 0.1 M $HClO_4$ did not enable the HER to occur at the RHE electrode. The procedure that helps to clean and activate the RHE Pt wire consists in a pre-electrolysis in sulfuric acid, briefly: the RHE capillary tip was rinsed with MilliQ water and then filled

with 0.5 M H_2SO_4 electrolyte, after which it was immersed in a beaker containing the very same electrolyte. As a counter electrode, a Pt electrode was used, whereas an already calibrated RHE was used as a reference electrode. A series of cyclic voltammetries were run limiting the scan range to [0; 1.2] V at 50 mV/s in order to avoid either extensive HER or OER, until ten equal consecutive scans were obtained. This procedure helps to clean and activate the Pt wire. After that, the electrode was rinsed many times with MilliQ water and filled with 0.1 M $HClO_4$ solution to generate a H_2 bubble, as previously described. A saturated calomel electrode (SCE) was inserted in the same beaker containing the just prepared RHE, and the potential variations were evaluated in three days, even if after a few hours it completely stabilised at a value of $E_{RHE/SCE}$= 0.260 V. The same measurement was repeated approximately after 1 month, but potential shifts were in all cases lower than 5 mV. This shift can be attributed to small differences in terms of electrodes positioning, ohmic drop, electrical connections and temperature.

The glass electrochemical cell is cleaned with Piranha solution (see section 3.2.5) to ensure complete elimination of organic contaminants. After that, it was thoroughly rinsed and sonicated with MilliQ water. This procedure was repeated before each experiment. Once rinsed, a 0.1 M $HClO_4$ solution is added as supporting electrolyte. The RHE reference electrode and the Pt counter-electrode, are inserted in two adjacent necks, while the central neck hosts the working electrode. The solution is deaerated by bubbling gaseous Ar or bubbled with O_2 gas when ORR is under investigation.

As a working electrode, single crystals of Au(111) or HOPG (high oriented pyrolytic graphite) were alternatively used. The Au working electrode is prepared by a thermal annealing treatment, as described in section 3.2.3. The HOPG working electrode is prepared according to section 3.2.4. It is then subjected to the functionalisation with macrocyclic molecules, as described in section 3.2.8 and 3.2.9. Finally, it is mounted in a homemade PEEK holder, which easily fits the electrochemical cell and brings the working electrode at the same level of both the CE and the RHE tips. In this way, an optimal triangular arrangement is attained and the distances among electrodes are minimised. This is essential for reducing the magnitude of uncompensated resistance, which always affords a certain contribution to the whole cell overpotential. The uncompensated resistance is an ohmic drop caused by physical separation through an electrolyte among electrodes, specifically between WE and RE, and its main effect is a shift in the applied WE potential:

$$V_u = iR_u \qquad 3.1$$

Modern potentiostats, like the Metrohm Autolab PGStAT204 in use, feature positive feedback circuits, which allow to electronically compensate the ohmic drop. To accomplish this, an impedance spectrum is registered and the value of ohmic drop is determined from the resulting curve as the point where it changes shape or slope. The value is then multiplied by 0.8, and the resulting number is inserted as the ohmic drop compensation resistance. The ohmic drop is compensated by the safe limit of 80% to avoid any possible overcompensation effects that would result in instrumental noise and

signal oscillations. In fact, if a positive oscillation sums to an already fully compensated resistance, then undesirable reactions can harmfully lead to a damage of the working electrode surface. Moreover, impedance determination of ohmic drop is conducted at the open circuit potential, at which no Faradaic processes occur at the WE surface, but CV are collected for a certain potential window. Ohmic drop can therefore change accordingly to a change in WE applied potential, confirming that full compensation must be avoided.

3.2 Electrochemical-STM

The electrochemical scanning tunnelling microscope used to accomplish this work can be defined as "Beetle-type" and the experimental setup was developed by the K. Wandelt group [1]. The term "beetle" refers to the tip-positioning and -approaching unit, as previously described in chapter 2. Investigating by means of EC-STM a sample means that a metallic tip scans the surface of a solid sample to obtain topographic profiles of it. In the meantime, the sample plays as a working electrode in a "four-electrodes setup". Therefore, EC-STM provides a combination of information, i.e. the topographic mapping of the sample associated with the electrochemical response of the involved system. Surface scanning is in fact performed at the solid/liquid interface, where the liquid is an electrolytic solution of 0.1 M $HClO_4$. The sample is fitted in the centre of a small cell, hereafter presented. The sample acts as WE and for this reason needs to be an electrical conductor. This property must be fulfilled also for the tunnelling event to occur, as already discussed in section 2.1. As a counter electrode, a Pt wire is chosen. Pt is a convenient choice because it is expected to not affect the good operation of the electroanalytical system [2]. It is in fact commonly regarded as an inert material towards many reactions, like oxidation. On the other hand, Pt is a sensitive material towards chemisorption of sulphur and nitrogen compounds, as well as CO. These contamination sources can be however excluded on the basis of reactants and compounds used in this work. As a reference electrode, the instrumentation offers two possibilities, both with advantages and disadvantages to be evaluated in order to attain the best compromise for the examined system. The two choices concern a Pt wire as a "pseudo-reference" electrode or an external RHE. It is worth noting that an external SCE ($KCl/Hg_2Cl_2/Cl^-$) or SSE ($K_2SO_4/Hg_2SO_4/SO_4^-$) can be employed as well, but RHE avoids any contaminations of chlorides or sulphate ions. A more detailed description of the pseudo-reference electrode is provided hereafter, while an extensive treatment of RHE has already been provided in section 3.1. Both types were employed, and they brought to equivalent electrochemical responses, apart from an obvious shift of the potential scale.
In any case, a "three-electrodes setup" is obtained, and it can actually be exploited to perform cyclic voltammetry. In this case, they are termed as "in situ cyclic voltammetry", because they are registered with the same experimental configuration used for EC-STM investigation, which presents some differences compared to a standard three-electrodes setup, previously described in section 3.1.

The fourth electrode is the tunnelling tip (tip electrode, TE), whose preparation is illustrated in section 3.2.2, while its operation principles have already been shown in

section 2.5.2. The use of a bipotentiostat allows to control the potential difference between WE and CE (with respect to the RE) and in the meantime the potential difference between WE and TE (or RE). A depiction of the Four-Electrodes setup is furnished in figure 3.2.

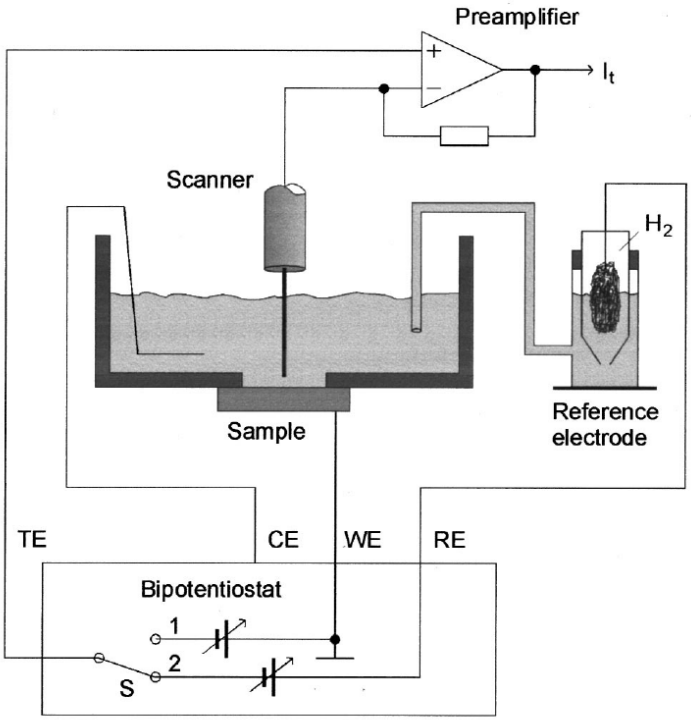

Figure 3.2. Scheme of the four-electrodes setup [1]. The switch S in position 1 enables an internal bias control between TE and WE, whereas in position 2 enables an external bias control between TE and RE.

It must be remarked that, being the tip a polarised electrode with respect to the WE (or the RE), on its surface some Faradaic processes can occur if the polarisation of the WE is changed. The appearance of a Faradaic current is detrimental for EC-STM because its magnitude can overcome that of tunnelling current. Common values for tunnelling currents are in fact around 1 nA and in several cases also lower, therefore Faradaic currents of 1 μA, for example, will completely superimpose to the much smaller tunnelling current, making the STM imaging impossible to accomplish.

According to figure 3.2, if the switch *S* is in position 1, the bipotentiostat applies a constant potential difference between TE and WE (namely, a voltage *bias*). In this case, the EC-STM conveniently records *potentiostatic images* [1], since the WE potential is maintained constant during tip scanning and also among following images. This constant value can be manually selected by means of a knob (see figure 3.6). *Potentiostatic imaging* is useful at the beginning of an EC-STM measurement session, when tunnelling parameters (tunnelling current and *bias)* need to be optimised to achieve satisfactory image resolution. This optimisation essentially deals with two aspects: Faradaic current minimisation and tunnelling resonance conditions, as already illustrated in section 2.4. The procedure can be more efficiently performed if the WE is polarised at “safe”

potentials, at which minimal electrochemical reactions occur on the WE surface. If the switch *S* is in position 2, the EC-STM unit more conveniently records *potentiodynamic images*. Now the TE potential is held constant against the RE, while it varies with respect to the WE. Therefore, once found the best tunnelling parameters in the *potentiostatic mode* that in the meantime minimise unwanted Faradaic current at the TE, the switch is set in position 2 to fix the minimal Faradaic current upon varying the WE potential (versus the RE). It must be pointed out that, in this way, tunnelling resonance may not be preserved [1] as the WE potential is changed from its starting value. Nonetheless, in most cases that Faradaic current at TE produces a major impact on the final image compared to variations in tunnelling resonance. For this reason, *potentiodynamic imaging* has frequently been performed as previously described by fixing the TE potential versus RE, although each specific system can exhibit a different behaviour. Figure 3.3 provides an image of the full EC-STM experimental setup.

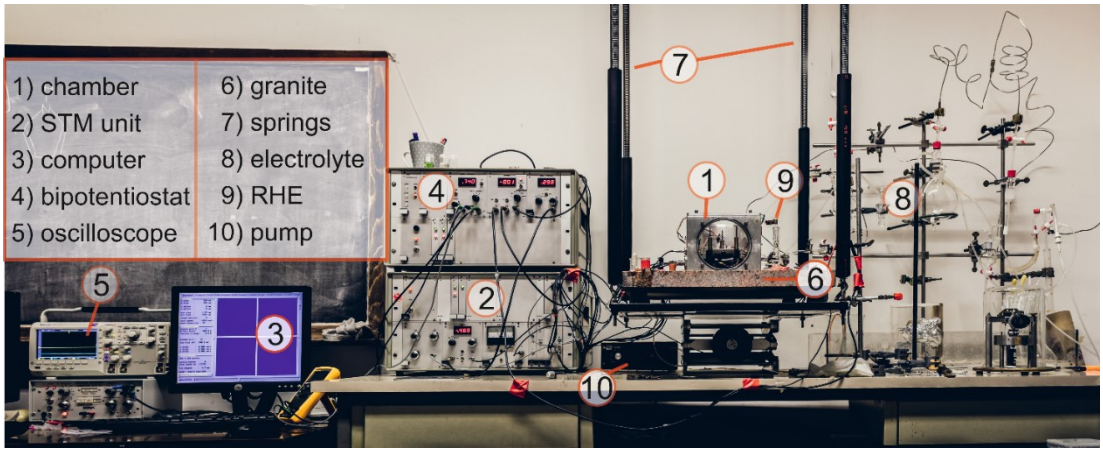

Figure 3.3. Image of the full EC-STM experimental setup.

The key-role is attributed to the aluminium chamber (1). It contains the STM amplifier and scanner, as well as the PEEK cell and the piezo-leg approaching system. The chamber is enclosed with a Plexiglas® slab on the front, to provide a direct visualisation of the inner components, and with an aluminium slab on the top. Both slabs can be tightened with screws to the chamber, exerting enough pressure on Viton® O-ring to guarantee a satisfactory sealing level. The chamber can be in fact filled with desired gas to condition the electrochemical analysis. In this work argon or oxygen, alternatively, were used. Tunnelling parameters are controlled thanks to the STM unit (2), which is interfaced to a computer (3) through a dedicated software. The bipotentiostat (4) allows to take *in situ* CV curves but it is also connected to the STM unit (2) to control the Four-Electrodes Setup. Another computer is assigned to the *in situ* CV recording. The oscilloscope (5) offers direct visualisation of tunnelling current and topographic profile for a quick adjustment of tunnelling parameters. The chamber (1) is mounted on a heavy granite plate (6). This plate is placed upon a brass stack through four rubber pieces, which damps high frequency (>100 Hz) vibrations. The brass stack, together with the granite plate, is suspended with four steel springs (7) from the ceiling. Electrolyte supply is provided by a glass flask (8) connected with Tygon® tubes to the cell. The RHE (9) is placed between

the flask and the cell. A peristaltic pump (10) is connected as outlet to the cell. Ar or O_2 are supplied through suitable glassware connected with Tygon® tubings.

The aluminium chamber acts as Faraday cage to shield the scanner from electromagnetic and acoustic noises, which would inexorably make impossible STM image acquisition. The aluminium cage also provides an electrical connection among the STM scanner, the cells and its electrodes and the steel springs providing a grounding circuit for dispersing charge accumulations.

A picture of the PEEK cell is provided in figure 3.4, where the Pt wire and the Au(111) single crystal are the CE and WE, respectively.

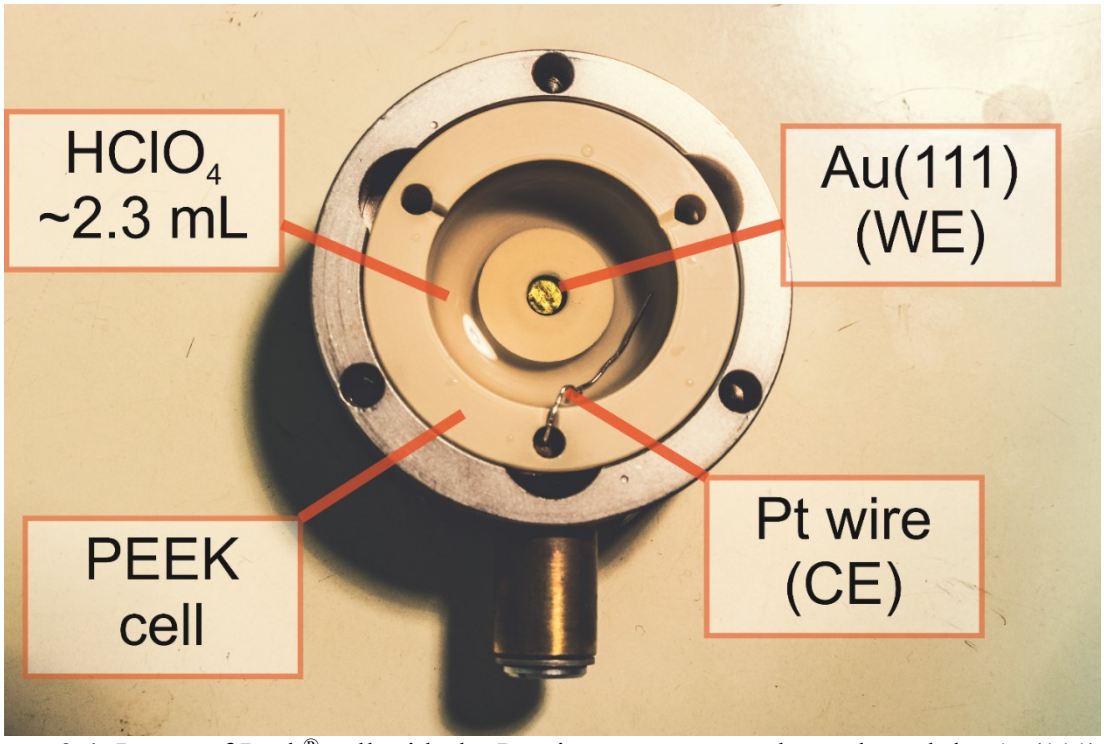

Figure 3.4. Image of Peek® cell with the Pt wire as a counter electrode and the Au(111) crystal.

The working electrode exposed surface corresponds to an area of $Area_{Au_{exposed}} = 0.1256\ cm^{-2}$, because the central hole exposes a disk of 0.4 cm diameter. Otherwise, the crystal would expose a circular area of 0.8 cm diameter. The electrochemical cell and the electrodes are assembled outside the STM chamber, this procedure assures that all the components are precisely mounted avoiding any possible electrolyte leakage or declivity of the WE. A 0.4 mm diameter Viton® ring is mounted prior to insert the WE sample in a dedicated groove. The cell is then mounted into a dedicated aluminium housing, which embeds the electrical connections and terminates with a Lemo® plug. The housing features three screws to tighten the sample to the Viton® ring, providing sealing against electrolyte.

The piezo-legs system is shown in figure 3.5.

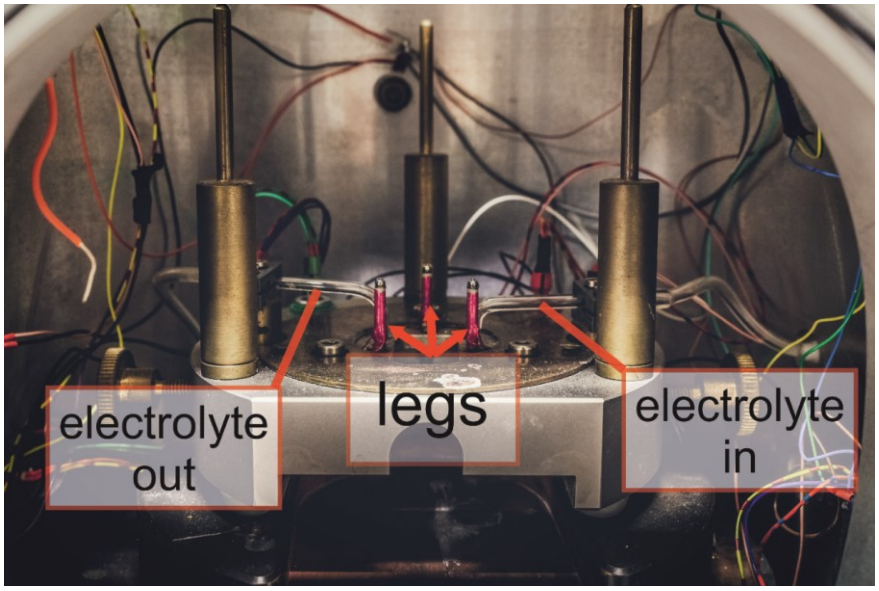

Figure 3.5. Piezo-legs system, on which the scanner undergoes a stick-and-slip mechanism.

Each leg consists of a piezoelectric tube with four electrodes. Upon applying proper polarisation among two or more electrodes of each leg and combining specific polarisation sequences at each leg, the piezo-leg system is then able to perform coarse approaching/retreating as well as lateral positioning along the four cardinal directions. By unscrewing a head screw, the STM scanner is released by a safety lock system and is free to lean on the three steel spheres that constitute the upper part of the three piezo-legs. The spheres rigidly transfer the leg oscillations to the scanner, allowing its rotation and therefore its approaching/retreating. The spheres must be properly isolated by the piezo-legs, otherwise undesired current would flow through the STM tip.

A coarse approaching is automatically accomplished and consists in a fast tip-sample distance reduction up to an initial tunnelling current set-point value. When the set-point tunnelling current is reached, a step-by-step manual approaching must be performed to achieve a stronger and more stable tunnelling signal.

The STM unit features two knobs to control the tunnelling current and voltage bias, respectively. Tunnelling current is held constant since the chosen mode of operation is the “constant current mode”, whose details had already been introduced in section 2.3. The knob allows to manually set a constant I_t value in the range [0; 50] nA. Another knob allows to vary the voltage bias in terms of potential difference between TE and WE. This is also named “internal bias”, as indicated by the switch in position “int.” in figure 3.6, which realises the same condition of the switch in position 1 of figure 3.2.

The tunnelling tip is also part of the four-electrodes setup and the STM unit must be therefore interfaced with a bipotentiostat. The bipotentiostat permits to polarise the WE respect to the RE by closing the circuit with the counter electrode, but it is also able to polarise the TE versus the WE (internal bias) or to the RE. This last case is also termed

as “external bias”, since the switch in figure 3.6 can be exchanged to “ext.” and it corresponds to the switch in position 2, in accordance with figure 3.2.

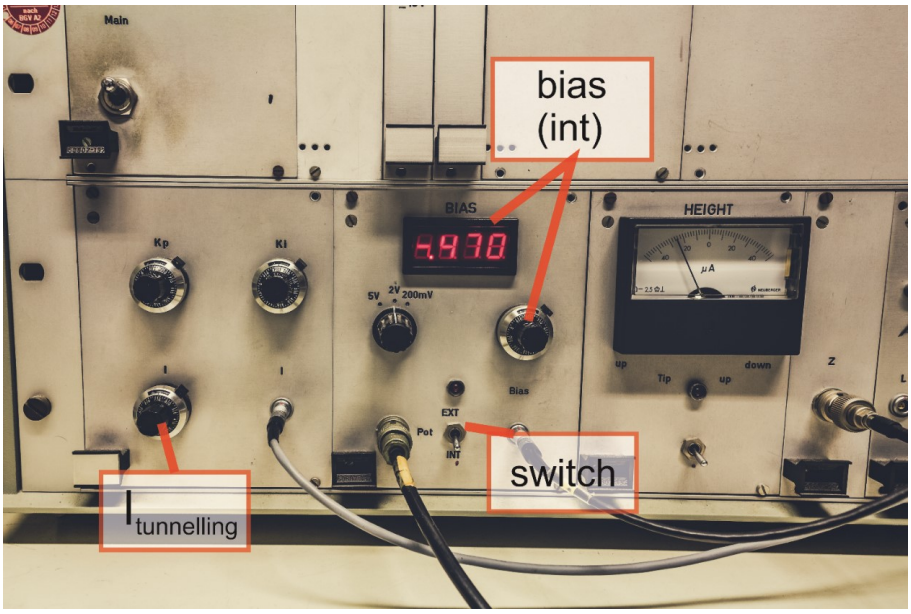

Figure 3.6. STM unit with indicated knobs for tunnelling current, internal bias control, as well as the switch for internal/external bias control.

Since the TE potential now relies on the RE, a different knob is required to vary the TE potential with respect to RE. This knob is indicated in figure 3.7 as “ext. bias control”, which offers an image of the bipotentiostat unit.

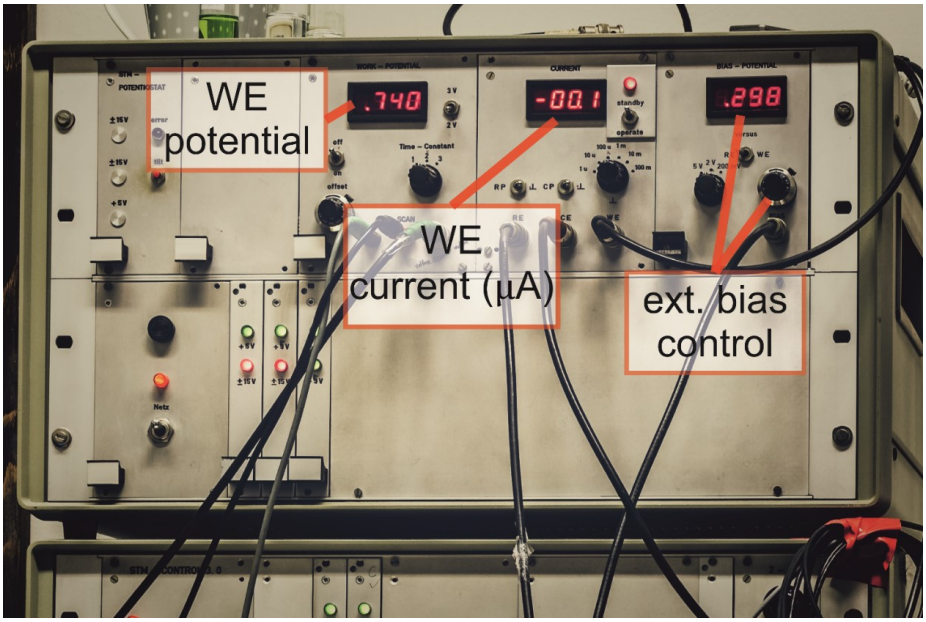

Figure 3.7. Picture of bipotentiostat for STM, with indicated knob for external bias control, as well as the displays for WE potential and WE current.

The bipotentiostat needs a voltage generator, already featured in figure 3.3, which applies a voltage to the WE through the bipotentiostat. It is also able to generate saw-tooth voltage

waves, from predefined upper and lower vertex potentials, allowing the recording of the so called *in situ* CVs with high sensitivity. However, this homemade instrumentation does not offer the possibility to compensate the iR ohmic resistance caused by the finite ionic conductivity of electrolyte and by the cell- and electrodes geometry.

As previously reported, a Pt wire can be used as pseudo-reference electrode (or quasi-reference electrode). This means that a Pt wire of the same dimensions and thickness of the CE Pt wire was fitted in a dedicated slot of the PEEK cell. In this way, the cleanness of the electrochemical environment can be more easily preserved and the iR ohmic drop can reach negligible values, generally $iR_{pseudo} < 5\,\Omega$, since the electrolyte volume is small (around 2.3 mL) and the electrodes are in close proximity. Despite the low ohmic drop, the use of Pt as pseudo-reference electrode can in principle cause potential shifts up to 100 mV, especially when freshly saturated electrolyte is exchanged in the cell. For this reason, the most part of STM measurements were recorded using the RHE as reference electrode. Due to an excessively small cell volume, the RHE cannot be fitted directly in the cell, but needs to be mounted externally, and for this reason it is also called external reference electrode. The major disadvantage of external reference electrodes for EC-STM comes from the distance of the RE with respect to WE. Long tubes are required to establish an electrolytic connection between the RHE and the cell, thus increasing the ohmic drop up to $100\,\Omega$. Another issue concerns the cleanness of additional glassware (the electrode itself and the glass holder terminating with a glass frit) and additional tubings. Nonetheless, a satisfactory level of cleanness had been reached by Piranha etching for a few hours the glassware, and by simply rinsing the Tygon tubings with at least 2 L MilliQ water. These drawbacks are balanced by noteworthy advantages. The RHE is in fact a reference electrode with a fixed and stable reference potential. It also avoids the Au(111) contamination from anions like Cl^- or SO_4^{2-}, whose presence is brought by many standard reference electrodes like Ag/AgCl, Cl^- $Hg/Hg_2Cl_2/Cl^-$, $Hg/Hg_2SO_4/SO_4^{2-}$ etc. These anions are indeed highly prone to specifically adsorb on Au(111) surface [3], thus interfering with desired macrocyclic molecules adsorption.

The oscilloscope is a useful tool during a STM measurement session, because it gives the chance to instantly visualise a current signal and the topographic profile of the sample. The displayed current signal is comprehensive of the tunnelling current together with Faradaic current flowing through the tunnelling tip. The other displayed signal belongs to the topographic profile, i.e. the correction of the tip nominal height to maintain a constant current. An example of the two displayed signals is given in figure 3.8.

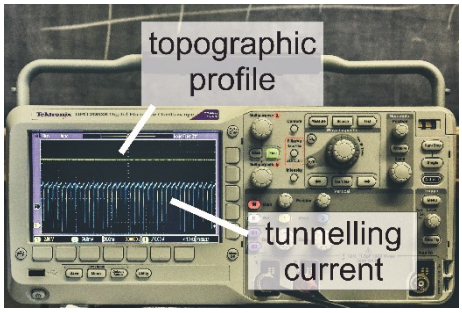

Figure 3.8. Picture of the oscilloscope with indicated signals for tunnelling current and topographic profile**.**

Their visualisation is particularly helpful when a new tip is mounted onto the scanner and in the early stages of image acquisition, when the instrumentation suffers of thermal and mechanical drift. The issue of instrumental drift will be later described in section 6.1. Through the use of the software dedicated to the STM control, the scanning direction is perpendicularly aligned with respect to the direction of maximum inclination of the sample. The aim is to reach a topographic profile as flat as possible on the oscilloscope, in order to get the maximum sensitivity and the least stroke for the tip scanning over the surface.

The heavy granite plate (7), together with the four rubber pieces and the four steel springs (8) are meant to damp high- and low-frequency vibrations, which would be detrimental to STM image recording. The granite plate serves as a stable stand platform for the STM chamber and it rests on four rubber pieces attached to a steel square structure. Four steel springs (2.5 mm wire diameter) are connected to its edges. When acquiring STM images, the plate is suspended on the four springs, thus efficiently decoupling the STM chamber from external low-frequency vibrations (< 1 Hz) [1]. Isolation from >100 Hz frequency vibrations comes from a brass stack (three plates) separated by rubber pieces. The STM base carrying the cell is positioned on the brass stack through three rubber pieces.

A two-neck terminating flask is used as electrolyte reservoir. One neck is used for a gas dispersion tube, while the other neck is used for filling the flask with new electrolyte. This flask must be mounted at a higher position with respect to the RHE and the cell taking advantage from communicating vessels principle, so that when the valve of the flask is opened, the electrolyte flows to the cell, also filling the RHE glass container. A valve placed before the RHE allows to quickly stop the electrolyte flux and reduces bubbles formation. The peristaltic pump prevents overflow of electrolyte from the cell and allows to exchange the cell electrolyte with newly saturated one. Electrolyte entry and exit is performed with glass capillary tubes, which are visible in figure 3.5. The entry tube is maintained at a lower height with respect to the exit tube, since it must also provide continuous electrolytic connection with the external RHE. Therefore, the exit tube must lie at higher position to avoid excessive suction of electrolyte, that would result in the disconnection with RHE.

The gas dispersion tube is connected to a T-shaped valve, whose two remaining capillary glass tubes are connected to the O_2 and Ar cylinders. The electrolyte (0.1 M $HClO_4$) is

bubbled (with Ar or with O_2) for at least 30 min. A second T-shaped valve enables to switch the Ar and O_2 lines for saturating the STM chamber. Connections among glassware are made with Tygon® tubes, which are highly chemical resistant and are cleaned by filling the flask with MilliQ that is then allowed to flow inside the tubes up to a Teflon® cell (in lieu of the PEEK® cell). A continuous flow of 3 L of MilliQ water assures the proper tube cleaning.

3.2.1 STM "head"

The STM "head" is the most important part of the STM unit. It features the piezoelectric system for the tip approaching and scanning, as well as the Besocke ramp for coarse approaching/retracting [4]. It also serves as support for the electronic connections needed to properly interface the STM unit to the software. In particular, it contains a pre-amplifying element, needed to amplify the tunnelling current signal, which otherwise would be too small to be accurately determined. Analog-to-digital and digital-to-analog converters are widely exploited to provide full communication between the analogic STM unit and the digital standard PC. Nonetheless, the use of an analogic-based instrumentation simplifies and enhances the STM images acquisition, since it increases frequency sampling rate and it reduces noise [1]**.** Moreover, tunnelling parameters can be directly varied during scanning, as aforementioned (section 3.2). An image of the STM head is provided in figure 3.9.

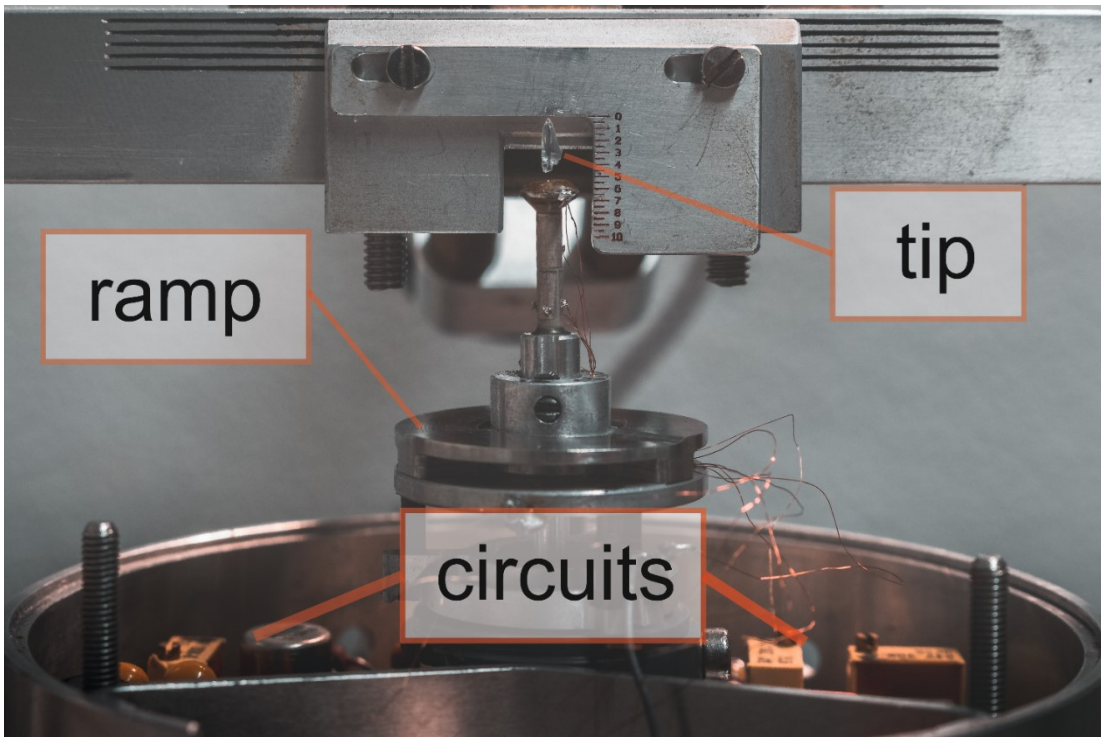

Figure 3.9. Image of STM scanner. The head is mounted upside down, with the ramp lying on the Piezo-legs, allowing the coarse approaching for the tip.

3.2.2 Tunnelling Tip

Platinum/Iridium alloy (90:10) or tungsten are common materials for tunnelling tips. Pt/Ir are stable in a wide range of applied potentials and this enhanced stability would require longer and harsher etching procedures, while tungsten can be better handled but suffers of more instability [5,6]. Pt/Ir are also more difficult to prepare due to lower hardness and tend to deform mechanically. On the other hand, tungsten exhibits better mechanical properties and an easier preparation procedure. For this reason, only tungsten tips were employed for all EC-STM measurements reported in this work. Tunnelling tips can be prepared in different ways, ranging from mechanical procedures to electrochemical etching, as well as CVD or field ion microscopy onto pre-existing tips to improve the apex [7]. "Possibly there are as many tip-preparation procedures as there are people making tips" [8]. In this work, tip preparation is accomplished through an etching method. An electrochemical circuit is built with a platinum wire (0.5 mm thickness), a tungsten wire (0.25 mm thickness) and a 2M KOH solution as electrolyte.

The Pt wire has a loop shape (6.5 mm inner diameter) and the tungsten wire is placed in its centre, using a calliper to reach ≈ 7 mm of tungsten wire length below the Pt ring. This will represent the final length of the tip. Positioning of the tungsten wire is carried out with clean tweezers. MilliQ water is used to rinse the Pt ring and the W wire after the positioning. The 2M KOH solution is poured in a small beaker and the W wire as well as the Pt ring are introduced in the KOH solution. A drop of KOH is retained by the ring in the form of a lamella. Bubbles instantly develop where the lamella embraces the W wire, since a square potential wave is applied between W and Pt. An AC voltage of 11.5 V (spike-spike) with a 100 Hz is initially applied for 2 minutes, going to 5.5 V for 30 seconds and then to 4 V up to falling of the tip. The tip drops off in a hole of a Teflon base and it is handled with clean tweezers; after rinsing it with MilliQ water it is placed in a dedicated box. This method is also regarded as "drop-off technique".

The aforementioned procedure accounts for an etching phenomenon induced by appropriate polarisation of the Pt/W circuit. Tungsten plays as anode because it is positively polarised, and it undergoes an oxidation reaction from metallic W to water-soluble tungstate anion WO_4^{2-}, thus reducing the thickness of the initial W wire. Platinum is chemically inert in this environment and acts only as an electron donor for the cathodic reaction, since it is subjected to negative polarisation. Anodic and cathodic reactions are widely recognised as [9-11]:

$$Anode: \ W_{(s)} + 8OH^-_{(aq)} \rightarrow WO^{2-}_{4(aq)} + 4H_2O + 6e^- \quad 3.2$$

$$Cathode: \ 6H_2O + 6e^- \rightarrow 3H_{2(g)} + 6OH^-_{(aq)} \quad 3.3$$

$$W_{(s)} + 2OH^-_{(aq)} + 2H_2O \rightarrow WO^{2-}_{4(aq)} + 3H_{2(g)} \quad 3.4$$

Having described the chemical aspects beyond tip etching allows to more deeply understand the *drop-off* phenomenon. When the W wire is inserted into the KOH drop, a meniscus is formed as consequence of capillary forces. A OH^- concentration gradient is

established between the wire and the ring, due to OH^- depletion at the anode (W wire). Moreover, WO_4^{2-} possesses higher molar mass than the aqueous electrolyte, thus forming a denser layer that slowly moves alongside the W wire and diminishing, together with the OH^- depletion, the W etching speed [12]. As a result, the upper part of the wire is subjected to a faster etching rate. A necking phenomenon occurs due to this anisotropic etching rate and the W wire *drops off* when its tensile strength cannot sustain its own weight anymore [12].

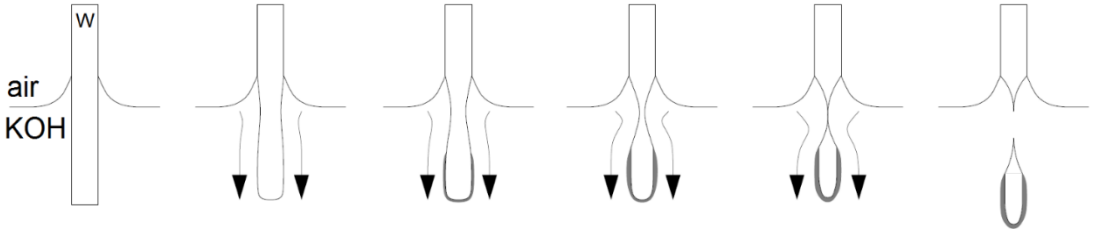

Figure 3.10. mechanism of tip etching [12].

After drying, which takes around 30 minutes, the tips can be coated with hot glue. UHU hot melt glue is cut in 3-4 mm pieces, and they are put in a beaker with MilliQ water to remove dust particles in a sonication bath. Glue pieces must be dried with dust-free paper tissues before placing 1-3 pieces on a homemade hot-plate 0.7 mm slit derived by a soldering station. The plate is heated up to 160°C and 1-3 pieces of glue are melted on the plate. The tip is aligned with the slit and by rotating an endless micrometric screw, on which the tip is mounted, it passes through the hot glue, which attaches on it forming a solid polymeric coating. The very end tip remains uncovered by the glue due to its low curvature radius. Coated tips need to be left dry overnight to allow proper glue solidification. A picture of the tip coating station is shown in figure 3.11.

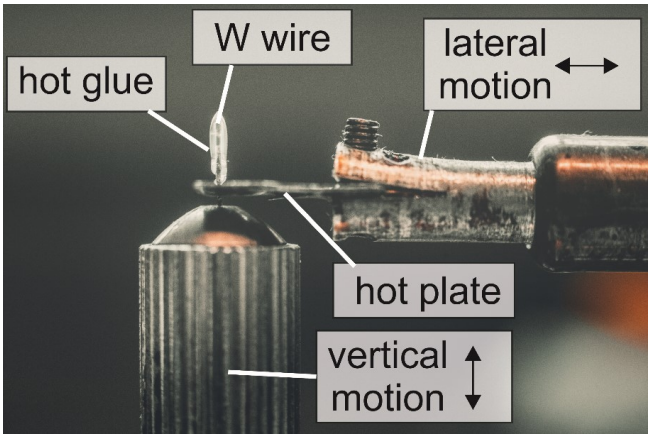

Figure 3.11. Picture of the tip coating station. Solid glue is placed on the hot-plate, where it melts. The tip is moved upwards through a slit, and the plate is withdrawn to remove the excess glue.

The glue-coated tip can now be mounted onto the STM scanner, which consists of a piezo-tube with a 4+1 electrodes design, as already presented in section 2.5.1 and as it will described in section 3.2.10. The non-coated lower part of the tip is squeezed with a

needle-nose pliers for flattening the wire, so that the tip remains more firmly stacked inside the canula holder of the piezo-tube.

3.2.3 Au(111) sample preparation

In this work, an Au(111) single crystal (MaTeck) was used as substrate for FeN_4 molecules characterisation. In the case of EC-STM, the PEEK cell exposes only a central circular area with a 4 mm diameter, while for Ex-Situ Cyclic Voltammetry a home-built PEEK holder allowed to expose the full polished 8 mm diameter surface.

The crystal undergoes a flame annealing process before each functionalisation, i.e. before each experiment, both in the case of EC-STM and *ex-situ* CV. For this purpose, the Au is positioned on a Ceran® plate, which provides a heat-resistant flat surface. A butane gas flame is directed over the top surface of the crystal, which after 1/2 minutes gains a faint red glowing colour, since the flame reaches a temperature of 600-700°C. The thermal treatment is accomplished under continuous Argon flux realised with a narrow-neck glass funnel placed 3-4 cm above the Au surface. The crystal is first brought to red-glowing colour for 4 minutes, then it is cooled down to room temperature for 10 minutes keeping it under Ar atmosphere (the funnel is moved closer to the sample). Flame annealing is repeated for 3 minutes, as well as cooling down. Finally, the Au is heated to reach the red-glowing state and then it is cooled down for 15 minutes, after which it is ready to be functionalised by dipping it in the desired FeN_4 solution (see section 3.2.8). This procedure guarantees that the gold surface is clean and flat during the deposition and the following experiment. The reducing environment, provided by the Ar flux together with the butane flame, prevents the surface to be oxidised and indeed removes the passivating surface layer formed by oxide but also by any other organic contaminants. Furthermore, the high temperatures (600-700°) lower the value for surface diffusion, so that wider atomic terraces with less defects are obtained [13,14].

A picture showing the flame annealing procedure is reported in figure 3.12.

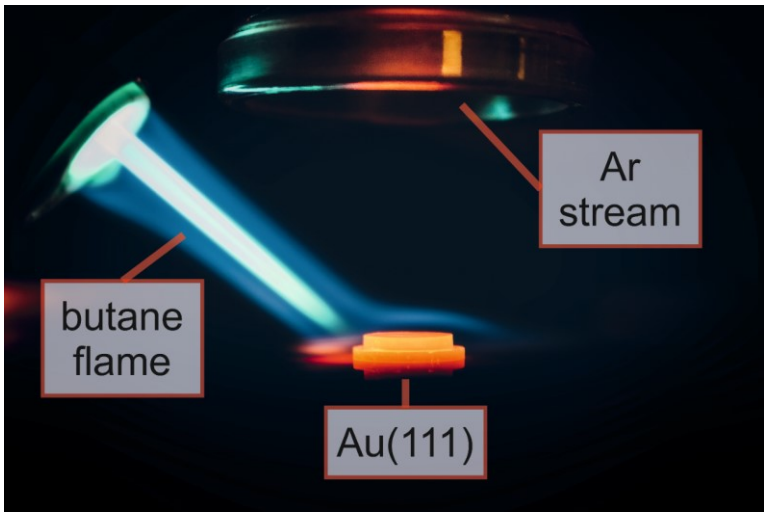

Figure 3.12. Flame-annealing procedure. A continuous Ar stream is maintained during flame-annealing. The glass tube is placed closer to Au when cooling down.

After continuative cycles of annealing, functionalisation and exposure to acids, the gold substrate may degrade, exhibiting a rougher surface, at the limit of making impossible to perform STM. Therefore, a harsher procedure was performed prior to flame annealing. It is the case of electrochemical polishing. For the purpose of this work, a brief description of the electrochemical polishing procedure is presented. It is based on the anodic polarisation of the single crystal gold substrate, brought to contact with the electrolyte with a hanging meniscus. The electrolyte is 2 M H_2SO_4, and as counter electrode a Pt foil is used. The gold substrate is subjected to an anodic current of 100 mA, which corresponds to an applied potential ≈ 3 V. Polarisation duration was set from 60 to 90 seconds. A picture of the electropolishing setup is shown in figure 3.13. After that, the substrate is rinsed with ultrapure water, and then immersed by hanging meniscus in 4 M HCl. Hydrochloric acid etches the so-formed gold oxide, restoring a fully metallic surface. This electropolishing procedure could be eventually repeated other times to provide an extensive renewal of the surface. This method was already known from literature [15,16].

Other electrochemical methods exist for improving surface smoothness, like the electro-oxidation in $HClO_4$ in presence of NaCl [17]

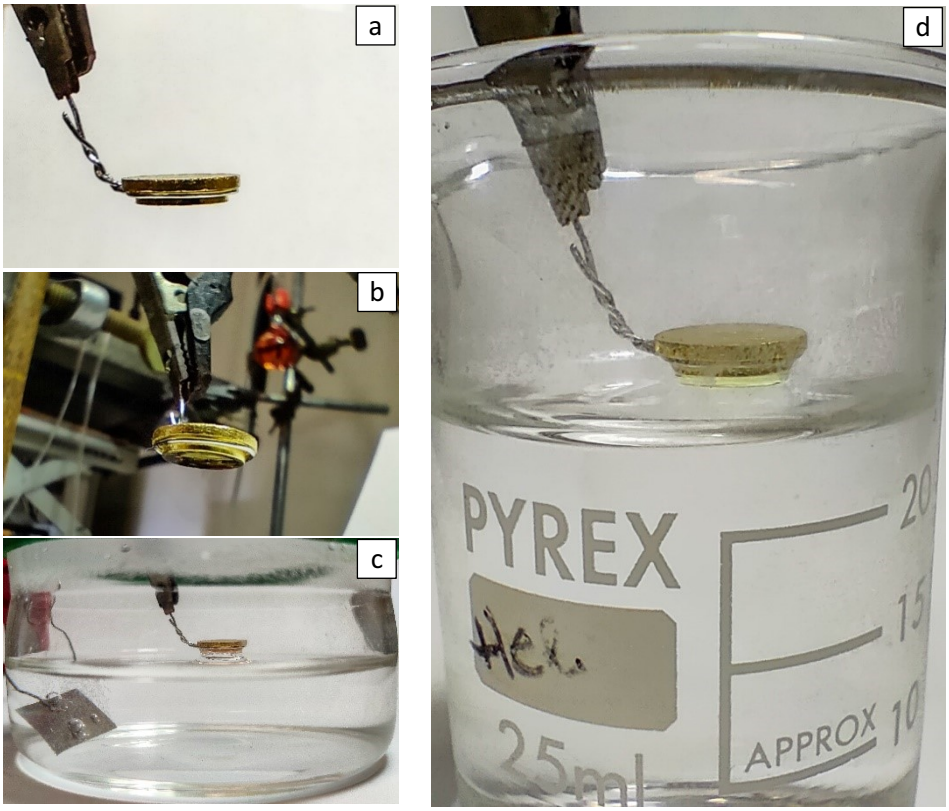

Figure 3.13. Instrumental setup for electrochemical polishing of Au(111). a) hat-shaped Au(111) single crystal placed on a Pt ring, providing a stable support and electrical contact to the gold crystal; b) view from below of Au(111) crystal leaned on the Pt ring; c) Au(111) contacting by hanging meniscus the electrolyte: bubbles develop at the Au(111) and Pt foil surfaces due to the intense applied current; d) etching of oxidised Au(111) by hanging meniscus contact with HCl aqueous solution.

Finally, the gold substrate was always flame-annealed, to remove residual anions and contaminations from the surface.

3.2.4 HOPG substrate preparation

HOPG was freshly cleaved prior to each experiment by scotch-taping. Magic Tape© was used thanks to its thickness and softness, which easily adapts to the HOPG macroscopic roughness. With a firm and sharp movement of the hand, the tape is removed, and the HOPG is cleaved (figure 3.14). This operation removes a small amount of material. The substrate can now be accommodated in the electrochemical cell and used as substrate for STM characterisation.

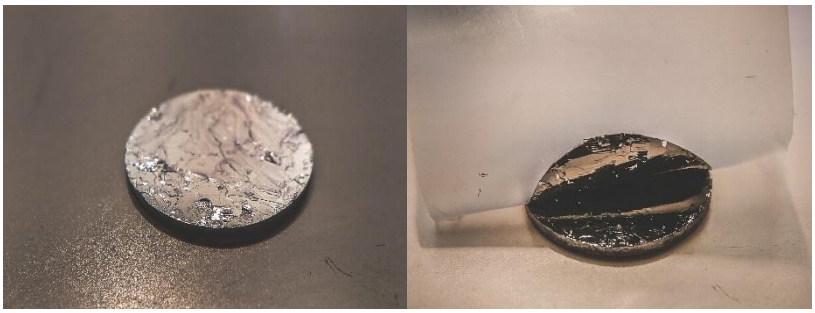

Figure 3.14. a) ruined HOPG surface before cleaving; b) scotch tape removal of a thin layer of graphite to expose a freshly cleaved HOPG surface.

3.2.5 Glassware cleaning

Thorough care must be paid for an EC-STM experiment, as already anticipated. Every source of contamination must be minimised or possibly eliminated. Inorganic contaminants can be easily eliminated by copious rinsing and ultrasonic baths, but organic carbon might still represent an issue. Extensive organic carbon removal can be accomplished by exposing the glassware to Piranha solution. Piranha etching must be performed by slowly and carefully adding hydrogen peroxide to concentrated Sulphuric Acid (>95%) [18]. The reaction is exothermic and leads to *in situ* production of peroxymonosulphuric acid, also known as Caro's acid. Its Lewis structure is shown in figure 3.15.

$$H_2SO_4 + H_2O_2 \leftrightarrows HSO_3OOH + H_2O \qquad 3.5$$

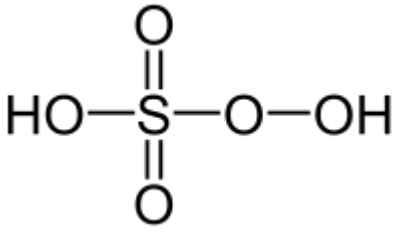

Figure 3.15. Lewis structure of Caro's acid, namely Peroxymonosulphuric acid.

Caro's acid had also been obtained by reaction of chlorosulfonic acid and 90% hydrogen peroxide [19]. However, the employment of high-test water peroxide requires thorough care and the mixing should be conducted at temperatures < 0°C, therefore this procedure was neglected. Although low-concentrated peroxymonosulphuric acid is known [20] to selectively oxidise some functional groups or to promote regioselective oxidative rearrangements, it is herein used as high-concentrated non-selective strong oxidising agent towards generic organic carbon. Despite the lack of extensive information about Caro's acid, its melting temperature was reported to be +45°C [21]. A qualitative verification can arise by direct observation of glassware filled with Piranha solution, since after few hours the solution turned opaque (especially if stirred, as the solid acid was probably precipitated).

3.2.6 Preparation of electrolyte

0.1 M $HClO_4$ was prepared using clean flasks (as described, sonication baths and Piranha solution). 67-72% Perchloric Acid (Fluka™ TraceSELECT™ Ultra, Honeywell) was properly diluted in MilliQ water (Specific Resistance > 18.2 MΩ cm, Total Organic Carbon < 5 ppb). This ensures the highest quality level for the final electrolytic solution and therefore the best conditions for running EC-STM experiments. Indeed, FeN_4 molecules possess dimensions at the nanometric scale and any other foreign molecule would interfere with the FeN_4 adsorption or would also adsorb on them, thus masking the functionalised Au surface from being scanned with the tip.

3.2.7 FeN_4 solutions preparation

Solutions of metal-phthalocyanines and -porphyrins were prepared using N,N-Dimethylformamide (DMF) to achieve a proper level of dissolution. Concentration plays a role in the achievement of a properly functionalised surface and it is strictly correlated with immersion time during functionalisation. DMF possesses a reasonably low vapour pressure (293 Pa at 20°C [22]) and therefore it can be degassed with Ar without any significant loss.

3.2.8 Au(111) functionalisation

The Au(111) surface was functionalised by hanging meniscus technique. This means that the sample surface is put in contact with the solution containing the FeN_4 macromolecules and then it is slightly withdrawn from the liquid level. However, due to capillary forces, the liquid remains in contact with the sample and a meniscus is formed. The choice of this method offers valuable advantages, such as the easy handling of the sample. It can be handled directly with clean tweezers, and indeed it allows better controlling of the immersion and retraction passages. Moreover, no particular holders are needed to fit the crystal, thus speeding up the insertion in the PEEK cell directly after functionalisation. The cleanness of the Au surface is maximised, since only the surface itself comes in contact with the FeN_4 solution.

The Au(111) sample is immersed (hanging meniscus) for 1 minute in the 0.1 mM FeN_4 solution and then quickly immersed (hanging meniscus) in a beaker containing MilliQ

water to rinse the surface from DMF residues. The sample is then directly transferred into the PEEK® cell in order to avoid air exposure of the surface. Moreover, the water drop left on the surface helps better and full contact with the electrolyte when it is introduced in the cell with the glass capillary. The PEEK® cell is in fact characterised by a finite size border that encloses the crystal and, owing to the small diameter (4 mm) of the circular aperture and to the hydrophobicity of PEEK® as well as of the FeN_4-functionalised surface, a bubble of air tends to form and stick to the Au surface, thus preventing proper contact with the electrolyte. With a clean Pasteur pipette, a drop of 0.1 M $HClO_4$ is placed onto the Au surface after it had been mounted in the cell. The presence of the water drop facilitates the 0.1 M $HClO_4$ drop adhesion itself. From now on electrolyte (at least 15 mL) can be allowed to flow in the cell through the glass capillary tube, to ensure complete removal of DMF and water traces.

As previously stated, concentration of FeN_4 solution and immersion time are key-factors for obtaining a good quality self-assembled monolayer (SAM). The optimisation of these two parameters lead to 1 minute and 0.1 mM as best immersion time and concentration, respectively, that guarantee the coverage of the entire Au surface, possibly without double- or multi-layer formation (i.e.: a molecule adsorbs on an already adsorbed one). Anyway, immersion time and concentration are just the macroscopic expression of a microscopic equilibrium among various interactions (electrostatic, hydrogen bonding, Van der Waals, hydrophobic, π-π), as already described in section 2.6.5.

3.2.9 HOPG functionalisation

HOPG generally requires longer functionalisation time with respect to Au(111) due to a lower interaction with macrocyclic molecules. HOPG, too, presents some advantages. First of all, it features an extremely easiness and quickness of exfoliation, leading to perfectly clean and flat surface at the atomic scale without any effort. Secondly, it is less sensitive to air and solution contamination. On this last aspect, no reports are known for specific adsorption of anions on its surface, contrary to Au(111) and other metallic surfaces which suffer from specific anion adsorption. However, the lower interaction with molecules forces to extend functionalisation time up to 30 min or even more. For this reason, it is not suitable for hanging meniscus functionalisation methos, also because it is fragile, and tweezers can crush its borders and surface. Like Au(111), the functionalisation procedure is based on the optimisation of time and concentration to achieve the best functionalisation results, governing the complex interplay of non-covalent forces among molecules and substrate.

3.2.10 Building an EC-STM scanner

The lifetime of a scanner piezoelectric tube is severely shortened by the continuous soldering operations to replace the very thin connection wires. Due to the homemade character of the EC-STM unit, no commercial solutions are available. For this reason, the EC-STM scanners were personally realised throughout the PhD period, starting from disassembling old scanners and trying to customise the new pieces. Differently from the

original scanners, the most accessible commercially available piezoelectric tubes are provided with a sputtered Cu/Ni coating, which confers good chemical durability. The inner and outer diameter, as well as the length, are close to the original tubes. A substantial difference lies in one of the two far end parts, which exhibits a small strip of non-conductive material to obtain a 2 mm long conductive sector. This 2 mm band is the continuation of the internal conductive material and it is of great importance, because it enables the application of a potential difference between the inner and the outer part of the tube. This polarisation causes the tube to manifest its piezoelectric nature, namely its deformation upon application of a voltage.

The purchased piezoelectric tubes therefore exhibit two electrodes: one is external, albeit not covering the full length of the tube, the other is fully covering the internal part and continues for 2 mm on one outer far end part. The external conductive part has a length of 10 mm, and it needs to be sectioned in 5 conductive sectors. Different procedures were attempted, but the only really effective yet partially "rough" is now described, referring to figure 3.16. A pristine piezoelectric tube is put through a steel stick, which is mounted itself on a brass cap featuring four grooves (1, 90° spacing among each other). A steel stick is pressed in a groove thanks to a spring (2). Upon manually releasing the spring, the brass cap can be rotated to select the 90° next groove. On the opposite side of the spring, a micrometre carries a sharp Widia tip (3). The mixture of carbides that characterise Widia make it a hard material, great for cutting applications. With the aid of the micrometre, the Widia tip is gently put in contact with the piezoelectric tube. Another micrometre is placed under the brass cap, enabling it to vertically pull it upward or downward. With the Widia tip in contact with the piezoelectric tube, a vertical movement is realised thanks to the micrometre, literally scratching the piezoelectric tube with the tip. This action leads to the removal of the conductive material coating the ceramic tube. Repeating this procedure for the other three grooves of the brass cap, four incisions remain on the piezoelectric tube. A final incision is performed around the middle of the tube. At this point, four stripes of conductive material as long as half-tube are electrically insulated by each other. Another unique sector remains on the other half of the tube. At this point, the piezoelectric tube can be cleaned with isopropyl alcohol to remove dust and dirt previously produced.

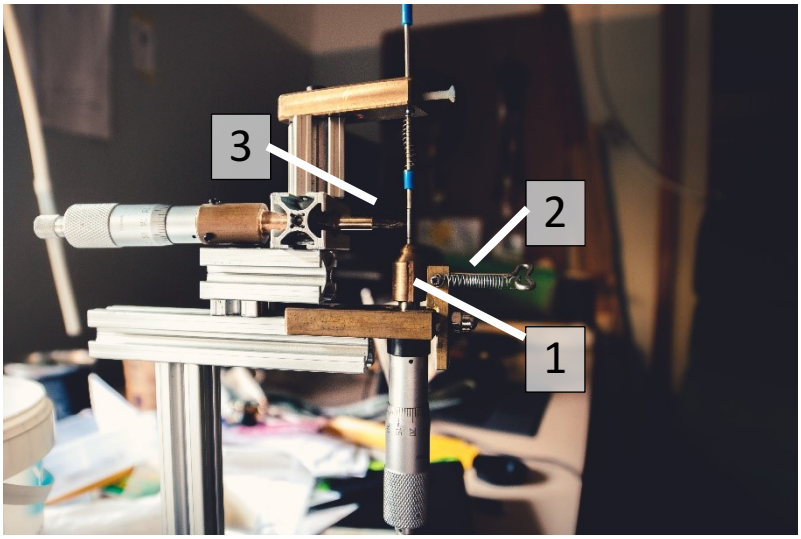

Figure 3.16. Homemade tool for dividing the piezoelectric tube in five sectors. (1) indicates the brass cap on which the tube is mounted; (2) indicates the system with stick and spring to allow 90° rotation of the tube; (3) sharp Widia tip for piezoelectric tube scratching.

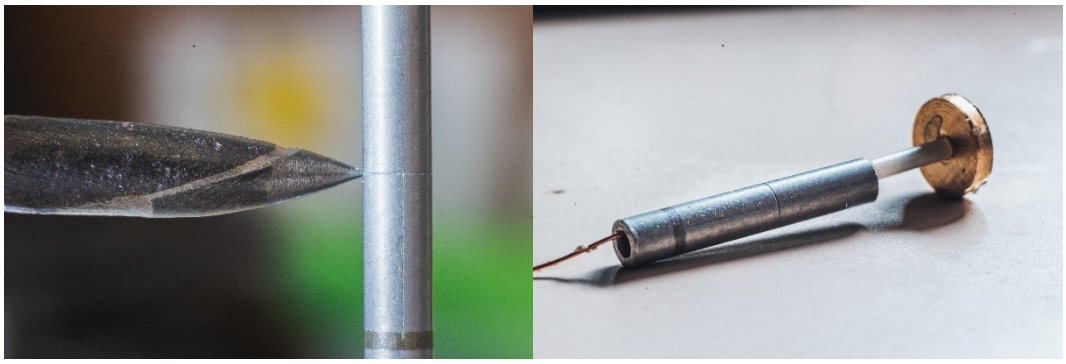

Figure 3.17. a) detail of piezoelectric tube scratching through the Widia tip; b) tip canula and brass ring system insertion into a piezoelectric tube with already divided sectors.

The tube can now be assembled. A 1 mm thin, 5 mm diameter, brass disk features a 1mm diameter hole in its centre, allowing the hosting of a ceramic tube. This tube is fixed by bi-component glue. Inside the ceramic tube, a small metallic canula is glued. This canula is obtained by carefully cutting and refining an insulin needle. Before gluing the canula to the ceramic tube, a 0.2 mm copper wire is pushed inside it and crimped, so that electrical contact is performed between the canula and the wire. At this point, the brass disk and the ceramic tube carrying the canula and the copper wire are glued together. The end part of the piezoelectric tube is instead put in an aluminium cylindrical holder and fixed with conductive glue (silver conductive paint). When the two aforementioned systems are fully dry, they can be joint together by passing the copper wire inside the piezoelectric tube until the brass disk touches the top of the piezoelectric tube, where a drop of bi-component glue definitely fixes and seals the scanner. It must be mentioned that the copper wire is actually covered by insulating material, and a small portion of insulation was removed before crimping it in the canula. In this way, the canula is

completely electrically insulated by the scanner and its aluminium holder, and the tunnelling signal can flow from the tip through the canula, then through the coated copper wire, and finally to a specific place of the amplification board where the copper wire is soldered.

The completed scanner can now be mounted on the "STM head", as shown in figure 3.9, surrounded by the beetle ramp. 0.05 mm thin copper wires can be soldered on each conductive sector of the scanner, so that they can be properly polarised to generate the in-plane *xy* displacement, and the vertical displacement along *z* as well.

At this point, the new scanner should be correctly calibrated, in order to record dimensionally accurate STM images. This is explained in detail in 4.3.

3.2.11 Re-building the amplification printed circuit board

A semi-circle shaped printed circuit board (PCB) is hosted on the aluminium head. The PCB function is to collect the tunnelling current signal measured by the tip and to amplify it, eliminating noise and disturbances of the signal. To provide more reliable and long-lasting performances of the EC-STM, new printed circuit board were designed, so that also new electronic components could be employed to realise the final amplification circuit. As shown in figure 3.18, the PCB features a number of resistors and capacitors, two inductors, four trimmers and three operational amplifiers. These are encircled in figure 3.18 and they are the core of the PCB and they allow to collect and amplify the measured signal.

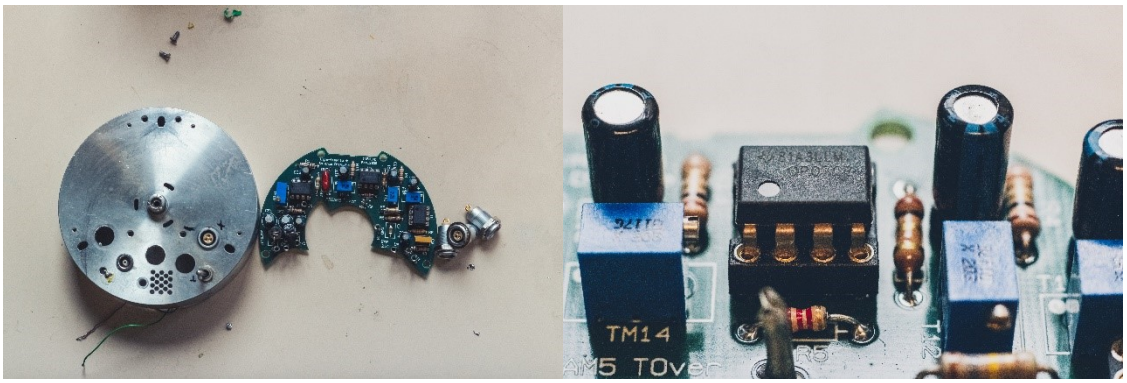

Figure 3.18. a) the circuit board featuring all electrical components is shown in the centre. This board is mounted on a steel holder shown on the left. Electrical contacts are ensured by LEMO® plugs shown on the right; b) detailed view of one operational amplifier (OP07).

3.3 Image Analysis

The output of an STM measurement is a series of topographic profiles, and each one is the result of scanning with the tunnelling tip above the sample along a scan line with definite length. By assigning colour grades to the vertical scale Z, each point of every curve is coloured on the basis of its Z value. Assuming the tip is accurately following the surface roughness, then the latter can be visualised on the false-colours image produced

by the registered topographic profiles. This can be accomplished thanks to a dedicated software. The software that controls the STM unit actually realises a first image processing, returning raw images. These can be thought of as the original image registered by the instrumentation, and they are also said to be unfiltered. There exists several third-party software that allow to enhance images by applying specific filters. These filters increase the contrast and reduce noise or bad data points, and for this reason their employment must be moderated, otherwise artefacts are introduced in the final image. In this work, the two software WSxM [23] and Gwyddion [24] were extensively used.

3.3.1 WSxM

WSxM [23] was extensively employed thanks to its outstanding usability. With few quick operations it can indeed process an image and make it ready for advanced analysis, for example Z profile extracting, distances or angles measuring, etc. A procedure which revealed to be suitable in most of the cases is now described. First of all, the desired raw image is loaded into the program, and colour grades will automatically be attributed. Frequently, images present a slope, which is a direct consequence of a non-ideally horizontal tip scanning over the surface. This is often due to a sample declivity, since its mounting in the PEEK cell is susceptible of small variations, which however can determine large effects considering the exceptional STM sensitivity. To correct this effect, the function “global plane” can be used. It acts by subtracting a plane to the series of topographic profiles forming the image, correcting the non-horizontal position of the sample at the moment of scanning. If one or more step edges are present in the image, this automatic procedure can fail to give back a proper result, therefore the “local plane” function can be used. Small areas that must have the same Z height are manually selected to aid the software subtracting a proper plane to the raw image. Another essential feature is called “flatten”. It exerts a smoothing effect on the image. STM images often present scars and stripes. Plenty of them are horizontal due to misalignment among consecutive scanning lines, as a result of, for example, bad response of the piezoelectric materials or small vertical oscillations, which were not completely attenuated. As a consequence, successive topographic lines may present an offset, which moves the entire topographic profiles to lower or higher Z values if compared to previous and following scan lines, causing scars and stripes to appear with very bright or very dark colour. The “flatten” function acts with a flattening effect to reduce stripes and scars. “Equalise” is the mostly employed tool. It has the ability to tune image contrast, enhancing the colour difference between flat areas and protruded features. The “equalise” function allows to manually select a range of heights, excluding too short or too large height values, provoked by tunnelling disturbances. Those values are therefore not representative of the real system and can be considered as artefacts. By contracting the range of heights, the colour grades are more finely redistributed, and the image appears more definite and easier to analyse. If a stripe is completely black or white, it can be eliminated by the “remove lines” tool.

The described filtering operations are always necessary to attain trustworthy images. The risk of introducing new artefacts in the image is minimum: filtering operations are

manually accomplished, and the effect of every parameter can be instantly displayed and therefore directly adjusted, if necessary.

Analysis of STM images is mostly performed by extraction of topographic profiles. The "profile" tool allows to trace any desired straight line on an image. This line will touch at least one point of the original topographic profiles registered during scanning. All the point that the line intersects will be retained and used to generate the corresponding topographic profile, as sequence of experimental data points. Straight lines are traced over regions of interest, like atoms, clusters, or molecules. This opens the possibility to gain fundamental information about the surface of the sample, especially if it had been intentionally functionalised with particular molecules, as did for this work with macrocyclic MN_4 compounds.

3.3.2 Gwyddion

Gwyddion [24] was also used for image analysis. Many features are in common with WSxM, even if different algorithms are used and a smaller level of manual actions is allowed, making image processing trickier. For image filtering, WSxM was preferred. Nonetheless, other actions are better performed or were no featured in the other software. A clear example is represented by profile extraction. A straight line can be drawn in whatever direction, and the software will return the corresponding topographic profile on the basis of the intersected data point. If, in the case of an oblique line, no points of a scanning line are intersected, then the software can perform an interpolation among the points that precede and follow the intermediate desired value. Moreover, many different interpolating functions are available: round, linear, Key, Nearest Neighbours Interpolation, etc. The main advantage is the possibility to select the "thickness" of the final topographic profile. If the thickness is increased, more points along the perpendicular direction of the drawn line will be averaged, originating a smoother and more definite final profile. This reveals to be a good a posteriori method for contrasting instrumental noise and to achieve more reliable morphological data.

It is worth to mention that the WSxM software features many additional functions and analysis instruments, which however go out of the purposes of the present work. The only quantitative information obtained by the analysis of an STM image basically lies in topographic profiles. The real and tangible capability of EC-STM lies in the structural and mechanistic information achieved by interpretation of the changes among multiple consecutive images, registered under potential control of the Working Electrode. As a matter of fact, information about surface structural order (or disorder) can also be extracted.

3.3.3 CorelDRAW® Graphics Suite 2019

CorelDRAW® is a vector graphics editor. Despite its high potentiality, its use was limited to simple graphics drawing for determining unit cell parameters, angles, domain boundaries, etc. Anyway, it allowed to reach high precision levels and an appreciably fast workflow, giving the opportunity to repeat the same measures for different areas of the

same image and for different images. Therefore, the resulting data possess a statistic-like nature.

References

[1] M. Wilms, M. Kruft, G. Bermes, K. Wandelt, A new and sophisticated electrochemical scanning tunneling microscope design for the investigation of potentiodynamic processes, Review of Scientific Instruments. 70 (1999) 3641–3650.

[2] A.J. Bard, L.R. Faulkner, Electrochemical Methods, Fundamentals and Applications, John Wiley & Sons, inc., 2001.

[3] O.M. Magnussen, Ordered anion adlayers on metal electrode surfaces, Chemical Reviews. 102 (2002) 679–725.

[4] M. Wilms, P. Broekmann, C. Stuhlmann, K. Wandelt, In-situ STM investigation of adsorbate structures on Cu (111) in sulfuric acid electrolyte, Surface Science. 416 (1998) 121–140.

[5] B.L. Rogers, J.G. Shapter, W.M. Skinner, K. Gascoigne, A method for production of cheap, reliable Pt-Ir tips, Review of Scientific Instruments. 71 (2000) 1702–1705.

[6] A.H. Sørensen, U. Hvid, M.W. Mortensen, K.A. Mørch, Preparation of platinum/iridium scanning probe microscopy tips, Review of Scientific Instruments. 70 (1999) 3059–3067.

[7] A. Lucier, Preparation and Characterization of Tungsten Tips Suitable for Molecular Electronics Studies, Master Thesis, 2004.

[8] I. Ekvall, E. Wahlström, D. Claesson, H. Olin, E. Olsson, Preparation and Characterization of electrochemically etching W tips for STM, Meas. Sci. Technol. 10 (1999) 11–18.

[9] J.P. Ibe, P.P. Bey, S.L. Brandow, R.A. Brizzolara, N.A. Burnham, D.P. DiLella, K.P. Lee, C.R.K. Marrian, R.J. Colton, On the electrochemical etching of tips for scanning tunneling microscopy, Journal of Vacuum Science & Technology A: Vacuum, Surfaces, and Films. 8 (1990) 3570–3575.

[10] R. Kazinczi, E. Szocs, E. Kálmán, P. Nagy, Novel methods for preparing EC STM tips, Applied Physics A: Materials Science and Processing. 66 (1998) 535–538.

[11] I. Ekvall, E. Wahlström, D. Claesson, H. Olin, E. Olsson, Preparation and Characterization of electrochemically etching W tips for STM, Meas. Sci. Technol. 10 (1999) 11–18.

[12] A. Lucier, Preparation and Characterization of Tungsten Tips Suitable for Molecular Electronics Studies, 2004.

[13] J. Clavilier, K. El Achi, M. Petit, A. Rodes, M.A. Zamakhchari, Electrochemical monitoring of the thermal reordering of platinum single-crystal surfaces after metallographic polishing from the early stage to the equilibrium surfaces, Journal of Electroanalytical Chemistry. 295 (1990) 333–356.

[14] P.J. Welford, B.A. Brookes, V. Climent, R.G. Compton, The hanging meniscus contact: Geometry induced diffusional overpotential. The reduction of oxygen in dimethylsulphoxide at Au(111), Journal of Electroanalytical Chemistry, 513 (2001) 8–15.

[15] B. Madry, K. Wandelt, M. Nowicki, Sulfate structures on copper deposits on Au(111): In situ STM investigations, Electrochimica Acta. 217 (2016) 249–261.

[16] B. Madry, I. Morawski, T. Kosmala, K. Wandelt, M. Nowicki, Porphyrin Layers at Cu/Au(111)–Electrolyte Interfaces: In Situ EC-STM Study, Topics in Catalysis. 61 (2018) 1335–1349.

[17] K.T. Umezawa Noriko, Sano Shoko, Aoki Nana, Friedbacher Gernot, Step-by-step Investigation of Atomically Flattening Processes of Au(111) Single Crystal Surfaces, 82 (2014) 346–350.

[18] E.T. Fell, US2789954A. United States Patent Office, 1953.

[19] D.L. Ball, J.O. Edwards, The Kinetics and Mechanism of the Decomposition of Caro's Acid. I, Journal of the American Chemical Society. 78 (1956) 1125–1129.

[20] G.R. Krow, Monoperoxysulfuric Acid, Encyclopedia of Reagents for Organic Synthesis. (2001).

[21] J. D'Ans, W. Friederich, Synthese der Caroschen Säure und der Überschwefelsäure, European Journal of Inorganic Chemistry. (1910) 1880–1882.

[22] www.sigmaaldrich.com/dmf.pdf.

[23] I. Horcas, R. Fernández, J.M. Gómez-Rodríguez, J. Colchero, J. Gómez-Herrero, A.M. Baro, WSXM: A software for scanning probe microscopy and a tool for nanotechnology, Rev. Sci. Instrum., 2007, 78.

[24] D. Nečas, P. Klapetek, Gwyddion: An open-source software for SPM data analysis, Cent. Eur. J. Phys., 2012, 10, 181–188.

Chapter 4

Substrates

This chapter is meant to introduce the two substrates herein employed for electrochemical characterisation, both with cyclic voltammetry and EC-STM. The handling procedures concerning the substrates have already been discussed in sections 3.2.3, 3.2.4, and 3.2.8 and 3.2.9. Here, EC-STM images both of Au(111) and HOPG are first presented, followed by and eventually correlated to cyclic voltammograms. The precise knowledge of imaging and electrochemical responses of the substrates indeed allows a clearer understanding of the experimental data collected with more complex sample preparations, featuring for example metal-complexes like in this case.

4.1 Au(111)

Gold finds applications in many fields of science and arts, having also represented a valuable coinage metal, still in use nowadays as a refined raw material for expensive jewellery. Modern common and industrial applications concern dentistry and electronics. Its electronic configuration is $[Xe]4f^{14}5d^{10}6s^{1}$ and it therefore belongs to the 11th group and the 6th period of the periodic table of elements [1]. It melts at 1337.33 K and boils at 3129 K. Pure gold is non-magnetic and represents one of the most inert metallic elements: for this reason, it is also regarded as a noble metal [2]. It can be etched by *aqua regia*, as shown in the following reaction:

$$Au + 4HCl + HNO_3 \rightarrow H[AuCl_4] + 2H_2O + NO \qquad 4.1$$

The mixture of hydrochloric and nitric acid oxidises gold, producing chloroauric acid. Alternatively, it can be dissolved in aqueous solutions containing an oxidising agent and a ligand (for example HCl and $FeCl_3$) [2]. It is however insoluble in nitric acid, while poor solubility is retained in mercury, with which it forms a solid solution (amalgama) up to 16% Hg [3].

Apart from its decorative purposes, gold retains a primary role in nanoscience and nanotechnology, catalysis and self-assembled monolayers for physical chemical studies [3]. It is resistant towards oxidative corrosion [4] and it is widely regarded as an excellent thermal and electrical conductor.

Gold crystallises with a Face Centred Cubic (FCC) structure [5]. The unit cell for the bulk crystal has a lattice constant of 4.072 Å [6,7], whereas the atomic radius is 1.442 Å. The nearest-neighbours distance equals 2.884 Å. Being a single crystal, it was mostly studied for its low-indexes faces, namely (100), (110), (111). A representation of the three low-index faces is shown in figure 4.1 for a generic FCC crystal.

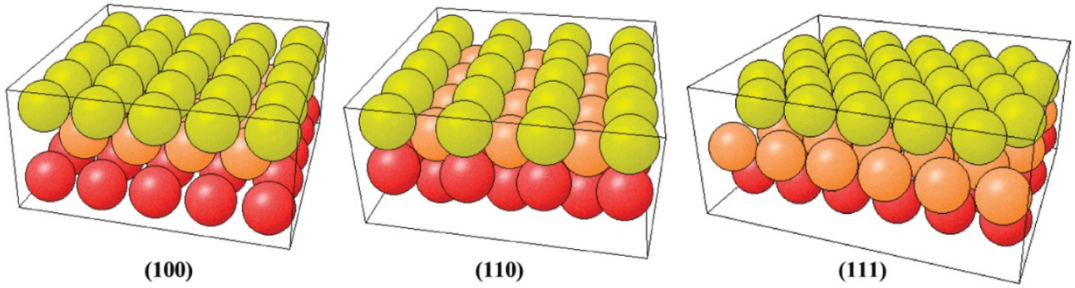

Figure 4.1. hard-spheres packing for the three low-index crystallographic faces for an FCC crystal [6].

4.1.1 EC-STM characterisation of Au(111)

Transition metals may present a change in the electronic state of the top layer, causing therefore the surface to behave differently from the corresponding bulk material [8]. Surface stress can arise and act as a driving force towards a surface reconstruction. In fact, all the three low-index gold surfaces exhibit a surface reconstruction. Au(100) is known to reconstruct with a (5 x 20) cell, producing a quasi-hexagonal top layer [6]. The missing row along the $< 1\underline{1}0 >$ direction causes the Au(110) to reconstruct into a (1 x 2) pattern [5]. The Au(111) face exhibits a remarkable reconstruction, called "herringbone reconstruction", and defined by a (22 x √3) unit cell [5,9-12]. This particular surface reconstruction is the outcome of two opposing tendencies [5,9,13,14]. The top layer prefers to contract, since surface atoms have a lower coordination number than bulk atoms (9 vs 12). Therefore, contraction of the top layer compensates for the reduced coordination. On the other side, surface atoms are also forced to occupy positions of minimum energy dictated by the underlying bulk atoms, thus forcing the growth of a commensurate layer. A misfit originates between top layer and bulk and a reconstruction of the surface occurs, also known as herringbone reconstruction. It is characterised by periodic arrays of pairs of partial dislocations, which act as domain walls among face-centred cubic FCC and hexagonal close-packed HCP domains. They are also termed as ridges. The compresence of both FCC and HCP domains is a consequence of the FCC bulk structure itself. Indeed, the stacking sequence along the <111> causes the atoms to occupy A, B, C positions with a …ABCAB… sequence for the bulk phase, whereby the surface atom can occupy either a FCC site (terminating the sequence with C, …ABCABC) or an HCP site (terminating the sequence with A, …ABCABA). The surface FCC and HCP positions both represent local minima of potential, but HCP are slightly higher in energy. This argument can justify the smaller width of HCP domains with respect to FCC domains. Alternating FCC and HCP domains are separated by domain walls, with a height of ~0.1 to 0.2 Å. These ridges are produced by the occupancy of bridge sites, which lie in between A and C sites. The (22 x √3) cell contains 23 atoms instead of 22. The extra atom relieves the tensile strength along the $< 1\underline{1}0 >$, causing in fact a 4.4 % contraction along that direction in the top layer. The outcome is then a surface superstructure made of alternating uniaxial domains arranged in a zig-zag pattern (herringbone) [13].

Figure 4.2 demonstrates the presence of zig-zag corrugations typical of herringbone reconstruction. This reconstruction is a clear proof of the (111) facet exposure [9,13–16]. Fig. 4.2a manages to provide a high-resolution image, showing close-packed atomic positions together with the long-range herringbone modulation. Focussing now on herringbone reconstruction, topographic profiles were extracted, to measure the height and the periodicity of the ridges. The typical height is expected to be collocated in the range of 0.1 – 0.2 Å [13]. For each extracted topographic profile, the height of each corrugation is calculated as the difference between one maximum (top of the corrugation) and the absolute minimum, which indicates the FCC domain. A local less deep minimum is found between each couple of corrugations and represents the HCP domain.

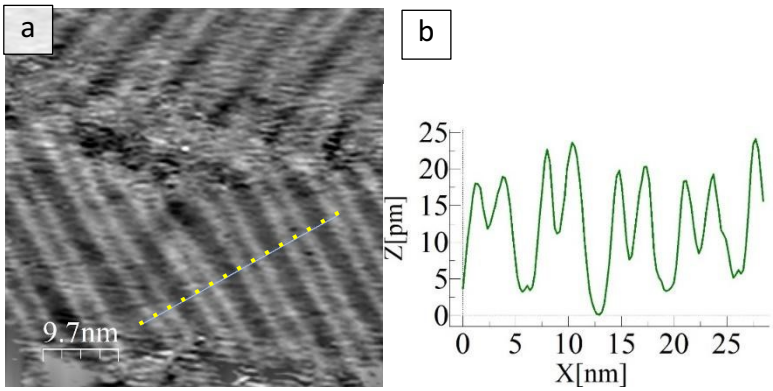

Figure 4.2. a) typical zig-zag pattern produced by herringbone reconstruction on Au(111). Tunnelling parameters are: I_t = 1.55 nA, U_b = -125 mV, E_{app} = 0.45 vs RHE; b) topographic profile corresponding to the yellow dashed line of figure 4.2.a.

The measured height of the ridges for image 4.2 is measured as $h = 0.124$ Å.

The measured value for the corrugation is close to the expected one (0.1-0.2 Å), so the instrumentation is proved to reliably probe the sample surface, without significant deviations from reality.

The periodicity of herringbone reconstruction is also measured by means of topographic profiles. Since many herringbone reconstruction lines are present in the image of figure 4.2, an average value of its periodicity can be obtained. The maximum distance between two identical points (in this case, the left border of the ridges) is divided by the number of repeating structures. The so-obtained average periodicity is $d = 6.9\ nm$.

This value can be compared with literature data obtained at the solid/UHV interface [17-19], revealing that the reference value is fully contained in the confidence interval of the experimental periodicity determination.

A high-resolution picture of the Au(111) surface is reported in figure 4.3.a. Few herringbone ridges are now occupying the entire image due to the reduced scan size, but gold atoms are also visible as small dots. The measured nearest neighbour distance is 0.295 nm, which is in good agreement with the theoretical value of 0.289 nm [10,12,17–19].

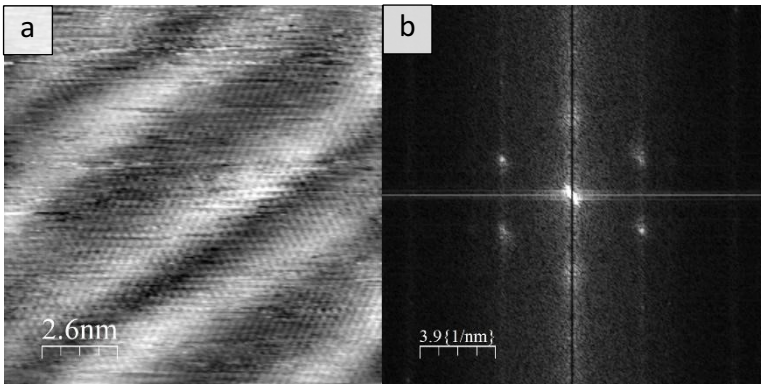

Figure 4.3. a) high-resolution EC-STM image collected for bare Au(111) in contact with deaerated 0.1 M $HClO_4$. Tunnelling parameters are: I_t = 3.65 nA, U_b = -100 mV, E_{app} = OCP. b) corresponding FFT of image 4.3.b.

The above figures 4.2 and 4.3 are also a clear example of cleanness of the Au single crystal surface, thanks to the substrate preparation procedure by flame annealing. Moreover, it is also a proof that external gases do not contaminate the sample surface. In fact, the chamber can be saturated with Ar gas, but the Au single crystal is mounted in the PEEK cell and transferred in the STM unit by direct air exposure for a few minutes, which for other surfaces would inevitably lead to extensive contamination, as theoretically calculated in section 2.1.

Finally, an example of Au(111) step edge is reported in figure 4.4. The tabulated value for step edge thickness is 0.24 nm, and the topographic profile extracted by image 4.4.a returns a value of 0.23 nm, which is in the range of the expected one, as visible in figure 4.4.b [17].

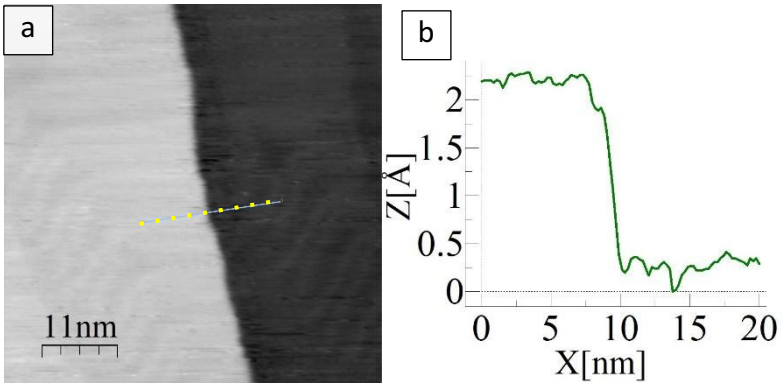

Figure 4.4. a) EC-STM image of bare Au(111) in contact with deaerated 0.1 M $HClO_4$. Tunnelling parameters are: I_t = 1.00 nA, U_b = -150 mV, E_{app} = 0.6 V vs RHE: b) topographic profile corresponding to the yellow dashed line of figure 4.4.a.

4.1.2 Electrochemistry of Au(111)

The (111) gold facet is known to exhibit the (22 x √3) pattern even at the solid/electrolyte interface. There is however a significant effect of the applied working electrode potential when the Au single crystal is mounted in an electrochemical cell and plays as working

electrode. For a metal surface contacting an electrolytic solution in an electrochemical cell setup, a Point of Zero Charge (PZC) will always exist, at which no excess charge appears at the electrode surface [20]. If the electrode is intentionally polarised at whatever potential different from PZC, an excess charge will be present at the surface. The electrode potential in fact represents the electrochemical potential of electrons in the electrode and it is directly connected to the metal Fermi level, which in turn depends on the metal work function [21]. When the applied electrode potential is more negative then to the PZC, the surface reconstructs within the herringbone pattern. Conversely, if a more positive potential than PZC is applied, the reconstruction is lifted, and the surface exhibits the unreconstructed (1 x 1) surface. This phenomenon is called *potential-induced reconstruction* and it is the evidence of the implication of surface charges in the reconstruction behaviour of surfaces. The lifting/reconstructing mechanisms are quickly accomplished: few seconds are usually enough for the completion of reconstruction (or its lifting). However, the lifting/reconstruction phenomenon at the Au(111) surface is somewhat tricky. The herringbone pattern is in fact recognised as the energetically more stable state of the Au(111) surface. Thus, the (1 x 1) unreconstructed surface is a metastable state, and the application of a definite negative potential (vs PZC) simply acts on the activation barrier for reconstruction, but not on the thermodynamic state of the surface [21].

When the original herringbone pattern is lifted, monoatomic-thick Au islands are formed [22]. They are originated by the excess Au atoms that were fitted in the ridges of the more densely packed (22 x √3) surface, as previously explained in section 4.1.1. The Au islands also act as nucleation centres during the potential-induced reconstruction, since they are the easiest source of extra Au atoms to be fitted in the compressed herringbone top layer. The potential-induced reconstruction is not completely innocent. A potential-induced reconstructed surface can be in fact distinguished by a more pronounced zig-zag pattern, and one terrace often presents more than one orientational domains of reconstruction rows.

The lifting/reconstruction phenomenon can be easily probed by means of cyclic voltammetry. The (22 x √3) → (1 x 1) transition causes the appearance of a positive current peak at $E_{p,lift} \approx 0{,}75\ V\ (vs\ RHE)$ if an anodic scan is performed from negative potentials with respect to PZC. Vice versa, a negative current peak appears at $E_{p,rec} \approx 0{,}70\ V\ (vs\ RHE)$ when the potential is swept back to more negative potential than PZC. These features are visible in the cyclic voltammetry shown in figure 4.5. The herringbone reconstruction/lifting is regarded as a reversible process [23] and it occurs each time the electrode potential overcomes the PZC potential in cathodic or anodic sweeps.

An Au(111) cyclic voltammogram exhibits other features which are worth to be described. Three main peaks are noticeable, and they are regarded as a fingerprint of an Au single crystal exposing the (111) crystallographic plane [27]. They are connected to the oxidation mechanism of the substrate, as well as its reduction [19]. Gold behaves like many other metals when inserted in an electrochemical cell and exposed to an electrolytic

acid solution. If it is positively polarised, it undergoes oxidation through a two-electron mechanism formulated as:

$$M + H_2O \rightleftarrows MOH + H^+ + e^- \quad 4.2$$

$$MOH \rightleftarrows MO + H^+ + e^- \quad 4.3$$

$$M + H_2O \rightleftarrows MO + 2H^+ + 2e^- \quad 4.4$$

The two major oxidation peaks are labelled OA3 ($E_{OA3} \approx 1{,}34\ V$) and OA4 ($E_{OA4} \approx 1{,}56\ V$) [20]. Minor peaks or waves are found to precede E_{OA3} and are named OA1 and OA2. OA1, OA2 and OA3 (figure 4.5) are concerned with the first electron transfer of reaction (1). In particular, OA1 and OA2 are related to OH deposition in between specifically adsorbed anions [24,25]. The $HClO_4$ solution provides perchlorate ClO_4^- anions, which are known for their low adsorption tendency on gold [24,26-29]. This is not true for any applied potential window. If a consistent positive excess charge is realised at the Au surface, even least adsorbing anions find favourable conditions for specific adsorption. This implies that large positive potentials need to be applied: in this case, E_{app} > 1.2 V is required to attain adsorption, whereas many other anions, like halides (I^-, Br^-, Cl^-) or even sulphate SO_4^{2-} specifically adsorb at much lower applied potentials (frequently, E_{app}< 0.7 V) [30]. For ClO_4^-, H_2O molecules of the primary hydration shell are H-bonded to the O-atoms forming perchlorate [24,31]. Therefore, a significant part of the gold surface is hindered towards OH deposition by already adsorbed perchlorate anions. By positively raising the applied potential, a progressive discharge of the H-bonded water occurs, and the previously adsorbed anions are replaced by OH. This process is considered completed at OA3. At this stage, gold has been subjected to the first reaction of eq. (4.2). Now the surface is exposing M-OH dipoles, which may form 2 or 3 sublattices. Nonetheless, the most part of dipoles undergoes the following reconstruction mechanism (turn-over) [24,25]:

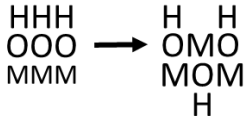

4.5

This first stage of gold oxidation is also referred as Under Potential Deposition of OH species between the adsorbed perchlorate anions [32].

Upon applying even more positive potentials, a second electron is transferred, and a monolayer-thick oxide film is formed, as shown in the second reaction of eq. (4.2). This justifies the presence of the anodic peak at $E_{OA4} \approx 1.60\ V$. This peak actually exhibits a higher current than expected by a simple one-electron transfer, and the claimed reason lies in an already not completed perchlorate desorption even when E_{OA3} was reached.

The oxide monolayer then undergoes complete reduction at $E_{OC} \approx 1.15\ V$, as proven by the intense peak in fig. 4.3. The reverse mechanism with respect to (4.3) is first required, namely the turn-over of the surface:

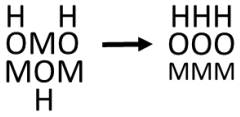

4.6

Now the actual reduction can take place, as:

$$MOH + H^+ + e^- \rightarrow M + H_2O \qquad 4.7$$

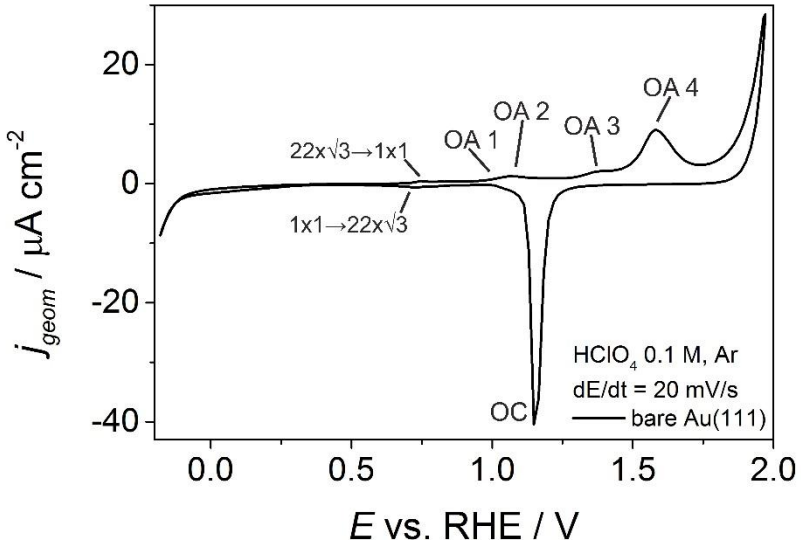

Figure 4.5. CV of Au(111) single crystal in argon purged 0.1 M $HClO_4$ recorded at 0.2 V/s.

4.2 HOPG

Graphite is an allotropic form of carbon, based on layers of hexagonally arranged carbon atoms. These atoms build the planar condensed ring system of graphene. The hexagonal close-packed stacking of a multiple number of graphene layers brings to the final graphite structure [33]. That of graphite is therefore a lamellar structure, and carbon atoms within a plane interact much stronger than with atoms belonging to adjacent planes. This is due to the weak Van der Waals interactions of delocalised π orbitals. For this reason, graphene planes can easily slide on each other, making graphite a good lubricant. Another effect of the layered structure is the anisotropy of the electrical and thermal conductivity, which is good along the planes and poor in the perpendicular direction [34]. Natural graphite presents numerous defects and inclusions, but techniques do exist to increase the degree of order and extent of graphene layers [35]. In particular, highly oriented pyrolytic graphite (HOPG) is obtained by applying high uniaxial pressure at high temperature (≈3000 °C) to a graphite slab. Depending on time, pressure, duration of the treatment and on the specific part of the graphite slab, a certain quality of the final HOPG piece is achieved. The quality of HOPG samples is expressed in terms of mosaic spread. HOPG is in fact made of layered polycrystals which can be disoriented from each other. Mosaic spread ranges from 0.4° for maximum grade HOPG (ZYA), to 0.8° (ZYB) and finally to

3.5° for lower quality samples (ZYH) [35]. In this work, HOPG specimens with either ZYA or ZYB were employed.

4.2.1 EC-STM characterisation of HOPG

Graphene appears as a honeycomb-like hexagonal lattice, and it is characterised by two triangular sub-lattices, referred as A and B, each one containing half of the carbon atoms. Each A atom is surrounded by three B atoms, and vice versa. Two coupled hexagonal lattices are stacked according to ABAB, and an A carbon lies above another A carbon, while a B carbon lies above an empty site (centre of a hexagon). Distance between carbon atoms is 0.1415 nm, even if a caveat must be introduced when imaging HOPG surface with a scanning probe microscopy technique, like STM. In fact, bright spots usually originate from only three out of six carbon atoms of a graphene hexagon, with a distance between these spots equal to 0.246 nm. This effect is reconducted to the AB stacking and the result is called “three-for-six” pattern [36]. A single step edge has a height of 0.34 nm, even if it must be clarified that terrace steps can exhibit thickness from one to several layers of graphene [36–38].

Figure 4.5.a features a high-resolution EC-STM image of HOPG. The bright dots correspond to C atoms and they are arranged within a hexagonal array. As demonstration, the FFT image is reported in figure 4.5.b. The outcoming bright dots in the reciprocal space allow to extract distance values, in this case agreeing with the expected 0.246 nm “three-for-six” pattern periodicity.

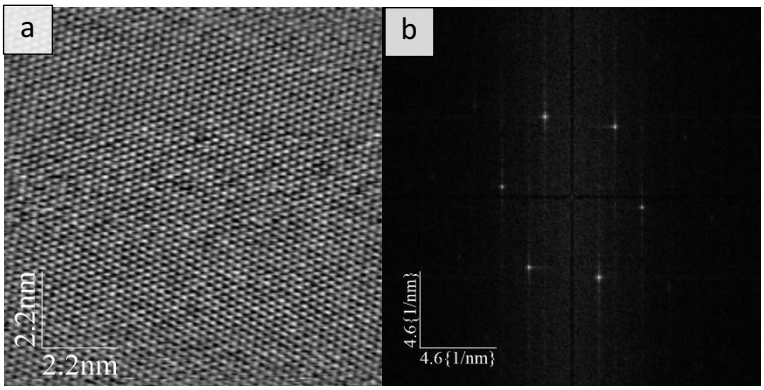

Figure 4.5. a) EC-STM image of bare HOPG in contact with 0.1 M $HClO_4$. Tunnelling parameters are: I_t = 0.32 nA, U_b = - 700 mV, E_{app} = 0.65 vs RHE; b) FFT of image 4.5.a, showing the typical hexagonal periodicity of graphite.

Figure 4.6.a is an example of graphene layers stacking. In this case, a unique layer is superimposed to another, and the extracted topographic profile correctly exhibits a value of 0.35 nm, in good agreement with the expected value of 0.34 nm. [38]

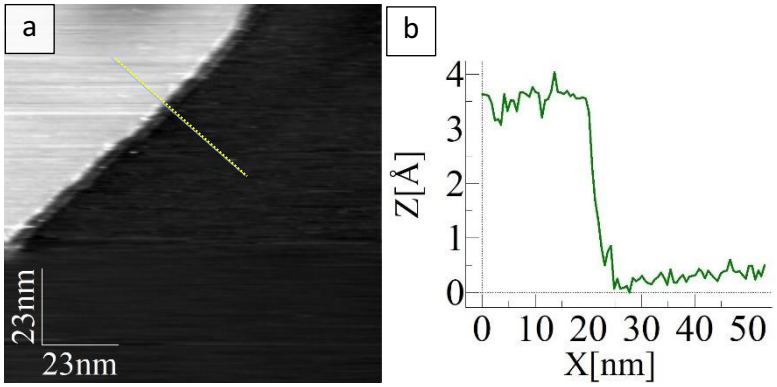

08/10/2019

Figure 4.6. a) EC-STM image of bare HOPG in contact with 0.1 M $HClO_4$. Tunnelling parameters are: I_t = 0.32 nA, U_b = - 650 mV, E_{app} = 0.65 vs RHE.

4.2.2 Electrochemistry of HOPG

From the electrochemical point of view, HOPG presents a rather featureless cyclic voltammogram in Ar purged electrolyte. Graphite is in fact quite an inert electrode and no significant phenomena occur in the scanned potential range. For further information, it must be remarked that certain anions, like perchlorate and sulphate, are known to be able to intercalate in the HOPG basal plane, leading to blisters formation and exfoliation [39]. The intercalation mechanism is based on solvated anions that, thanks to a sufficiently positive working electrode applied potential (≈1.8 V vs. RHE), penetrate from the HOPG surface through basal planes. Once anions are intercalated, delamination of graphite is promoted. Anyway, these positive potentials were avoided, since CVs were limited to +1.5 V vs RHE.

Oxygen reduction reaction on carbon usually proceeds via the $2e^-$ pathway, thereby leading to H_2O_2 production, without its further reduction to H_2O. It must be remarked that, especially for basal plane graphite (like HOPG), ORR kinetics is sluggish. In fact, the ORR peak potential is even more negative than -0.5 V, as shown in figure 4.7. This behaviour is ascribed to a more extensive presence of functional groups on edge planes, rather than on basal planes. The two main reaction steps proposed for ORR on graphite electrodes are:

$$O_{2(ads)} + e^- \rightarrow O^-_{2(ads)} 2O^-_{2(ads)} + H_2O \rightarrow O_2 + HO_2^- + OH^- \qquad 4.8$$

Concerning the catalytic sites on carbon materials, the main role is generally attributed to the quinone groups [40,41].

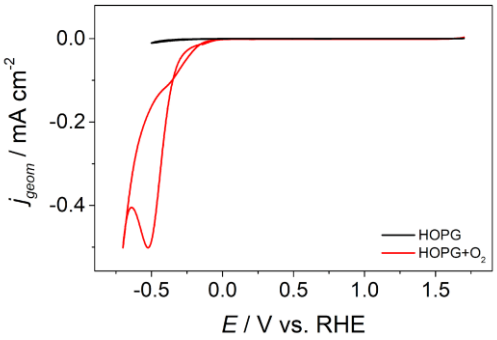

Figure 4.7. cyclic voltammogram of bare HOPG in contact with 0.1 M $HClO_4$. Scan rate is 50 mV s^{-1}.

For the above explained reasons, HOPG represents a suitable substrate for ORR investigations on metal-centre macrocycles, since it offers a wide potential window in which no electrochemical processes occur, especially when dealing with O_2 saturated electrolyte. Any effect of intercalation and exfoliation is disregarded since these processes occur only at very positive applied potential.

4.3 Calibration of EC-STM piezoelectric scanner

The instrumentation is so built, that it requires to be manually calibrated to return dimensionally accurate STM images. Basically, the conductive sectors of the piezoelectric tube are polarised by the STM unit, so that the tube deforms and displaces the tip across the sample surface. The STM unit allows recording images with fixed predetermined size. This means that discrete values of potential are applied to the conductive sectors, and a certain deformation characterises the piezoelectric tube. Known substrates must be analysed to assign the correct conversion value, so as to determine how many nanometres the scanner moved for a certain applied voltage.

This was accomplished with three different substrates, whose structure and unit cell parameters are well-known. The three crystals are: Au(111), Cu(111) and HOPG.

4.3.1 Lateral calibration

Gold guarantees an accurate calibration, especially for the vertical *z* direction, since it structures with well-defined monoatomic-thick terraces. Nearest neighbours distance is 0.289 nm, whereas the monoatomic step-edge is 0.24 nm [10,12,17–19]. Unfortunately, high resolution up to the atomic scale was barely achieved, therefore, for a more systematic and accurate calibration procedure, HOPG was selected as the primary substrate. In fact, HOPG requires a simple and quick preparation, and guarantees a rather flat surface, with large or very large terraces (> 100 nm wide). This is a benefit for the STM tip, since blunting is reduced at minimum and image quality can last longer. The complete passages to scanner calibration are now reported. First of all, it is necessary to achieve imaging at atomic resolution of the HOPG substrate, as shown in figure 4.8.a. A hexagonal pattern of dots is visible. Each dot represents a carbon atom. Nevertheless, a caveat is required. In a normal STM image, bright spots originate from only three out of

six carbon atoms of each hexagon, and the distance between two adjacent bright spots is 0.246 nm [42]. This value is taken as reference to compare with the obtained EC-STM images. Figure 4.8.b features the fast Fourier transform (FFT) of figure 4.8.a. A Fourier transform is an integral transform that expresses a function as an infinite sum of amplitudes, wavelengths and phases. It is defined as:

$$f(\omega) = F\{g(x)\} = \frac{1}{\sqrt{2\pi}} \int_{-\infty}^{\infty} g(x) e^{-i2\pi x\omega} dx \qquad 4.9$$

where $g(x)$ is the original function in the spatial domain [43]. $f(t)$ is the Fourier transform of $g(x)$ function and it is defined in the frequency ω domain. However, calculators deal with finite integrals, so the Fast Fourier Transform (FFT, also known as 2D-FFT) must be selected. The FFT is made of finite summations and defined as [44]:

$$F(k,l) = F(k,l) = \sum_{i=0}^{N-1} \sum_{j=0}^{N-1} f(i,j) e^{-i2\pi\left(\frac{k_i}{N} + \frac{l_j}{N}\right)} \qquad 4.10$$

where $f(i,j)$ is the image as defined in the spatial domain, whereas the exponential term is the linkage between a point (*i*;*j*) in the direct space (spatial domain) and the corresponding point (*k*;*l*) in the reciprocal space (frequency domain). *N* is the number of one-dimensional FT used to compute the integral of eq. (1). Eq. (2) states that Fast Fourier Transform $F(k,l)$ is obtained by summing the result of the multiplication of the spatial image with the basis function. The basis function is a complex exponential function, and it can be expressed as the sum of sine and cosine waves. At the end, the resulting FFT is a complex number, but it can be visualised thanks to its real and imaginary part. Indeed, one can define the Magnitude of the FFT as [45]:

$$Magnitude(f) = \sqrt{Re^2 + Im^2} \qquad 4.11$$

whereas the Phase as:

$$Phase(f) = arctan\ arctan\left(\frac{Im}{Re}\right) \qquad 4.12$$

The DC-component, also named 0 Hz term, is positioned at the centre of the Fourier Transform image and represents the average brightness of the picture. If the dynamic range of the resulting FFT is too large to be properly displayed, then it is more convenient to apply a logarithmic or a square root scale, as *WSxM* enables. Generally, Magnitude images are used due to an easier interpretation capability. *WSxM* then can display the real or imaginary part only, the modulus, a Power Spectrum, or the Root Mean Square of the FFT.

What is worth to remember is the reciprocal relation between direct space and Fourier space, for which the modulus of a reciprocal vector ***r*** is given by (for *WSxM* software):

$$|r| = \frac{1}{|d|} \qquad 4.13$$

where *d* is a direct-space vector. Hence, largely-spaced periodicities in the real space will become low-spaced in the reciprocal space, and vice versa. The reciprocal lattice vector modulus is obtained by measuring the distance between the centre (F(0,0)) and the centre of a bright spot in the FFT generated panel (a generic F(*k,l*) point). Bright spots arise if there exist objects with same dimensions which repeat with same distances and angles, so that they will be described by the same Fourier coefficients.

The real space domain is therefore converted into a frequency domain, and axes are expressed in terms of reciprocal vector *k*.

Anyway, the software provides a direct conversion to the real value. Figure 4.8.b shows six bright spots arranged in a hexagonal fashion, meaning that the most part of the real image is built by periodic features, which actually is by observing figure 4.8.a. Focussing on the FFT, the bright spots correspond to distances of 1.4 Å, 0.9 Å and 1.1 Å. These values are more than half of the expected value of 2.46 Å. Therefore, the conversion factor is changed from its original value of 8 nm/V to 12 nm/V.

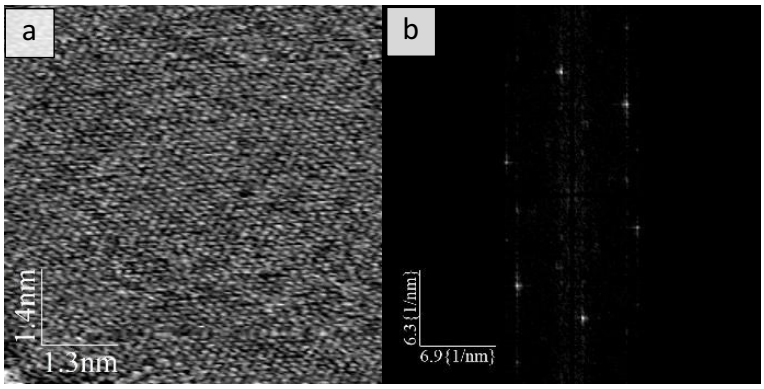

Figure 4.8. a) EC-STM image of bare HOPG in contact with 0.1 M $HClO_4$. Tunnelling parameters are: I_t = 0.32 nA, U_b = - 700 mV, E_{app} = 0.65 vs RHE; b) FFT of image 4.8.a, showing the typical hexagonal periodicity of graphite.

The result is shown in figure 4.9. The FFT reveals distances values of 1.5 Å, 1.6 Å, 1.9 Å. These values are still low compared to the expected value. Hence, further adjustments to the conversion factors were performed, resulting in figure 4.10.

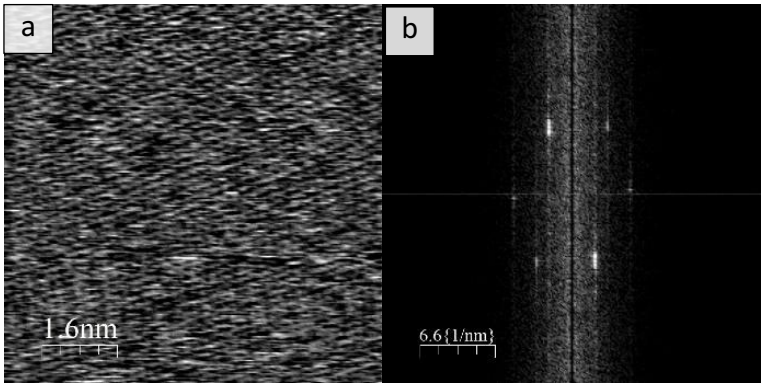

Figure 4.9. a) EC-STM image of bare HOPG in contact with 0.1 M $HClO_4$. Tunnelling parameters are: I_t = 0.32 nA, U_b = - 700 mV, E_{app} = 0.65 vs RHE; b) FFT of image 4.9.a, showing the typical hexagonal periodicity of graphite.

Figure 4.10.a possesses a high lateral resolution, and the corresponding FFT confirms the regular hexagonal arrangement, with periodicities of 2.3 Å, 2.4 Å, 2.5 Å, so with great agreement with the theoretical value of 2.4 Å.

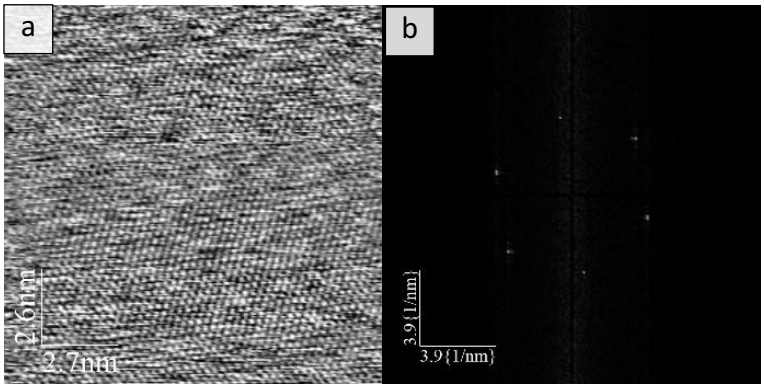

Figure 4.10. a) EC-STM image of bare HOPG in contact with 0.1 M $HClO_4$. Tunnelling parameters for both images are: I_t = 0.32 nA, U_b = - 700 mV, E_{app} = 0.65 vs RHE; b) FFT of image 4.10.a, showing the typical hexagonal periodicity of graphite.

The goodness of calibration can be periodically checked, as shown in figure 4.11. This image was obtained after ten months from the previous calibration. The obtained FFT shows a good agreement with the expected value for the HOPG.

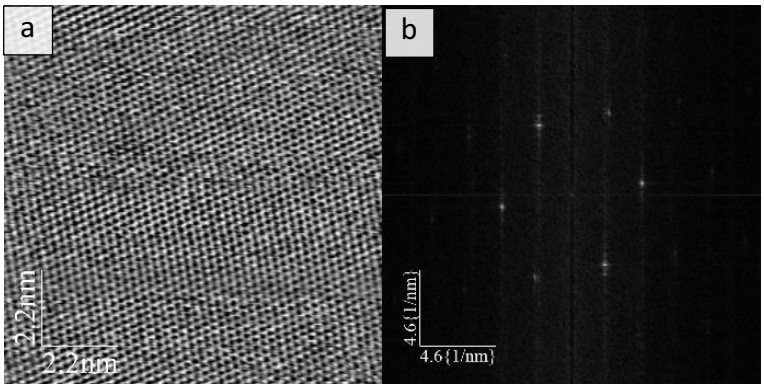

Figure 4.11. a) EC-STM image of bare HOPG in contact with 0.1 M $HClO_4$. Tunnelling parameters are: I_t = 0.50 nA, U_b = - 750 mV, E_{app} = 0.55 vs RHE; b) FFT of image 4.11.a, showing the typical hexagonal periodicity of graphite.

Few high-resolution images were obtained also for the Au(111) substrate, as shown in figure 4.12.a. The image shows a hexagonal pattern of dots, each one ascribed to a gold atom. The periodicity is close to the theoretical value of 0.289 nm, taken as the nearest neighbour distance [7,42]. The brighter irregularly distributed stripes are associated to the herringbone reconstruction [11,12,20,23,46].

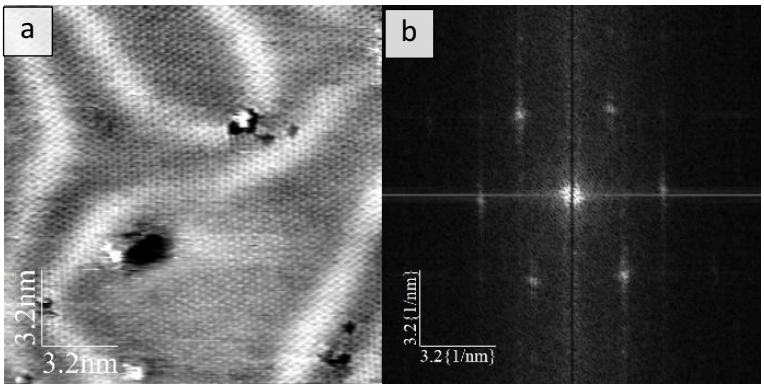

Figure 4.12. a) EC-STM image of bare Au(111) in contact with 0.1 M $HClO_4$. Tunnelling parameters are: I_t = 1.00 nA, U_b = - 250 mV, E_{app} = OCP; b) FFT of image 4.12.a, showing the typical hexagonal periodicity of the (111) gold facet.

An additional confirmation for the calibration is given by a Cu(110) substrate in HCl electrolyte, figure 4.13. Cu(110) in presence of chloride is known to exhibit a tetragonal pattern, with unit cell vectors equal to 2.56 Å and 3.66 Å, respectively. The measured values, as the FFT in figure 4.13.b confirms, are in good agreement with the tabulated ones, confirming the *xy* lateral calibration.

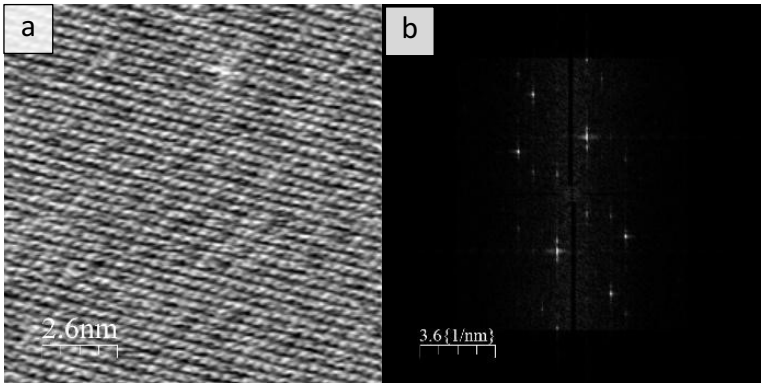

Figure 4.13. a) EC-STM image of Cu(110) in contact with 0.01 M HCl. Tunnelling parameters are: I_t = 1.00 nA, U_b = -300 mV, E_{app} = -0.2 V vs RHE; b) FFT of image 4.13.a, showing the typical tetragonal periodicity of Cu(110) in presence of chloride.

4.3.2 Vertical calibration

The calibration procedure of the *z* vertical movement is now presented. The passages are similar to those presented for lateral calibration. In particular, images of terraces and step edges are pursued. The aim is to extract topographic profiles across the borders between two adjacent terraces. The resulting topographic profile will exhibit the step edge, and by comparing the measured value with the theoretical one the calibration can be completed, eventually adjusting the nm/V value in the calibration page of the software. As shown in figure 4.14, the step edge of a gold terrace is correctly measured 2.4 Å [17].

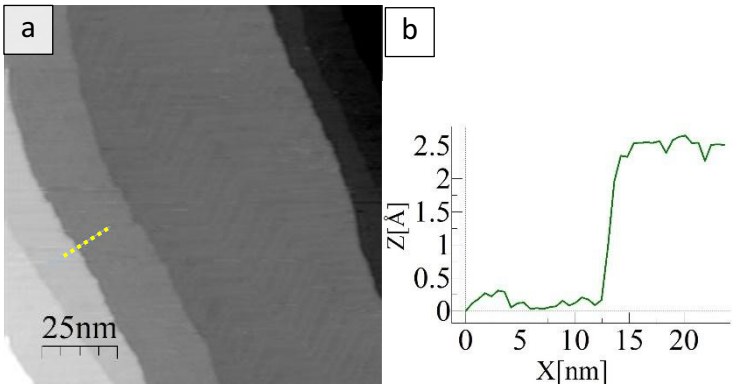

Figure 4.14. a) EC-STM image of bare Au(111) in contact with 0.1 M $HClO_4$. Tunnelling parameters are: I_t = 1.00 nA, U_b = - 110 mV, E_{app} = 0.65 V vs RHE; b) topographic profile corresponding to the yellow dashed line of figure 4.14a.

A further confirmation for the goodness of *z* calibration is brought by imaging the surface of HOPG. In this case, however, careful inspection of the STM images is needed to avoid misinterpretation. In fact, graphite presents a layered structure, and the border between two terraces can actually feature multiple graphene layers. The vertical spacing of graphene layers is 3.35 Å, but multiple values are also possible due to HOPG layered structure [37,38]. As visible from the topographic profile of figure 4.15.b, the measured step agrees with the expected value, finally validating the *z* calibration.

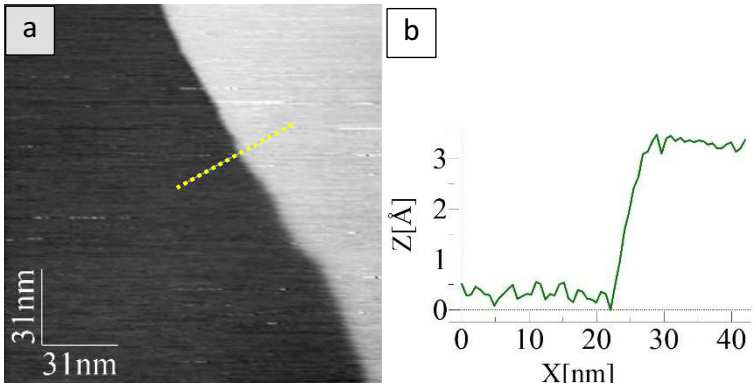

Figure 4.15. a) EC-STM image of bare HOPG in contact with 0.1 M $HClO_4$. Tunnelling parameters are: I_t = 0.47 nA, U_b = - 550 mV, E_{app} = OCP; b) topographic profile corresponding to the yellow dashed line of figure 4.15a.

References

[1] https://www.webelements.com/gold/

[2] J.C. Yannopoulos, The Extractive Metallurgy of Gold Extractive of Gold, 1991.

[3] J. Gong, Structure and surface chemistry of gold-based model catalysts, Chemical Reviews. 112 (2012) 2987–3054.

[4] C.D. Bain, E.B. Troughton, Y.T. Tao, J. Evall, G.M. Whitesides, R.G. Nuzzo, Formation of Monolayer Films by the Spontaneous Assembly of Organic Thiols from Solution onto Gold, Journal of the American Chemical Society. 111 (1989) 321–335.

[5] J. Gong, Structure and surface chemistry of gold-based model catalysts, Chemical Reviews. 112 (2012) 2987–3054.

[6] https://www.webelements.com/gold/crystal_structure.html.

[7] A. Maeland, T.B. Flanagan, Lattice Spacings of Gold-Palladium Alloys, Can. J. Phys. 42 (1964) 2364–2366.

[8] Crljen, P. Lazić, D. Šokčević, R. Brako, Relaxation and reconstruction on (111) surfaces of Au, Pt, and Cu, Physical Review B - Condensed Matter and Materials Physics. 68 (2003) 1–8.

[9] Crljen, P. Lazić, D. Šokčević, R. Brako, Relaxation and reconstruction on (111) surfaces of Au, Pt, and Cu, Physical Review B - Condensed Matter and Materials Physics. 68 (2003) 1–8.

[10] F. Hanke, J. Björk, Structure and local reactivity of the Au(111) surface reconstruction, Physical Review B. 87 (2013) 235422.

[11] Y. Hasegawa, P. Avouris, Manipulation of the Reconstruction of the Au (111) Surface with the STM, Science. 258 (1992) 1763–1765.

[12] S. Narasimhan, D. Vanderbilt, Elastic Stress Domains and the Herringbone Reconstruction on Au(111), Physical Review Letters. 69 (1992) 1564–1568.

[13] Y. Hasegawa, P. Avouris, Manipulation of the Reconstruction of the Au (111) Surface with the STM, Science. 258 (1992) 1763–1765.

[14] S. Narasimhan, D. Vanderbilt, Elastic Stress Domains and the Herringbone Reconstruction on Au(111), Physical Review Letters. 69 (1992) 1564–1568.

[15] F. Hanke, J. Björk, Structure and local reactivity of the Au(111) surface reconstruction, Physical Review B. 87 (2013) 235422.

[16] T. Niu, Surface strain mediated dipole alignment of ClAlPc on Au(111), Applied Physics Letters. 106 (2015) 1–6.

[17] J.V. v. Barth, H. Brune, G. Ertl, R.J. Behm, Scanning tunnelling microscopy observations on the reconstructed Au(111) surface: atomic structure, lon-range superstructure, rotational domains, and surface defects, Physical Review B. 42 (1990) 9307–9318.

[18] D.D. Chambliss, R.J. Wilson, S. Chiang, Ordered nucleation of Ni and Au islands on Au(111) studied by scanning tunnelling microscopy, Journal of Vacuum Science & Technology B. 9 (1991) 933–937.

[19] C. Wöll, S. Chiang, R.J. Wilson, P.H. Lippel, Determination of atom positions at stacking-fault dislocations on Au(111) by scanning tunnelling microscopy, Physical Review B. 39 (1989) 7988–7991.

[20] D.M. Kolb, Reconstruction Phenomena at Metal-Electrolyte Interfaces, Progress. 51 (1996) 109–173.

[21] D.M. Kolb, Reconstruction Phenomena at Metal-Electrolyte Interfaces, Progress. 51 (1996) 109–173.

[22] T. Kosmala, M. Blanco, G. Granozzi, K. Wandelt, Potential Driven Non-Reactive Phase Transitions of Ordered Porphyrin Molecules on Iodine-Modified Au(100): An Electrochemical Scanning Tunnelling Microscopy (EC-STM) Study, Surfaces. 1 (2018) 12–28.

[23] D.M. Kolb, J. Schneider, Surface reconstruction in electrochemistry: Au(100-(5 × 20), Au(111)-(1 × 23) and Au(110)-(1 × 2), Electrochimica Acta. 31 (1986) 929–936.

[24] H. Angerstein-Kozlowska, B.E. Conway, A. Hamelin, L. Stoicoviciu, Elementary steps of electrochemical oxidation of single-crystal planes of Au - Part II. A chemical and structural basis of oxidation of the (111) plane, Journal of Electroanalytical Chemistry. 228 (1987) 429–453.

[25] H. Angerstein-Kozlowska, B.E. Conway, A. Hamelin, L. Stoicoviciu, Elementary steps of electrochemical oxidation of single-crystal planes of Au – Part I. Chemical

basis of processes involving geometry of anions and the electrode surfaces, Electrochimica Acta. 31 (1986) 1051–1061.

[26] M. Hugelmann, W. Schindler, Tunnel barrier height oscillations at the solid/liquid interface, Surface Science. 541 (2003) L643–L648.

[27] A. Hamelin, S. Morin, J. Richer, J. Lipkowski, Adsorption of pyridine on the (110) face of silver, Journal of Electroanalytical Chemistry. 272 (1989) 241–252.

[28] T. Vitanov, A. Popov, E.S. Sevastyanov, Electrical double layer on (111) and (100) faces of silver single crystals in solutions containing ClO_4^- and F^-, Journal of Electroanalytical Chemistry. 142 (1982) 289–297.

[29] G. Valette, Double layer on silver single crystal electrodes in contact with electrolytes having anions which are slightly specifically adsorbed. Part II. The (111) face, Journal of Electroanalytical Chemistry. 269 (1989) 191–203.

[30] O.M. Magnussen, Ordered anion adlayers on metal electrode surfaces, Chemical Reviews. 102 (2002) 679–725.

[31] G. Brink, M. Falk, Infrared spectrum of HDO in aqueous solutions of perchlorates and tetrafluoroborates, Canadian Journal of Chemistry. 48 (1970) 3019–3025.

[32] A. Hamelin, Cyclic voltammetry at gold single-crystal surfaces. Part 1. Behaviour at low-index faces, Journal of Electroanalytical Chemistry. 407 (1996) 1–11.

[33] https://goldbook.iupac.org/terms/view/G02684.

[34] D.D.L. Chung, Review: Graphite, Journal of Materials Science. 37 (2002) 1475–1489.

[35] https://www.spmtips.com/test-structures-HOPG.html.

[36] http://nanoprobes.aist-nt.com/apps/HOPG%20info.html.

[37] P. Truncano, R. Chen, Structure of graphite by neutron diffraction, Nature. 248 (1975) 136–137.

[38] H. Chang, A.J. Bard, Observation and Characterization by Scanning Tunnelling Microscopy of Structures Generated by Cleaving Highly Oriented Pyrolytic Graphite, Langmuir. 7 (1991) 1143–1153.

[39] B. Schnyder, D. Alliata, R. Kötz, H. Siegenthaler, Electrochemical intercalation of perchlorate ions in HOPG: An SFM/LFM and XPS study, Applied Surface Science. 173 (2001) 221–232.

[40] E. Yeager, Dioxygen electrocatalysis: mechanisms in relation to catalyst structure, Journal of Molecular Catalysis. 38 (1986) 5–25.

[41] J. Zhang, ed., PEM Fuel Cell Electrocatalysts and Catalyst Layers Fundamentals and Applications, Springer, 2008.

[42] http://nanoprobes.aist-nt.com/apps/HOPG%20info.html.

[43] https://www.encyclopediaofmath.org/index.php/Fourier_transform.

[44] https://homepages.inf.ed.ac.uk/rbf/HIPR2/fourier.htm.

[45] http://www.cs.unm.edu/~brayer/vision/fourier.html.

[46] F. Rossel, P. Brodard, F. Patthey, N. v. Richardson, W.D. Schneider, Modified herringbone reconstruction on Au(111) induced by self-assembled Azure A islands, Surface Science. 602 (2008) 24–26.

Chapter 5

Electrochemical characterisation

In this chapter, the electrochemical properties of metal-centred macrocyclic molecules are taken into exam. Let us now focus on porphyrins, since they constitute the major class of investigated metal-macrocycles investigated in this work.

Their parent monocyclic system is pyrrole, shown in figure 5.1a.

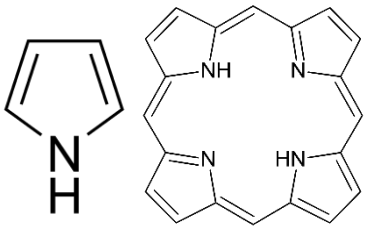

Figure 5.1. a) Chemical structure of pyrrole, b) chemical structure of porphyrin.

Two pyrrole rings linked at a α-carbon to a carbon atom form a dipyrrolylmethane, and the combination of two dipyrrolylmethanes lead to the basic structure of porphin, presented in figure 5.1b. However other fundamental units exist, like chlorin, phorbin, bacteriochlorin and porphynogen.

Porphyrins and phthalocyanines are the only type of macrocyclic molecules featured in this chapter, and they are exploited as macrocyclic ligands for metals, in order to produce MN_4 sites. Indeed, both porphyrins and phthalocyanines are characterised by four internal nitrogen atoms, and they become a tetradentate ligand (porphyrinato ligand). Porphyrinato ligands are therefore able to stabilise the coordination of a metal centre, becoming very versatile in coordination chemistry. A large number of metals can be accommodated in a porphyrin cavity, remembering that Mg, Mn, Fe, Co, Ni, Cu and Zn were already inserted by nature in some vital complexes, for example haemoglobin [1].

The region extending from the porphyrin core to the peripheral carbon atoms passing through the four nitrogen atoms is called the equatorial plane. Therefore, in an octaethylporphyrin, the eight ethyl groups formally belong to the equatorial plane. Being the porphyrinato a tetradentate ligand, square-planar geometry of the metal complex should be obtained. However, few metals are stable with such a kind of coordination, and the most part of metal ions complete their coordination sphere with additional ligands. Being metal accommodated on a fourfold rotational axis, these additional ligands are termed “axial ligands”, and they protrude from the equatorial plane of the porphyrin [1].

Few general concepts regarding the role of oxidation state of the metal carrier during the metalation process of a free-base porphyrin are now presented. It is easier to insert metal with a low oxidation state: indeed, the high charge of a high oxidation state would impede the deconvolution of the metal centre. Coordination number of a metal centre plays also a role, in the sense that a metal ion preferring a low coordination number will be more easily inserted [1]. Sometimes, a change of oxidation state could occur during the process

of metalation. Usually, the most stable oxidation state is the lower one, but some exceptions exist, like Mn(III), which was analysed in this work, or Mo(V), W(V), Re(V), Os(VI). These metals can access a large number of oxidation states compared to other transition metals, therefore these unusual states are actually the most stable ones. In particular, it seems that stability is mostly determined by a most favourable ionic radius with reference to the porphyrinato cavity. The optimal ionic radius should in fact lie between 0.60 and 0.69 Å for a metal to remain coplanar with the porphyrinato ligand, in other words to stay in the equatorial plane. Sn(II) is for example too big and protrudes out of the equatorial plane, with strong consequences in the adsorption and imaging process, further explained in section 6.1.8.

The presence of four nitrogen atoms not only characterises the tetradentate binding ability of the porphyrinato ligand, but also gives birth to MN_4 sites (M = metal, usually belonging to transition metals, N_4 = four nitrogen atoms belonging to porphine). These sites retain a major role in O_2 electrocatalysis, and they emerged as a valid alternative to Pt-based materials [2–6]. From a mere performance-point of view, Pt-based catalysts represent the best choice, giving the highest efficiency in the catalysis of the sluggish O_2 reaction. However, the high costs of Pt, as well as its scarcity and geopolitical problems related to its extraction and distribution, force to consider alternative methods to catalyse ORR [2,4,7].

One first attempt would be the reduction of Pt usage by dispersing it in the form of nanoparticles, which can be tuned in size up sub-nanometric scale. Other strategies involve alloying with other metals to make use of synergistic effects or building Pt-rich nanometric structures to enhance platinum surface activity [6]. Within Pt-based materials, ORR proceeds via a direct 4e- pathway, with water being released as the main reaction product in acidic environment. ORR is strongly dependent on the shape and size of nanoparticles, and the activity increases on the Pt facets in the order Pt(100)<<Pt(110)≈Pt(111) (in HClO4) [6]. The reduction in the Pt nanoparticle size guarantees a reduction of Pt usage and a more convenient exploitation of the active surface. Pt nanoparticles behave in fact as a heterogeneous catalyst. Dispersing a certain amount of Pt into nanometric size particles enhances the exposed surface area, where catalysis actually occurs. Moreover, the number of defects like kinks, steps, edges is higher, contributing to a further increase of the final performance [8]. Being the sole fraction of surface exposed platinum atoms to be active towards ORR, strategies should be developed to maximise Pt surface exposure, for example building hollow nanoparticles or also single-dimension crystals (nanowires) [6,9]. Platinum alloying with transitions metals appears to modify the *d* band centre, and to change O_2 adsorption/desorption tendency, as well as that of reaction intermediates and products [10]. The preparation of Pt-skin structures consists in preparing nanoparticles with different shapes, like nanocubes, nanoplates or other polyhedra, with the intent to expose Pt atoms experiencing a tensile strength, which modifies the *d* band character, causing a more optimized Pt-O bond strength, resulting in better ORR performance [6].

Despite many attempts to produce a catalyst material with reduced platinum usage and improved efficiency, alternative materials are also needed to completely avoid platinum employment in fuel cell devices. Among different materials, non-precious M-N-C catalysts (metal nitrogen sites embedded in a carbonaceous matrix) emerged as a valid alternative. Actually, their birth could be dated back to 1964, when Jasiski discovered ORR catalytic activity for cobalt phthalocyanine [6,11]. M-N-C catalysts could indicate non-pyrolysed structures, like metal complexes featuring a metal centre contoured by a nitrogen-containing ligand, or pyrolysed materials, with metal centres embedded in a nitrogen-doped carbonaceous matrix. Pyrolysed materials are more widely employed due to a better and longer stability compared to non-pyrolysed ones. Moreover, the involved transition metals are of great availability, making the rather good catalytic activity together with durability and cheapness of abundant raw materials the key-points of a valid alternative to platinum-based materials [5].

However, additional features must be pointed out, such as the intrinsic and/or achieved porosity and texture of the matrix, as well as the presence of additional (possible) active sites (often referring to nitrogen-carbon groups, but also sulphur-carbon groups) [5,12–14]. These aspects further complicate the heterogeneous catalyst so far described, eventually requiring a method to study in detail each single feature.

For this reason, non-pyrolysed structures, besides a low stability, continue to be intensively studied. They offer in fact a more handful approach to fine-tuning of single features, thereby becoming useful model systems. This brings to the metal-porphyrins presented in this work. Indeed, different metals within an equal porphyrinato ligand were investigated, to point out uniquely the effect of metals on the final ORR performances. Different ligands within an equal metal centre were also employed, aiming to describe the effect of peripheral substituents onto the catalytic performances towards O_2 reduction. Additionally, the substrate is believed to play a role in the catalytic behaviour of the overlying self-assembled molecules, and for this reason some metal-porphyrins were tested on different substrates (HOPG and Au(111)).

MN_4-based complexes are therefore prone to electrocatalytic activity modulation. Now specifically referring to ORR occurring on MN_4 complexes, certain descriptors can conveniently be employed to interpret electrochemical data. Number of *d* electrons of the central transition metal ion, formal potential of the $M^{n+}/M^{(n-1)+}$ redox couple, donor-acceptor intermolecular hardness, pH, peripheral substituents were selected as the most impacting parameters in determining ORR performances [15–17].

The number of *d* electrons had already been included in volcano plot correlations with the electrochemical activity (measured potential at a fixed current density), evidencing that iron is located on top of this volcano trend (figure 5.2). Considering this parameter (referred to alkaline electrolyte), for an equal ligand (here: phthalocyanine) iron guarantees the best option to catalyse ORR. Mn, Co and Cr phthalocyanines, as well, provide valuable results due to their partially filled *d* orbitals, and further investigations are worth to be carried on [15,17].

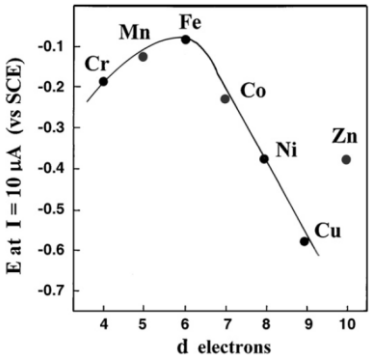

Figure 5.2. Measured potential at fixed current in O_2 saturated electrolyte for different first-raw transition metal macrocycles correlated with the corresponding number of *d* electrons. Figure from ref. [18].

A common reactivity descriptor is the $M^{n+}/M^{(n-1)+}$ redox potential [15,18–22]. A linear correlation exists between the redox potential and the metal-oxygen adduct binding energy [15], assuming that the metal has a (II) oxidation state when adsorbing O_2. This linear correlation shows that FePc has an intermediate Fe-O_2 binding energy. This represents a favourable catalytic behaviour, since according to Sabatier's principles for catalysis, an active species should not bind the reactant species neither too strongly nor too weakly [15,16].

The donor-acceptor molecular hardness is a reactivity concept that derives from Pearson's theory for catalysis [15,16,23,24]. It is defined as follows:

$$\eta_{DA} = \frac{1}{2}(IP_D - EA_A) \qquad 5.1$$

IP_D is the ionisation potential of the donor molecule (here: the metal porphyrin), EA_A is the electron affinity of the acceptor species (here: the oxygen molecule). Upon applying the Koopman's theorem, η_{DA} can be expressed as the difference of LUMO energy of the acceptor and HOMO energy of the donor [15,16,20]:

$$\eta_{DA} = \frac{1}{2}(\varepsilon_D - \varepsilon_A) \qquad 5.2$$

A large HOMO-LUMO gap (hard donor-acceptor pair) implies a stronger bond between donor and acceptor, resulting in a reduced reactivity. Similarly, a narrow HOMO-LUMO gap (soft donor-acceptor pair) determines a high reactivity due to poorly bonded donor-acceptor species. The concept of intermolecular hardness suggests that upon proper tuning of the HOMO and LUMO levels, reactivity is modulated as well. This can be achieved for example by changing the central metal ion, but also by varying the macromolecular ligands, or even its peripheral substituents alone. In fact, electron-withdrawing groups are expected to deplete electron density from the metal centre, lowering its HOMO level, with the result of increasing the HOMO-LUMO gap between donor and acceptor ("harder" M-O_2 complex, difficult to be further reduced). Electro-donating groups are expected to raise the HOMO level of the metal-porphyrin, thereby

reducing the HOMO-LUMO gap ("soft" M-O_2 complex, easier to be reduced, higher catalytic activity expected).

Ring substitution exerts a pivotal role also on the redox potential of metal-complexes. Indeed, electron-withdrawing substituents act pauperizing electron density the metal centre, making it easier for the metal to accept electrons, undergoing reduction. Therefore, in this case the redox potential is made more positive. Contrary, electron-donating groups provide electron density to the metal centre, with the metal being harder to be reduced. Of course, it is the entity of electron withdrawal or donation that determines the entity of positive or negative shift of the reduction potential of the metal.

The metal redox potential retains a major role in the field of ORR electrocatalysis. The linear correlation of the $M^{n+}/M^{(n-1)+}$ redox potential with M-O_2 binding energy was previously figured out, but there exists a direct correlation also with O_2 reduction mechanism. O_2 reduction occurring in the presence of MN_4 sites is regarded as an inner-sphere reaction, occurring at the inner Helmholtz plane of solid/liquid interface [15,17,20]. This means that a number of electrons >1 is transferred between the active site and the reacting molecule (O_2). O_2 binds to the metal centre through its *d* orbital levels [15,17,20,22]. This is definitely an adsorption process, but this is not a trivial step, and real evidence can come only within experimental data provided by scanning tunnelling microscopy. Its imaging ability at atomic level can in fact capture a snapshot of the situation of individual molecules, also monitoring their evolution in time if consecutive images were collected. Moreover, EC-STM performs these operations at the solid/electrolyte interface, and a working electrode potential is constantly applied, definitely justifying the *in operando* terminology of this technique. So, it can be stated that the O_2 presence onto a catalytic site is not something evanescent, but it can be truly proved by a sophisticated imaging technique like the herein presented EC-STM. It can be further stated whether O_2 is bonded preferentially with an *end-on* or *side-on* geometry. These features will be presented in chapter 6. The *end-on* adsorption geometry is known as Pauling model [22] and it implies that a σ bond establishes between the outward-pointing metal dz^2 orbital ($3dz^2$ in the case of first-row transition metals) and the in-plane antibonding symmetric $1\pi^s_g$ orbital of the O_2 molecule [15,20,22]. This σ interaction accounts for an electron transfer event from the metal to the O_2 molecule. A π interaction is also established and it involves the metal $3d_{xy}$ orbital and the antisymmetric anti-bonding $1\pi^a_g$ orbital of the O_2 molecule. This π interaction acts as a back-bonding interaction. A simple depiction of the just described orbitals superimposition is given in figure 5.3. The *side on* geometry, known as Griffith model [22], sees the presence of a σ bond formed by the overlap of the π oxygen orbital and the dz^2 and *s* orbitals of the metal ion. A π back-bond interaction is again established, this time between the dπ metal orbital and the partially unoccupied π* oxygen antibonding orbital. The two adsorption geometries are illustrated in figure 5.3.

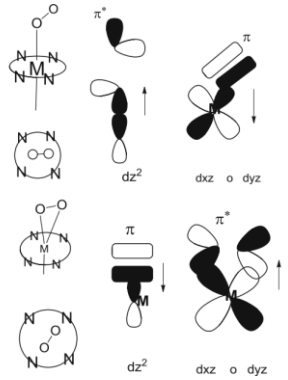

Figure 5.3. Depiction of *end-on* (upper part) and *side-on* (lower part) O_2 adsorption geometries on a transition metal centre, together with the corresponding *d* orbitals overlapping. Figure from [20].

That of MN_4 sites is mostly recognised as a "redox catalysis", for which the reduction of the metal centre should occur firstly to form the M-O_2 adduct [15,17,20,22,25]. The M-O_2 regains the higher oxidation state alongside the O_2 molecule reduction to water or hydrogen peroxide, freeing the active site within its restored higher oxidation state. The actual reaction mechanism is more complicated and comprises several steps where electron and hydrogen ions are transferred. The corresponding simple catalytic for an iron centred scheme is hereafter reported in figure 5.4:

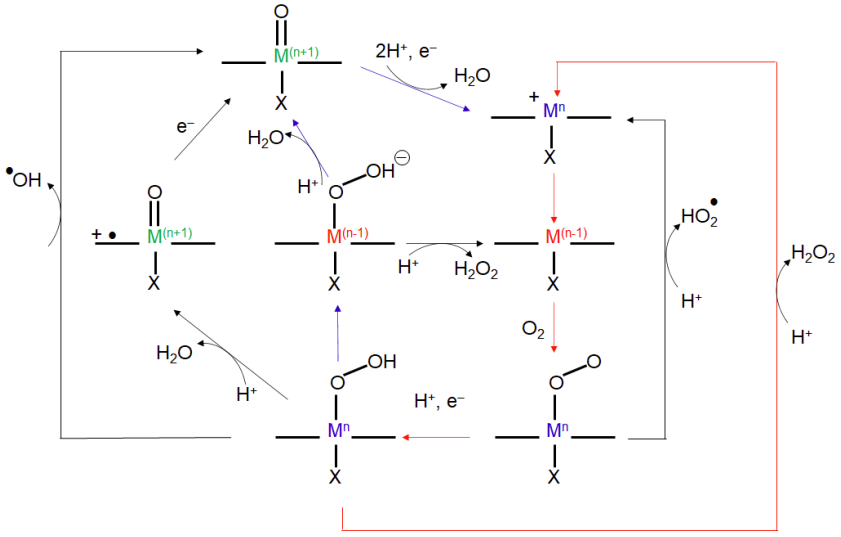

Figure 5.4. Proposed mechanism for the electrochemical reduction of oxygen catalysed by metal porphyrins.

According to this simple scheme, the electrochemical potential at which O_2 reduction occurs should be close to the $M^{n+}/M^{(n-1)+}$ formal potential. If this finds confirmation for some transition metals like Fe and Mn [18,21], cobalt-based complexes show a different behaviour, with the Co(III)/Co(II) redox reaction occurring at far more positive potential than ORR [15,17,18,20–22]. This is an important indication for the catalyst design, because it is true that in principle a higher $M^{n+}/M^{(n-1)+}$ redox potential determines a higher ORR onset potential, but a too positive redox potential, like in the case of Co macrocycles,

a systematic worsening effect will be obtained. Remember that negative redox formal potentials are associated with a hardly reducible metal centre, whereas positive redox formal potentials determine a difficult metal ion oxidation [17,20]. The redox formal potential had in fact already been correlated with the ORR activity, for example with the current recorded at a defined working electrode potential, with volcano-shaped trends being obtained, as shown in figure 5.5 [17,18,20,22,26–28].

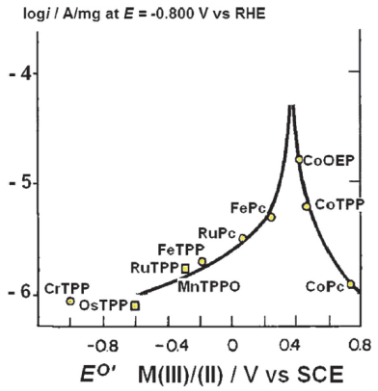

Figure 5.5. Correlation between the current logarithm at a fixed potential and the redox formal potential of various transition metal complexes. Figure from [15].

More details on the reduction mechanism for ORR occurring in acidic media for a FePc adlayer are reported, by R. Baker et alii [29] and literature cited therein. Although many other transition-metal complexes will be further presented, it is worth to examine at least one significant example. As first step, the reduction of the metal centres makes Fe(III) centres to become Fe(II) when a sufficiently negative potential is applied at the electrode surface:

$$Fe(III)Pc + e^- \rightleftarrows Fe(II)Pc \qquad 5.3$$

The catalyst is now active towards O_2 binding, a situation that is realised when the electrolyte is subjected to O_2 saturation:

$$Fe(II)Pc + O_2 \rightleftarrows O_2\text{-}Fe(II)Pc \qquad 5.4$$

The Fe-O_2 adduct is now formed and Fe, possessing a (II) oxidation state, is able to transfer an electron to the adsorbed O_2 molecule, contributing to its reduction:

$$O_2\text{-}Fe(II)Pc + e^- + H^+ \rightleftarrows [HO_2\text{-}Fe(III)Pc] \qquad 5.5$$

The above described reaction is considered the rate determining step of the global ORR process, and from now on three different reaction pathways are possible. One route is a chemical reaction that leads to hydroperoxyl radicals formation:

$$[HO_2\text{-}Fe(III)Pc] \rightleftarrows HO_2^{\bullet -} + Fe(III)Pc \qquad 5.6$$

Another route is an additional electron transfer, with hydrogen peroxide being produced:

$$[HO_2\text{-Fe(III)Pc}] + e^- + H^+ \rightleftarrows H_2O_2 + \text{Fe(III)Pc} \quad 5.7$$

When hydrogen peroxide is produced, two electrons are finally transferred, from which the notation "$2e^-$ mechanism". Finally, the third possible route involves the transfer of four electrons, leading to water as main reaction product [30]:

$$[HO_2\text{-Fe(III)Pc}] + e^- + H^+ \rightleftarrows H_2O + [\text{O-Fe(III)Pc}] \quad 5.8$$

$$[\text{O-Fe(III)Pc}] + e^- + H^+ \rightleftarrows [\text{HO-Fe(III)Pc}] \quad 5.9$$

$$[\text{HO-Fe(III)Pc}] + e^- + H^+ \rightleftarrows \text{Fe(II)Pc} + H_2O \quad 5.10$$

Since in this case a total number of four electrons are transferred, this reaction pathway is termed as "$4e^-$ mechanism". It is also the case of an EC mechanism (electron transfer E, followed by a chemical reaction C), because FePc must be first reduced to Fe(II) before acting as catalyst [19].

For a PEMFC (proton exchange membrane fuel cell), the $4e^-$ is the most desirable reaction pathway, since H_2O_2 generation would be detrimental for the membrane electrode assembly (MEA) [29,31]. Moreover, a higher energy conversion efficiency is attained when O_2 is reduced directly to water via the $4e^-$ mechanism [20,31].

Cyclic voltammetry was the main standard characterisation technique herein employed to characterise metal-porphyrin and metal-phthalocyanine complexes. The primary aim was to extract basic information like the peak potential, which is in any case one fundamental reactivity descriptor for ORR occurring on metal-nitrogen sites. A further advantage is the possibility to compare data obtained from a common characterisation technique from those obtained by electrochemical scanning tunnelling microscopy. Another non-negligible aspect is that cyclic voltammetry can be used as explorative technique. Before conducting EC-STM experiments under potential control, the collection of a cyclic voltammetry allows to evaluate the "potential window" of the investigated system. Being the employed electrolyte an aqueous solution, the potential window was mainly limited by hydrogen evolution reaction and oxygen evolution reaction, as water is the far most abundant species. The standard electrode potential for hydrogen evolution reaction (HER) is equal to 0 V, while that of oxygen evolution reaction (OER) is equal to 1.23 V. The potential window in aqueous electrolyte could be, depending on the conducted study, very narrow. The dependency on many factors like proton concentration and substrate surface can expand and shift this potential window up to about 2 V [3]. Recording preliminary cyclic voltammetry therefore allows to set the potential windows limit for further "safe investigation" with EC-STM equipment, where undesired HER and OER do not occur.

All cyclic voltammetries were recorded in 0.1 M $HClO_4$, as described in section 3.1. the electrode functionalisation was diversified with respect to the substrates. HOPG required

long functionalisation duration, at least 30 minutes, followed by an Ar flux step to dry the electrode surface from excess solvent (i.e. DMF). Au(111) allowed much shorter functionalisation duration, generally limited to 1 minute. The crystal was immersed by hanging meniscus in the DMF solution containing the desired molecules, then it was rinsed with ultrapure water and mounted in the electrochemical cell. All measurements were performed with freshly renewed electrode surface: HOPG was subjected to a simple exfoliation, while Au(111) was electropolished and flame-annealed.

Before introducing the electrochemical behaviour of each molecular species, it is worth reporting a brief mention to the electrochemical response of the bare substrates within the employed electrolyte.

Au(111) guarantees a potential window of almost 2 V, but with additional limitations. Gold oxidation is in fact a complex phenomenon and it must be taken into account. Its onset potential can be found at ≈1 V vs RHE. A thorough description of the multi-step Au(111) oxidation was already provided in section 4.1.2. HOPG has a potential window which surpasses 2 V of extension, and unlike Au(111), its voltammogram in aqueous electrolyte is rather featureless, with the curve remaining flat up to the two discharge processes (HER and OER), as already presented in section 4.2.2.

5.1 Voltammetric characterization of HOPG functionalised electrodes

The electrochemical activity is now presented for metal-porphyrins deposited on the HOPG surface. At this purpose, cyclic voltammetries recorded in Ar purged electrolyte are first presented, in order to elucidate phenomena occurring without O_2 presence. In particular, the redox behaviour of transition metal centres is expected to manifest, so that it can be directly correlated with the eventual O_2 reduction peak.

5.1.1 H_2OEP

First of all, the electrochemical response of the free-base octaethylporphyrin adlayer is presented, recorded in 0.1 M $HClO_4$ previously thoroughly deaerated with pure Ar gas. Voltammograms collected at different scan speeds are reported in figure 5.6.a. The voltammograms show a reduction peak in the potential range between 0.15 V and and 0.2 V. In particular, at a scan rate of 50 mV/s, fig. 6.b, the peak potential is placed at $E_{OEP,Ar}$ = 0.16 V vs RHE. This electrochemical response is definitely attributed to the metal-free porphyrin, since the HOPG cyclic voltammetry is completely flat in the same potential window. Before trying to give an explanation to this electrochemical behaviour, it is worth presenting the eventual O_2 reduction activity. In figure 5.6.c, cyclic voltammograms at different scan speed are listed, evidencing a certain catalytic activity towards ORR at potentials close to the previously observed peak in Ar purged electrolyte ($E_{OEP,O2}$=0.16 V), indicating a correlation should exist between H_2OEP redox activity and the capability to reduce oxygen. In any case, the catalytic activity arising for H_2OEP is modest compared to the later on presented metal-complexes. A tentative explanation to the ORR electrocatalytic activity shown by the metal-free porphyrin is now provided. The activity of metal-free porphyrins towards ORR had already been reported for some metal-

free porphyrins at the polarised water/dichloroethane interface, therefore in homogeneous phase. It was found that the protonated form of this molecules, like H_4TPP^{2+} in the case of protonated tetraphenylporphyrin, were proven to bind molecular oxygen, which can be further reduced in organic phase by ferrocene or decamethylferrocene [32–34]. It was then found that a fine-tuning of the activity is possible by acidifying the solution with tetrakis-(pentafluorophenyl)boric acid and adjusting the acid-to-catalyst molar ratio [32]. The role of the acid is to protonate the porphyrins, so that NH^+ sites are generated in the inner cavity. These serve as binding sites towards O_2, and a NH^+ - O_2 hydrogen bond is formed (figure 5.7) [32–34]. However, the borate anion actually behaves as a coordinating species, and a reversible exchange of the anion with O_2 should first occur for ORR to proceed. Once O_2 reaction occurs through the mediation of ferrocene, the metal-free molecules can be further associated with the acid, forming the initial catalytic species.

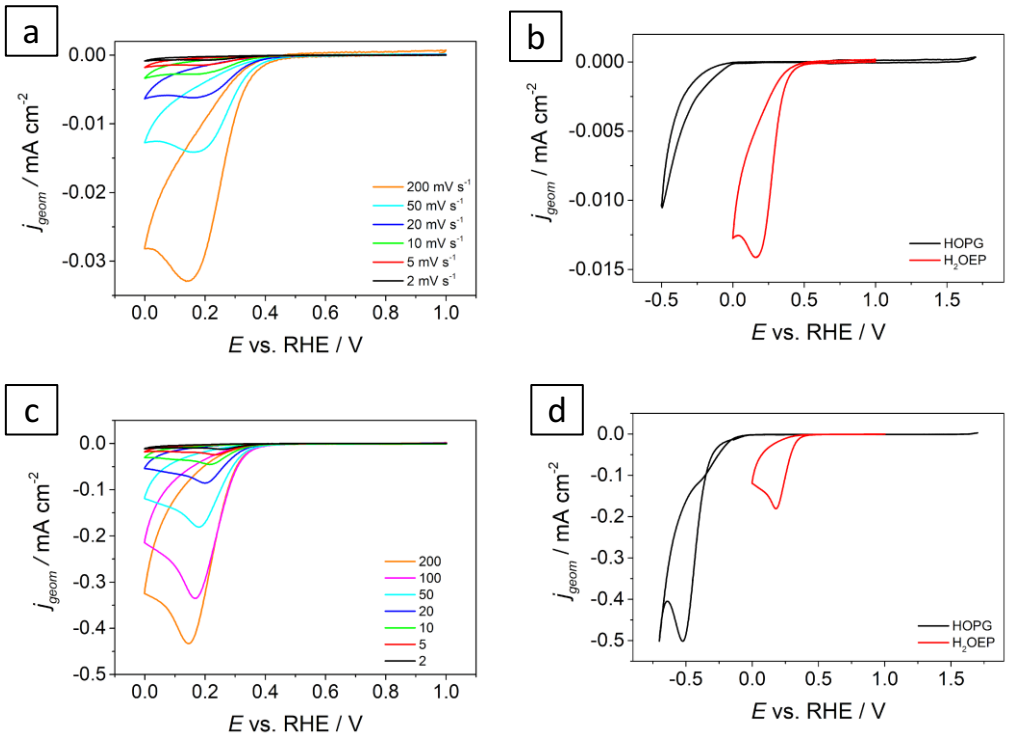

Figure 5.6. Cyclic voltammograms of a) H_2OEP functionalised on HOPG in deaerated 0.1 M $HClO_4$; b) comparison of CV of H_2OEP and bare HOPG, both recorded at 50 mV s^{-1} in deaerated 0.1 M $HClO_4$. c) H_2OEP functionalised on HOPG in O_2-saturated 0.1 M $HClO_4$; d) comparison of CV of H_2OEP and bare HOPG, both recorded at 50 mV s^{-1} in O_2-saturated 0.1 M HClO4.

Other authors also demonstrated a role of the peripheral substituents, especially those located at the *meso* positions, with electron-withdrawing groups giving a stronger catalytic activity, since charge is more strongly depleted from the inner cavity and NH^+ species being readily formed [35]. However, the previously described examples for an efficient O_2 reduction catalysis are valid for a homogeneous catalysis process, whereas the activity shown in figure 5.6 were obtained for monolayer film immobilised on an HOPG surface, therefore behaving more like a heterogeneous catalyst. This field is in fact

rather unexplored and additional characterisations are needed to understand what governs the reaction mechanism. As a matter of fact, an example exists of a 2,2′-dipyridylamine adsorbed on a glassy carbon support, as an efficient ORR heterogeneous catalyst, moreover selective towards H_2O_2 production [36]. Different mechanisms were proposed, and the anchoring sites were identified in the pyridyl- and amino-N groups [36].

Furthermore it was proven that intermolecular charge transfer via noncovalent functionalization can modulate the charge density on the carbon or nitrogen atoms of the porphyrinato ligand. It can be inferred that upon the adsorption of octaethylporphyrins on HOPG electrons are transferred from HOPG to the porphyrinato ring, resulting in net positive charge on HOPG surface. In this case it would be the exposed edge sites, positively charged, of HOPG to be the active sites for ORR, but it is difficult to have a conclusive model without the support of computational analysis.

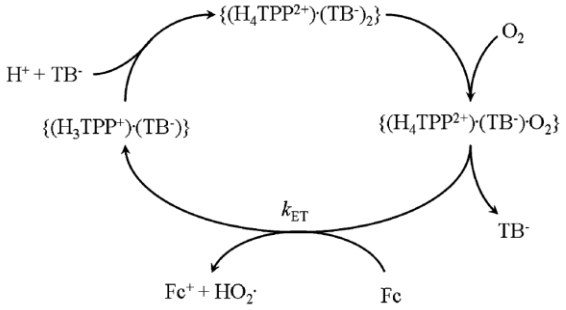

Figure 5.7. catalytic cycle for O_2 reduction in a homogeneous organic phase containing free-base tetraphenyl porphyrin. Figure from [32].

The data herein presented constitute part of a published article [37]. Additional electrochemical characterisations were also conducted, such as CV of H_2OEP on a glassy carbon substrate, linear sweep voltammetry at rotating ring and disk characterisation. CV collected in Ar purged and O_2 saturated electrolyte are reported in figure 5.8.a and 5.8.b respectively. The electrochemical behaviour of H_2OEP@GC both in presence and absence of oxygen is less clear than H_2OEP@GC, however it is clear that H_2OEP@GC can be reduced at potential very close to the hydrogen evolution limit and that occurrence of a faradaic process (Figure 5.8b).

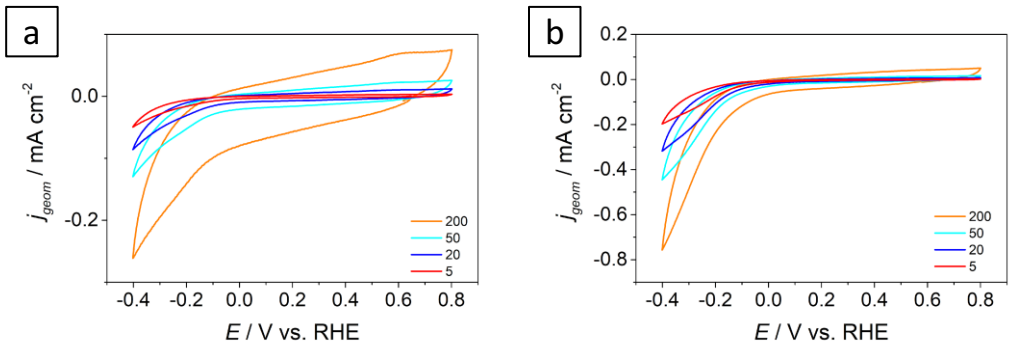

Figure 5.8. a) CV at different scan speed collected for H_2OEP on glassy carbon in deaerated 0.1 M $HClO_4$; b) CV at different scan rates collected for H_2OEP on glassy carbon in O_2-saturated 0.1 M $HClO_4$.

H_2OEP was then subjected to RRDE characterisation, and the resulting LSV recorded at 1600 rpm with a scan rate of 5 mV s^{-1} is reported in figure 5.9.a, both for the disk and ring currents. The produced hydrogen peroxide percentage is reported in figure 5.9.b, and the number of exchanged electrons is featured in figure 5.9.c. H2OEP showed a kind of intermediate response, with a ≈ 30% hydrogen peroxide production, and a number of involved electrons lower of 3.5, attesting that both bielectronic and tetraelectronic mechanisms are at play [37].

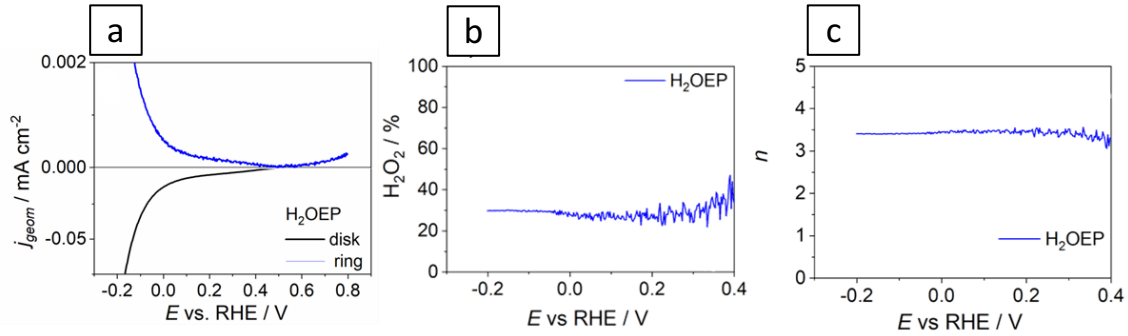

Figure 5.9. a) RRDE polarization curves of H_2OEP@GC in O_2-saturated 0.1 M $HClO_4$; rotation rate 1600 rpm, scan rate 5 mVs^{-1}; b) H_2O_2 yield determined by RRDE experiment; c) number of exchanged electrons.

5.1.2 FeOEP

Iron (III) octaethylporphyrin chloride was solubilised in DMF to attain 0.1 mM concentration. The solution was drop-casted on the freshly cleaved HOPG surface, letting it rest for 30 minutes; after that, an argon flush was directed over the sample to speed up DMF evaporation.

FeOEP along with H_2OEP, had been the main topic of a published article. Therefore, the main results are in this context only briefly elucidated, referring to the article for the extensive data presentation and discussion [37].

Cyclic voltammetries at different scan rates collected in deaerated electrolyte are reported in figure 5.10.a. Thanks to a thorough degassing of the electrolyte solution, the reduction

peak at $E_{Fe,Ar,red}$ = 0.31 V vs RHE can be associated to the weak oxidation peak at $E_{Fe,Ar,ox}$ = 0.40 V vs RHE. FeOEP is therefore characterised by the Fe(III)/Fe(II) redox couple, with many other examples being reported elsewhere [15,18,38–41]. Although reversibility increased upon increasing the scan rate, the unavoidable limited stability of the FeOEP adlayer limits a complete clarification of the electron transfer process, and the involvement of an EC mechanism (electron transfer followed by a chemical process) remained the most probable explanation to the electrochemical response. In figure 5.10.b, the FeOEP CV collected at 50 mV s^{-1} was superimposed to the CV of bare HOPG.

Oxygen reduction reaction was studied upon saturating the electrolyte solution with pure gaseous oxygen, and the resulting CVs at different scan rates are reported in figure 5.10.c. The ORR peak is individuated at $E_{Fe,O2}$ = 0.25 V vs RHE. As comparison, the 50 mV s^{-1} cyclic voltammetry of FeOEP is superimposed with that of bare HOPG, showing the poor catalytic activity of HOPG with respect to FeOEP@HOPG (figure 5.10.d).

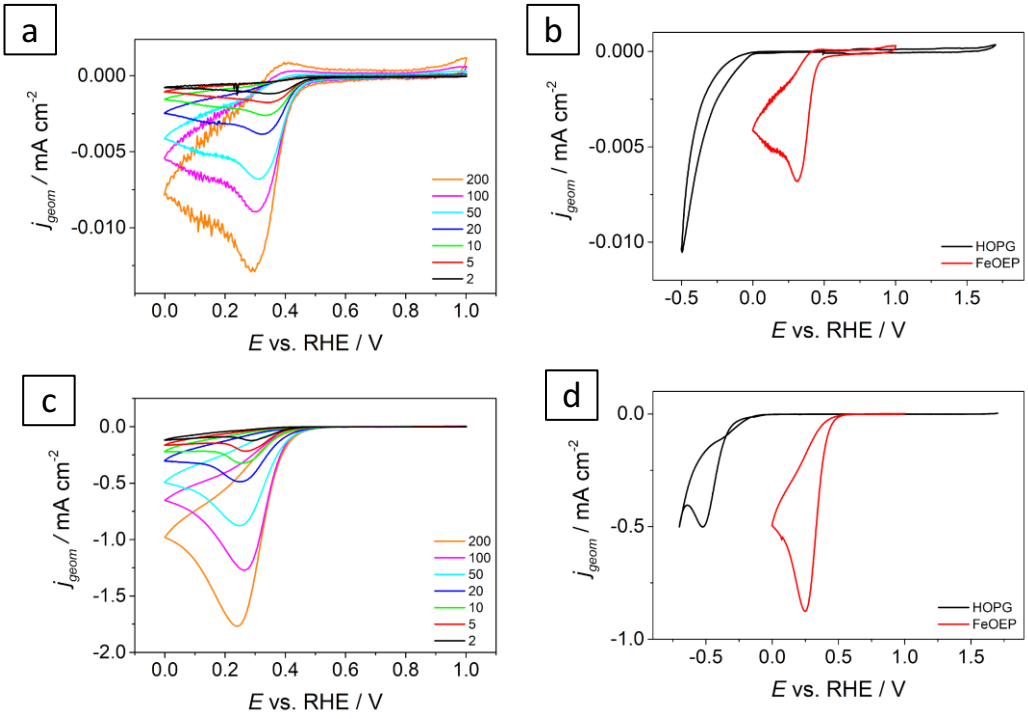

Figure 5.10. a) cyclic voltammograms of FeOEP functionalised on HOPG in deaerated 0.1 M $HClO_4$; b) comparison of CV of FeOEP and bare HOPG, both recorded at 50 mV s^{-1} in deaerated 0.1 M $HClO_4$; c) cyclic voltammograms of FeOEP functionalised on HOPG in O_2 saturated 0.1 M $HClO_4$; b) comparison of CV of FeOEP and bare HOPG, both recorded at 50 mV s^{-1} in O_2 0.1 M $HClO_4$.

To get a deeper understanding of the O_2 reduction mechanism, the glassy carbon surface of the rotating ring and disk electrode was functionalised with the FeOEP solution. A linear sweep voltammetry was collected at a rotation speed equal to 1600 rpm, and in the meantime the ring current was also measured. The resulting disk and ring currents are reported in figure 5.11.a. The number of exchanged electrons is reported in figure 5.11.b, while the detected hydrogen peroxide percentage is shown in figure 5.11.c. It is evident

that the produced H_2O_2 is significantly low, remaining below 10% in almost the entire ORR region. In fact, the number of electrons reflect this behaviour, with *n* approaching to 4. This means that ORR at the FeOEP units proceeds almost exclusively via a $4e^-$ mechanism, with water being released as the main reaction product. Actually, Fe porphyrins and phthalocyanines were already known for promoting ORR electrocatalysis by a $4e^-$ mechanism [15,18].

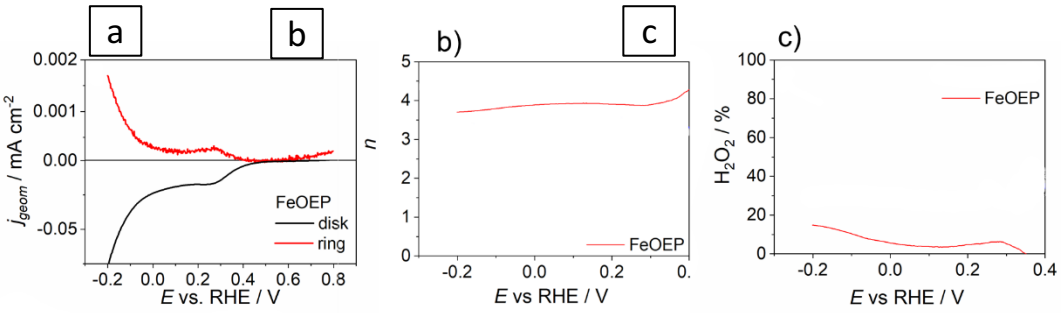

Figure 5.11.a) ring and disk current detected for a FeOEP adlayer adsorbed on glassy carbon in O_2 saturated 0.1 M $HClO_4$; b) hydrogen peroxide percentage production in the ORR regime for FeOEP adsorbed on glassy carbon; c) calculated number of exchanged electrons for a FeOEP adlayer on glassy carbon.

5.1.3 MnOEP

MnOEP was probed by cyclic voltammetry. A 0.1 mM MnOEP solution in DFM was drop-casted on the freshly cleaved HOPG surface, letting it functionalise for 30 min, and then it was dried under an Ar stream. A higher number of reduction peaks is noticeable with respect to the free-base counterpart, evidencing at a first glance a role of the metal centre. As visible from figure 5.12.a, the most positive reduction peak appears at $E_{Mn,Ar,1}$ = 0.18 V vs RHE, then a second peak, which is also the most intense in terms of current density, is detected at $E_{Mn,Ar,2}$ = -0.08 V vs RHE, and finally a third peak, much less intense than the previous two, is present at $E_{Mn,Ar,3}$ = -0.31 V vs RHE. It has to be mentioned the appearance of a sharp oxidation peak at $E_{Mn,Ar,ox}$ = 0.16 V vs RHE. Being manganese a transition metal, it is widely accepted its redox behaviour, especially regarding the Mn(III) and Mn(II) oxidation states. However, the peak at $E_{Mn,Ar,1}$ = 0.18 V should be attributed to the ligand itself (octaehtylpoprhyrinato), since a peak at very close potential was detected also for H_2OEP. Indeed, a consistent number of literature works claim that manganese undergoes the reduction Mn(III)/Mn(II), in a potential range close to the herein detected peak [39–44]. However, most part of these studies were conducted in organic and homogeneous phase, so differences can in principle arise with the current study, where Mn porphyrins are adsorbed on the electrode surface in contact with an aqueous phase. Nonetheless, the differences are minimal, with a widely acceptable explanation of the Mn(III)/Mn(II) reduction occurring at $E_{Mn,Ar,2}$ = -0.09 V vs RHE. Mn(II)/Mn(I) reduction is also documented [39], but its occurrence should be placed at far more negative potential than $E_{Mn,Ar,3}$ = -0.31 V vs RHE, so another porphyrin ring-related phenomenon is likely to manifest at this potential.

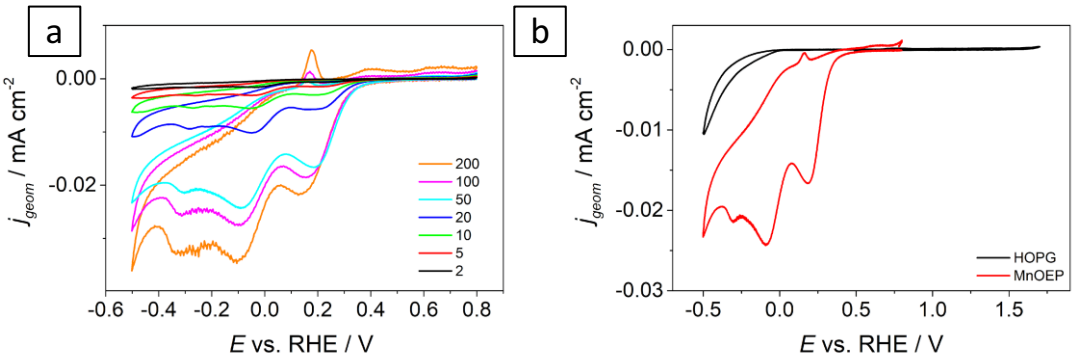

Figure 5.12. a) cyclic voltammograms at different scan rates of MnOEP functionalised on HOPG in deaerated 0.1 M $HClO_4$; b) comparison of CV of MnOEP and bare HOPG, both recorded at 50 mV s^{-1} in deaerated 0.1 M $HClO_4$.

Cyclic voltammetry was then conducted in O_2 saturated electrolyte, to study O_2 reduction capability of MnOEP. The outcome is reported in figure 5.13. The voltammograms are characterised by two peaks. The most positive one is found at $E_{Mn,O2,1}$= 0.27 V vs RHE, but the associated current density is modest compared to a second more negative peak, at $E_{Mn,O2,2}$= -0.09 V vs RHE, which is more intense and definite. Remarkably, this measured peak potential is almost equal to the previously determined peak potential in argon, which was ascribed to the Mn(III)/Mn(II) redox behaviour of the manganese centre. This superposition again confirms the strictly correlated redox catalysis of transition metal-centred porphyrins. Therefore, metal coordination by suitable nitrogen groups appears to stabilise the metal centre, making it prone to accept oxygen adsorption and further reduce it. Oxygen reduction electrocatalysis by manganese porphyrins also finds other external confirmation, [39,42,44], justifying the choice of MnN_x sites precursors to produce MnN_x-doped carbons as advanced catalyst materials [43,45–48].

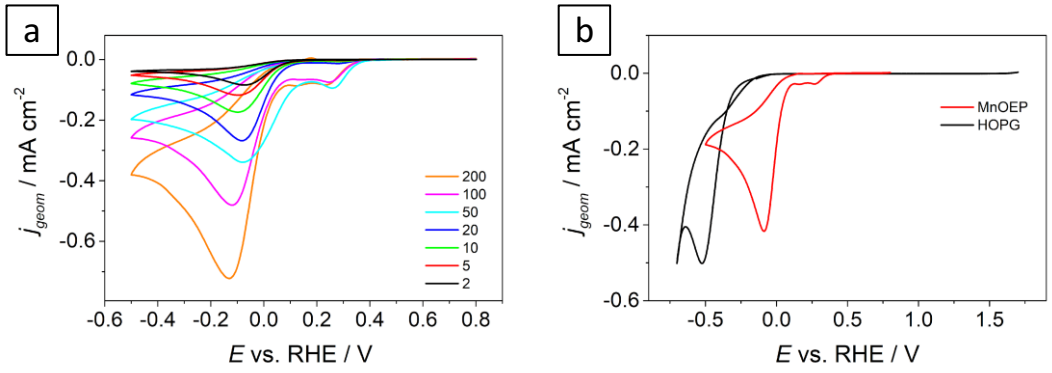

Figure 5.13. a) cyclic voltammograms of MnOEP functionalised on HOPG in O_2 saturated 0.1 M $HClO_4$; b) comparison of CV of MnOEP and bare HOPG, both recorded at 50 mV s^{-1} in O_2 saturated 0.1 M $HClO_4$.

The cyclic voltammetry recorded in Ar purged electrolyte was further investigated, with dedicated experiments aimed to isolate each single peak, and four different scan speed being recorded to appreciate any eventual scan speed dependency. Indeed, in figure 5.14.a, CV was cathodically limited to $E_{app,1}$= 0.1 V vs RHE, and the peak $E_{Mn,Ar,1}$ = 0.18 V vs RHE made its appearance. In figure 5.14.b, by extending the CV to $E_{app,2}$= -0.15 V

vs RHE, a second peaks arises, at $E_{Mn,Ar,2}$ = -0.06 V vs RHE, which is just 20 mV more positive than the previously measured homologue one in figure 5.12. It must be noted that the peak shapes start to become less definite, probably due to consecutive and repetitive potential scanning, which worsens the molecular monolayer quality. Then, CV was extended to $E_{app,3}$= -0.4 V vs RHE, and a third peak, as expected, emerged at $E_{Mn,Ar,3}$ = -0.32 V vs RHE. Having already elucidated the electrochemical response of Mn(III)/Mn(II) redox couple, this peak can be tentatively assigned to the porphyrinato ligand even if its intensity is far lower than the previous two peaks that account for a monoelettronic process each. This does not find a direct confirmation in the CV of H_2OEP, figure 5.6, since it was recorded in a too small potential window, even if in literature it is reported that free-base porphyrins undergo at least two one-electron reduction processes in homogeneous organic phase [49]. Those measurements were conducted in organic solvent and in homogeneous conditions, and the peak potential separation between the two reduction phenomena is ΔE_{lit} = 0.42 V [52]. Considering $E_{Mn,Ar,1}$ = 0.18 V and $E_{Mn,Ar,3}$ = -0.31 V, the potential difference is ΔE_{exp} = 0.49 V, which is 50 mV larger than the literature value. Taking into account that in this case porphyrins are adsorbed onto an electrode surface, and the electrolyte is aqueous with a remarkably low pH value, certain differences may come up. An alternative explanation is that the third peak is responsible for ET associated with the formation of species formed upon the previous reduction process such as clusters of MnOEP containing direct Mn-Mn bonds [39,50].

An additional extension of the cyclic voltammetry was operated, and another peak emerged at $E_{Mn,Ar,4}$ = -0.53 V, but its origin remains unclear. There is in fact the possibility that Mn(II)/Mn(I) occurs, but peak to peak separation with the counterpart Mn(III)/Mn(II) reduction would lead to a too small value with respect to reference data recorded in organic phase, even considering dissimilarities brought by the aqueous solvent and the adsorbed form of the porphyrins. Peak to peak separation value would be too small also for another reduction process involving the porphyrinato ligand alone (nearly half of the previously determined ΔE_{exp}). Actually, those very negative working electrode potentials were not achieved even during EC-STM experiments (later presented in section 6.1.3), so the attribution of this negative peak is for the moment discarded.

A final mention should be made on the intense oxidation peak, already pointed out in figure 5.12.a, which appears only when CV was inverted in cathodic verse after the appearance of the third reduction peak ($E_{app,3}$= -0.4 V vs RHE), i.e. only when a sufficiently negative applied potential is reached. So it is reasonable to assert that the oxidation peak at $E_{Mn,Ar,ox}$ = 0.16 V vs RHE is the chemical reversibility of the process occurring at $E_{Mn,Ar,3}$ = -0.31 V. Again, comparison with literature data, although recorded in organic solvent, seems the only way out to unravel the physical chemical phenomenon behind this rather unusual peak manifestation. It is likely that this oxidation peak is related to reoxidation of μ-oxo species but also of agglomerates containing direct Mn-Mn bonds, which are more frequent when Mn retains a low oxidation state, like Mn(II) [39,50]. The

case of agglomerates is not odd: indeed, a clear evidence of MnOEP clusters presence is brought by EC-STM investigation, which is later on presented in section 6.1.3.

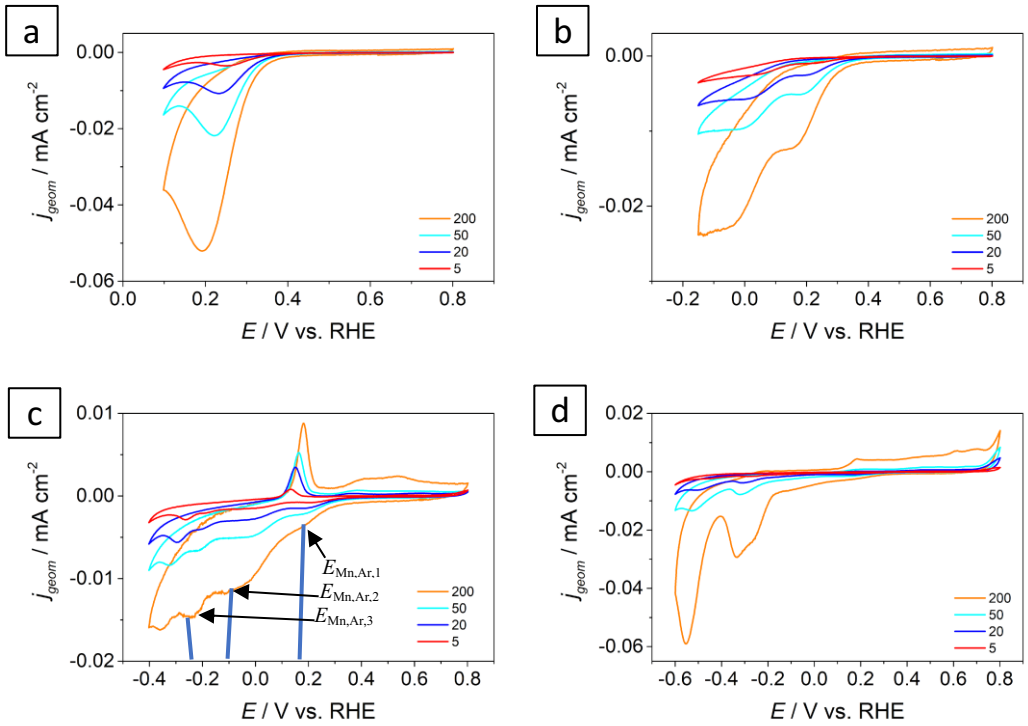

Figure 5.14. Cyclic voltammograms at different scan rates of MnOEP adlayer adsorbed on HOPG, and cathodically limited to: a) 0.1 V vs RHE; b) -0.15 V vs RHE; c) -0.4 V vs RHE; -0.6 V vs RHE.

MnOEP was also functionalised on a glassy carbon disk substrate for rotating ring and disk experiments. The same molecular concentration in DMF was adopted, and this solution was drop-casted on the freshly polished glassy carbon surface, which was preventively masked with a Teflon ring to avoid DMF leakage on the externa platinum ring. The so-formed DMF drop was subsequently exposed to an Ar stream, to facilitate solvent evaporation. As in the case of functionalised HOPG, excess molecules are expected to leave the substrate surface once exposed to the electrolyte solution. The revealed electrochemical response is presented in figure 5.15.a, in the case of deaerated solution, and in figure 5.15.b, in the case of O_2 saturated electrolyte. CVs in argon purged electrolyte are more stretched, with a feeble reversible couple being detected at $E_{Mn,Ar,red}$= -0.100 V and at $E_{Mn,Ar,ox}$= -0.028 V, for the reduction and oxidation peak, respectively. The reduction peak potential position shows a great overlap with that recorded for MnOEP-functionalised HOPG. Therefore, this, though feeble, reversible should be ascribed to the Mn(III)/Mn(II) redox manifestation. It is not surprising that, upon saturating the electrolyte with oxygen gas, a distinct reduction peak appears at EMn,O2= -0.21 V vs RHE. With respect to the MnOEP-HOPG case, this peak is ≈90 mV more negative, although still being attributed to the oxygen reduction reaction at the MnN4 centres. This should be intended as a weak substrate effect on the MnOEP final performances towards ORR. A first possible explanation could be related to a different nature of interaction between MnOEP and the carbon atoms of glassy carbon, but a more

plausible one would account for a lower number of active sites present on the surface, due to a rougher surface with respect to the very flat HOPG.

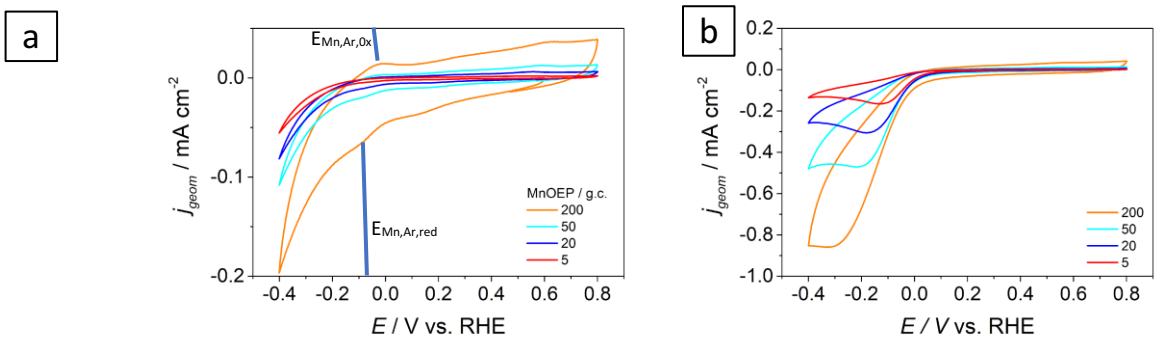

Figure 5.15. a) cyclic voltammograms of MnOEP functionalised on GC in deaerated 0.1 M $HClO_4$; b) cyclic voltammograms of MnOEP functionalised on GC in O_2 saturated 0.1 M $HClO_4$.

Linear sweep voltammetries were then collected at different rotation speeds, as reported in figure 5.16.a. The LSVs do not reach a plateau, just a change of slope is visible in correspondence of the previously detected peak potential. Anyway, the absence of a plateau is not detrimental for further analysis [15,21]. In fact, the percentage of produced H_2O_2 could be successfully measured, also thanks to the ring current, as shown in figure 5.16.b. H_2O_2 percentage is reported in figure 5.16.c, as calculated using disk and ring current, following the method explained in section 5.1.1. Hydrogen peroxide production starts close to E=0 V vs RHE, and it reaches almost a steady value starting from E=-0.10 V vs RHE, which coincides with the cyclic voltammetry ORR peak. The percentage is slightly lower than 30%, so the selectivity towards the sole H2O production is lower compared to FeOEP. This reflects into a calculated number for exchanged electrons, figure 5.16.d, which in the case of MnOEP reaches the value of ≈3.5, which in the end indicates the preferential direct conversion of O2 to H2O instead of hydrogen peroxide generation. Despite a general scarcity of comparison data for this observation, Zagal et alii observed a similar trend in alkaline environment [21]. In fact, they showed that only an iron phthalocyanine and a manganese phthalocyanine derivatives had a major tendency towards direct H_2O production, with the Fe derivative performing better than the Mn homologue, whilst V, Cr, Co and Zn almost exclusively give $2e^-$ pathway [21].

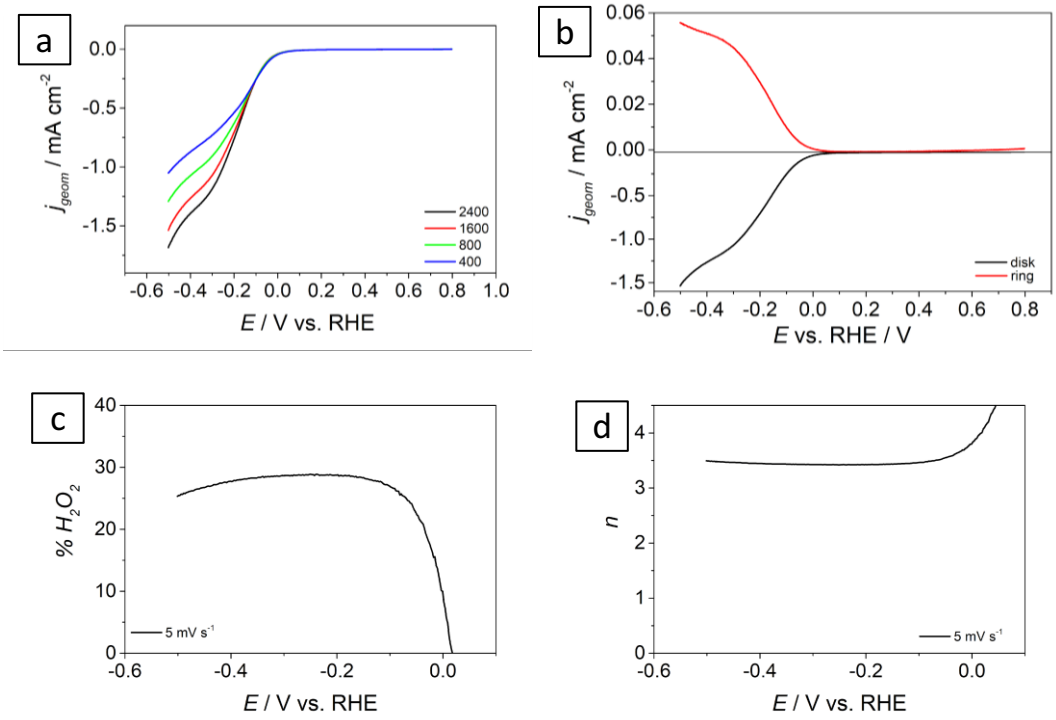

Figure 5.16. a) linear sweep voltammograms at different rotation speed of MnOEP functionalised glassy carbon in deaerated 0.1 M $HClO_4$; b) ring and disk current for MnOEP on glassy carbon; c) hydrogen peroxide production percentage for MnOEP; d) calculated number of exchanged electrons in the ORR regime for MnOEP.

5.1.4 CoOEP

A 0.1 mM CoOEP solution was realised with DMF solvent, and it was drop-casted on the freshly cleaved HOPG surface. An Ar stream was directed over the sample to facilitate DMF evaporation. The sample was inserted in the electrochemical cell. Figure 5.17.a reports the cyclic voltammogram obtained at scan speed of 50 mV s^{-1}, together with the CV of bare HOPG as reference. CV was collected starting from near-OCP value, namely E_{start} = 0.93 V, and the potential was firstly swept cathodically. For this reason, peaks are listed following the scan direction. A cathodic peak is almost immediately recorded at $E_{Co,Ar,red1}$ = 0.70 V vs RHE. Then a cathodic wave commences at $E_{Co,Ar,on} \approx$ 0.50 V vs RHE. Two weak peaks are visible, being $E_{Co,Ar,red2}$ = 0.28 V vs RHE and $E_{Co,Ar,red3}$ = 0.11 V vs RHE, respectively. An intense oxidation wave culminates into a peak at $E_{Co,Ar,ox1}$ = 1.00 V vs RHE. Finally, a cathodic peak appears when the potential is inverted before being stopped, $E_{Co,Ar,red4}$ = 0.96 V vs RHE.

The considerable number of peaks appearing in the CoOEP voltammogram are now carefully assigned based on a vast literature production, trying to focus on experimental conditions as closest as possible to the herein studied system. Redox potential in fact depends on the experimental condition, especially on pH [18,54–56].

One first key-point is the recognised redox behaviour of cobalt, which is able to easily access either Co (II) and Co(III). Therefore, this redox feature should in principle be

visible in the CV. CoOEP had recently been reported to undergo redox transition Co(III)/Co(II) at $E_{CO(III)/Co(II),}1 \approx 0.4$ V vs SCE (0.65 V vs SHE) [15]. Other similar cobalt chelates were reported at close values for the Co(III)/Co(II) redox potential [22]. Another cobalt derivative, cobalt tetraminophthalocyanine, was adsorbed on a glassy carbon substrate and tested in aqueous sulfuric acid, with noticeable reduction potential for Co(III)/Co(II) positioned at $E_{ECo(III)/Co(II),2} \approx 0.45$ V vs SCE (becoming 0.69 V vs SHE) [54]. Actually, differently substituted cobalt porphyrins and phthalocyanines show slight to moderate redox potential variations, in a range of [0.4; 0.8] V vs SCE, which turns into [0.6; 1.0] V vs SHE. Cobalt definitely possesses the highest redox potential among all the metal complexes so far examined. Basing on these considerations, it seems reasonable to individuate in the right part of figure 5.17.b the region in which the reduction Co(III)□Co(II) takes place. What remains under debate is whether the reduction of Co(III) to Co(II) occurs at more negative potential, $E_{Co,Ar,red1} = 0.70$ V, or at more positive potential, $E_{Co,Ar,red4} = 0.96$ V. One would claim that the distinct redox peak couple is at positive potential, with $E_{Co,Ar,ox1}$ and $E_{Co,Ar,red3}$. Most part of published data agree in associating the reduction potential Co(III)/Co(II) at values of $E_{Co(III)/Co(II)} \approx 0.6 – 0.7$ V vs SCE (0.8 - 0.9 V vs SHE) [15,18,21,55,57]. $E_{Co,Ar,red4}$ is more suitable on this regard. Basing on the voltammogram of figure 5.17.a, the peak potential separation of $E_{Co,Ar,red4}$ and $E_{Co,Ar,ox1}$ would be $\Delta E_1 = 0.04$ V, which would be too small for a fully reversible one electron redox process . Hence, cyclic voltammetry was repeated, restraining the data collection to a limited potential range around the peaks under discussion. The output is reported in figure 5.17.c.

Peak potentials are now listed referring to figure 5.17.c. Potential scan started at $E_{start} = 0.83$ V vs RHE, and a first weak reduction peak is observed at $E_{Co,Ar,red1} = 0.68$ V vs RHE. The scan direction was inverted, and a distinct oxidation wave was revealed. In this case, it is clear that this wave shape is generated by the contribution of at least two peaks, and a peak potential could be assigned at $E_{Co,Ar,ox} = 1.07$ V vs RHE. Finally, before closing the voltammetric circle, a reduction peak appears at $E_{Co,Ar,Red2} = 0.98$ V vs RHE. With these two new peak potential values, $E_{Co,Ar,Red2}$ and $E_{Co,Ar,ox}$, the peak-to-peak separation becomes $\Delta E_2 = 0.09$ V, thus higher than the expected value for a fully reversible process. Indeed, for such a complex experimental environment, it is difficult to obtain a “clean” electrochemical response, also considering the low number of active species and their electrostatic-based interaction with the substrate. It is worth noting that, the signal is forced to decrease upon prolonged electrochemical testing, due to an unavoidable molecular desorption, whose depletion cannot be restored in aqueous phase.

The effect of pH should be kept in consideration, since an identical Co phthalocyanine compound tested either in alkaline or acid electrolyte saw an increase in peak potentials when passing to the acid environment, but with a less resolved peak shape [52]. One reference claims to clarify the redox behaviour of Co tetrasulfonated phthalocyanine both in alkaline and acid media. Focussing on the acid media experiments, it appears that the Co phthalocyanine exhibit three major reduction waves, the two more positive ($E_1 \approx 0.2$ vs SCE ≈ 0.4 V vs SHE, $E_2 \approx 0.8$ vs SCE ≈ 1.0 V vs SHE, [53]) being superimposable

to the voltammetric reduction peaks here detected for Co octaethylporphyrin. These two peaks are so assigned: E_2 to Co(III)/Co(II) reduction, E_1 to changes of axial coordination for Co centres [53]. Therefore, on the basis of both literature information and by disentangling the experimental data the assignation to the Co(III)/Co(II) process finds sufficient agreement in the $E_{Co,Ar,ox}$/ $E_{Co,Ar,Red2}$ redox couple.

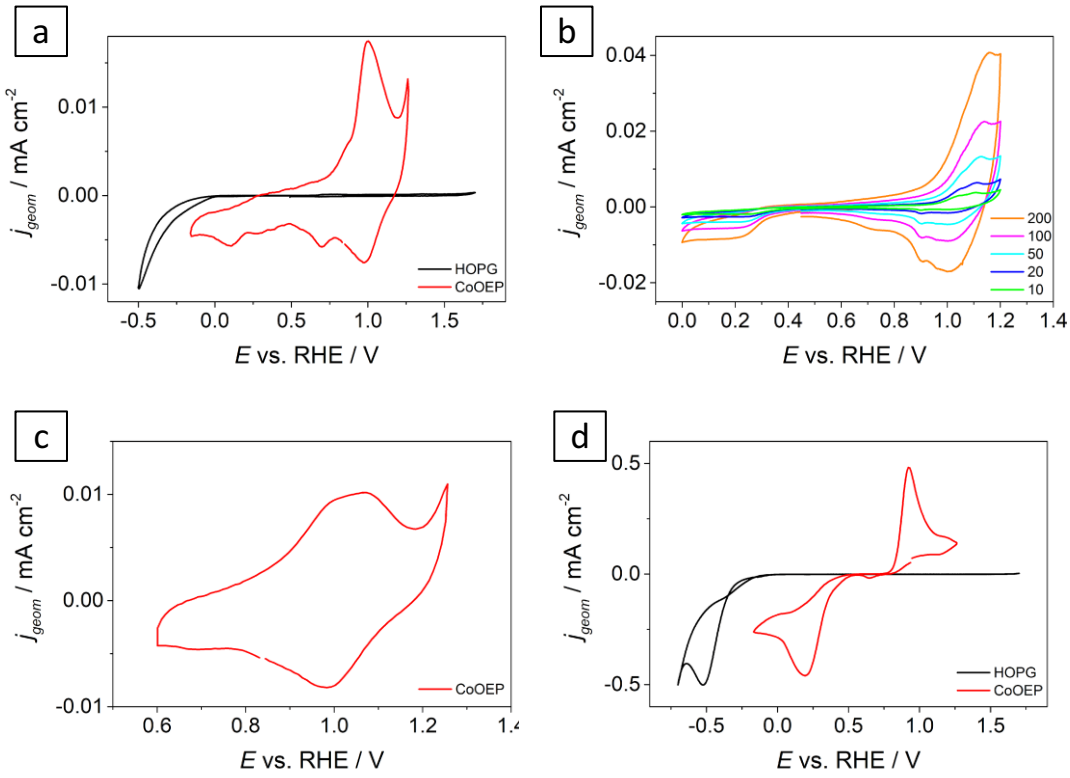

Figure 5.17. a) comparison of CV of CoOEP and bare HOPG, both recorded at 50 mV s^{-1} in deaerated 0.1 M $HClO_4$ b) comparison of CV of CoOEP and bare HOPG, both recorded at 50 mV s^{-1} in O_2 saturated 0.1 M $HClO_4$; c) cyclic voltammogram of CoOEP functionalised on HOPG in deaerated 0.1 M $HClO_4$ with shorter potential window scan with respect to 17.a; d) comparison of CV of CoOEP and bare HOPG, both recorded at 50 mV s^{-1} in O_2 saturated 0.1 M $HClO_4$.

At this point, it is worth examining the O_2 saturation case, as reported in figure 5.17.d. CV was started at E_{start} = 0.93 V, close to OCP. A first small current peak was detected at $E_{Co,O2,red1}$ = 0.65 V vs RHE. This peak is close to the previously determined $E_{Co,Ar,red1}$ = 0.68 V vs RHE. Indeed, the strong ORR-related peak is measured at $E_{Co,O2,red2}$ = 0.19 V vs RHE. Other cases are reported for which O_2 reduction on Co-macrocycles occurs at much more negative potential than that of Co(III)/Co(II) redox potential [18,21,55]. This explains why the redox behaviour of the metal centre is fundamental but it requires to be neither too negative nor too [18].

Another major feature to be mentioned is the intense oxidation peak at $E_{Co,O2,ox}$ = 0.92 V vs RHE. Moreover, the current density at the peak potential is $i_{p,ox}$ = 0.48 mA cm^{-1}, whereas for the reduction peak it is $i_{P,red2}$ = -0.46 mA cm^{-1}. It seems that all the reaction product generated during the cathodic scan is re-converted during the anodic scan. This

behaviour accounts for the possibility of hydrogen peroxide H_2O_2 being solely produced during ORR on the Co centres, which is then re-oxidised to O_2 on the same catalytic centres at sufficiently positive applied potential. Indeed, evidence of H_2O_2 oxidation ability by Co phthalocyanines had already been reported for variously substituted cobalt phthalocyanines [55]. Polarisation curves were in fact recorded with Co complexes in presence of H_2O_2, observing the appearance of a clear oxidation peak in the potential range $E_{H2O2} \approx$ [0.60; 0.80] V vs SCE, which turns into $E \approx$ [0.80; 1.00] V vs SHE [55]. In this latter potential window, the peak observed with cobalt octaethylporphyrin $E_{Co,O2,ox}$ is fully demonstrated, providing a proof of H_2O_2 oxidation. The suggested mechanism still deals with Co(III)/Co(II) redox behaviour. In fact, the oxidation is observed at potential where Co(II) is still the predominant species and becomes inhibited when Co(II) centres are converted to Co(III) upon sufficiently positive potential. The Co(III)/Co(II) redox potential is therefore a useful reaction descriptor and modulating its value upon proper peripheral substitution of the molecular ligand also enables a catalysis tunability [55].

To sum up, an unambiguous peak assignment cannot be made for what concerns CoOEP cyclic voltammograms in deaerated electrolyte. Many similarities were encountered upon comparison with literature data, and a plausible data interpretation embraces the role of Co(III)/Co(II) redox couple in determining the major electrochemical response of Co complexes. The Co(III)/Co(II) redox couple is also to be a key aspect for O_2 reduction electrocatalysis. The complexity that came up in interpreting CoOEP cyclic voltammograms forces new dedicated experiments to be conducted in future, with the aim to clarify the real electrochemical phenomena at the basis of ORR electrocatalysis. Attempts were made to functionalise the glassy carbon surface of a RRDE electrode to enhance the information regarding the percentage of produced hydrogen peroxide and therefore to gain a better understanding of the ORR mechanism, but poor results due to an improper functionalisation procedure were obtained and they are not shown.

5.1.5 CuOEP

Copper octaethylporphyrin was solubilised to attain a 0.1 mM concentration in DMF solvent. The solution was drop-casted onto a freshly cleaved HOPG substrate (CuOEP@HOPG), letting it rest for 30 min prior to speeding up the solvent evaporation by using an Ar steam. Resulting voltammograms obtained with Ar purged electrolyte (0.1 M $HClO_4$) at different scan rates are reported in figure 5.18.a. Two distinct reduction peaks are visible, together with one clear oxidation peak and a weak oxidation peak. The first reduction peak is observed at $E_{Cu,Ar,red1}$ = 0.19 V vs RHE, the second at $E_{Cu,Ar,red2}$ = -0.24 V vs RHE. At a first impression, it would be easy to ascribe one or both these peaks to the redox behaviour of the transition metal, i.e. copper. However, reduction from Cu(II) to Cu(I) is not easily achieved, with few examples being reported. Among these, a substituted copper tetraphenylporphyrin exists, namely copper tetracyano tetraphenylporphyrin $CuTPP(CN)_4$, for which the redox electrochemical reaction Cu(II)/Cu(I) in homogeneous organic phase was reported at strong negative potential [56,57]. Moreover, in the same work, the two reversible peak couples observed at more positive potential are not ascribed to a redox activity of the central copper, but rather to

the electron-accepting ability of the porphyrinato ligand. This leads back to the electrochemical response already described for H_2OEP and MnOEP. Indeed, the peak-to-peak separation measured in the case of CuOEP, focussing on the 50 mV s^{-1} cyclic voltammetry reported in figure 5.18.b, is equal to ΔE_{exp} = 0.43 V, which is extremely close to the reported ΔE value for metal-free octaethylporphyrin, corroborating the hypothesis that the two reduction peaks should be associated with the porphyrinato ring reduction rather than to the copper metal center [49]. Anyway, other works claim the existence of the Cu(II)/C(I) peak, but its position is always confined to rather negative values, which for the purpose of this work should be disregarded [56–59].

Another study, conducted in 10 mM aqueous HCl, demonstrates that a substituted copper porphyrin does not undergo copper reduction Cu(II)/Cu(I), but rather a reduction of the porphyrinato ligand occurs [60].

Concerning the oxidation peak at $E_{Cu,Ar,ox1}$ = 0.44 V vs RHE, its attribution remains unsolved and further evidence needs to be gathered for a reliable hypothesis.

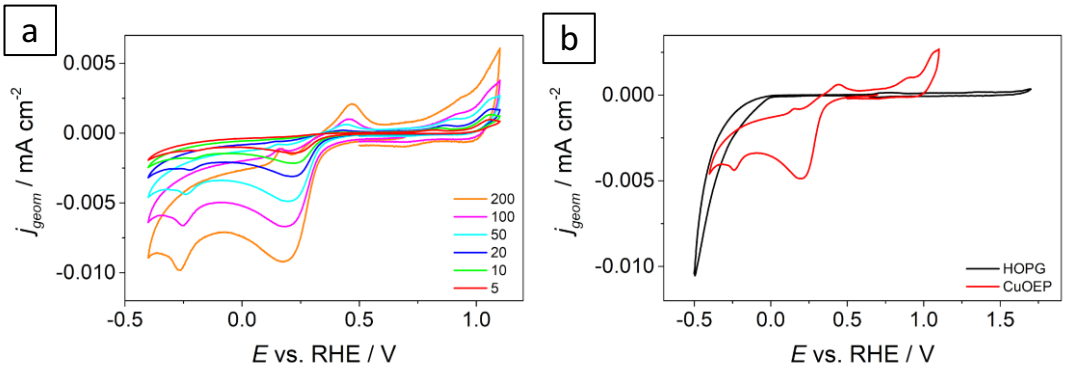

Figure 5.18. a) cyclic voltammograms of CuOEP functionalised on HOPG in deaerated 0.1 M $HClO_4$; b) comparison of CV of CuOEP and bare HOPG, both recorded at 50 mV s^{-1} in deaerated 0.1 M $HClO_4$.

The activity of CuOEP towards ORR was then tested, and the outcome is reported in figure 5.19a, where the the oxygen reduction at CuOEP@HOPG is compared to the unfunctionalized HOPG. A definite reduction peak is observed only in the case of the fastest scan rate (figure 5.19b), i.e. 200 mV s^{-1}, probably because it was the first being recorded. For the remaining scan rates, a cathodic wave is in any case visible, and it culminates at a potential of $E_{Cu,O2}$ = -0.40 vs RHE. It is worth noting that the ORR process falls more negative with respect to the previous investigated metal OEPs. Various examples of copper-based catalyst materials have been explored, some of them having also a bio-inspired character. In fact, oxidase enzymes, like laccase, are based on multi-copper site cooperation to efficiently catalyse ORR [61–63]. Therefore, different attempts have been made to replicate this multi-copper site cooperative catalysis [61,64,65]. Besides the performances that in some cases can be really appealing, all these complexes suffer from poor stability and durability in electrochemical environment, especially when the pH is lowered from the alkaline environment [61].

For the specific case of copper porphyrins and phthalocyanines, their limit should be recognised with respect to previously presented metal-complexes. The origin of a substantially poor catalytic activity is reconducted to the *d* orbital population. Whilst for Fe, Co and Mn, partially filled *d* orbital population is realised, Cu has a complete *d* shell, a particularly stable configuration which leaves an unpaired 4s electron. However, this inhibits the redox behaviour of Cu, which is almost unable to exhibit a Cu(III)/Cu(II) redox behaviour, with the couple Cu(II)/Cu(I) being also difficult to attain as foretold [69–73]. For copper phthalocyanines and porphyrins, almost no data exist about a Cu(II)/Cu(I) behaviour, except for Cu tetrakis(4-hydroxy-3-methoxyphenyl)porphyrin, for which the Cu(II)/Cu(I) redox transition is reported at E = 0.10 V vs Ag/AgCl [69]. However, the source paper does not explicitly make a reference to the Cu(II)/Cu(I) redox behaviour, but it rather indicates that the reduction process occurs on the porphyrinato ligand [74]. It is true that a certain ORR activity is exerted by Cu tetrakis(4-hydroxy-3-methoxyphenyl)porphyrin functionalised on the edge-plane graphite surface, but RDE data were not presented due to instability of the Cu porphyrin [74].

Furthermore, the key-factor for a satisfactory ORR electrocatalysis operated by copper is the creation of di-copper or multi-copper sites, so that a cooperative mechanism of O_2 reduction can explicate [69], that as will be clear from STM image is a condition not fully accomplished for the CuOEP case, i.e. the copper centers are not sufficiently close or "interacting" and this might explain the scarse catalytic activity.

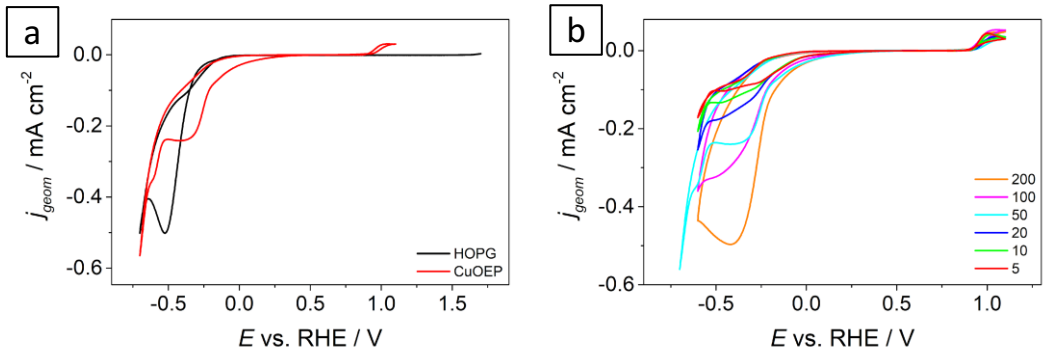

Figure 5.19.a) comparison of CV of CuOEP and bare HOPG, both recorded at 50 mV s^{-1} in O2 saturated 0.1 M HClO4; b) cyclic voltammograms of CuOEP functionalised on HOPG in O_2 saturated 0.1 M HClO4 at different scan rates.

5.1.6 PtOEP

PtOEP was tested with cyclic voltammetry technique. At this purpose, a 0.1 mM PtOEP solution was realised with DMF, and it was drop-casted on the freshly cleaved HOPG surface (PtOEP@HOPG), the resulting cyclic voltammograms being shown in figure 5.20.a. Focussing on the Ar saturated electrolyte case, PtOEP voltammogram does not appear totally flat, as HOPG does. There is in fact a cathodic wave, with an onset at $E_{Pt,Ar,onset} \approx 0.2$ V vs RHE, and culminating at $E_{Pt,Ar}$ = -0.5 V vs RHE. In this quite large potential window, it is not well ascertained what is the ongoing electrochemical process, but redox activity should be dismissed with Pt, since its only recognised stable oxidation

states are Pt(II) and Pt(0), namely metallic platinum, with some Pt(IV) complexes being recognised as stable [75], and in fact no metallic platinum deposition was observed in the experimented potential window. It must be remembered that the electron-accepting behaviour of metal-free octaethylporphyrin was already extensively explained in section 5.1.1 and 5.1.3, so it is expected at least a similar response also in the case of PtOEP. A remark should be done on the oxidation feature commencing at $E_{Pt,ox,onset} \approx 1.2$ V vs RHE. On this regard, a comparison is possible with a platinum phthalocyanine film in contact with an alkaline aqueous solution. Disregarding from possible pH effects, it was evidenced a clear anodic current increase in the same potential region, together with the feeble cathodic wave spotted at $E_{Pt,Ar,2} \approx 0.9$ V vs RHE, but no resolutive explanation was provided to explain this electrochemical response [76].

CV obtained in O_2 saturated electrolyte is now taken into exam (figure 5.20.b). Although PtOEP was proved to adsorb on the HOPG surface, see section 6.1.7. at this scope, the resulting cyclic voltammogram collected at a scan rate of 50 mV s^{-1} is showing a rather poor catalytic activity if compared to the previously described FeOEP and MnOEP, and the cathodic peak is centred at $E_{Pt,O2}$ = -0.72 V vs RHE. As a comparison, CV of bare HOPG electrode is superimposed in figure 5.20.b, showing that even HOPG is performing better than the PtOEP adlayer. This behaviour is quite unexpected, considering that Pt is regarded as the best-performing catalyst material for many reactions, among which ORR [77]. However, common Pt-based catalyst materials for fuel-cell application are in the form of dispersed nanoparticles on a supporting matrix, with many different sizes and shapes being pursued to minimise Pt usage and maximise electrocatalytic performances. In these cases, Pt retains a (0) oxidation state, being found in the (nano) form of metallic Pt. For the purpose of this work, Pt is studied as a nitrogen-coordinated single atom site, with a (II) oxidation state, without any significant evidence (neither CV nor EC-STM) of metallic Pt being in some way produced or *in situ* generated. Actually, a scarce activity of a Pt phthalocyanine film directly functionalised on a carbon electrode had already been discovered [78], with a significant performance improvement being detected only if a gold film was employed as anchoring substrate for PtPc. In this regard, the same platinum octaethylporphyrin was tested on Au(111) as different substrate (data presented in section 5.2.2.) but the ORR activity is in any case modest. At this point of the discussion, one wonders what is the mechanism ruling ORR in presence of PtN_4 sites (the same could be said for CuN4, which behaves similarly). The same study on Pt phthalocyanine deposited on a gold film over a carbon substrate suggests that the catalytic behaviour of PtPc cannot be understood in the framework of a classical redox-mediated catalysis. It was observed that a 0.38 nm Pt-Pt distance characterises PtPc, realising a suitable condition for a cooperative oxygen reduction mediated by Pt-Pt couples, in which the oxygen molecules dispose in bridge position between two Pt centres as the initial stage of ORR [22,76,78,79].

$$PtPc + O_2 + PtPc + 2e^- \leftrightarrow PtPc - O^- - O^- - PtPc \qquad 5.11$$

However, such a distance is far lower than the Pt-Pt distance observed for the PtOEP@HOPG system (see later in section 6.1.7) and this should explain why in the absence of cooperative effects between two metal centres the electrocatalysis of Pt centres drops drastically.

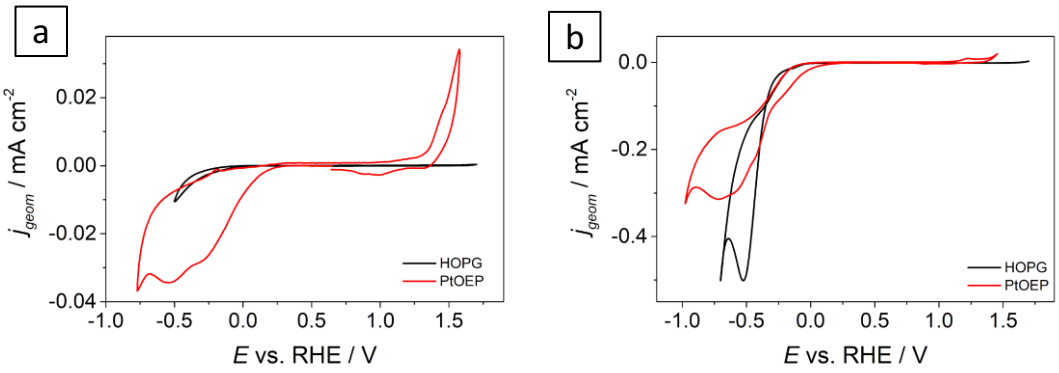

Figure 5.20. a) comparison of CV of cyclic voltammograms of PtOEP functionalised on HOPG in deaerated 0.1 M $HClO_4$; b) comparison of CV of PtOEP@HOPG and bare HOPG, both recorded at 50 mV s^{-1} in O_2 0.1 M $HClO_4$.

It is possible that noncovalent functionalisation imparts ORR electrocatalytic activities to the Pt metal center of the molecule. This is a curious effect since the support itself is not active, nor is the molecule, but the ensemble of both let arise new properties and new catalytic activity. When Pt octaethylporphyrin is adsorbed on HOPG we may infer that charge density is transferred from the Pt metal center to the HOPG support, making the metal center, *de facto,* able to adsorb O_2 and catalyse the ORR process, even in the absence on a redox catalysis. Future investigations are needed, especially concerning linear sweep voltammetry on glassy carbon substrate and rotating ring and disk experiments to assess the number of exchanged electrons and therefore understand the ORR mechanism on PtOEP.

5.1.7 RuOEP

Ru(II) carbonyl octaethylporphyrin was adsorbed at the HOPG surface from a 0.1 mM DMF solution. After a resting period of 30 minutes, an Ar flush was directed over the surface to help DMF evaporation obtaining RuOEP@HOPG. The sample was then transferred to the electrochemical cell for cyclic voltammetry tests. A cyclic voltammogram recorded at a scan speed of 50 mV s^{-1} is reported in figure 5.21.a, within the superimposed CV of the bare HOPG surface. A first reduction peak is visible at $E_{Ru,Ar,red1}$ = 0.89 V vs RHE. At more negative potential, a cathodic wave appears with a peak potential at $E_{Ru,Ar,red2}$ = 0.21 V vs RHE. Both reduction peaks show a counter-part oxidation peak. The first is placed at $E_{Ru,Ar,ox1}$ = 0.40 V vs RHE and it actually is very weak. The second is located at $E_{Ru,Ar,ox2}$ = 1.13 V vs RHE and it is followed by a rapid current increase. CV recording was prudentially stopped at E = 1.30 V vs RHE.

Most of the studies conducted on Ru porphyrins and their substituted derivatives were conducted in organic phases, where the number of reversible couples can arrive to 3, depending on the potential scan window [80–83]. Based on these studies, an important

distinction should be made between axially coordinated or uncoordinated ruthenium centres. It seems that non-CO-containing complexes enable the achievement of a higher metal oxidation state, Ru(III). Generally, two oxidation waves are observed in the range [0; +0.50 V] vs Ag/AgCl, and they are ascribed to the ability of porphyrins to accept and release two electrons (one-electron step each) [80,83]. When carbonyl CO is bound to Ru(II) centres, the electrochemical processes pertaining to the Ru porphyrin are believed to change. First of all, the presence of CO causes the redox peak to shift to positive values, meaning that the Ru(CO) porphyrins are harder to oxidise. CO acts as electron-withdrawing ligand, which strongly stabilises Ru(II) oxidation state, thus explaining the fact that Ru(CO) porphyrins are not expected to exhibit the Ru(III)/Ru(II) redox behaviour [59,80].

This is reflected also on the O_2 reduction electrocatalysis. A Ru tetraphenylporphyrin derivative was at this purpose functionalised on a carbon surface, and measurements were conducted in aqueous acid electrolyte. A certain catalytic activity was observed, but it disappeared for the same complex featuring a carbonyl as axial ligand, again pointing out the strong binding and the stabilising role of CO towards the Ru centre, at the point of inhibiting the catalytic activity [83].

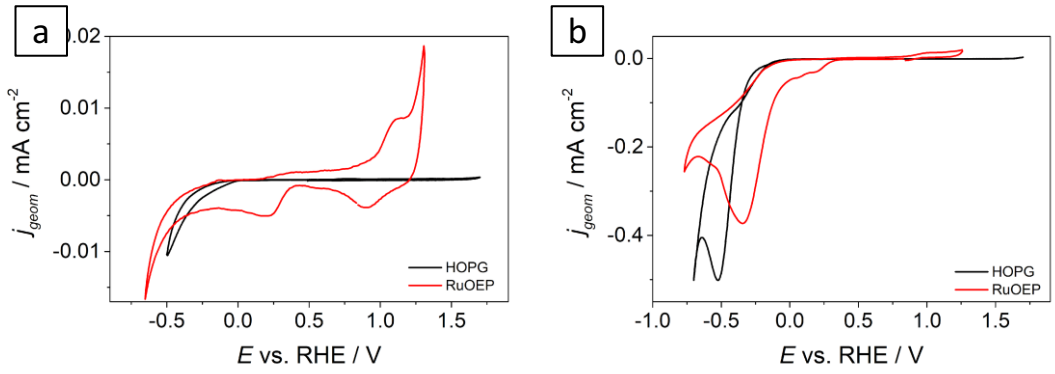

Figure 5.21. a) comparison of CV of RuOEP and bare HOPG, both recorded at 50 mV s^{-1} in deaerated 0.1 M $HClO_4$; b) comparison of CV of RuOEP and bare HOPG, both recorded at 50 mV s^{-1} in O_2 saturated 0.1 M $HClO_4$.

5.1.8 SnOEP

Similarly to the other porphyrin complexes, Tin (IV) octaethylporphyrin dichloride was solubilised in DMF (0.1 mM), and drop-casted on the freshly cleaved HOPG surface, letting it functionalise for 30 min prior to subject it to an Ar stream to facilitate DMF evaporation. The so-obtained functionalised substrate (SnOEP@HOPG) was probed by cyclic voltammetry, first in deaerated solution, namely 0.1 M $HClO_4$. The resulting voltammogram, recorded at scan rate of 50 mV s^{-1}, is reported in figure 5.22.a, together with the superimposed CV of the bare HOPG substrate.

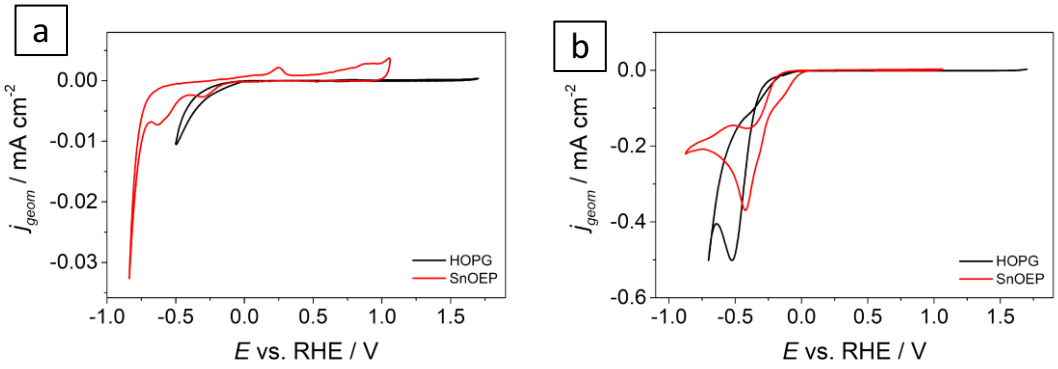

Figure 5.22. a) comparison of CV of SnOEP@HOPG and bare HOPG, both recorded at 50 mV s^{-1} in deaerated 0.1 M $HClO_4$; b) comparison of CV of SnOEP@HOPG and bare HOPG, both recorded at 50 mV s^{-1} in O_2 saturated 0.1 M $HClO_4$.

A limited number of publications deal with Sn porphyrin electrochemical response, with the most part describing it in homogeneous organic phases [59,84,85]. A further example exists, in which a water-soluble tin (IV) porphyrin (tin (IV) tetrakis-carboxyphenyl porphyrin dichloride), was subjected to electrochemical investigation in an aqueous electrolyte solution. It was basically demonstrated that the tin porphyrin undergoes electrochemical reduction, but the tin (IV) centre is not affected. Reduction in fact occurs at the porphyrinato ligand, which is able to undergo two one-electron reduction steps [86]. Differently from hitherto analysed metal porphyrins, these reductions are claimed to represent irreversible reactions. Indeed, also in the present work, no evident oxidation peaks are visible, with the exception of two weak anodic waves at $E_{Sn,AR,ox1}$ = 0.24 V s RHE and at $E_{Sn,AR,ox2}$ = 0.90 V s RHE. The cathodic part of the voltammogram also shows two cathodic waves, centred at $E_{Sn,Ar,red1}$ = -0.30 V vs RHE and at $E_{Sn,Ar,red2}$ = -0.62 V vs RHE. Due to a very large potential separation between the reduction and the oxidation peaks, it is believed that they are not electrochemically correlated, with additional characterisations being required, especially at different potential windows, to assess a more realistic hypothesis on this regard. At least, upon comparison [86], it can be stated that the two reduction features should not stand for the Sn(IV) reduction to Sn(II).

Let us now take into exam the cyclic voltammogram recorded at 50 mV s^{-1} scan speed for the SnOEP layer on HOPG in oxygen saturated electrolyte, figure 5.22.b . The SnOEP adlayer shows some catalytic behaviour towards ORR, it is better performing than PtOEP, but the potential is among the lowest compared to all the herein analysed metal porphyrins ($E_{Sn,O2,red}$ = -0.42 V vs RHE). It is in any case a starting point the fact that *p* block metal centre does exert a certain activity towards ORR. Actually, a very remarkable demonstration of the catalytic activity of Sn(IV)N_x moieties towards ORR was recently published [87]. It claimed that a Sn-N-C catalysts material (based on SnN_x moieties embedded in a carbonaceous matrix) can possess a catalytic activity comparable to those of a homologue Fe-based material, both in terms of performance and product selectivity. The experimental conditions are the very same as of this work, 0.1 M $HClO_4$. As already discussed for PtOEP, the catalytic activity should be reconducted outside of the classical

framework of redox catalysis, due to a completely filled *4d* shell. Mössbauer and XAS spectroscopies demonstrated the (IV) oxidation state of the Sn centres, and DFT calculations were run in support of the experimental results, evidencing that pyridinic nitrogen coordinating Sn(IV) centres should represent the real active site towards ORR. Different active site shapes were tested, including porphyrinic Sn(IV), but it was found that this configuration leads to a too strong oxygen binding. This could probably explain the scarce catalytic activity evidenced with Sn(IV)OEP, even if the same experimental conditions were adopted [87].

5.1.9 FeTPP

Fe(III) tetraphenylporphyrin chloride was solubilised in DMF to reach a 0.1 mM concentration. The freshly cleaved HOPG surface was functionalised with FeTPP solution by drop-casting, for a total time of 60 minutes, composed by 30 minutes in a closed container and the remaining 30 minutes under an Ar stream to facilitate DMF evaporation. In this way, FeTPP@HOPG was obtained, and it was tested by cyclic voltammetry in deaerated 0.1 M $HClO_4$. The outcome is reported in figure 5.23a.

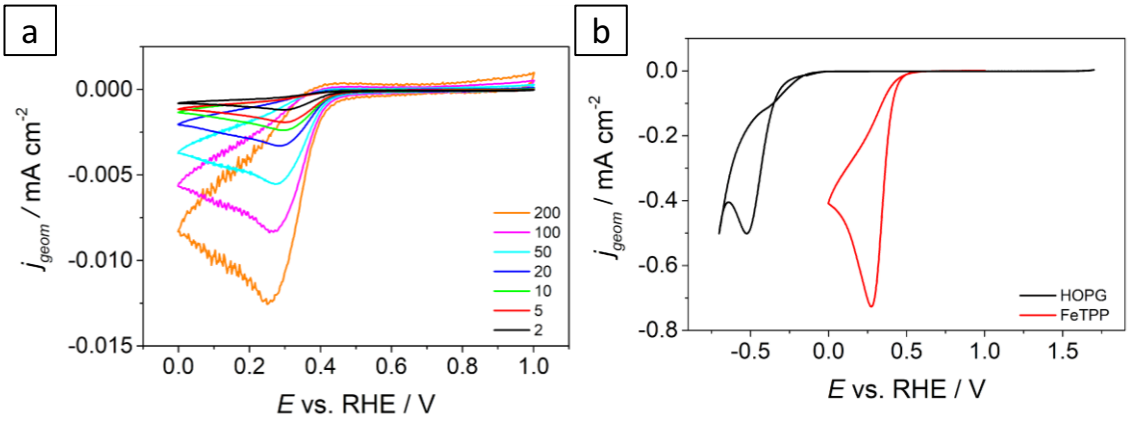

Figure 5.23. a) Cyclic voltammograms at different scan rates of FeTPP functionalised on HOPG in deaerated 0.1 M $HClO_4$; b) comparison of CV of FeOEP and bare HOPG, both recorded at 50 mV s^{-1} in O_2 saturated 0.1 M $HClO_4$.

Thanks to a thorough degassing of the electrolyte solution, the reduction peak at $E_{Fe,Ar,red}$ = 0.27 V vs RHE can be associated to the weak oxidation peak at $E_{Fe,Ar,ox}$ = 0.42 V vs RHE. FeTPP therefore behaves very similarly to FeOEP, which was already examined in section 5.1.2. This means that it is characterised by the presence of the Fe(III)/Fe(II) redox couple. Again, reversibility increased upon increasing the scan rate, and the relatively low stability of the FeTPP adlayer limits a complete clarification of the electron transfer process, and the involvement of an EC mechanism (electron transfer followed by a chemical process) remained the most probable explanation to the electrochemical response. A difference with respect to FeOEP lies in the Fe(III)/Fe(II) reduction potential, since for FeTPP it is slightly more negative. This is an example of peripheral substituent effect exerted on the reduction potential of the central metal. Electron-donating substituents are in fact expected to cathodically shift the reduction potential [15,16]. Though modest, electron-donating effect of phenyl groups surpasses that of simple alkyl

groups, thus potentially explaining the slightly more negative potential revealed for FeTPP with respect to FeOEP. This did not directly translate into a more negative ORR peak always comparing FeTPP to FeOEP. In fact, the resulting CV collected in O_2 saturated electrolyte at different scan rates is reported in figure 5.23b, together with the superimposed HOPG CV. The ORR peak is individuated at $E_{Fe,O2}$ = 0.26 V vs RHE, which is actually 10 mV more positive than FeOEP, so that the two iron porphyrins can be basically considered equal in terms of ORR electrocatalysis. Indeed, the substituents were not significantly chemically different, and different or additional substituents, preferably featuring heteroatoms, should be employed to emphasise the substituents effect onto M(III)/M(II) reduction potential and ORR peak potential.

5.2 Voltammetric characterization of Au(111) functionalised electrodes

5.2.1 H_2OEP

Free-base octaethyl porphyrin was solubilised in DMF and a 0.1 mM concentration was realised. The newly flame-annealed Au(111) single crystal was functionalised by the hanging meniscus method. Cyclic voltammetry at scan speed of 50 mV s^{-1} I in deaerated solution is reported in figure 5.24.a, together with the CV of bare Au(111). The free-base porphyrin CV is almost featureless, with very feeble oxidation waves being detected at $E_{OEP,ox1}$ = 0.2 V vs RHE and $E_{OEP,ox1}$ = 0.5 V vs RHE. It had already been demonstrated that H_2OEP on HOPG substrate undergoes a redox transition thanks to electron-donating and -accepting ability of the porphyrinato ligand, having also found vast agreement with literature data [52]. In this case, it appears that the Au(111) substrate is in some way interfering with the electrochemical response of the free-base species, resulting in an almost flat cyclic voltammogram.

Having previously detected a certain electrocatalytic activity of H_2OEP towards ORR (section 5.1.1), a similar behaviour could be expected also with Au(111) as substrate. However, only a large cathodic wave was measured by cyclic voltammetry in O_2 saturated electrolyte, as shown in figure 5.24.b. Moreover, its potential range is more negative than the cathodic wave observed for Au(111), whose CV is also reported in the same figure. The electrochemical response of Au(111) had already been discussed in section 4.1.2.

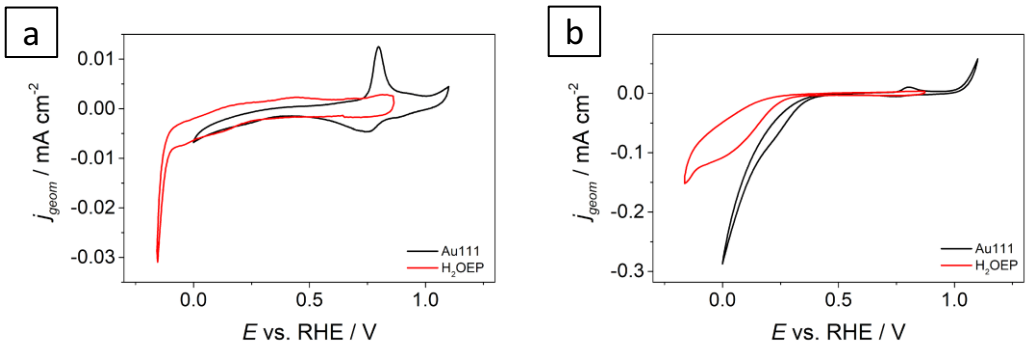

Figure 5.24. a) comparison of CV of H_2OEP@Au(111) and bare Au(111), both recorded at 50 mV s^{-1} in deaerated 0.1 M $HClO_4$; b) comparison of CV of H2OEP@Au(111) and bare Au(111), both recorded at 50 mV s^{-1} in O_2 saturated 0.1 M $HClO_4$.

5.2.2 PtOEP

A 0.1 mM platinum (II) octaethylporphyrin solution was prepared with DMF solvent, and the flame-annealed Au(111) surface was immersed by hanging meniscus in the PtOEP solution. The functionalised electrode PtOEP@Au(111) was tested by cyclic voltammetry in deaerated electrolyte, the resulting CV being displayed in figure 5.25.a. Contrary to what previously observed in section 5.1.6 for the same species supported on the HOPG surface, the CV appears rather flat, with a feeble cathodic wave centred at $E_{Pt,Ar,red}$ = 0 V vs RHE, and another feeble oxidation wave at $E_{Pt,Ar,ox}$ = 0.5 V vs RHE. It is clear from previous section 5.2.1 concerning H_2OEP that the redox features characterising the free-base porphyrin are hard to detected with Au(111) substrate. Therefore, PtOEP is also not likely exhibiting this redox behaviour. Pt itself is not expected to show any redox couple, as already discussed in section 5.1.6.

Conversely, in O_2 saturated electrolyte, the PtOEP layer behaves differently from H_2OEP, with a non-well defined but intense cathodic peak, whose centre might be attested at $E_{Pt,O2,red}$ = 0.1 V vs RHE. Even if PtOEP shows a cathodic peak owed to ORR also when supported on the HOPG surface, the peak potential revealed with Au(111) is far more positive. Despite this observation, Pt is still considered incapable of a redox-like catalysis. A tentative explanation could be addressed with Pt centres placed at a convenient distance among each other in order to trigger a cooperative O_2 reduction process [22,76,78,79].

Further investigations with rotating ring and disk electrodes, where the disk material should be gold, are planned, with the aim to gain more in-depth knowledge about reaction mechanisms.

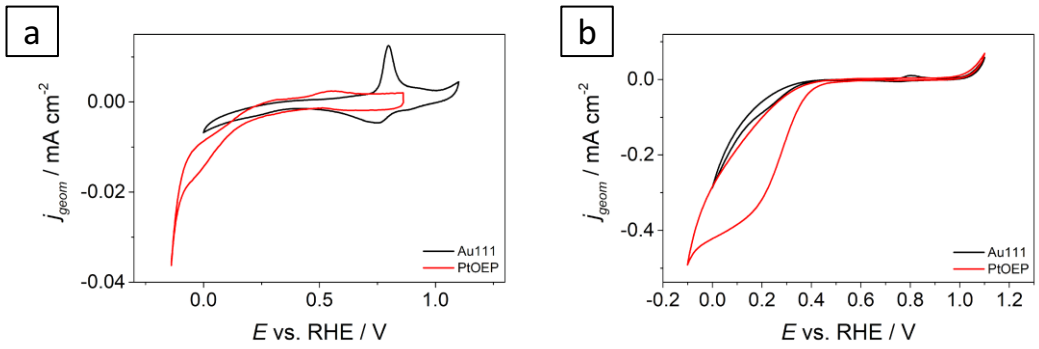

Figure 5.25. a) comparison of CV of PtOEP@Au(111) and bare Au(111), both recorded at 50 mV s^{-1} in deaerated 0.1 M $HClO_4$; b) comparison of CV of PtOEP@Au(111) and bare Au(111), both recorded at 50 mV s^{-1} in O_2 saturated 0.1 M $HClO_4$.

5.2.3 FeOEP

Iron (III) octaethylporphyrin chloride was solubilised in DFM to reach a 0.1 mM concentration. The flame-annealed Au(111) sample was functionalised by hanging meniscus method with FeOEP (FeOEP@Au(111)), rinsed, and transferred to electrochemical cell. Resulting voltammetries in deaerated electrolyte are shown in figure 5.26.a.

FeOEP@Au(111) shows a pair of voltammetric peaks in the potential range 0.3 to 0.5 V vs RHE non present in the Au(111) support (25.b): the reduction potential is $E_{Fe,Ar,red}$ = 0.36 V vs RHE, the oxidation potential is $E_{Fe,Ar,ox}$ = 0.38 V vs RHE. Their shape is symmetrical, and a small peak separation (≈ 20 mV) is indicative of a reversible one-electron transfer adsorption process. The reversible redox process is attributed to the Fe(III)/Fe(II) redox transition, and it is worth noting that the reversibility is function of the scan rate (Figure 5.26.a). In fact, the reversibility decreases at lower scan rate and this phenomenon is explained by considering a following chemical reaction, such as the reaction with O_2 that might be present as contamination even after extensive Ar purging.

Anyway, the existence of a Fe(III)/Fe(II) redox behaviour has already been confirmed [15,18,38–41].

The saturation of the electrolyte with pure oxygen, a very intense and irreversible reduction process, is observed in the close proximity of the Fe(III)/Fe(II) transition (Figure 5.26.c). This reduction peak was not present in the absence of O_2, and it can be stated that the reduction of oxygen occurs thanks to the functionalization of the surface of Au(111) with iron porphyrin centres. The O_2 reduction mechanism is therefore a redox mediated reduction process where it is first necessary to reduce Fe(III) to Fe(II), which in turn reduces O_2 to the final product. The numerous literature examples [15,17,18,22], together with two previously published articles on similar Fe-based macrocycles both on Au(111) and HOPG substrates strongly support this explanation [37,88].

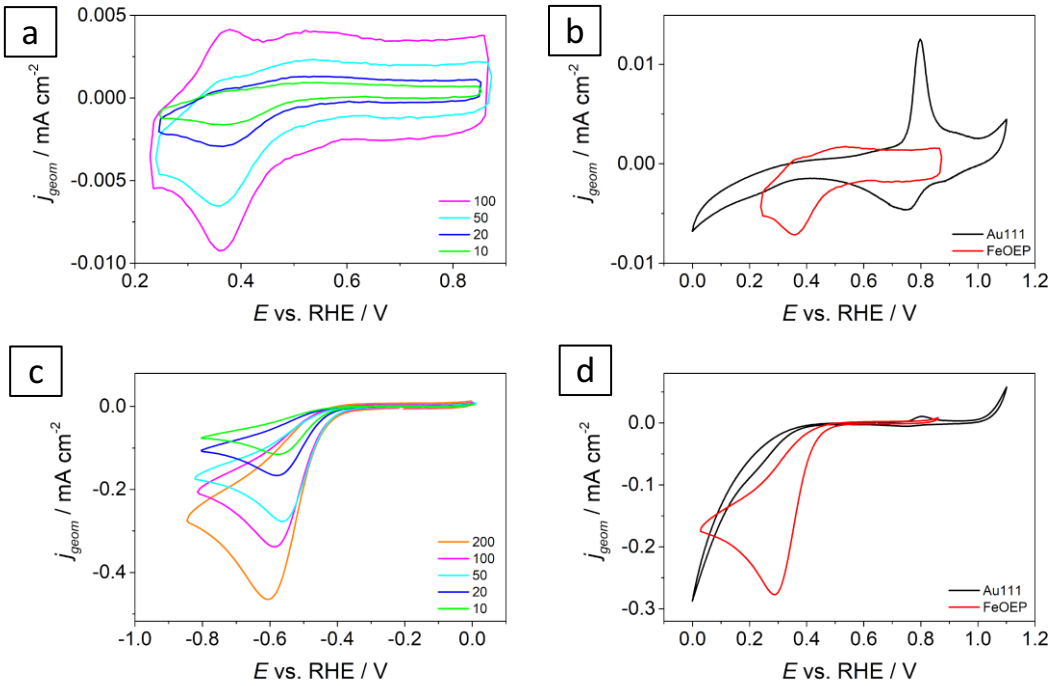

Figure 5.26. a) cyclic voltammograms of FeOEP@Au(111) in deaerated 0.1 M $HClO_4$; b) comparison of CV of FeOEP@Au(111) and bare Au(111), both recorded at 50 mV s^{-1} in deaerated 0.1 M $HClO_4$; c) cyclic voltammograms of FeOEP functionalised on Au(111) in O_2 saturated 0.1 M $HClO_4$; d) comparison of CV of FeOEP@Au(111) and bare Au(111), both recorded at 50 mV s^{-1} in O_2 saturated 0.1 M $HClO_4$.

References

[1] David Dolphin, The Porphyrins, volume I, 1978. pages 394, 410, 419.

[2] M.X. Chen, L. Tong, H.W. Liang, Understanding the Catalytic Sites of Metal–Nitrogen–Carbon Oxygen Reduction Electrocatalysts, Chemistry - A European Journal. 27 (2021) 145–157.

[3] H. Tomiyasu, H. Shikata, K. Takao, N. Asanuma, S. Taruta, Y.Y. Park, An aqueous electrolyte of the widest potential window and its superior capability for capacitors, Scientific Reports. 7 (2017) 1–12.

[4] M.K. Debe, Electrocatalyst approaches and challenges for automotive fuel cells, Nature. 486 (2012) 43–51.

[5] G. Daniel, T. Kosmala, F. Brombin, M. Mazzucato, A. Facchin, M.C. Dalconi, D. Badocco, P. Pastore, G. Granozzi, C. Durante, Highly Graphitized Fe-N-C Electrocatalysts Prepared from Chitosan Hydrogel Frameworks, (2021) 1–16.

[6] X. Wang, Z. Li, Y. Qu, T. Yuan, W. Wang, Y. Wu, Y. Li, Review of Metal Catalysts for Oxygen Reduction Reaction: From Nanoscale Engineering to Atomic Design, Chem. 5 (2019) 1486–1511.

[7] C. Sealy, The problem with platinum, Materials Today. 11 (2008) 65–68.

[8] M. Shao, Q. Chang, J.P. Dodelet, R. Chenitz, Recent Advances in Electrocatalysts for Oxygen Reduction Reaction, Chemical Reviews. 116 (2016) 3594–3657.

[9] H.W. Liang, X. Cao, F. Zhou, C.H. Cui, W.J. Zhang, S.H. Yu, A free-standing Pt-nanowire membrane as a highly stable electrocatalyst for the oxygen reduction reaction, Advanced Materials. 23 (2011) 1467–1471.

[10] S. Mukerjee, S. Srinivasan, Enhanced electrocatalysis of oxygen reduction on platinum alloys in proton exchange membrane fuel cells, Journal of Electroanalytical Chemistry. 357 (1993) 201–224.

[11] R. Jasinski, A New Fuel Cell Cathode Catalyst, Nature. 201 (1964) 1212–1213.

[12] G. Daniel, E. Foltran, R. Brandiele, L. Nodari, R. Pilot, E. Menna, G.A. Rizzi, A. Ahmed Isse, C. Durante, A. Gennaro, Platinum-free electrocatalysts for oxygen reduction reaction: Fe-Nx modified mesoporous carbon prepared from biosources, Journal of Power Sources. 402 (2018) 434–446.

[13] G. Daniel, T. Kosmala, M.C. Dalconi, L. Nodari, D. Badocco, P. Pastore, A. Lorenzetti, G. Granozzi, C. Durante, Upcycling of polyurethane into iron-nitrogen-carbon electrocatalysts active for oxygen reduction reaction, Electrochimica Acta. 362 (2020) 137200.

[14] G. Daniel, Y. Zhang, S. Lanzalaco, F. Brombin, T. Kosmala, G. Granozzi, A. Wang, E. Brillas, I. Sirés, C. Durante, Chitosan-Derived Nitrogen-Doped Carbon Electrocatalyst for a Sustainable Upgrade of Oxygen Reduction to Hydrogen Peroxide in UV-Assisted Electro-Fenton Water Treatment, ACS Sustainable Chemistry and Engineering. 8 (2020) 14425–14440.

[15] J.H. Zagal, M.T.M. Koper, Reactivity Descriptors for the Activity of Molecular MN4 Catalysts for the Oxygen Reduction Reaction, Angewandte Chemie - International Edition. 55 (2016) 14510–14521.

[16] J. Masa, W. Schuhmann, Systematic selection of metalloporphyrin-based catalysts for oxygen reduction by modulation of the donor-acceptor intermolecular hardness, Chemistry - A European Journal. 19 (2013) 9644–9654.

[17] J.H. Zagal, F. Bedioui, J.P. Dodelet, N4-Macrocyclic Metal Complexes, Springer, 2006.

[18] J.H. Zagal, S. Griveau, J.F. Silva, T. Nyokong, F. Bedioui, Metallophthalocyanine-based molecular materials as catalysts for electrochemical reactions, Coordination Chemistry Reviews. 254 (2010) 2755–2791.

[19] Y. Oliver Su, T. Kuwana, S.M. Chen, Electrocatalysis of oxygen reduction by water-soluble iron porphyrins. Thermodynamic and kinetic advantage studies, Journal of Electroanalytical Chemistry. 288 (1990) 177–195.

[20] M. Shao, Electrocatalysis in Fuel Cells, Springer, 2015.

[21] J.H. Zagal, M.A. Paez, A.A. Tanaka, J.R.Jr. dos Santos, C.A. Linkous, Electrocatalytic activity of metal phthalocyanines for oxygen reduction, Journal of Electroanalytical Chemistry. 339 (1992) 13–30.

[22] J.H. Zagal, Metallophthalocyanines as catalysts in electrochemical reactions, Coordination Chemistry Reviews. 119 (1992) 89–136.

[23] R.G. Pearson, Absolute electronegativity and hardness correlated with molecular orbital theory., Proceedings of the National Academy of Sciences of the United States of America. 83 (1986) 8440–8441.

[24] R.G. Parr, R.G. Pearson, Absolute Hardness: Companion Parameter to Absolute Electronegativity, Journal of the American Chemical Society. 105 (1983) 7512–7516.

[25] K. Wiesener, D. Ohms, V. Neumann, R. Franke, N4 macrocycles as electrocatalysts for the cathodic reduction of oxygen, Materials Chemistry and Physics. 22 (1989) 457–475.

[26] J.A.R. van Veen, J.F. van Baar, H.A. Colijn, J.G.F. Coolegen, N. de Wit, Oxygen Reduction on Transition-Metal Porphyrins in Acid Electrolyte I. Activity, Berichte Der Bunsengesellschaft Für Physikalische Chemie. 85 (1981) 693–700.

[27] J.A.R. van Veen, C. Visser, Oxygen reduction on monomeric transition metal phthalocyanines in acid electrolyte, Electrochimica Acta. 24 (1979) 921–928.

[28] J. Manassen, A. Bar-Ilan, Metal complexes of phthalocyanine and α,β,γ,δ-tetraphenyl porphyrin as heterogeneous catalysts in oxidative dehydrogenation. Correlation between catalytic activity and redox potential, Journal of Catalysis. 17 (1970) 86–92.

[29] R. Baker, D.P. Wilkinson, J. Zhang, Electrocatalytic activity and stability of substituted iron phthalocyanines towards oxygen reduction evaluated at different temperatures, Electrochimica Acta. 53 (2008) 6906–6919.

[30] Y. Wang, H. Yuan, Y. Li, Z. Chen, Two-dimensional iron-phthalocyanine (Fe-Pc) monolayer as a promising single-atom-catalyst for oxygen reduction reaction: A computational study, Nanoscale. 7 (2015) 11633–11641.

[31] T.S. Olson, S. Pylypenko, J.E. Fulghum, P. Atanassov, Bifunctional Oxygen Reduction Reaction Mechanism on Non-Platinum Catalysts Derived from Pyrolyzed Porphyrins, Journal of The Electrochemical Society. 157 (2010) B54.

[32] A. Trojánek, J. Langmaier, J. Šebera, S. Záliš, J.M. Barbe, H.H. Girault, Z. Samec, Fine tuning of the catalytic effect of a metal-free porphyrin on the homogeneous oxygen reduction, Chemical Communications. 47 (2011) 5446–5448.

[33] I. Hatay, B. Su, M.A. Méndez, C. Corminboeuf, T. Khoury, C.P. Gros, M. Bourdillon, M. Meyer, J.M. Barbe, M. Ersoz, S. Záliŝ, Z. Samec, H.H. Girault, Oxygen reduction catalyzed by a fluorinated tetraphenylporphyrin free base at Liquid/Liquid interfaces, Journal of the American Chemical Society. 132 (2010) 13733–13741.

[34] A. Trojánek, J. Langmaier, B. Su, H.H. Girault, Z. Samec, Electrochemical evidence of catalysis of oxygen reduction at the polarized liquid-liquid interface by tetraphenylporphyrin monoacid and diacid, Electrochemistry Communications. 11 (2009) 1940–1943.

[35] S. Wu, B. Su, Metal-free-porphyrin-catalyzed oxygen reduction at liquid-liquid interfaces, Chemistry - A European Journal. 18 (2012) 3169–3173.

[36] X. Yin, L. Lin, U. Martinez, P. Zelenay, 2,2′-Dipyridylamine as Heterogeneous Organic Molecular Electrocatalyst for Two-Electron Oxygen Reduction Reaction in Acid Media, ACS Applied Energy Materials. 2 (2019) 7272–7278.

[37] A. Facchin, M. Zerbetto, A. Gennaro, A. Vittadini, D. Forrer, C. Durante, Oxygen Reduction Reaction at Single-Site Catalysts: A Combined Electrochemical Scanning Tunnelling Microscopy and DFT Investigation on Iron Octaethylporphyrin Chloride on HOPG, ChemElectroChem. 8 (2021) 2825–2835.

[38] T.H. Phan, K. Wandelt, Redox-activity and self-organization of iron-porphyrin monolayers at a copper/electrolyte interface, Journal of Chemical Physics. 142 (2015) 101917.

[39] J. Maruyama, C. Baier, H. Wolfschmidt, P. Bele, U. Stimming, Enhancement of oxygen reduction at Fe tetrapyridyl porphyrin by pyridyl-N coordination to transition metal ions, Electrochimica Acta. 63 (2012) 16–21.

[40] L. Zhang, K.P. Kepp, J. Ulstrup, J. Zhang, Redox Potentials and Electronic States of Iron Porphyrin IX Adsorbed on Single Crystal Gold Electrode Surfaces, Langmuir. 34 (2018) 3610–3618.

[41] Z.F. Cai, T. Chen, J.Y. Gu, D. Wang, L.J. Wan, Ionic interaction-induced assemblies of bimolecular "chessboard" structures, Chemical Communications. 53 (2017) 9129–9132.

[42] A.N. Marianov, Y. Jiang, Effect of Manganese Porphyrin Covalent Immobilization on Electrocatalytic Water Oxidation and Oxygen Reduction Reactions, ACS Sustainable Chemistry and Engineering. 7 (2019) 3838–3848.

[43] W. T., K. I., M. Z., B.-H. I., B. M., Acid-base and Electrochemical Properties of Manganese meso(ortho- and meta-N-ethylpyridyl)porphyrins: Voltammetric and Chronocoulometric Study of Protolytic and Redox Equilibria, Dalton Transactions. 42 (2013).

[44] O. Ramirez-gutierrez, J. Claret, J.M. Ribo, Cyclic voltammetry of water-soluble manganese porphyrins in the presence of cyclodextrins, (2005) 368–376.

[45] P.R. Bettelheim A., Ozer D., Electrochemical and spectroscopic properties of oligoanilines, J. Chem. Soc., Faraday Trans. 1. 79 (1983) 1555–1564.

[46] R. Zhang, J. Zhang, F. Ma, W.Y. Wang, R.F. Li, Preparation of Mn-N-C catalyst and its electrocatalytic activity for the oxygen reduction reaction in alkaline medium, Ranliao Huaxue Xuebao, Journal of Fuel Chemistry and Technology. 42 (2014) 467–475.

[47] G. Passard, D.K. Dogutan, M. Qiu, C. Costentin, D.G. Nocera, Oxygen Reduction Reaction Promoted by Manganese Porphyrins, ACS Catalysis. 8 (2018) 8671–8679.

[48] C.M. Parnell, B. Chhetri, A. Brandt, F. Watanabe, Z.A. Nima, T.K. Mudalige, A.S. Biris, A. Ghosh, Polydopamine-Coated Manganese Complex/Graphene Nanocomposite for Enhanced Electrocatalytic Activity Towards Oxygen Reduction, Scientific Reports. 6 (2016) 1–12.

[49] N. Garino, M. Castellino, A. Sacco, F. Risplendi, J.A. Munoz-Tabares, M. Armandi, A. Chiodoni, D. Salomon, M. Quaglio, C.F. Pirri, G. Cicero, Proving the existence of Mn porphyrin-like complexes hosted in reduced graphene oxide with outstanding performance as oxygen reduction reaction catalysts, 2D Materials. 6 (2019).

[50] Z. Lu, G. Xu, C. He, T. Wang, L. Yang, Z. Yang, D. Ma, Novel catalytic activity for oxygen reduction reaction on MnN4 embedded graphene: A dispersion-corrected density functional theory study, Carbon. 84 (2015) 500–508.

[51] J. Li, M. Chen, D.A. Cullen, S. Hwang, M. Wang, B. Li, K. Liu, S. Karakalos, M. Lucero, H. Zhang, C. Lei, H. Xu, G.E. Sterbinsky, Z. Feng, D. Su, K.L. More, G. Wang, Z. Wang, G. Wu, Atomically dispersed manganese catalysts for oxygen reduction in proton-exchange membrane fuel cells, Nature Catalysis. 1 (2018) 935–945.

[52] P. Worthington, P. Hambright, R.F.X. Williams, J. Reid, C. Burnham, A. Shamim, J. Turay, D.M. Bell, R. Kirkland, R.G. Little, N. Datta-Gupta, U. Eisner, Reduction potentials of seventy-five free base porphyrin molecules: Reactivity correlations and the prediction of potentials, Journal of Inorganic Biochemistry. 12 (1980) 281–291.

[53] M. Sasayama, Y. Naruta, Importance of Mn-Mn Separation and their Relative Arrangement on the Development of High Catalase Activity in Manganese Porphyrin Dimer Catalysts, J. Chem. Soc. Chem. Commun. (1994) 2667–2668.

[54] S. Zheng, Z. Jiujun, Density functional theory study of transitional metal macrocyclic complexes' dioxygen-binding abilities and their catalytic activities toward oxygen reduction reaction, Journal of Physical Chemistry C. 111 (2007) 7084–7090.

[55] A. van der Putten, A. Elzing, W. Visscher, E. Barendrecht, Redox potential and electrocatalysis of O2 reduction on transition metal chelates, Journal of Electroanalytical Chemistry. 221 (1987) 95–104.

[56] B. Simic-Glavaski, A.A. Tanaka, M.E. Kenney, E. Yeager, Spectroscopic and electrochemical studies of transition-metal tetrasulfonated phthalocyanines, Journal of Electroanalytical Chemistry and Interfacial Electrochemistry. 229 (1987) 285–296.

[57] J. Pavez, M. Páez, A. Ringuedé, F. Bedioui, J.H. Zagal, Effect of film thickness on the electro-reduction of molecular oxygen on electropolymerized cobalt tetra-aminophthalocyanine films, Journal of Solid State Electrochemistry. 9 (2005) 21–29.

[58] C. Zúñiga, F. Tasca, S. Calderon, D. Farías, F.J. Recio, J.H. Zagal, Reactivity indexes for the electrocatalytic oxidation of hydrogen peroxide promoted by several ligand-substituted and unsubstituted Co phthalocyanines adsorbed on graphite, Journal of Electroanalytical Chemistry. 765 (2016) 22–29.

[59] K.M. Kadish, The Electrochemistry of Metalloporphyrins in Nonaqueous Media, Progress in Inorganic Chemistry. 34 (2007) 435–605.

[60] A. Giraudeau, A. Louati, M. Gross, H.J. Callot, L.K. Hanson, R.K. Rhodes, K.M. Kadish, Reduction of Copper Tetracyanotetraphenylporphyrin in Nonaqueous Media. Formation of Copper(I), Inorganic Chemistry. 21 (1982) 1581–1586.

[61] H. Yokoi, A.W. Addison, Spectroscopic and Redox Properties of Pseudotetrahedral Copper(II) Complexes. Their Relationship to Copper Proteins, Inorganic Chemistry. 16 (1977) 1341–1349.

[62] C.P. Tidwell, L. Dalila Fondren, D.E. Nikles, Copper 5,10,15,20-Tetra(N-ethyl-3-carbazolyl) Porphyrin, MolBank. 2011 (2011) 5–8.

[63] N.T.M. Hai, S. Furukawa, T. Vosch, S. de Feyter, P. Broekmann, K. Wandelt, Electrochemical reactions at a porphyrin-copper interface, Physical Chemistry Chemical Physics. 11 (2009) 5422–5430.

[64] Y.M. Zhao, G.Q. Yu, F.F. Wang, P.J. Wei, J.G. Liu, Bioinspired Transition-Metal Complexes as Electrocatalysts for the Oxygen Reduction Reaction, Chemistry - A European Journal. 25 (2019) 3726–3739.

[65] E. Salvadeo, L. Dubois, J.M. Latour, Trinuclear copper complexes as biological mimics: Ligand designs and reactivities, Coordination Chemistry Reviews. 374 (2018) 345–375.

[66] E.I. Solomon, Dioxygen Binding, Activation, and Reduction to H2O by Cu Enzymes, Inorganic Chemistry. 55 (2016) 6364–6375.

[67] S. Gentil, D. Serre, C. Philouze, M. Holzinger, F. Thomas, A. le Goff, Electrocatalytic O2 Reduction at a Bio-inspired Mononuclear Copper Phenolato Complex Immobilized on a Carbon Nanotube Electrode, Angewandte Chemie - International Edition. 55 (2016) 2517–2520.

[68] E.C.M. Tse, D. Schilter, D.L. Gray, T.B. Rauchfuss, A.A. Gewirth, Multicopper models for the laccase active site: Effect of nuclearity on electrocatalytic oxygen reduction, Inorganic Chemistry. 53 (2014) 8505–8516.

[69] M.A. Thorseth, C.E. Tornow, E.C.M. Tse, A.A. Gewirth, Cu complexes that catalyze the oxygen reduction reaction, Coordination Chemistry Reviews. 257 (2013) 130–139.

[70] M. Savy, P. Andro, C.B. et G. Magner, Etude de la reduction de l'oxygene sur les phthalocyanines monomeres polymeres-I. Principes fondamentaux, choix de l'ion central, Electrochimica Acta. 18 (1973) 191–197.

[71] P. Vasudevan, Santosh, N. Mann, S. Tyagi, Transition metal complexes of porphyrins and phthalocyanines as electrocatalysts for dioxygen reduction, Transition Metal Chemistry. 15 (1990) 81–90.

[72] S. Yoshimoto, A. Tada, K. Suto, K. Itaya, Adlayer structures and electrocatalytic activity for O2 of metallophthalocyanines on Au(111): In situ scanning tunneling microscopy study, Journal of Physical Chemistry B. 107 (2003) 5836–5843.

[73] H. Orita, M. Shimizu, C. Nishihara, T. Hayakawa, K. Takehira, Raman spectroscopy and electrochemistry of water-soluble porphyrins at a silver electrode, Canadian Journal of Chemistry. 68 (1990) 787–790.

[74] G. Richards, S. Swavey, Electrooxidation of Fe, Co, Ni and Cu metalloporphyrins on edge-plane pyrolytic graphite electrodes and their electrocatalytic ability towards the reduction of molecular oxygen in acidic media, European Journal of Inorganic Chemistry. (2009) 5367–5376.

[75] L.M. Mink, M.L. Neitzel, L.M. Bellomy, R.E. Falvo, R.K. Boggess, B.T. Trainum, P. Yeaman, Platinum(II) and platinum(IV) porphyrin complexes: Synthesis, characterization, and electrochemistry, Polyhedron. 16 (1997) 2809–2817.

[76] C. Paliteiro, B. Goodenough, S.P. Road, Study of The Electroreduction of Platinum Phthalocyanine of Dioxygen On Thin Films in Alkaline Solutions - Part I. Electrochemical Investigations, J. Electroanal. Chem. 239 (1988) 273–289.

[77] M.X. Chen, L. Tong, H.W. Liang, Understanding the Catalytic Sites of Metal–Nitrogen–Carbon Oxygen Reduction Electrocatalysts, Chemistry - A European Journal. 27 (2021) 145–157.

[78] C. Paliteiro, A. Hamnett, J.B. Goodenough, Cathodic reduction of oxygen by platinum phthalocyanine thin films, Journal of Electroanalytical Chemistry. 160 (1984) 359–367.

[79] C. Paliteiro, A. Hamnett, J.B. Goodenough, The electroreduction of oxygen on thin films of platinum phthalocyanine in alkaline solutions. Part II. Spectroelectrochemical data and mechanism, Journal of Electroanalytical Chemistry. 249 (1988) 167–180.

[80] A. Berkessel, E. Ertürk, P. Kaiser, A. Klein, R.M. Kowalczyk, B. Sarkar, On the redox states of ruthenium porphyrin oxidation catalysts, Dalton Transactions. (2007) 3427–3434.

[81] K.M. Kadish, P. Tagliatesta, Y. Hu, Y.J. Deng, X.H. Mu, L.Y. Bao, Evaluation of Electron-Transfer Sites in Ruthenium(II) Octaethylporphyrin Complexes of the Type (OEP)Ru(CO)(L), Inorganic Chemistry. 30 (1991) 3737–3743.

[82] G.M. Brown, F.R. Hopf, T.J. Meyer, D.G. Whitten, Effect of Extraplanar Ligands on the Redox Properties and the Site of Oxidation in Iron, Ruthenium, and Osmium Porphyrin Complexes, Journal of the American Chemical Society. 97 (1975) 5385–5390.

[83] E.S.S. A, A. Bettelheim, D. Ozer, R. Harth, R.W. Murray, Redox and Electrocatalytic Properties towards Dioxygen reduction of Ruthenium Tetra(Ortho-Aminophenyl) Porphyrin Complexes with Various Axial Ligands, J. Electroanal. Chem, 246 (1988) 139–154.

[84] M. Ravikumar, A. Kathiravan, A. Neels, E.M. Mothi, Tin(IV) Porphyrins Containing β-Substituted Bromines: Synthesis, Conformations, Electrochemistry and Photophysical Evaluation, European Journal of Inorganic Chemistry. 2018 (2018) 3868–3877.

[85] D.P. Arnold, J. Blok, The coordination chemistry of tin porphyrin complexes, Coordination Chemistry Reviews. 248 (2004) 299–319.

[86] A.M. Manke, K. Geisel, A. Fetzer, P. Kurz, A water-soluble tin(iv) porphyrin as a bioinspired photosensitiser for light-driven proton-reduction, Physical Chemistry Chemical Physics. 16 (2014) 12029–12042.

[87] F. Luo, A. Roy, L. Silvioli, D.A. Cullen, A. Zitolo, M.T. Sougrati, I.C. Oguz, T. Mineva, D. Teschner, S. Wagner, J. Wen, F. Dionigi, U.I. Kramm, J. Rossmeisl, F. Jaouen, P. Strasser, P-block single-metal-site tin/nitrogen-doped carbon fuel cell cathode catalyst for oxygen reduction reaction, Nature Materials. 19 (2020) 1215–1223.

[88] A. Facchin, T. Kosmala, A. Gennaro, C. Durante, Electrochemical Scanning Tunneling Microscopy Investigations of FeN4-Based Macrocyclic Molecules Adsorbed on Au(111) and Their Implications in the Oxygen Reduction Reaction, ChemElectroChem. 7 (2020) 1431–1437.

Chapter 6

EC-STM

In this chapter, first of all the physisorption process is taken into exam and its results are presented for all the investigated molecules, for both the employed substrates, HOPG and Au(111). This means that the functionalised surfaces are probed by STM to reveal if a monolayer or multilayers are formed, if ordered layers are obtained, or if the molecules did experience a partial or insignificant adsorption. As a result, the studied molecules revealed the tendency to form mostly ordered monolayers, proving that the functionalisation procedure was optimal for each molecular system.

The ability of EC-STM to couple the STM unit to a bipotentiostat and to work at the solid/electrolyte interface further enhances the type of achievable information. Indeed, EC-STM pictures were systematically collected for each molecular system both with Ar purged and O_2 saturated electrolyte, giving a first mean of comparison to evaluate the presence/absence of the analyte molecule (O_2). Moreover, the presence of a potentiostat permits to "photograph" the behaviour at single molecule level at a precise applied working electrode potential, thereby capturing the fundamental steps of the studied electrocatalytic process.

This chapter is so organised, in order to point out the significant aspects that influence electrocatalysis of oxygen reduction reaction. First, keeping equal the molecular ligand (octaethyl porphyrin) and the substrate (HOPG), the effect of different metals (Fe, Co, Mn, Cu, Pt, Ru, Sn) is explored. This allows to evidence the effect of *d* electrons on the electrocatalysis. Secondly, by using the same metal-porphyrin , the effect of the substrate is analysed. This was attained by comparing images obtained for the same molecule functionalised on different substrates, namely HOPG or Au(111). Although the number of substrates is limited to two, it must be remarked that their nature is significantly different, being HOPG a layered crystal with metallic properties and Au(111) a noble transition metal (sections 4.1 and 4.2). This difference has consequences on the physisorption process and on the catalytic activity towards ORR as well. Finally, the effect of different molecular ligands was explored, considering the same substrate (Au(111)) and the metal centre (Fe), drawing the attention to minor but real dissimilarities in the electrocatalysis as a consequence of a certain chemical environment.

One would wonder what the relevance of EC-STM in the field of electrocatalysis is, but a first undeniable point is that electrode potential exerts a major role and allows to induce reactions which otherwise would not occur. On this regard, EC-STM allows to monitor these reactions at the single-site point of view. Namely, a precise potential can be applied at a working electrode, whose surface at the same time is scanned by the tunnelling tip and images of that specific situation at the electrode surface are obtained. Therefore, EC-STM is often wrongly regarded as a niche technique, but in reality, it can be applied for studying numerous types of reaction at the microscopic level. Upon a quick search on the web, very different examples of applications can be found, like copper oxide formation on Cu(111) and Cu(001), corrosion studies, small molecules reaction (like ORR, OER,

CO_2RR, HER and so on), anion intercalation in HOPG, adsorption layers and passive oxide films on metals, sulphate adsorption on copper, surface reactivity and corrosion mechanisms on metals, polymer electrodes characterisation, soft solution processes investigations, studying of dealloying at the atomic scale [1–9]. Among these very disparate fields of application, finds its place also the topic of this work, the oxygen reduction reaction occurring on metal centres coordinated by porphyrins and phthalocyanines. As already mentioned at the beginning of this introduction, these molecules present self-assembly phenomena which are worth to be studied with EC-STM. What is still under debate is the dynamics involved in the reduction of O_2 molecules. The crucial step which EC-STM is sensitive to is O_2 adsorption/desorption at the catalytic centre. This concept belongs to the field of heterogeneous catalysis, even if this is a subtle term when dealing with systems like those herein presented. A heterogeneous catalyst is held at a different phase (typically solid) with respect to reactants (usually in liquid or gas phase)[10,11]. In this case the solid phase would be constituted by a porphyrin monolayer, and the strict definition of heterogeneous catalyst should be addressed with caution, even if the same system cannot be considered as a homogeneous catalyst, since well-defined molecular species are proven to be physisorbed on the electrode surface. Therefore, the porphyrin-functionalised solid substrates must be considered as peculiar systems, deviating from the classical homogeneous/heterogeneous catalysis concept, and the EC-STM technique helps to determine the real active sites and how they modify during the catalytic process. EC-STM is then the answer to the question on how the catalytic behaviour on metal-nitrogen sites occurs.

6.1 Molecular adlayers on HOPG

All the hereafter presented macrocyclic molecules are able to form supramolecular architectures with a certain ordering extent. These molecules do not possess functional groups able to chemically attach to the substrate surface, so physisorption governs self-assembly at the molecular level. Therefore, there is an interplay of weak non-covalent interactions, in the form of hydrogen bonds, π-π stacking, electrostatic interaction, metal-ligand coordination, van der Walls interactions, hydrophobic interaction [11–22]. These forces exert not only among molecules, but they also involve the substrate. Therefore, the successful attainment of an ordered self-assembled monolayer is the result of a complex interplay between molecules-molecules and molecules-substrate interactions, and it should be thought as of a dynamic process, susceptible to modifications by external factors. Several articles deal with molecules-molecules and molecules-substrate interactions, trying to figure out by computational data how a specific system is governed by these interactions [23–25]. However, due to the complexity and the high degrees of freedom that characterise the herein presented study, no computational data are presented regarding specific porphyrin adsorption on substrates. Indeed, it must be remembered that EC-STM deals with imaging at the solid/liquid interface, where the solvent implies additional interaction phenomena, frequently difficult to be computed. Moreover, in this work charges are also involved, with an electrolyte being employed and a working electrode potential being applied, which brings additional complex aspects to be

considered, an example being the double-layer region described in section 2.6.2. Nevertheless, a qualitative evaluation will always be considered, often basing the obtained results with previously reported articles containing similar molecules or experimental conditions, even if, for the peculiarity of EC-STM, a straightforward data analysis and interpretation is only seldom achieved.

6.1.1 EC-STM investigation of H_2OEP at HOPG

A 0.1 mM octaethylporphyrin solution in DMF was drop-casted on the HOPG surface, letting it functionalise for 30 min and then dry under an argon stream, for a total process of about 60 minutes. Large, ordered domains were obtained, and almost no defects were encountered, indicating that the ethyl substituents are able to enhance the adsorption stability within the graphite basal plane, thereby stabilising the adlayer. Indeed, each -CH_2 of an alkyl chain was found to provide a 70 meV adsorption potential energy gain [26]. Therefore, the longer the alkyl chain, the higher the stabilisation energy, as confirmed for long-chain alkyl substituted phthalocyanines [26,27]. Therefore, alkyl substitution was proven to be a successful method for immobilising nearly planar molecules (like porphyrins and phthalocyanine) on a HOPG basal surface. In fact, it is known that small molecules or even larger molecules but without peripheral substituents, can adsorb on the HOPG surface but at the same time they are also very mobile under the scanning tip, due to the mechanical motion itself or to the high local electric field between tip and sample [26,28].

The unit cell vectors are $\overrightarrow{a_1} = (1.5 \pm 0.1)\, nm$, $\overrightarrow{a_2} = (1.6 \pm 0.1)\, nm$, the angle is $\measuredangle = (110 \pm 2)°$, the surface concentration is $4.43 * 10^{13}\, molecules\, cm^{-2}$ and the corresponding relative surface coverage is $\theta = 0.012$. The determination of surface concentration is based on geometrical arguments and few assumptions should be made to simplify the calculation, giving therefore just an estimation of the real surface molecular packing density.

The fundamental mathematical relation between molecules and substrate can be written as:

$$1\ cell_{OEP} : Xcells_{HOPG} = TOTcells_{OEP} : TOTcells_{HOPG} \qquad 6.1$$

Namely, one octaethylporphyrin unit cell (1 $cell_{OEP}$) will be covering *X* cells of HOPG ($Xcells_{HOPG}$), with *X*>1 since porphyrins are much larger than one HOPG unit cell. Therefore, the total number of molecules will be covering the total number of HOPG surface atoms, but molecules and atoms are connected to the respective number of cells ($TOTcells_{OEP}$ and $TOTcells_{HOPG}$). One octaethylporphyrin cell contains one molecule. The cell area is now calculated for HOPG and OEP. The area of one HOPG unit cell is:

$$A_{HOPG} = 0.246 * 0.246 * sin\ sin\ (60°) = 0.0524\ nm^2 = 5.24 * 10^{-16}\ cm^2 \qquad 6.2$$

The area of one octaethylporphyrin unit cell is:

$$A_{OEP} = 1.5 * 1.6 * sin\ sin\ (70°)\ \ = 2.256 * 10^{-14}\ cm^2 \qquad 6.3$$

The number of HOPG cells underlying one OEP cell is given by the ratio of areas of one OEP cell and one HOPG cell:

$$Xcells_{HOPG} = \frac{A_{cell}^{OEP}}{A_{cell}^{HOPG}} = 43.05 \qquad 6.4$$

The total number of HOPG cells is calculated as the geometrical area exposed by the sample to the electrolyte divided by the area of one HOPG unit cell, assuming that the surface has zero roughness:

$$TOTcells_{HOPG} = \frac{A_{geom}^{HOPG}}{A_{cell}^{HOPG}} = \frac{0.2 * 0.2 * \pi}{5.24 * 10^{-16}\ cm^2} = 2.398 * 10^{14}\ cells \qquad 6.5$$

The total number of OEP cells is calculated by multiplying one OEP unit cell with the total number of HOPG unit cells underlying the one HOPG cell:

$$TOTcells_{OEP} = \frac{1 * TOTcells_{HOPG}}{Xcells_{HOPG}} = 5.57 * 10^{12}\ cells \qquad 6.6$$

Each OEP unit cell contain one molecule, so the total number of OEP unit cells is also the total number of OEP molecules, and upon dividing this total number of molecules for the exposed geometrical area of the sample, one obtains the molecular surface concentration:

$$d_{OEP} = \frac{5.57 * 10^{12}}{0.2 * 0.2 * \pi} = 4.43 * 10^{13}\,\frac{molecules}{cm^2} \qquad 6.7$$

A rough estimation of the relative surface coverage can be obtained by the following expression:

$$d_{HOPG} : \theta_{HOPG} = d_{OEP} : \theta_{OEP} \qquad 6.8$$

The HOPG substrate is the reference, so its coverage is 1:

$$\theta_{OEP} = 0.012 \qquad 6.9$$

The unit cell parameters of H_2OEP adlayer are sketched in figure 6.1.a, where a dashed yellow line is traced to extract the corresponding topographic profile, reported in figure 6.1.b. This topographic profile confirms the bright/dark alternating contrast pertaining to molecular rows. This behaviour can be attributed to the torsion of molecules along a molecular row with respect to molecules in the adjacent row [29,30]. Another possibility is that the molecules are not actually twisted considering two adjacent rows, but that they possess different conformation, namely concave or convex [31]. In the case of a concave

molecule with respect to the surface, the contrast would result brighter, conversely for a convex molecule the STM contrast would result darker.

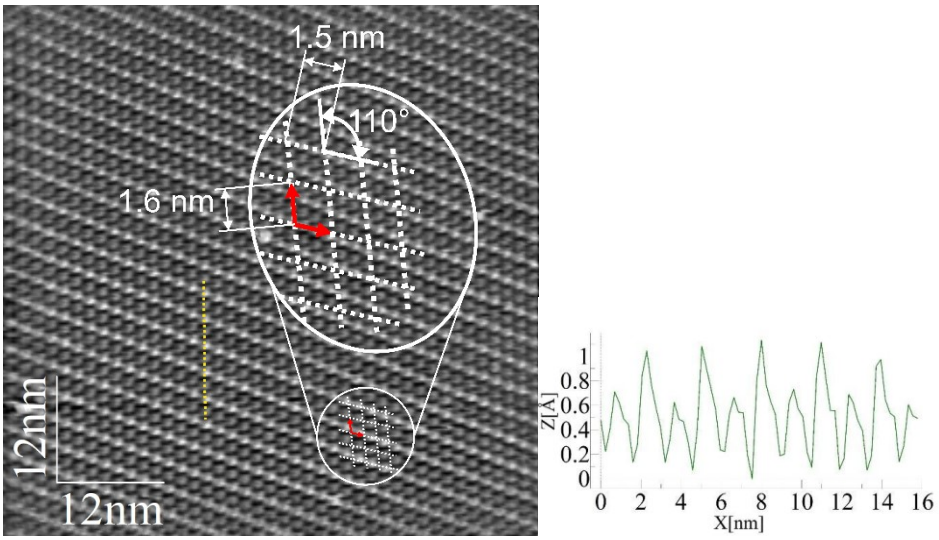

Figure 6.1. Large size EC-STM image of H_2OEP adsorbed on HOPG in deaerated 0.1 M $HClO_4$. Tunnelling parameters are: I_t = 0.7 nA, U_b = -600 mV, E_{app} = 0.55 V vs RHE; b) topographic profile corresponding to the yellow dashed line of figure 6.1.a.

High resolution images of H_2OEP adlayer are reported in figure 6.2. Apart from the aforementioned alternating line contrast, the key point is the STM contrast at the single molecular level. Indeed, each molecule shows a dark spot in its centre, and basing on the working principles of STM described in section 2.4, it is clear that the reason must be reconducted to a depletion of electronic states in this part of the molecule. In fact, in this case the molecules do not host a metal centre, as it will be the case in the next sections, and no reason exists for H_2OEP to show a bright protrusion, as confirmed elsewhere [32–35].

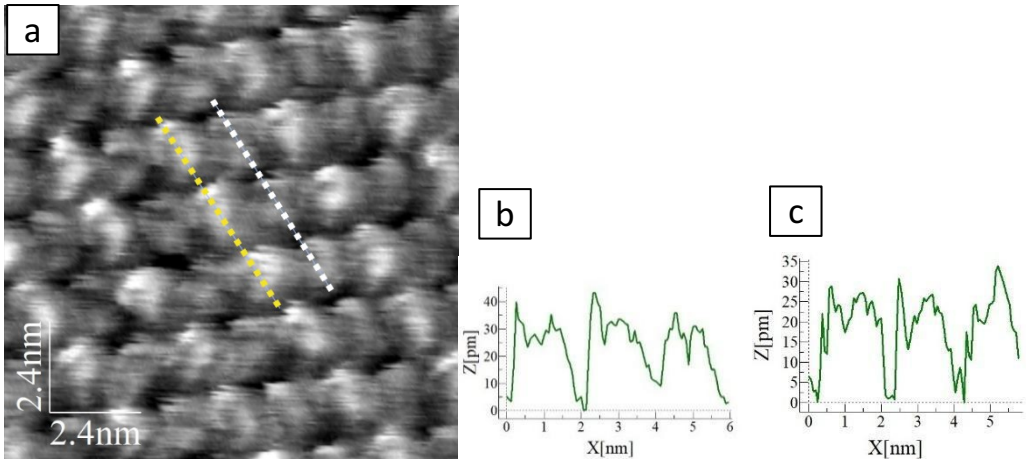

Figure 6.2. (a) High-resolution EC-STM image of H_2OEP adsorbed on HOPG. Tunnelling parameters are: It = 0.72 nA, Ub = - 840 mV, Eapp = 0.50 V vs RHE; topographic profile corresponding to the b) yellow and c) white dashed lines of figure 6.2.a.

The H_2OEP adlayer was further investigated in Ar purged electrolyte under potential control. Precise electrode potentials were applied in the search of changes of contrast upon variation of the applied working electrode potential. The result is shown in figure 6.3. As expected, no changes occur at single molecular level, and the reason can be again reconducted to the absence of a metal centre. The corresponding cyclic voltammetry in section 5.1.1 showed a peak that was attributed to the reduction of the porphyrinato ligand, but the STM response demonstrates that the H_2OEP adlayer is stable in the explored potential window and is not affected by significant desorption.

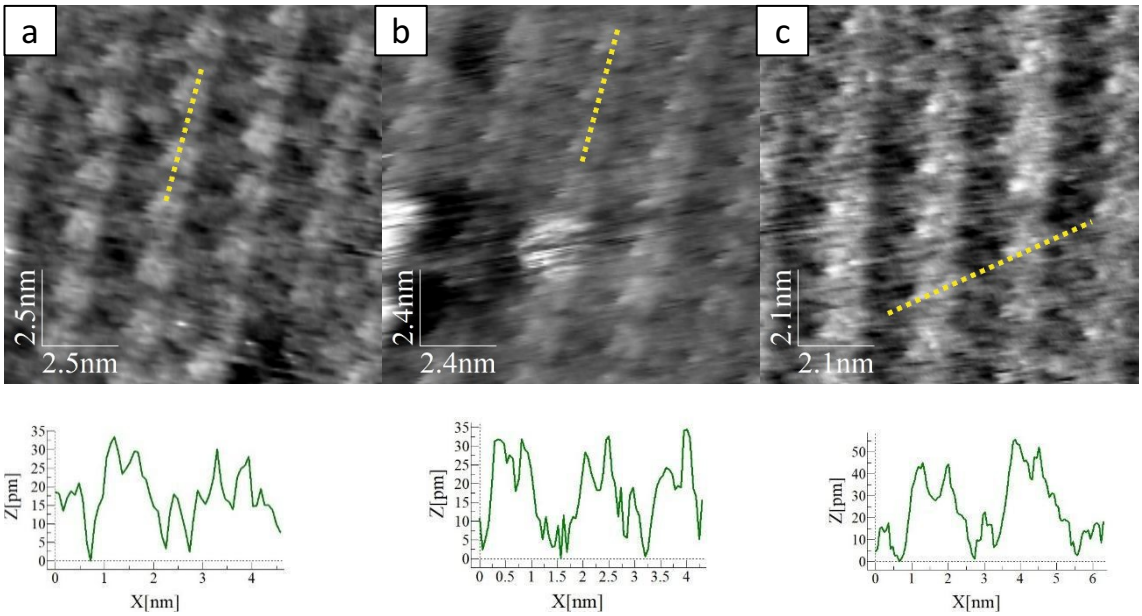

Figure 6.3. Potentiodynamic EC-STM images of H_2OEP adsorbed on HOPG in deaerated 0.1 M HClO4. Tunnelling parameters are: a) It = 0.47 nA, Ub = - 650 mV, Eapp = 0.45 V vs RHE; b) It = 0.47 nA, Ub = -650 mV, Eapp = 0.25 V vs RHE; c) It = 0.47 nA, Ub = -650 mV, Eapp = 0.45 V vs RHE. Topographic profiles corresponding to the yellow dashed lines are reported below the corresponding images.

O_2 was then introduced by bubbling O_2 pure gas in the perchloric acid electrolyte solution. The high-resolution picture, reported in figure 6.4, does not exhibit a significant difference with respect to the Ar saturation case, previously described. The H_2OEP molecules continue to display a dim spot in their centres, indicating that O_2 is not likely to adsorb on the H_2OEP unit.

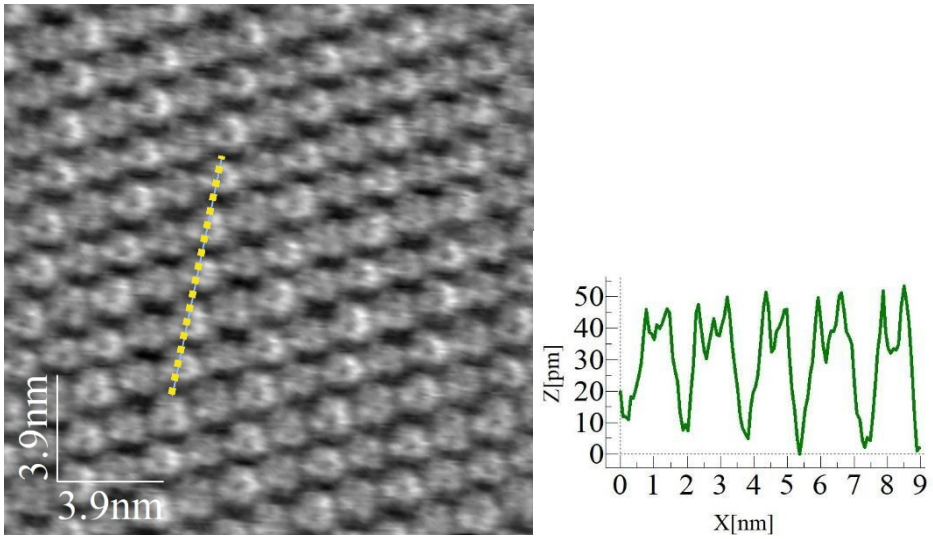

Figure 6.4. High-resolution EC-STM image of H_2OEP adsorbed on HOPG in O_2 saturated 0.1 M $HClO_4$. Tunnelling parameters are: It = 0.72 nA, Ub = - 840 mV, Eapp = 0.50 V vs RHE and topographic profile corresponding to the yellow dashed line.

Despite the fact that corresponding cyclic voltammetry (section 5.1.1) shows a cathodic peak ascribed to oxygen reduction reaction, EC-STM images obtained under potentiodynamic condition do not exhibit features worth to be mentioned. Figure 6.5 contains EC-STM images collected from E_{app} = 0.35 V vs RHE to E_{app} = 0.25 V vs RHE, and in all the figures the layer remains stable, always showing a depression at the centre of the molecules. This indicates that oxygen is not adsorbing on the H2OEP units.

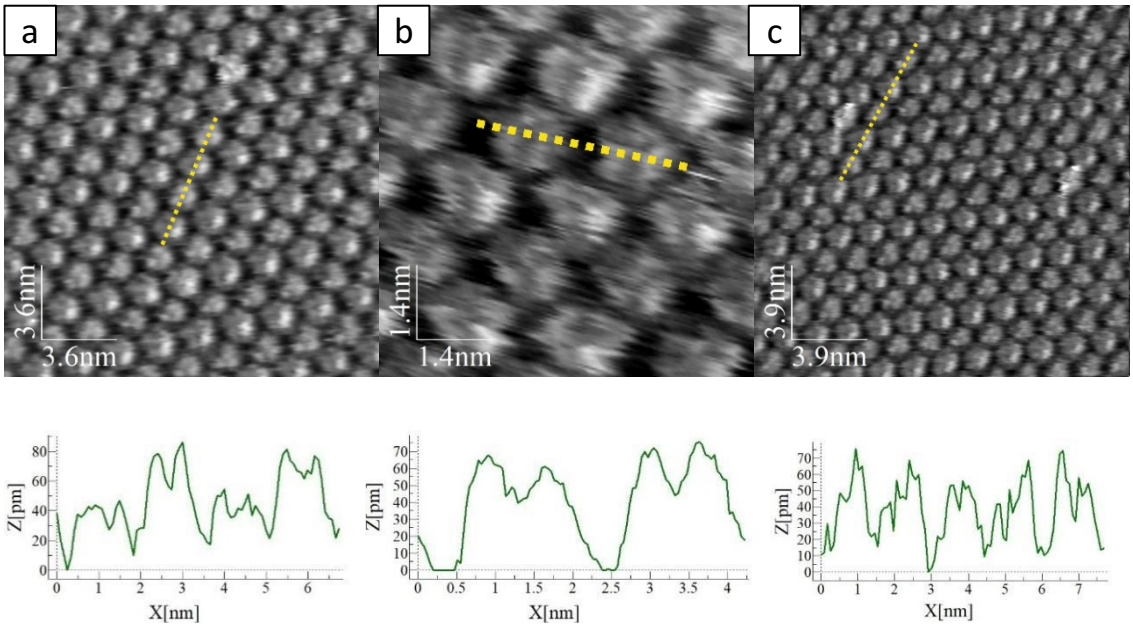

Figure 6.5. Potentiodynamic EC-STM images of H_2OEP adsorbed on HOPG in O_2 saturated 0.1 M $HClO_4$. Tunnelling parameters are: a) I_t = 0.70 nA, U_b = -50 mV vs RHE, E_{app} = 0.45 V vs RHE; b) I_t = 0.70 nA, U_b = -330 mV vs RHE, E_{app} = 0.25 V vs RHE; c) I_t = 0.70 nA, U_b = -50 mV vs RHE, E_{app} = 0.55 V vs RHE. Topographic profiles corresponding to the yellow dashed lines are reported below the corresponding images.

The free-base octaethylporphyrin showed a great tendency to self-assemble on the HOPG surface, with large ordered domains being found elsewhere. A peculiar alternated contrast was observed and ascribed to a slight rotation/torsion of molecules. High resolution pictures proved the existence of a dark depression at the centre of each molecule, fixing a proof of how the STM contrast appears when a metal is absent from the internal porphyrin cavity. The central depression was logically revealed both in Ar and O_2 saturated electrolyte, for the entire investigated potential window, due to the absence of a metal ion. Despite a non-negligible though modest catalytic activity revealed by cyclic voltammetry (section 5.1.1), it was not possible a correlation with EC-STM images, and ORR catalysis occurring at C-N_x sites remains an hypothesis. In the light of the foregoing, H_2OEP will be used as a direct means of comparison with all the following metal-octaethylporphyrins, sometimes also with an intermixed layer experiment.

6.1.2 EC-STM investigation of FeOEP at HOPG

A 0.1 mM Fe(III)-octaethyl porphyrin chloride solution in DMF was drop-casted on the HOPG surface, letting it rest for 30 min and then dry under an argon stream. FeOEP was found to adsorb on HOPG, forming an extended ordered monolayer, as shown in figure 6.6. All the observed molecular domains retain a hexagonal symmetry, evidencing a role of the substrate as templating agent due to its hexagonal surface lattice, too. Indeed, the HOPG surface can be imagined as a graphene layer, with typical honeycomb structure, as already explained in section 4.2. The unit cell parameters are $\overrightarrow{b_1} = (1.5 \pm 0.1)\ nm$ and $\overrightarrow{b_2} = (1.4 \pm 0.1)\ nm$, the measured angle between the two vectors is $\measuredangle = (110 \pm 2)°$. The surface concentration is $5.07 * 10^{13}\ molecules\ cm^{-2}$ and the corresponding surface coverage is $\theta = 0.013$.

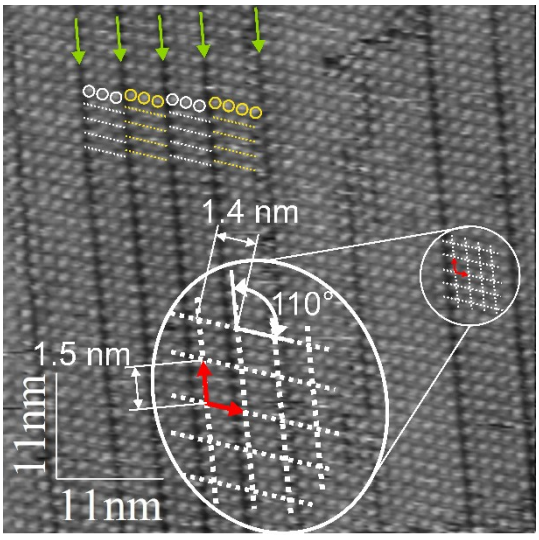

Figure 6.6. Large size EC-STM image of FeOEP adsorbed on HOPG in deaerated 0.1 M $HClO_4$. Tunnelling parameters are: I_t = 0.58 nA, U_b = - 450 mV, E_{app} = 0.65 V vs RHE.

One point that has to be mentioned is the systematic presence of domain boundaries, identified by a larger spacing between adjacent molecular rows, often accompanied by their misalignment, as shown in figure 6.6 with explanatory sketches. White and yellow

circles enclose each one a molecule, and in this case domains large as three or as four molecules are evidenced, but even larger domains can be perceived in the same image. Additionally, the white and yellow dashed lines pass through the centre of each molecule in one domain, and it can be appreciated that there exists a misalignment among white and yellow arrows, and therefore among adjacent molecular domains.

High-resolution images of FeOEP adlayer are reported in figure 6.7. A bright sharp central spot is visible in the centre of each molecule, and the extracted topographic profile confirms a protrusion of ≈150 pm. Having already characterised the STM contrast for a pure layer of H2OEP, it is easy to associate this new contrast feature to the presence of the Fe atom in the centre of OEP. The appearance of iron as a bright spot finds extensive and consolidated confirmation elsewhere [33,36,37].

However, different conjectures can be made about the STM contrast of *d* orbital populated species. If the tunnelling current is mainly LUMO-mediated, then the $3dz^2$ orbital is primarily involved in these first-raw transition metal complexes. If the tunnelling current is mostly HOMO-mediated, the d_{xy}, d_{xz}, d_{yz} orbitals are contributing to the contrast. Finally, the *d* electrons of the central metal could couple with the underlying substrate, causing an enhanced d_z^2 electron density and therefore explaining the protrusion revealed by STM. Even if this possibility should be discarded because HOPG is not featuring *d* electrons, as Au(111) does, another aspect should be taken into account. It is the case of the *surface trans effect*, and it occurs due to the presence of a substrate on which molecules are deposited. Namely, the substrate acts as a ligand for the metal complex functionalised on it. For a traditional metal-centred porphyrin, featuring a metal centre coordinated by four nitrogen atoms, the substrate would play as the "fifth ligand" [38]. It must be specified that the *surface trans effect* slightly differs from the traditional *trans effect*. The latter involves a direct interaction between the metal and the substrate, whereas the former involves an interaction among delocalised electronic states of the surface with those of the metal centre [39]. This effect acquires great relevance because this new coordination gives a new reactivity to the porphyrin molecule, but this effect could also be undesired since it appears, in some cases, to reduce the catalytic activity towards reactions which occur to the supported molecule [38,39]. Although the previous concept was developed specifically for a metal support, a similar behaviour was also observed for a cobalt octaethylporphyrin adlayer on a HOPG slab, whose properties were already discussed in section 4.2. In this case, the "fifth ligand" coordination acted as an electron-donating ligand, increasing the affinity of cobalt to oxygen, thereby increasing the catalytic behaviour of the CoOEP [40,41].

Having considered the impact that the substrate produces on molecular adsorption and its subsequent imaging, the other important factor worth to be further described is the STM response based on the *d* orbital population. UHV-STM studies demonstrated that there is a strong linkage between the number of *d* electrons and the bright/dark STM contrast. d9 and d6 metal centres were in fact imaged as dark spots, whereas d7 and d8 metal centres were visualised as bright protrusions. In first approximation, those metals showing a depression in the STM image behave as insulators, whereas those showing a bright spot

behave as conductors. Cobalt in Co(II) complexes possesses a d7 orbital configuration, which leaves a partially filled $3dz^2$ orbital. This partial occupancy should in principle allow a major number of tunnelling events, therefore explaining the bright contrast in the final image. Conversely, a fully occupied $3dz^2$ orbital like in the case of Cu(II) porphyrins and phthalocyanines, brings to a lower number of tunnelling events and so to a dark STM contrast. The same is valid for d6 and d8 metals, like Fe(II) and Ni(II), respectively.

Although the previous seemed a straightforward argument to explain the STM contrast, it must be remarked that the present work is verting on *in situ* STM measurements, for which additional considerations with respect to UHV were made in section 2.2 explaining the tunnelling mechanisms.

An additional consideration regards the orbital mediated tunnelling spectroscopy (OMTS). In this case, the applied bias voltage is swept from negative to positive values, or vice versa, and the tunnelling current is recorded. Its derivative versus the bias voltage is plotted with the bias voltage itself, and a curve with eventual maxima and minima is obtained. In other words, when the bias voltage is low, electrons elastically tunnel the barrier. When a definite onset bias is reached, electrons start to inelastically tunnel the barrier, a rounded step in the dI/dV vs V curve appears. For a quasi-resonant tunnelling process, where the electron loses almost no energy to the adsorbate, the curve shows a peak. This means that when the energy of the tunnelling electrons matches that of the LUMO (or LUMO+1 and so on) a peak in the dI/dV vs V curve is obtained. This is valid for negative bias values (with respect to the tip, so that electrons travel from the tip to unoccupied sample states), whereas when positive bias values (with respect to the tip) are applied, the same processes occur with the HOMO. The key aspect is that STM images can be correlated with dI/dV curves and significant variations in the STM contrast can be perceived once the applied bias voltages match the values of a dI/dV peak, therefore when specific orbital energies are reached. This means that there is a strict correlation between applied bias voltage and molecular energy levels, and since energy levels change under physical chemical variations (i.e. redox behaviour of the molecule), the STM contrast changes accordingly [42]. A demonstration of the STM contrast dependence from the bias voltage was clearly given by a mixed NiTPP/CoTPP layer. At a negative bias value (-1.4 V) the two components were barely distinguishable, whereas at a different value (-1.0 V) sharp bright spots appeared for the CoTPP units only, due to OMT-involved tunnelling behaviour [43]. Another undeniable example of STM contrast dependence from the applied bias was shown with a mixed H_2TPP, CoTPP, FeTPP adlayer on an Ag(111) substrate. At the bias value U_b=-0.81 V, the free-base tetraphenylporphyrin was imaged with a dark contrast, with a depression at the centre. Fe and Co moieties were indiscernible, with a typical saddle-like shape. The same adlayer at the bias Ub=-0.24 V appeared differently, with the free-base units still exhibiting the dark depression, the Fe-porphyrins still appearing with a saddle shape, but with Co centres now shining with a bright central protrusion [44]. Other remarkable examples exist concerning an intermixed H_2TPP and CoTPP layers on Ag(111)[45], an intermixed H_2TPyP and FeTPyP layer on Ag(111) [32] and a Au(III) tetrapenylporphyrin on Au(111)[46].

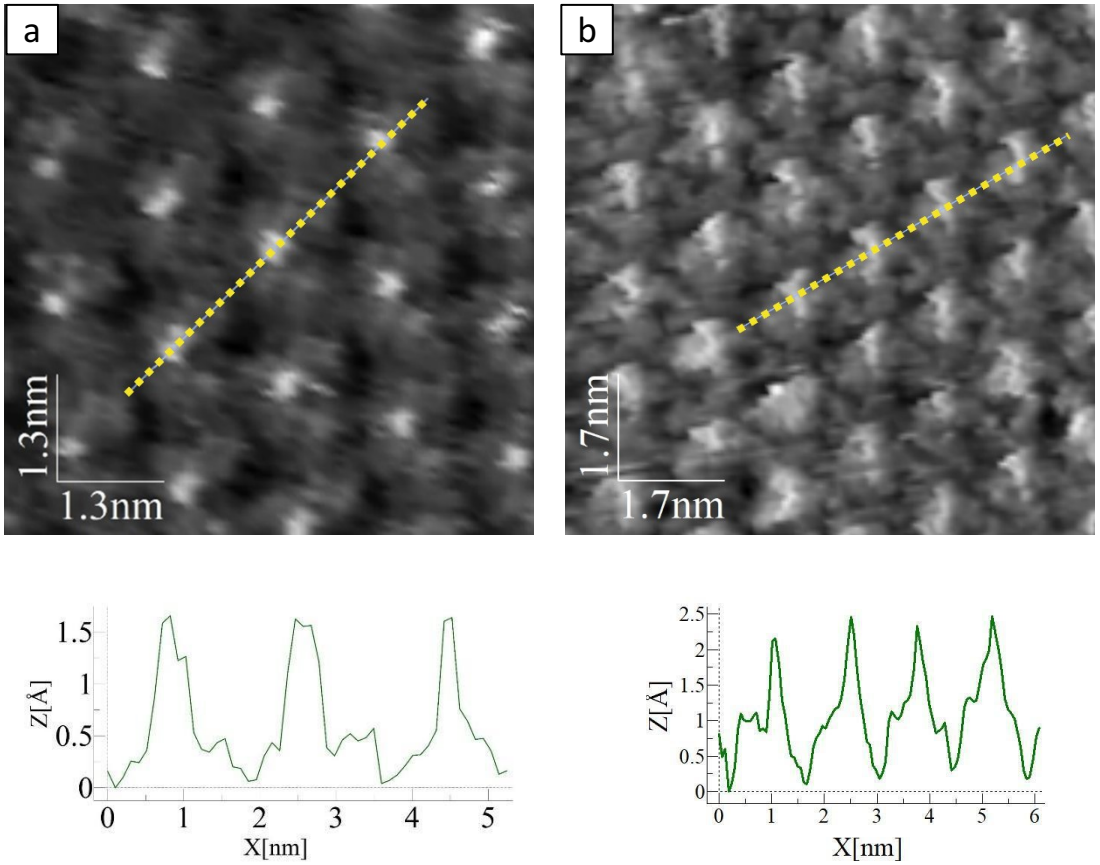

Figure 6.7. high-resolution EC-STM images of FeOEP adsorbed on HOPG in deaerated 0.1 M $HClO_4$. Tunnelling parameters are for both images: I_t = 0.58 nA, U_b = - 450 mV, E_{app} = OCP. Topographic profiles corresponding to the yellow dashed lines of figures 6.7.a and 6.7.b are reported below each image.

FeOEP was then investigated in Ar purged electrolyte under precise electrode polarisation condition. At this purpose, images were purposely collected with a rather small scan size, to achieve a sufficiently high lateral resolution. In this way, sub-molecular features could be distinguished, allowing to really assess the behaviour at the single site level.

In particular, for FeOEP a peculiar experiment was conducted: the FeOEP solution was mixed in equal parts with a H_2OEP one, leading to an intermixed surface coverage of both molecular species, as visible in figure 6.8. The mixed layer provides an interesting way to work with an internal reference. Indeed, the free-base porphyrins was previously characterised both in Ar purged and O_2 saturated electrolyte, and its STM contrast features should have been already elucidated. Thus, dealing with an intermixed layer, besides leading to a new system with potentially different characteristics compared to the single components, is a good means to directly compare in situ two (or more) similar molecular systems, as visible in preceding works [44,45,47,48].

A new structural characterisation was performed, bringing to new unit cell parameters, as follows: $\overrightarrow{b_1} = (1.6 \pm 0.1)\ nm$ and $\overrightarrow{b_2} = (1.6 \pm 0.1)\ nm$, the measured angle between the two vectors is $\measuredangle = (114 \pm 2)°$. The surface concentration is $4.27 * 10^{13}\ molecules\ cm^{-2}$ and the corresponding surface coverage is $\theta = 0.011$.

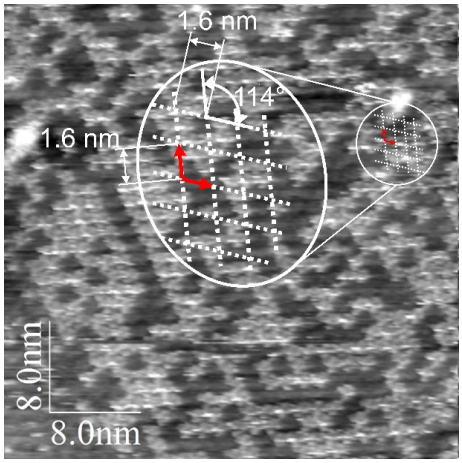

Figure 6.8. Large size EC-STM image of a mixed H_2OEP / FeOEP adlayer adsorbed on HOPG in deaerated 0.1 M $HClO_4$. Tunnelling parameters are: I_t = 0.58 nA, U_b = - 500 mV, E_{app} = OCP.

Having already analysed the potentiodynamic behaviour of the pure H_2OEP adlayer, it is now employed as an internal reference in the intermixed system with FeOEP, which is expected to manifest adsorption features for O_2. Indeed, three significant EC-STM images are reported in figure 6.9. They were collected in Ar purged electrolyte at three different applied working electrode potentials, whose value was chosen based on the cyclic voltammetry previously recorded for FeOEP and reported in section 5.1.2.

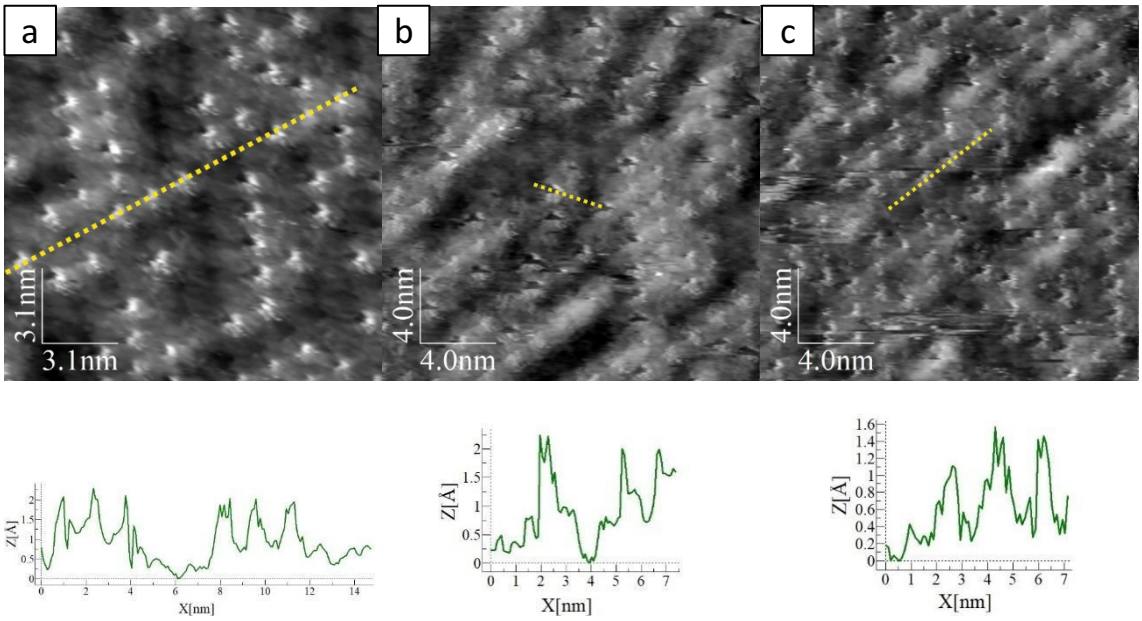

Figure 6.9. potentiodynamic EC-STM images of a mixed H_2OEP / FeOEP adlayer adsorbed on HOPG in deaerated 0.1 M $HClO_4$. Tunnelling parameters are: I_t = 0.7 nA, U_b = - 450 mV, E_{app} = 0.55 V vs RHE; b) I_t = 0.7 nA, U_b = - 350 mV, E_{app} = 0.35 V vs RHE; c) I_t = 0.7 nA, U_b = - 450 mV, E_{app} = 0.55 V vs RHE. Topographic profiles corresponding to the yellow dashed line of figures 6.9.a,b,c are reported below each image.

The H_2OEP molecules can be easily recognised by the darker contrast, and the topographic profile is coherently low and comparable to the case of pure H_2OEP adlayer. At the same time, also FeOEP can be clearly distinguished by the bright central spot, and the topographic profile is in accordance with the one shown in figure 6.7. The starting applied potential, figure 6.9.a, is E_{app}=0.55 V, and Fe retains the (III) oxidation state. When the potential is stepped to Eapp=0.35 V, which is almost corresponding with the peak potential of Fe(III)/Fe(II) , the STM contrast changes and protrusions are substituted by dark spots. The change in oxidation state might explain the change in STM contrast when passing from (III) to (II) oxidation state, and vice-versa. Indeed, when Fe is in (II) oxidation state, an additional electron populates the *d* orbital shell, attaining a d^6 configuration, and the *d* orbital population related contrast issue was already explained at the beginning of this chapter.

The 0.1 M $HClO_4$ electrolyte was saturated with gaseous O_2, and the effects were evaluated with high-resolution images, reported in figure 6.10. Pictures of figure 6.10 differ from images of figures 6.7 and 6.9 (obtained in Ar) for the different contrast of the spot. In this case, it appears larger, less sharp, and shifted from the molecular centre. Moreover, the extracted topographic profile evidences the reduction of almost one order of magnitude in the protrusion height (≈30-40 pm). Even if O2 is an additional feature on the FeOEP molecule, the result is a reduced protrusion, but similar circumstances were already observed at the solid/liquid interface for a CoOEP-functionalised HOPG surface [40] .

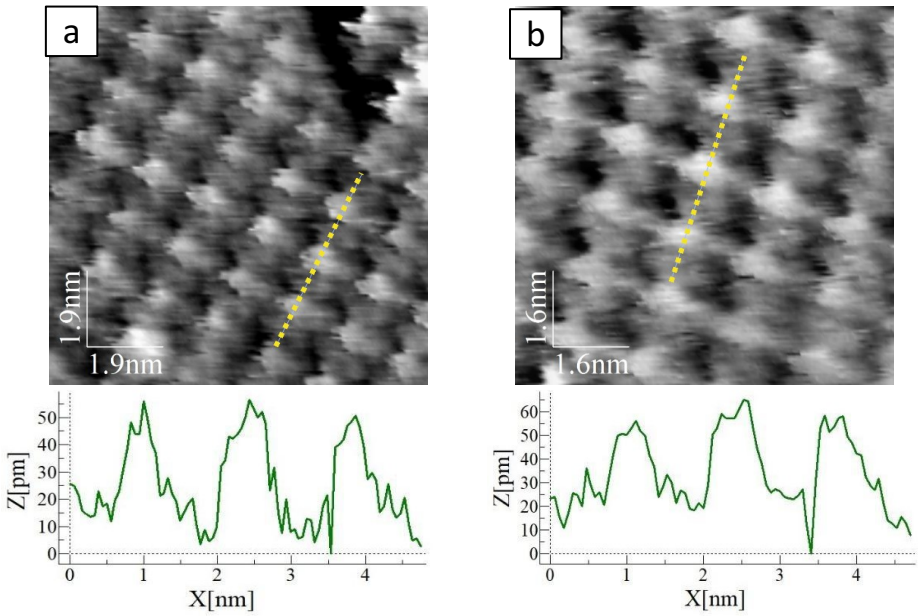

Figure 6.10. high resolution EC-STM images of FeOEP adsorbed on HOPG in O_2 saturated 0.1 M $HClO_4$. Tunnelling parameters for both figures 6.10.a and 6.10.b are: I_t = 0.76 nA, U_b = - 450 mV, E_{app} = 0.50 V vs RHE; topographic profiles corresponding to the yellow dashed lines of figures 6.10.a,b are reported below each image.

The potentiodynamic experiment with intermixed FeOEP/H_2OEP was repeated in O_2 saturated electrolyte. From figure 6.11.a, the selective adsorption of O_2 on the Fe sites can be perceived at sufficiently positive applied working electrode potential (Eapp=0.55 V). Indeed, H_2OEP molecules can still be recognised as the dim molecules, having already characterised their behaviour in the case of a pure H_2OEP adlayer. Conversely, the FeOEP molecules show the expected reduced topographic profile due to the presence of O_2 bonded to the Fe site. At more negative potential, close to the ORR peak potential (Eapp=0.35 V), the STM contrast changes, noise arises and a fuzzy contrast is present, even though single molecules can still be distinguished. In this case, the extracted topographic profiles account for a protrusion around 1.5 Å, comparable to the Ar case. This is compatible with the situation of a oxygen free Fe centre. In fact, from the corresponding CV (section 5.1.2), at this potential ORR is expected to occur and catalytic centres to undergo a continuous turn-over, making it impossible to image a static situation of an adsorbed molecule.

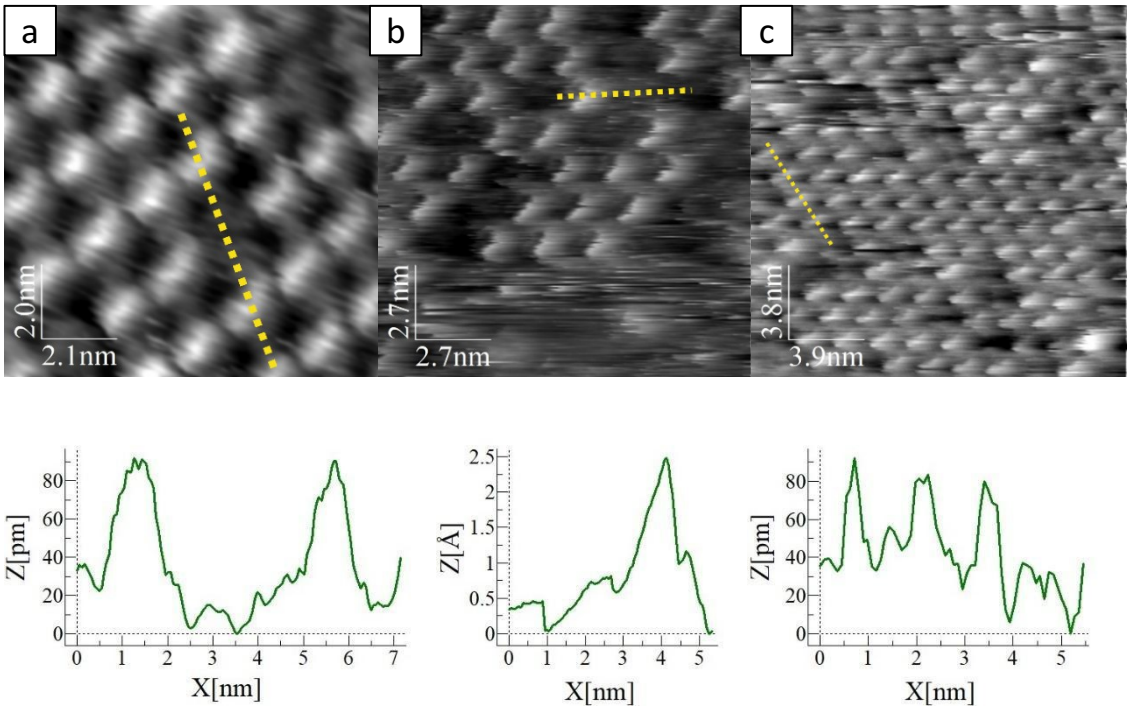

Figure 6.11. Potentiodynamic EC-STM images of a mixed H_2OEP / FeOEP adlayer adsorbed on HOPG in O_2 saturated 0.1 M $HClO_4$. Tunnelling parameters are: a) I_t = 1.00 nA, U_b = - 400 mV, E_{app} = 0.55 V vs RHE; b) I_t = 1.00 nA, U_b = - 350 mV, E_{app} = 0.35 V vs RHE; c) I_t = 1.00 nA, U_b = - 350 mV, E_{app} = 0.55 V vs RHE; topographic profiles corresponding to the yellow dashed lines of figure 6.11.a,b,c are reported below each image.

In conclusion, FeOEP adlayer successfully formed a self-assembled monolayer onto the HOPG surface, but additional defects appeared if compared to free-base octaethylporphyrin, due to the presence of iron which modified molecules-molecules and molecules-substrates interactions. In particular, many domain borders were observed, often accompanied by a molecular mismatch among adjacent domains. Potentiodynamic

imaging in Ar revealed the loss of very bright protrusions at positive applied potential, indicating the change of oxidation state Fe(III)→Fe(II). This was observed on an intermixed layer of FeOEOP with H2OEP. A fundamental correlation between applied bias and number of *d* electrons was established and elucidated, as a necessary tool to interpret STM images of all the metal-complexes hereafter presented.

The presence of oxygen determined a lowering in the protrusion as an indication of O_2 adsorption, with this effect being attributed to a modification of LDOS. Potentiodynamic imaging in O_2 saturated electrolyte proved the reversible nature of O_2 adsorption on the catalytic site.

This study conducted on H_2OEP and FeOEP, presented in sections 6.1.1 and 6.1.2, was thoroughly described in a recently published article [50].

6.1.3 EC-STM investigation of MnOEP at HOPG

A 0.1 mM manganese(III)-octaethyl porphyrin chloride solution in DMF was drop-casted on the HOPG surface, letting it rest for 30 min and then dry under an argon stream. MnOEP was found to adsorb on HOPG, forming extended ordered domains, as shown in figure 6.12. The unit cell parameters are sketched in figure 6.12.c and are: $\overrightarrow{b_1} = (1.6 \pm 0.1)\, nm$ and $\overrightarrow{b_2} = (1.5 \pm 0.1)\, nm$, the measured angle between the two vectors is $\measuredangle = (118 \pm 2)°$. The surface concentration is $4.55 * 10^{13}\ molecules\ cm^{-2}$ and the corresponding surface coverage is $\theta = 0.012$.

However, large size images, reported in figures 6.12.a and 6.12.b, show that the MnOEP adlayer can be characterised by numerous defects (green arrows), especially domain boundaries and molecular aggregates (green circles). The presence of such defects is the result of the interplay of molecules-molecules and molecules-substrates interactions, and the presence of similar bright-dots-contrast was already observed [51–53] .

Actually, macrocyclic molecules like metal-centred porphyrins are suitable to be employed in self-assembly, since their organic part helps to stabilise transition metal atoms and they should prevent clustering into larger aggregates [53]. However, MnOEP shows a deviation from this prediction, hence showing a multitude of domain boundaries, indicated by green arrows in figure 6.12.a and 6.12.b and molecular clusters, indicated by green circles in the same figure. Having already observed the behaviour of the free-base octaethylporphyrin and of Fe(III) octaethylporphyrin (some domain boundaries were also observed), it seems legit to attribute this deviation to the presence of Mn inside the porphyrin cavity, which therefore seems to favour a somewhat stronger molecules-substrate interaction. Molecules are therefore constrained to prefer an anchoring position with respect to other available ones, thereby arising the presence of the aforementioned defects.

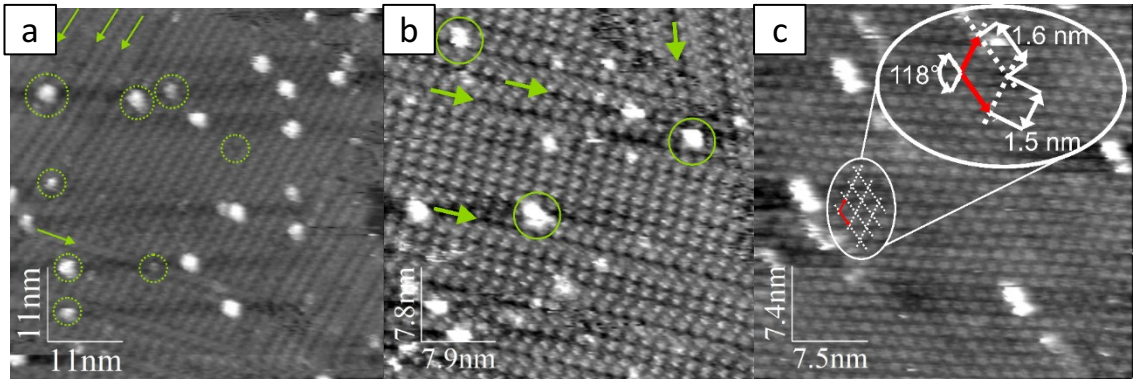

Figure 6.12. Large size EC-STM images of MnOEP adsorbed on HOPG in deaerated 0.1 M $HClO_4$. Tunnelling parameters are: a) I_t = 0.39 nA, U_b = - 700 mV, E_{app} = OCP; b) I_t = 0.47 nA, U_b = - 650 mV, E_{app} = OCP; c) I_t = 0.39 nA, U_b = - 475 mV, E_{app} = 0.45 V vs RHE.

The presence of molecular clusters can be detrimental when focussing on high-resolution pictures in search of changes at single molecular scale, so their presence was systematically analysed under precise potential control. The result is presented in figure 6.13. At applied potential close to the OCP, namely E_{app}= 0.45 V vs RHE, a great number of bright dots and stripes is present over all the scanned surface. Dashed yellow ellipses are sketched to point out some of the mentioned defects. This number seems to increase, rather than diminish, upon lowering the potential up to E_{app}= +0.05 V vs RHE. At this potential, collecting consecutive images, a reduction of these defects can be appreciated, until the surface reaches almost an absence of bright dots. By further lowering the applied potential, E_{app}= -0.15 V vs RHE, the defects completely disappeared. After having swept the potential to E_{app}= +0.35 V vs RHE, a number of defects are again formed. This means that the presence/absence of bright stripes and spots can be ascribed to an intrinsic feature of this molecular system, with molecular clusters being generated or disrupted upon potential control.

The presence of this type of defects did not change even if the functionalisation procedure was tuned by lowering the concentration of the molecule solution in DMF and by reducing and increasing the functionalisation time. Nevertheless, the situation did not positively evolve, confirming once again the intrinsic nature of the molecular cluster appearance, which is therefore judged impossible to avoid fully and intentionally.

After all these observations, it must be remarked that some areas could be found to be almost free of defects. For example, in figure 6.14, the number of initial defects is lower compared to figure 6.13. Again, by lowering the applied potential to E_{app}= +0.05 V vs RHE, the surface becomes free of any defect, and the layer is proved to be stable up to E_{app}= -0.25 V vs RHE, which is quite a negative potential referring to the CV reported in section 5.1.3. The yellow arrows of figure 6.14 at E_{app}= +0.25 V vs RHE indicate the boundaries among different molecular domains.

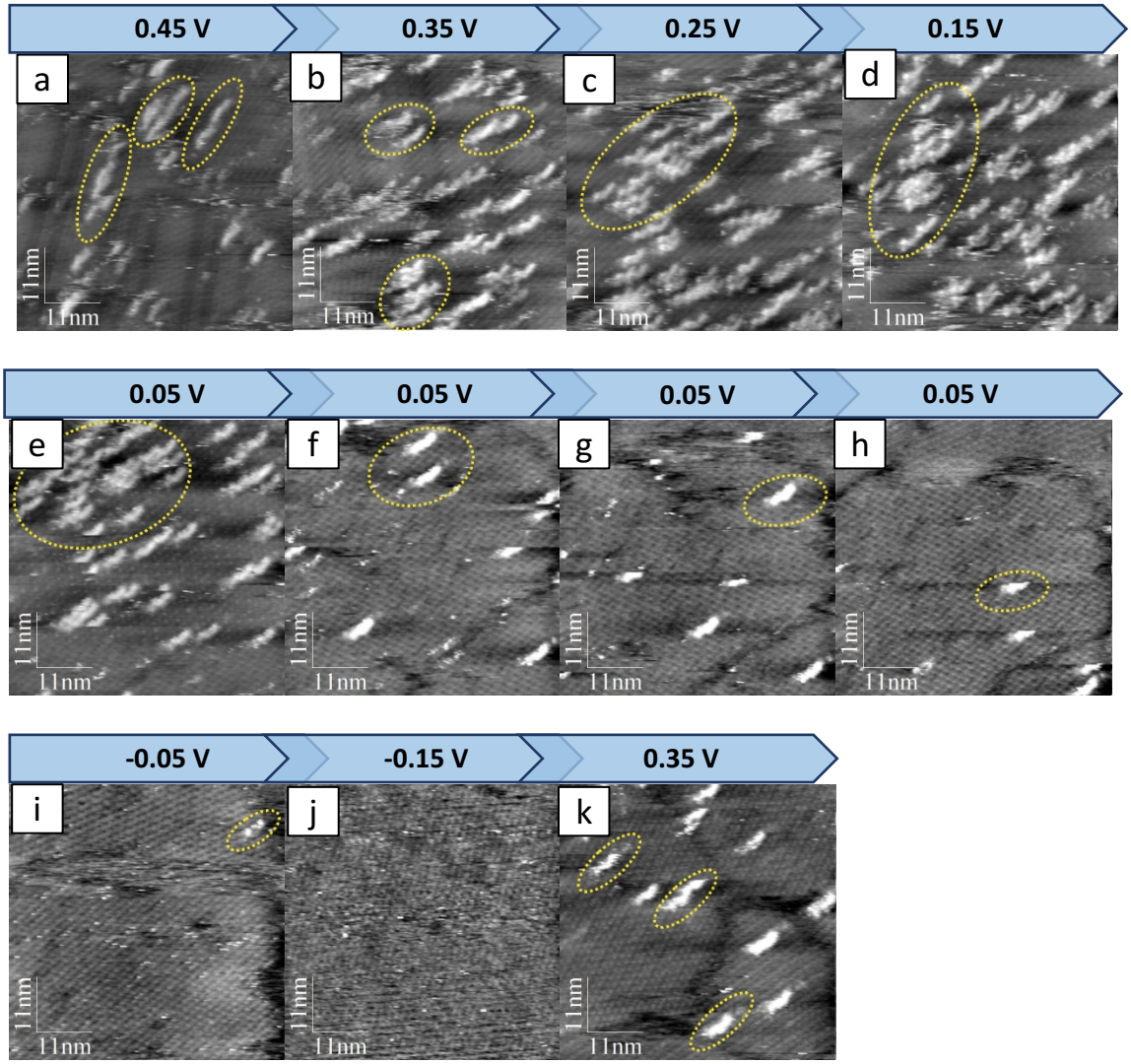

Figure 6.13. Potentiodynamic large-size EC-STM images of MnOEP adlayer adsorbed on HOPG in deaerated 0.1 M $HClO_4$. For all images, tunnelling parameters are: I_t = 0.47 nA, U_b = -0.15 V vs RHE. The applied potential is: a) E_{app}= +0.45 V vs RHE; b) E_{app}= +0.35 V vs RHE; c) E_{app}= +0.25 V vs RHE; d) E_{app}= +0.15 V vs RHE: e-h) E_{app}= +0.05 V vs RHE; i) -0.05 V vs RHE; j) E_{app}= -0.15 V vs RHE; k) E_{app}= +0.35 V vs RHE.

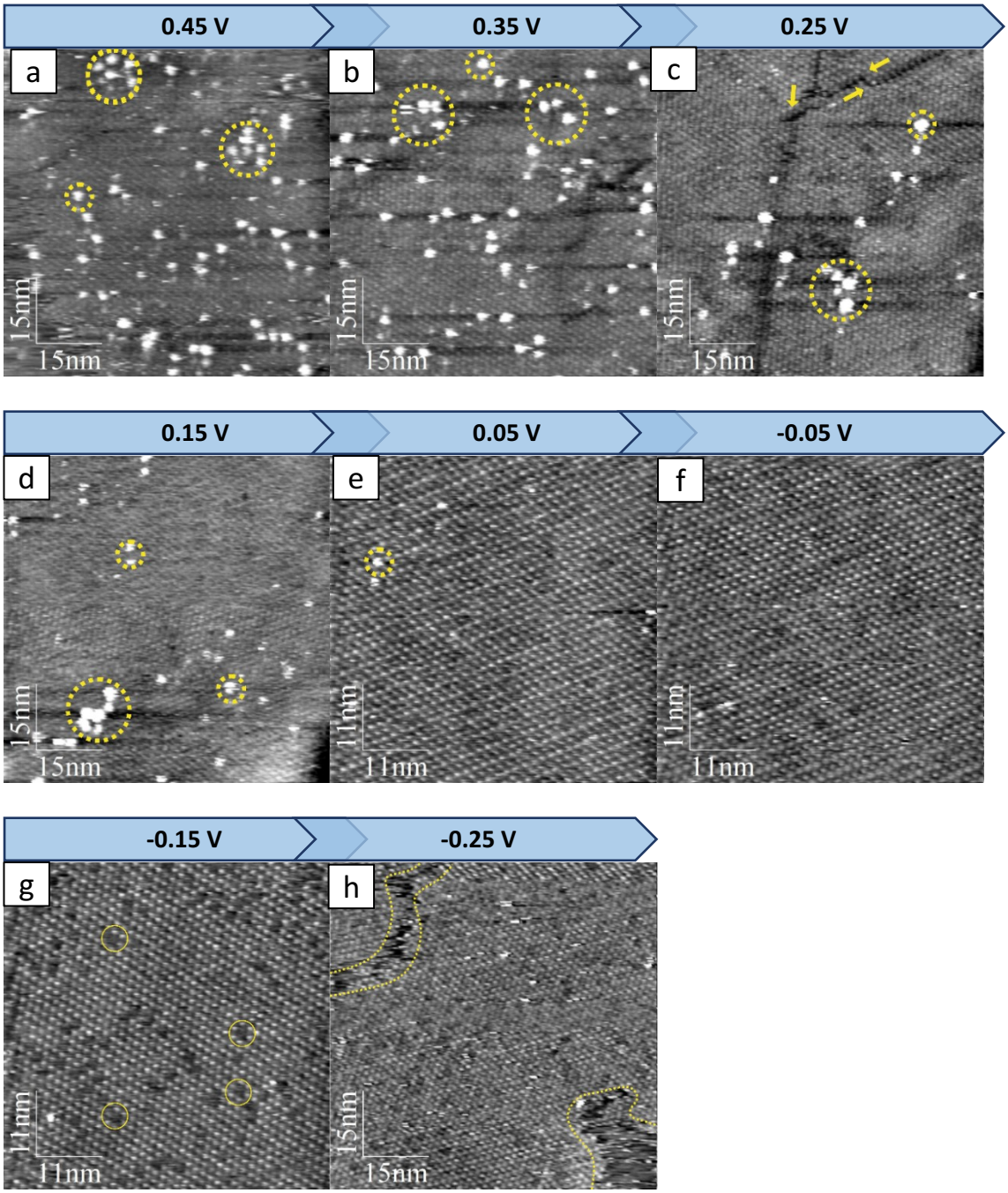

Figure 6.14. Potentiodynamic large-size EC-STM images of MnOEP adlayer adsorbed on HOPG in deaerated 0.1 M $HClO_4$. For all images, tunnelling parameters are: I_t = 0.32 nA, U_b = -950 mV vs RHE. The applied potential is: a) E_{app} = +0.45 V vs RHE; b) E_{app} = +0.35 V vs RHE; c) E_{app} = +0.25 V vs RHE; d) E_{app} = +0.15 V vs RHE; e) E_{app} = +0.05 V vs RHE; f) E_{app} = -0.05 V vs RHE; g) E_{app} = -0.15 V vs RHE; h) E_{app} = -0.25 V vs RHE.

A high resolution STM picture for the MnOEP adlayer is reported in figure 6.15. Molecules appear as propellers, with a bright spot in the centre. The associated topographic profile confirms a protrusion, which is in the order of 50-60 pm. This means that the presence of the manganese atom increases the local density of state, resulting in enhanced tunnelling phenomena compared to the outer part of the porphyrin. Actually,

the presence of a protrusion for manganese porphyrins is not ambiguous, and it was already observed both in UHV [54] and at the solid-liquid interface [55,56]. Both the complexes featuring M(III) or Mn(II) would lead to an unpaired *d* orbital population, which should justify the presence of the bright spot. Another issue concerns the presence/absence of chloride as axial ligand of the Mn centre. Chloride is in fact present in the crystal form of manganese octaethylporphyrin, but it could have been lost during the stage of solubilisation in DMF, or also during the subsequent functionalisation procedure of HOPG. These possibilities had been already formulated for the FeOEP adlayer on HOPG and computational results demonstrated the loss of chloride at the deposition stage, thereby excluding the influence of chloride in determining the final STM contrast. Therefore, an extension of this result seems natural also for the MnOEP case, at least as first hypothesis.

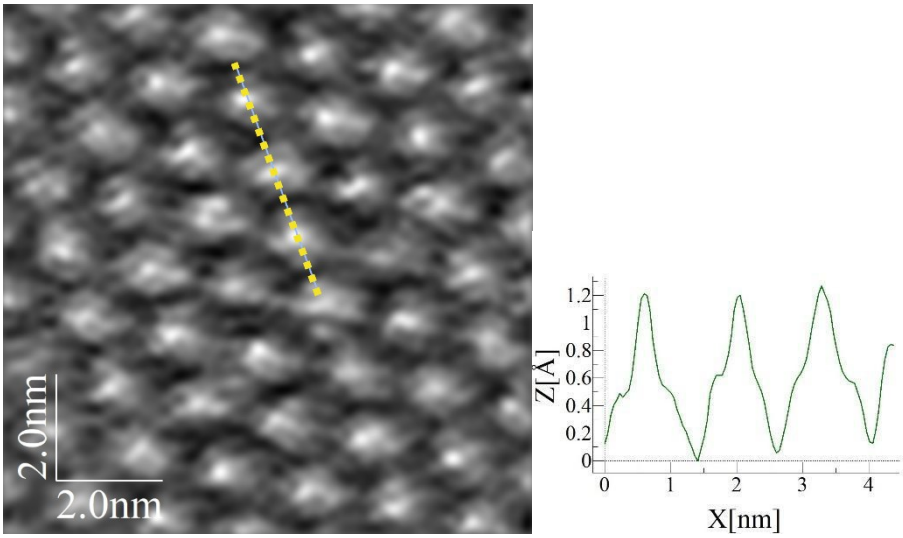

Figure 6.15. High-resolution EC-STM image of MnOEP adsorbed on HOPG in deaerated 0.1 M $HClO_4$. Tunnelling parameters are: I_t = 0.39 nA, U_b = -300 mV, E_{app} = 0.3 V vs RHE. The topographic profile reported on the right corresponds to the yellow dashed lines.

The behaviour of the MnOEP adlayer was investigated under precise applied potential control with high-resolution STM images, reported in figure 6.16, trying to isolate regions sufficiently free of defects. At E_{app}= 0.55 V vs RHE, despite a non-optimal resolution, molecules coherently show a topographic profile of 50-60 pm, in accordance with the previously analysed figure 6.15. The situation is unchanged up to E_{app}= 0.35 V vs RHE, while starting from E_{app}= 0.25 V vs RHE, additional features in the STM contrast start to appear. In fact, two topographic profiles were extracted, one featuring molecules appearing with a darker contrast, another containing brighter contrast molecules. In fact, in the first case the extracted topographic profiles indicate protrusion of 50-60 pm, as already determined. In the second case, higher protrusions were revealed, in the order of 100 pm. These protrusions remain and become predominant at negative applied potential, up to E_{app}= -0.05 V vs RHE. Imaging at high resolution with more negative applied potential was not achieved due to a decrease in the image quality.

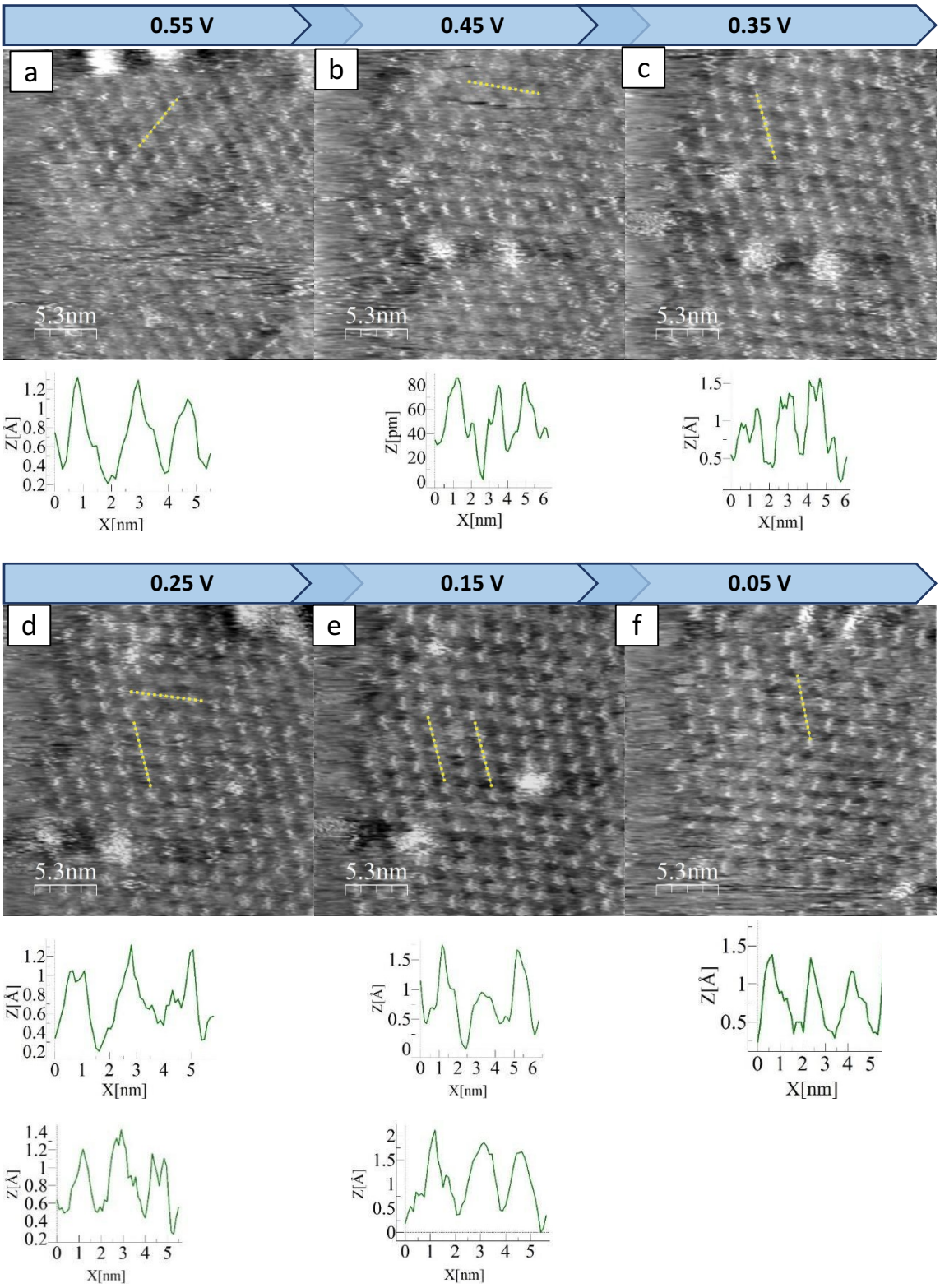

Figure 6.16. High-resolution EC-STM images of MnOEP adlayer on HOPG in deaerated 0.1 M $HClO_4$. For all images, tunnelling parameters are: I_t = 1.5 nA, U_b = -150 mV vs RHE. The applied potential is: a) E_{app} = +0.55 V vs RHE; b) E_{app} = +0.45 V vs RHE; c) E_{app} = +0.35 V vs RHE; d) E_{app} = +0.25 V vs RHE; e) E_{app} = +0.15 V vs RHE; f) E_{app} = +0.05 V vs RHE. Topographic profiles corresponding to the yellow dashed lines of figure 6.16.a-e are reported below each image.

A large scale STM image of the MnOEP adlayer in contact with O_2 saturated electrolyte is reported in figure 6.17 the unit cell parameters are $\overrightarrow{b_1} = (1.6 \pm 0.1)\, nm$ and $\overrightarrow{b_2} = (1.7 \pm 0.1)\, nm$, the measured angle between the two vectors is $\measuredangle = (115 \pm 2)°$. The unit cell vector modules are similar to other herein studied metal-porphyrins and slightly differ from those measured for the same layer in Ar purged electrolyte, thereby indicating a probable effect of drift in the aforementioned parameters.

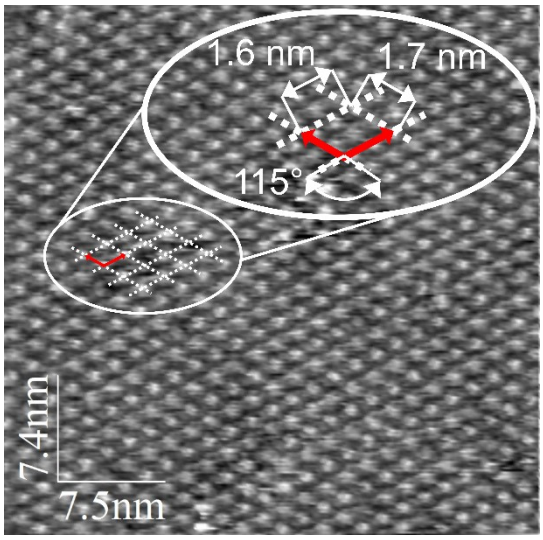

Figure 6.17. Large size EC-STM image of MnOEP on HOPG in contact with O_2 saturated 0.1 M $HClO_4$. Tunnelling parameters are: I_t = 0.47 nA, U_b = -50 mV vs RHE, E_{app} = +0.35 V vs RHE.

A high-resolution picture for the MnOEP adlayer in contact with O_2 saturated electrolyte is reported in figure 6.18. A topographic profile was extracted along the yellow dashed line, and, as a result, the revealed protrusion was in the order of 100 pm. This picture was collected at E_{app} = 0.35 V vs RHE, and the corresponding topographic profile obtained in the Ar saturation case in figure 6.15 was half compared to the O_2 saturation case. This is an indication of the O_2 adsorption at the Mn centre, thereby identifying it as the catalytic site for the oxygen reduction reaction. A "dark" molecule was also imaged, and this could be reconducted to a non-metalated molecule or to a non-O_2 binded Mn centre, considering also that the global protrusion is around 60 pm and therefore compatible with a regular MnOEP unit, as seen in figure 6.15 (Ar saturation case). A similar complex, Mn(III) tetraphenylporphyrin chloride was studied on a Ag(111) surface with UHV-STM, and it was demonstrated that manganese retained chloride as axial ligand, explaining in this way the protrusion revealed in UHV. A depression then appeared after annealing the porphyrin layer thanks to the elimination of chloride. A considerably higher protrusion was then revealed when the layer was exposed to O_2 [54]. More uncertain is the O_2 adsorption geometry: upon visual inspection, *side-on* geometry seems more probable, since no significant displacement of the bright spot from the centre of the molecules is observed. Although Mn-porphyrins were already examined in their ability to bind O_2, one only case exists for the O_2 adduct adsorption geometry, which indeed accounts for a *side-on* binding geometry [57].

Besides some differences in STM contrast and topographic profiles in the Ar saturation case, the behaviour of this manganese porphyrin agrees with previous UHV-STM studies. It must be remarked that the *in situ* experimental condition forces us to consider that deviations are likely to occur with respect to UHV environment, and axial coordination could be (transiently) obviated by aqueous species, like H_2O or ClO_4^-. Although their coordination strength is regarded as one of the weakest, their large abundance in solution could enhance the probability of interaction [58].

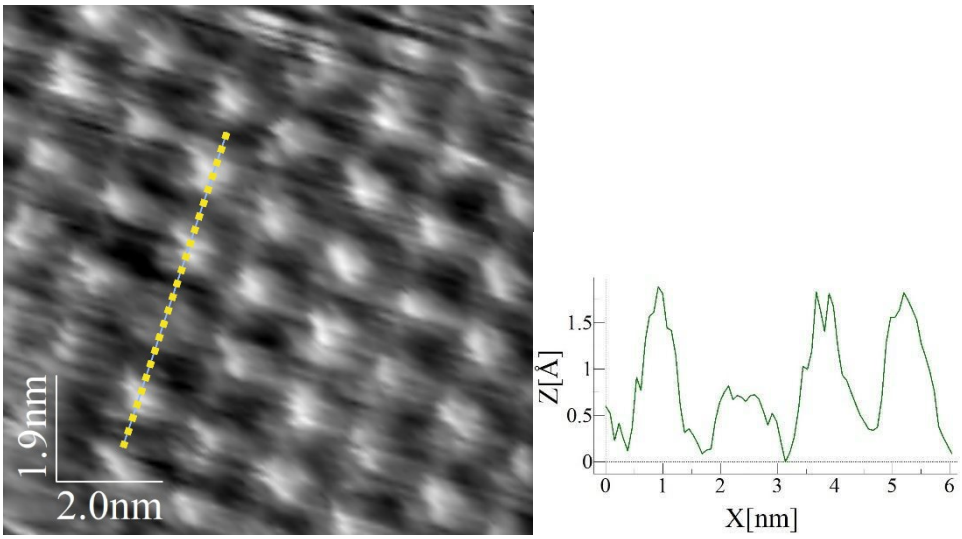

Figure 6.18. high-resolution EC-STM image of MnOEP on HOPG in O_2 saturated 0.1 M $HClO_4$. Tunnelling parameters are: I_t = 0.38 nA, U_b = -900 mV vs RHE, E_{app} = +0.25 V vs RHE. The topographic profile corresponding to the yellow dashed line is reported on the right.

Potentiodynamic imaging was performed on the MnOEP adlayer in O_2 saturated electrolyte. In this case, defects concerning the molecular clusters could not be fully avoided, but images at single molecular levels were in any case obtained, as shown in figure 6.19. Starting at E_{app}= +0.55 V vs RHE, the extracted topographic profile accounts for protrusions of 90-100 pm, in accordance with previously analysed image in O_2 saturated electrolyte, figure 6.18. At E_{app}= 0.45 V vs RHE, the situation is unchanged, while starting from E_{app}= 0.35 V vs RHE the image quality is worsened. Images collected at E_{app}= 0.25 V vs RHE and E_{app}= 0.15 V vs RHE are not reported, due to poor contrast and low resolution. Attempts were made to collect pictures at slightly more negative potential, E_{app}= 0.05 V vs RHE, which is close to the ORR peak potential as determined by CV (Figure 5.13.a chapter 5), and the result is figure 6.19.d. The layer is still stable even with the concurrent ORR. In this last case, the topographic profile shows protrusions of 40-50 pm, which are similar to the MnOEP layer in Ar saturated electrolyte (figure 6.15).

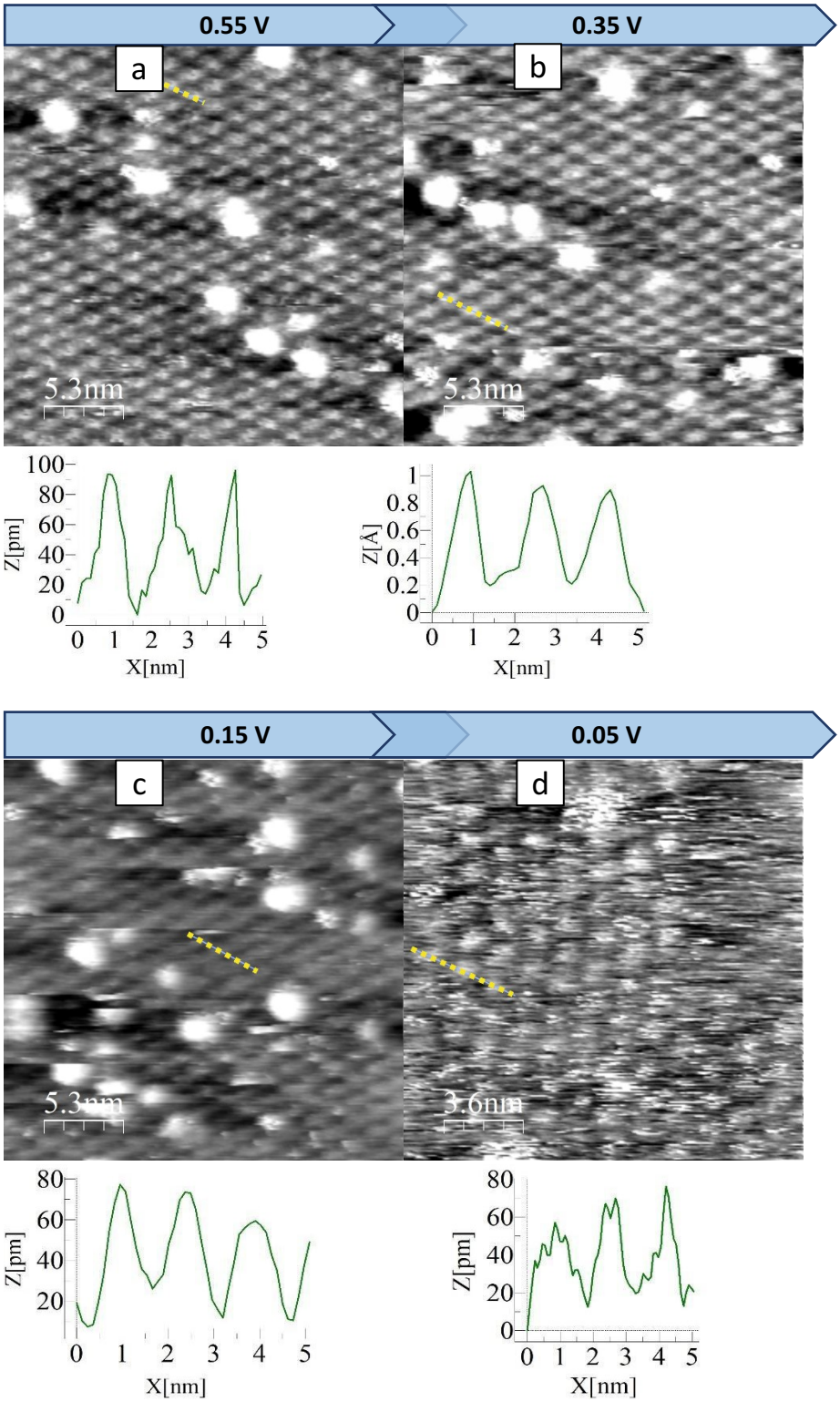

Figure 6.19. Potentiodynamic high-resolution EC-STM images of MnOEP adlayer adsorbed on HOPG in contact with O_2 saturated 0.1 M $HClO_4$. For all images, tunnelling parameters are: I_t = 2.2 nA, U_b = - 150 mV vs RHE. The applied potential is: a) E_{app} = +0.55 V vs RHE; b) E_{app} = +0.35 V vs RHE; c) E_{app} = +0.15 V vs RHE; d) E_{app} = +0.05 vs RHE. Topographic profiles corresponding to the yellow dashed lines of figure 6.19.a-d are reported below each image.

To sum up, MnOEP shows to form ordered layers on the HOGP surface but with a higher number of defects compared to FeOEP. Both domain boundaries and molecular clusters were imaged, frequently mining the attainment of high-resolution pictures. A potentiodynamic study in Ar saturated electrolyte conducted in Ar purged electrolyte demonstrated the applied potential sensitivity to molecular cluster formation/depletion. In O_2 saturated electrolyte, MnOEP showed an increase in the topographic profiles ascribed to O_2 adsorption, differently from the lowering ascertained with FeOEP, and it was attributed to the first step of electrocatalysis, namely O_2 adsorption within a probable s*ide-on* geometry.

6.1.4 EC-STM investigation of CoOEP at HOPG

A 0.1 mM Cobalt (II) octaethylporphyrin solution in DMF was drop-casted on the freshly cleaved HOPG surface and it was let functionalised and dry for a total time of 60 min. Self-assembled ordered monolayers were obtained, even if with minor extent compared to other metal-octaethylporphyrins previously and subsequently presented. In this case it is worth to directly focus on the potentiodynamic imaging of CoOEP in deaerated electrolyte, in particular focussing on a positive applied potential window. Indeed, CoOEP was found to undergo an order/disorder transition based on the applied working electrode potential, and the unit cell parameters are presented accordingly to the different observed structures. The potential at which most of the order/disorder phenomena occur was found to be E_{app}= 0.95 V vs RHE; that corresponds to a redox active area in the cyclic voltammetry of the corresponding CoOEP@HOPG system, and assigned to the Co(III)/Co(II) redox process. Therefore, images recorded at slightly lower and higher potentials are also presented and evaluated. Figure 6.20.a was collected at Eapp= 0.85 V vs RHE, and the corresponding unit cell parameters are sketched. The unit cell vectors are $\overrightarrow{b_1} = (1.4 \pm 0.1)\ nm$ and $\overrightarrow{b_2} = (1.6 \pm 0.1)\ nm$, the measured angle between the two vectors is $\measuredangle = (121 \pm 2)°$. The surface concentration is $5.21 * 10^{13}\ molecules\ cm^{-2}$ and the corresponding surface coverage is $\theta = 0.013$. Therefore, being the measured angle very close to 120°, the adlayer retains a hexagonal symmetry as the HOPG surface. At Eapp= 0.95 V vs RHE, figure 6.20.b, the adlayer seems to change its structure, passing from a completely hexagonal symmetry to a mostly tetragonal one, with an angle closer to 90°, with unit cell parameters becoming $\overrightarrow{b_1} = (1.6 \pm 0.1)\ nm$ and $\overrightarrow{b_2} = (1.7 \pm 0.1)\ nm$, the measured angle between the two vectors is $\measuredangle = (98 \pm 2)°$. The surface concentration is $3.69 * 10^{13}\ molecules\ cm^{-2}$ and the corresponding surface coverage is $\theta = 0.010$. At Eapp=1.05 V vs RHE, figure 6.20.c the adlayer maintains the tetragonal symmetry, with $\overrightarrow{b_1} = (1.5 \pm 0.1)\ nm$ and $\overrightarrow{b_2} = (1.6 \pm 0.1)\ nm$, and measured angle between the two vectors $\measuredangle = (98 \pm 2)°$. The surface concentration is $3.69 * 10^{13}\ molecules\ cm^{-2}$ and the corresponding surface coverage is $\theta = 0.010$.

In figure 6.20.a-c, some examples of monolayer defects are evidenced with green arrows (domain boundaries) and green circles (missing molecules). At Eapp = 0.85 V vs RHE the monolayer is characterised by missing molecules and bi-layer molecules as main defects, where at Eapp = 0.95 V vs RHE and more positive potential, the main defects are

constituted by domain boundaries, and missing molecules as well, while bi-layer molecules are almost absent.

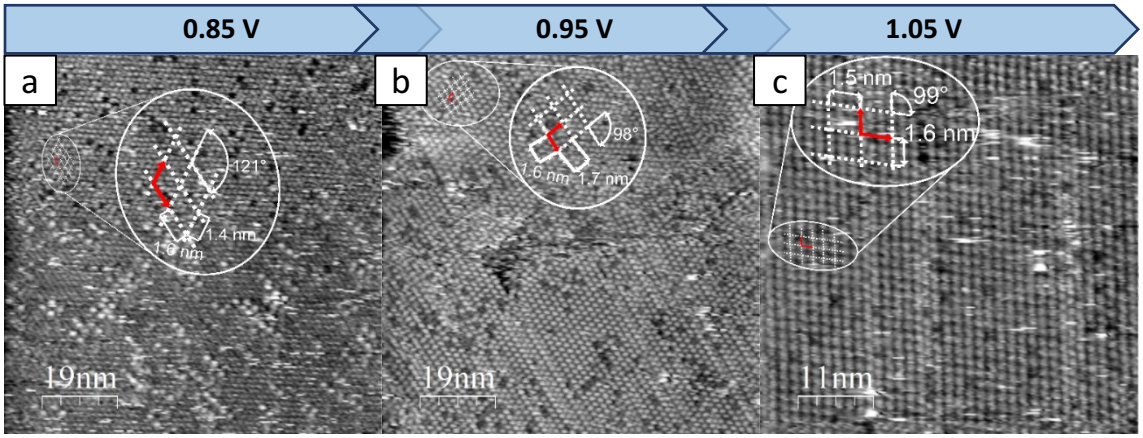

Figure 6.20. EC-STM images obtained under potential control for a CoOEP adlayer adsorbed on HOPG in deaerated 0.1 M $HClO_4$. Tunnelling parameters are: I_t = 0.47 nA, U_b = -350 mV vs RHE. The applied potential is: a) E_{app} = +0.85 V vs RHE; b) E_{app} = +0.95 V vs RHE; c) E_{app} = +1.05 V vs RHE.

Another set of images obtained under precise applied potential variation is reported in figure 6.21. At lower applied potential, E_{app} = 0.85 V vs RHE, the monolayer uniquely presents a hexagonal symmetry, with the following unit cell parameters: $\overrightarrow{b_1} = (1.6 \pm 0.1)\ nm$ and $\overrightarrow{b_2} = (1.4 \pm 0.1)\ nm$, the measured angle between the two vectors is $\measuredangle = (108 \pm 2)°$. The surface concentration is $4.69 * 10^{13}\ molecules\ cm^{-2}$ and the corresponding surface coverage is $\theta = 0.012$. Upon increasing the potential to E_{app} = 0.95 mV, figure 6.21.b, domains of tetragonally arranged molecules start to form, and the corresponding unit cell measures are $\overrightarrow{b_1} = (1.5 \pm 0.1)\ nm$ and $\overrightarrow{b_2} = (1.6 \pm 0.1)\ nm$, the measured angle between the two vectors is $\measuredangle = (92 \pm 2)°$. The surface concentration is $1.52 * 10^{14}\ molecules\ cm^{-2}$ and the corresponding surface coverage is $\theta = 0.040$. Hexagonally arranged domains are still present in the left and top part of figure 6.21.b. Figure 6.21.c was collected few minutes after raising the potential to 200 mV, and it shows that the central tetragonal domain is enlarged, and new tetragonal domains can be observed on the right HOPG layer. A hexagonal domain is maintained on the left HOPG layer. Finally, at E_{app}=1.05 V vs RHE, the tetragonal domains are wider and therefore better stabilised by the more positive applied potential. This type of event could therefore justify the intense reversible absorption peak observed at Eapp = 1.0 vs. RHE, and previously assigned to the Co(III)/Co(II) redox process on the basis of literature comparisons. If this were the case, one could identify the $E_{Co,Ar,red2}$ = 0.28 V vs RHE peak as a metal centre reduction process in agreement also with the observed oxygen reduction process, which falls exactly in this potential windows. Clearly these are hypotheses that need to be consolidated with further and different experiments of a spectro-electrochemical nature.

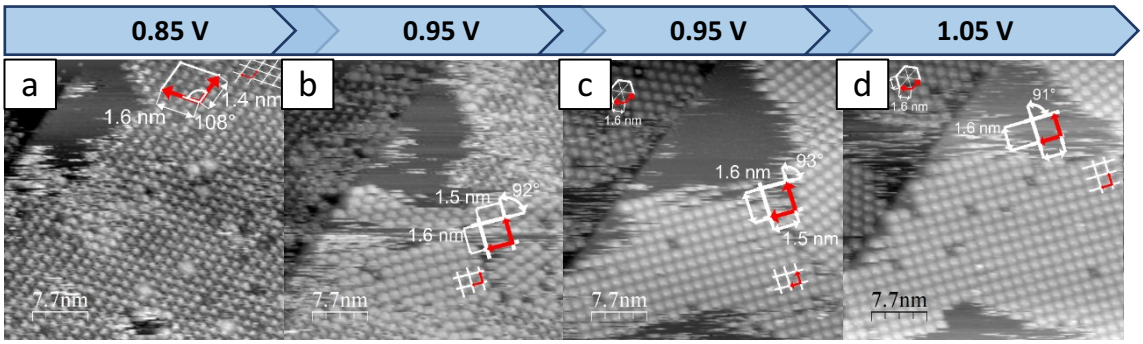

Figure 6.21. Large scale EC-STM images of CoOEP adsorbed on HOPG obtained under potential control in deaerated 0.1 M $HClO_4$. Tunnelling parameters are: I_t = 0.47 nA, U_b = - 150 mV vs RHE. The applied potential is: a) E_{app} = +0.85 V vs RHE; b) E_{app} = +0.95 V vs RHE; c) E_{app} = +0.95 V vs RHE; d) E_{app} = +1.05 V vs RHE.

Order/disorder transitions are delicate processes and can become difficult to properly and systematically analyse, considering the complexity of the phenomenon and the in operando measuring conditions. A successful result in obtaining the final EC-STM images is therefore not granted and requires many trials. Nevertheless, other examples exist that show the occurrence of order/disorder transitions upon variation of the applied electrochemical potential [36,59–63]. All these examples show distinct order/disorder transitions, or a change in the ordering symmetry of the components, and in all cases the explanation is reconducted to the remodulation of surface charges in response of the varied applied potential. In particular, when the potential is swept to more negative values, the surface tends to negatively charge, thereby making electron-rich molecules more mobile on the surface due to electrostatic repulsion. The opposite occurs within a more positive applied potential. It is possible that, upon a certain applied potential variation, a redox process occurs at the metal-porphyrin centre, and this can translate into a different molecular charge distribution, so that a different adlayer geometry or adsorption/desorption phenomena are favoured.

A high-resolution STM picture is presented for CoOEP in figure 6.22. A bright spot was detected at the centre of each molecule, indicating enhanced tunnelling phenomena occurring at the Co centre. Indeed, the half-filled $3d_z^2$ orbital of Co is widely recognised as a favourable tunnelling path for electrons [48,64–66]. The result is therefore a sharp and high protrusion (≈ 100-120 pm), as visible from the topographic profile reported in figure 6.22.

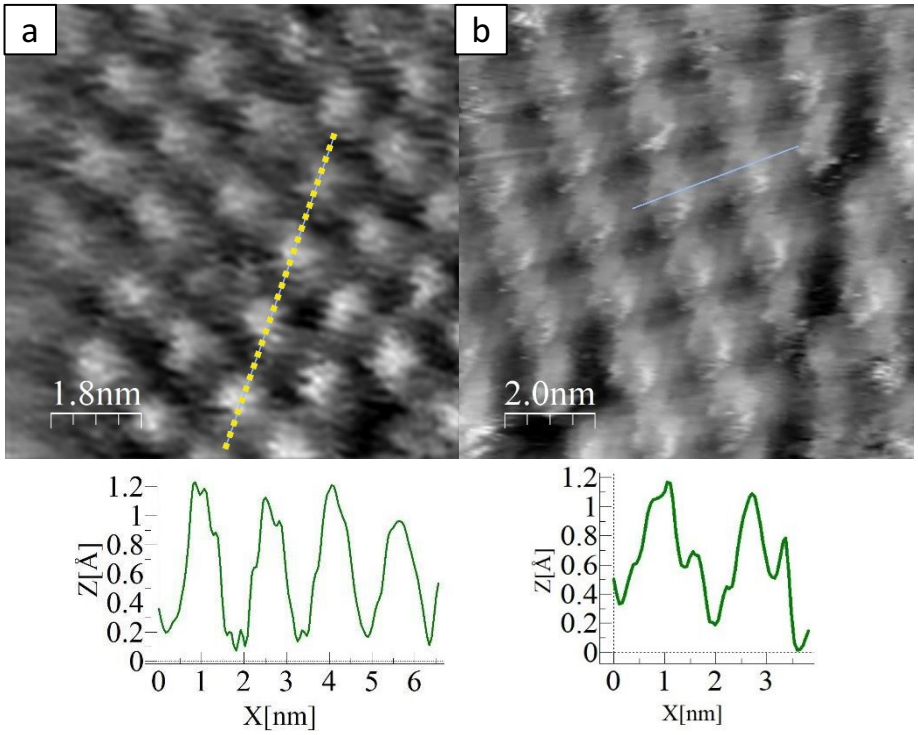

Figure 6.22. High-resolution EC-STM images for CoOEP adsorbed on HOPG in: a) deaerated 0.1 M $HClO_4$ and b) O_2 saturated 0.1 M $HClO_4$. The topographic profiles corresponding to the yellow dashed lines are reported below each corresponding image.

Unfortunately, CoOEP was only partially analysed due to an intrinsic scarce tendency to physisorb on the HOPG surface. In fact, few ordered domains were discovered, with a limited number of high-resolution images being collected. Anyway, a CoOEP@HOPG high-resolution image obtained in O2 saturated electrolyte was collected and reported in figure 6.22b. A drastic change in the topographic profile could be observed, and the topographic profile indicates a protrusion of ≈ 60 pm, which is nearly half of the corresponding value recorded in O2-free electrolyte. CoOEP therefore appears to behave similarly to FeOEP in terms of STM response in presence of adsorbed O_2.

6.1.5 EC-STM investigation of CuOEP at HOPG

A 0.1 mM copper (II) octaethylporphyrin solution in DMF was drop-casted on the freshly cleaved HOPG surface and it was let functionalise and dry for a total time of 60 min. Self-assembled ordered monolayers were obtained, and they were among the SAMs with the lowest number of defects compared to other metal-porphyrins. Only the free-base porphyrin presented a similar defect-free surface, thereby evidencing a strong effect of the central metal in determining the physisorption position. A large-scale image of the CuOEP adlayer on a HOPG substrate obtained in Ar purged electrolyte is reported in figure 6.23, together with sketched unit cell parameters. The layer was found to possess the following unit cell parameters: $\overrightarrow{b_1} = (1.6 \pm 0.1)\ nm$ and $\overrightarrow{b_2} = (1.5 \pm 0.1)\ nm$, the measured angle between the two vectors is $\measuredangle = (124 \pm 2)°$. The surface concentration is $5.03 * 10^{13}\ molecules\ cm^{-2}$ and the corresponding surface coverage is $\theta = 0.013$. The hexagonal symmetry of the HOPG surface therefore reflects on the molecular adlayer

symmetry, which in fact features a measured angle between the unit cell vector close to 120°, indicating a mostly hexagonally arranged molecular array.

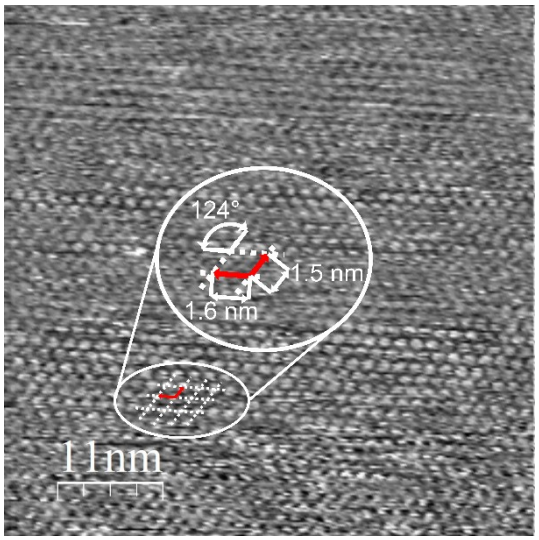

Figure 6.23. Large scale EC-STM image of a CuOEP adlayer adsorbed on HOPG in deaerated 0.1 M $HClO_4$. Tunnelling parameters are: I_t = 2.2 nA, U_b = - 150 mV vs RHE. The applied potential is: a) E_{app} = +0.55 V vs RHE; b) E_{app} = +0.45 V vs RHE; c) E_{app} = +0.35 V vs RHE;

Focussing on high-resolution pictures recorded in deaerated electrolyte, a peculiar feature regarding on-surface molecular arrangement is represented by the twisting of molecules along the molecular rows. In particular, this twisting is schematically drawn in figure 6.24.a, with yellow and red propeller shapes. One can appreciate that yellow shapes describe an angle of 110° with respect to the white dashed molecular row, whereas red shapes have an angle of 99°, meaning that a difference of 20° exists between the two adjacent rows. The twisting phenomenon was not regularly observed, and it is a feature mostly belonging to single domains, rather than to the full SAM. Indeed, in figure 6.24.b only yellow propeller shapes are drawn since no twisting was observed on this molecular domain.

A topographic profile was also extracted, as indicated by the yellow dashed line of figure 6.24.b; in this case, a dark spot is present in the centre of each molecule, as confirmed by the dips of the profile below figure 6.24.b. In cases of lower resolution, no particular spot (neither bright nor dark) could be evidenced. The absence of a bright spot is actually coherent with the electron orbital population of copper.

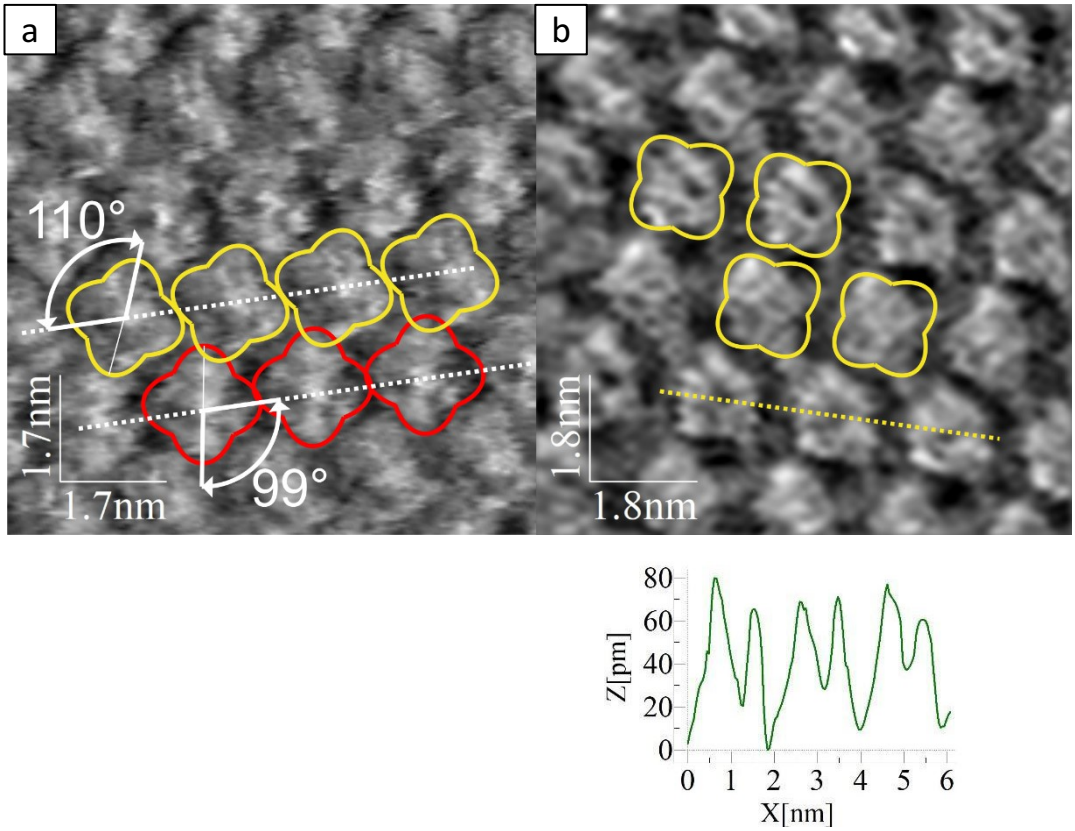

Figure 6.24. High-resolution EC-STM images of CuOEP adlayer on HOPG in deaeated 0.1 M $HClO_4$. Tunnelling parameters are: I_t = 0.47 nA, U_b = - 450 mV vs RHE. The applied potential is: a) E_{app} = +0.65 V vs RHE; b) E_{app} = +0.655 V vs RHE.

The CuOEP adlayer was subjected to potentiodynamic imaging in deaerated electrolyte, to unveil any possible change pertaining to image contrast or adlayer morphology. The result is shown in figure 6.25. At Eapp = 0.55 V vs RHE, figure 6.25.a, the layer is stable and CuOEP unit are coherently visualised with a feeble dark spot in the centre, confirming the depletion of tunnelling phenomena through the copper centres due to their filled *d* orbital shell. The corresponding topographic profile reveals a protrusion in correspondence of the entire molecule, with the profile line remaining flat or following a small depression when passing through the Cu centre. The situation is unchanged up to Eapp = 0.15 V vs RHE: this potential is close to the first reduction peak revealed in cyclic voltammetry in section 5.1.5. That process was ascribed to a porphyrinato ring reduction, retaining Cu no concrete possibilities to undergo reduction to Cu(I). At this potential, figure 6.25.e, molecules appear sharper, even if a true change of topographic profile was not observed. Therefore, it is believed that a sort of redistribution of electronic charge due to porphyrinato reduction might lead to temporary different contrast shapes of the molecules. Upon further reducing the potential, the image quality is worsened, even if individual molecules could be distinctively perceived up to Eapp = -0.15 V vs RHE (figure 6.25.g). Returning to a much more positive applied potential Eapp= +0.65 V, figure 6.25.h, the initial contrast with central depressions is restored.

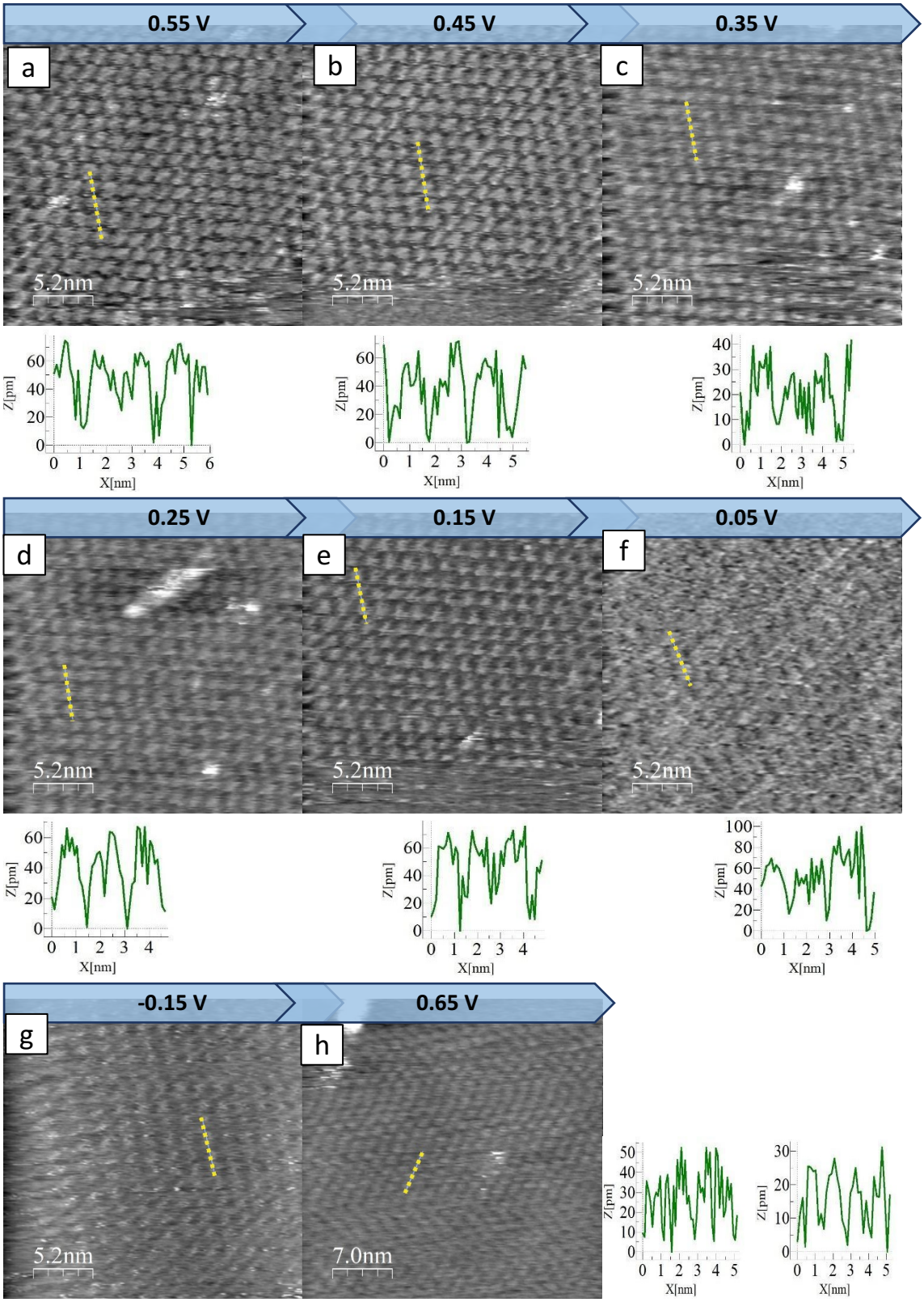

Figure 6.25. Large scale EC-STM images of CuOEP adsorbed on HOPG obtained under potential control in deaerated 0.1 M $HClO_4$. Tunnelling parameters are: I_t = 1.00 nA, U_b = - 250 mV vs RHE. The applied potential is: a) E_{app} = +0.55 V vs RHE; b) E_{app} = +0.45 V vs RHE; c) E_{app} = +0.35 V vs RHE; d) E_{app} = +0.25 V vs RHE; e) E_{app} = +0.15 V vs RHE; f) E_{app} = +0.05 V vs RHE; g) E_{app} = -0.15 V vs RHE; h) E_{app} = +0.65 V vs RHE.

A large area picture of the CuOEP adlayer deposited on HOPG in contact with O_2 saturated electrolyte is reported in figure 6.26. The unit cell parameters are close to the previously determined ones in the case of deaerated electrolyte, so the layers can be considered identical in terms of unit cell parameters.

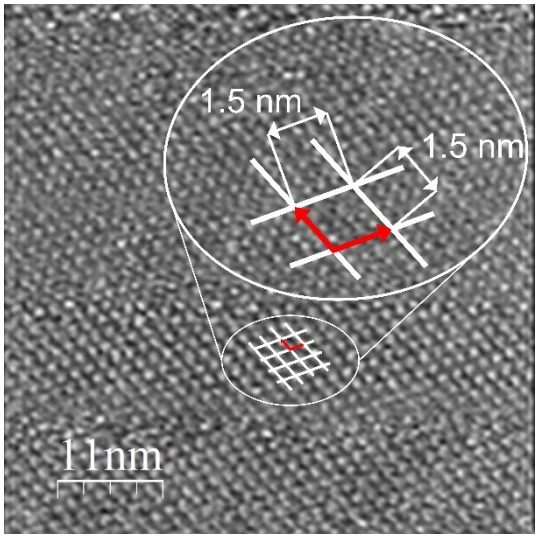

Figure 6.26. large scale EC-STM image of CuOEP adlayer on HOPG in the case of O_2 saturated 0.1 M $HClO_4$. Tunnelling parameters are: I_t = 0.47 nA, U_b = - 900 mV, E_{app} = +0.65 V vs RHE.

An example of high-resolution picture is presented in figure 6.27. The yellow dashed line stands for the extracted topographic profiles, shown on the right side. The STM contrast is mostly unchanged if compared to the high-resolution pictures obtained in Ar purged electrolyte, with no significant spot appearing in the centre of the molecules. Indeed, the topographic profiles obtained in both Ar purged and O_2 saturated electrolyte are rather comparable. This leads to the conclusion that oxygen is not adsorbing on the Cu centres, which in fact were expected not to be active towards oxygen reduction reaction. The reason is readily explained with the poor ability of copper to bind O_2, due to a neglectable backbonding effect [61–63].

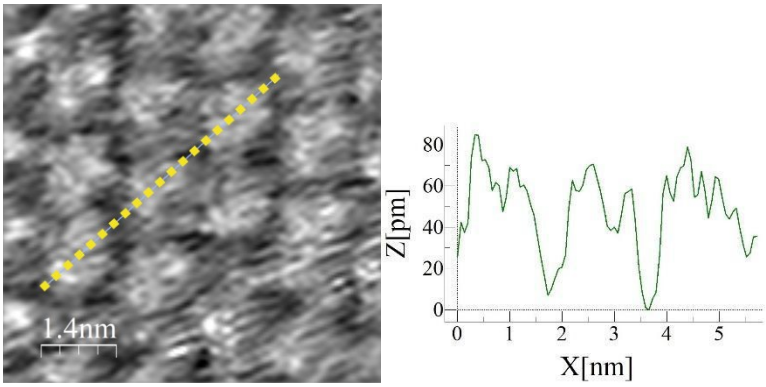

Figure 6.27. High-resolution EC-STM image of CuOEP adsorbed on HOPG obtained in O_2 saturated 0.1 M $HClO_4$. Tunnelling parameters are: I_t = 0.47 nA, U_b = - 900 mV vs RHE, E_{app} = +0.65 V vs RHE.

Potentiodynamic imaging was performed on the CuOEP functionalised HOPG surface (figure 6.28), starting from an applied potential of Eapp= 0.65 V vs RHE. At this potential, molecules are regularly imaged with an empty centre. At Eapp= 0.45 V vs RHE, figure 6.28.b, the situation is unchanged, with a slight loss of resolution. Upon further lowering the applied potential up to Eapp= -0.15 V vs RHE, the contrast seems not to undergo significant changes, even if the cyclic voltammetry of section 5.1.5 was showing a certain but poor activity towards ORR.

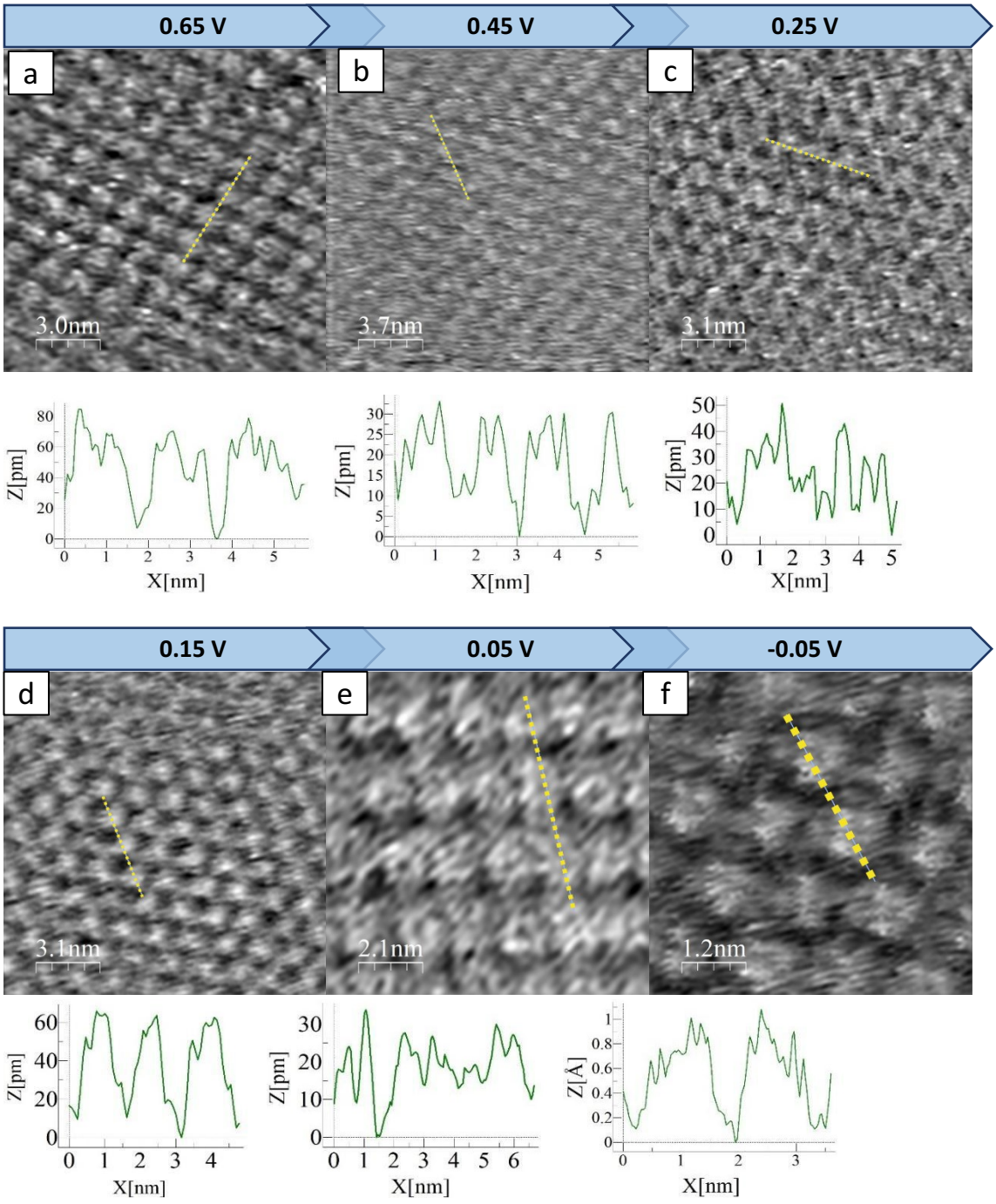

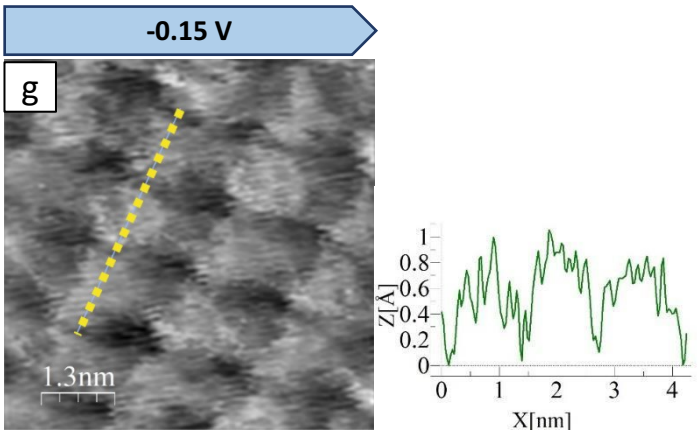

Figure 6.28. High-resolution EC-STM images of CuOEP adsorbed on HOPG obtained under potential control in O_2 saturated 0.1 M $HClO_4$. Tunnelling parameters are: I_t = 0.47 nA, U_b = - 50 mV vs RHE. The applied potential is: a) E_{app} = +0.65 V vs RHE; b) E_{app} = +0.45 V vs RHE; c) E_{app} = +0.25 V vs RHE; d) E_{app} = +0.15 V vs RHE; e) E_{app} = +0.05 V vs RHE; f) E_{app} = -0.05 V vs RHE; g) E_{app} = -0.15 V vs RHE.

Summarizing, copper octaethylporphyrin, like the corresponding free-base counterpart, presented large, ordered domains with almost no defects being detected. Moreover, it confirms the relevance of a subtle interplay between molecules-molecules and molecules-substrate interactions, whose impact and result should be evaluated case-by-case. From high resolution pictures of CuOEP, it emerged that molecules are characterised by a rather flat profile, and sometimes depressions are more pronounced. This is in accordance with previously reported literature, confirming the role of *d* electrons in determining the STM contrast. In this case, a fully occupied $3dz^2$ orbital led to a total absence of bright protrusions. This has also chemical consequences, in the sense that Cu was also incapable of binding O_2, explaining why EC-STM images collected in O_2 saturated electrolyte are almost featureless.

6.1.6 Intermixed CuOEP / CoOEP layer

A particular sample was prepared, in which cobalt and copper octaethylporphyrin were simultaneously placed in contact with the clean Au(111) surface, with the intention to produce a mixed adlayer consisting of the two metal porphyrins. This experiment resembles the one described in section 6.1.2 featuring iron octaethylporphyrin and the free-base counterpart. In this case, too, copper octaethylporphyrin could be figured out as an internal standard, since its behaviour was already thoroughly described in section 6.1.5. Moreover, the mixed system can provide additional properties, which the single molecules did not exhibit, both in terms of molecular adlayer stability and electrochemical performances. In this case, an enhanced stability was revealed considering the adlayer of pure CoOEP and the mixed one CoOEP / CuOEP.

The unit cell parameters of this mixed layer are: $\overrightarrow{b_1} = (1.6 \pm 0.1)\, nm$ and $\overrightarrow{b_2} = (1.5 \pm 0.1)\, nm$, the measured angle between the two vectors is $\measuredangle = (123 \pm 2)°$. The surface concentration is $4.97 * 10^{13}\ molecules\ cm^{-2}$ and the corresponding surface

coverage is $\theta = 0.013$. The hexagonal symmetry of the HOPG surface therefore reflects on the molecular adlayer symmetry, which in fact features a measured angle between the unit cell vector close to 120°, indicating a mostly hexagonally arranged molecular array.

At a first glance, the two molecules can be easily distinguished. Cobalt is actually ascribed to the brighter molecules appearing in figure 6.29, while copper is associated with the darker molecules in the same figure. This contrast is coherent with the one evidenced for the corresponding pure adlayers (section 6.1.4 and 6.1.5).

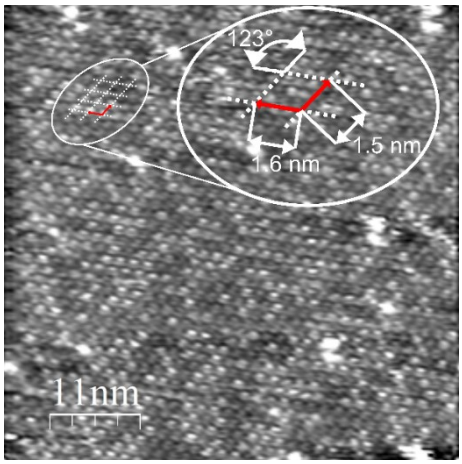

Figure 6.29. large scale EC-STM image of intermixed CuOEP / CoOEP adlayer on HOPG in the case of deaerated 0.1 M $HClO_4$. Tunnelling parameters are: I_t = 0.47 nA, U_b = - 250 mV vs RHE, E_{app} = +0.75 V vs RHE.

Imaging at precise electrode potential control was performed in deaerated electrolyte, with the following results being presented. At E_{app} = 0.75 V vs RHE, the surface shows few bright dots as defects, which are attributed to molecular clusters, as already discussed for MnOEP in section 6.1.3. An example of these is marked with a green solid circle in each of the following images featured in figure 6.30. The layer displays both bright and dark molecules, according to the previously described presence of both cobalt and copper octaethylporphyrins. The potential is then lowered to E_{app} = 0.65 V vs RHE, and defects of molecular clusters still are present. The contrast of cobalt and copper porphyrins did not significantly change, maintaining the bright/dark contrast for cobalt and copper. The number of molecular clusters seemed not to significantly change, as well. A loss of contrast occurs at potentials between 0.45 and 0.25 V vs RHE, and more specifically the difference between bright and dark molecules is faintly noticeable. According to cyclic voltammetry of CoPEP and CuOEP, section 5.1.4 and 5.1.5, this potential region roughly corresponds to the reduction of the porphyrinato ring. However, it must be stated that also a temporary loss of resolution could have been occurred, due to continuous collection of STM images. When E_{app} reaches the value of 0.05 V vs RHE, the distinction between cobalt and copper (bright and dark, respectively) could be again clearly perceived. Basing on the above consideration, this can be the outcome of two different possibilities. The first is that at sufficiently low potential the cobalt porphyrins are all reduced from Co(III) to Co(II). As we said before the assignation of Co(III)/Co(II) is anything but

straightforward, since it was done principally following literature indications, but if the main redox process for CoOEP, that falls around E_{app} = 1.0 vs. RHE is, as we said, associated with the change in the adsorption process from hexagonal to tetragonal, then the redox processes recorded between 0.5 and 0.00 V vs RHE must somehow also involve the reduction of the metal centre and this could also explain why oxygen reduction only occurs in these potential ranges. The second is that the resolution of the tip positively changed, leading to better resolved images which allowed the distinction between cobalt and copper. A second loss of resolution occurs when the potential is swept to positive values, like E_{app} = 0.85 V vs RHE. In this case, a general noise covers the image, making it impossible to distinguish single molecules. Upon returning to the initial E_{app} = 0.75 V vs RHE, the surface is again stabilised, bright and dark molecules could be imaged, but a higher number of molecular clusters, indicated also with green circles, appears. This can be thought as a consequence of the positive potential sweeping, which probably caused a weakening in the molecules-substrates forces and made molecules mobile above the HOPG surface, facilitated also by the action of the tip. In fact, when finally returning to E_{app} = 0.75 V vs RHE, stability of the layer is restored, noticing that a higher number of molecular cluster had formed, and the green circle encloses more than one bright spot.

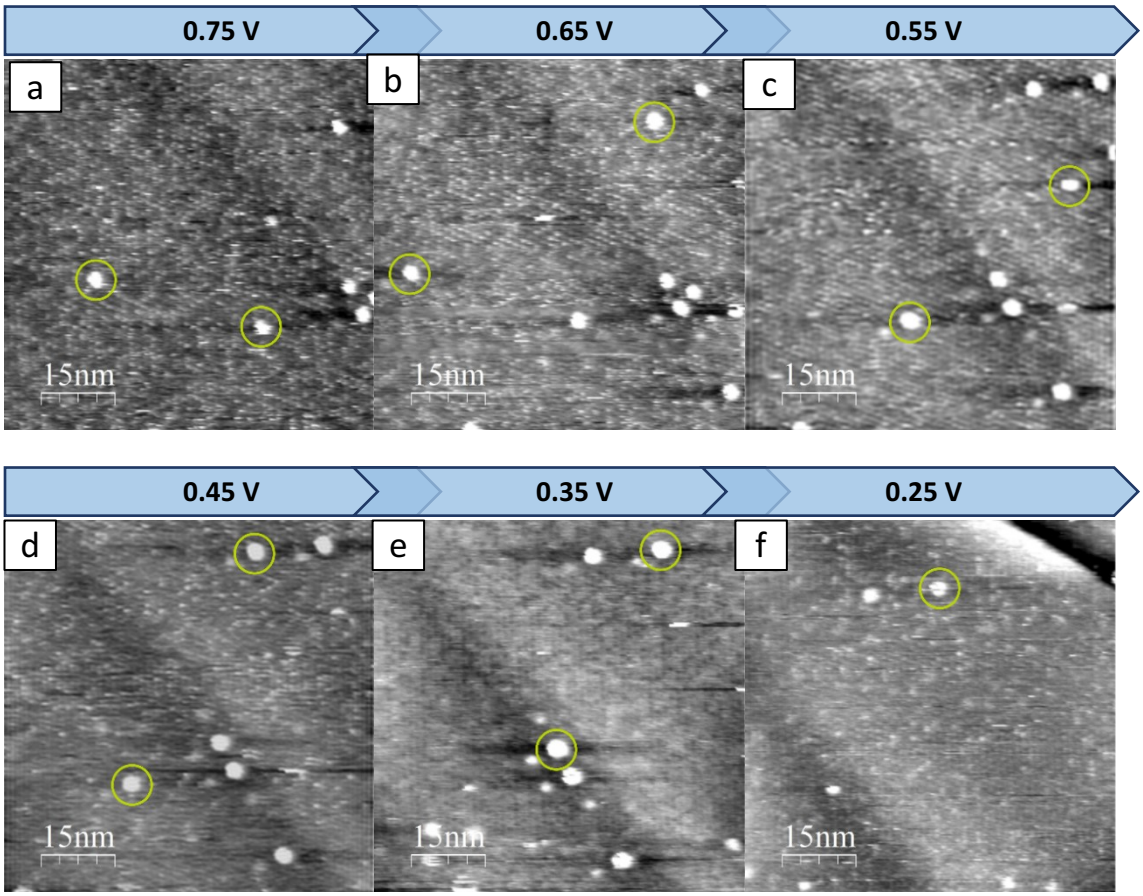

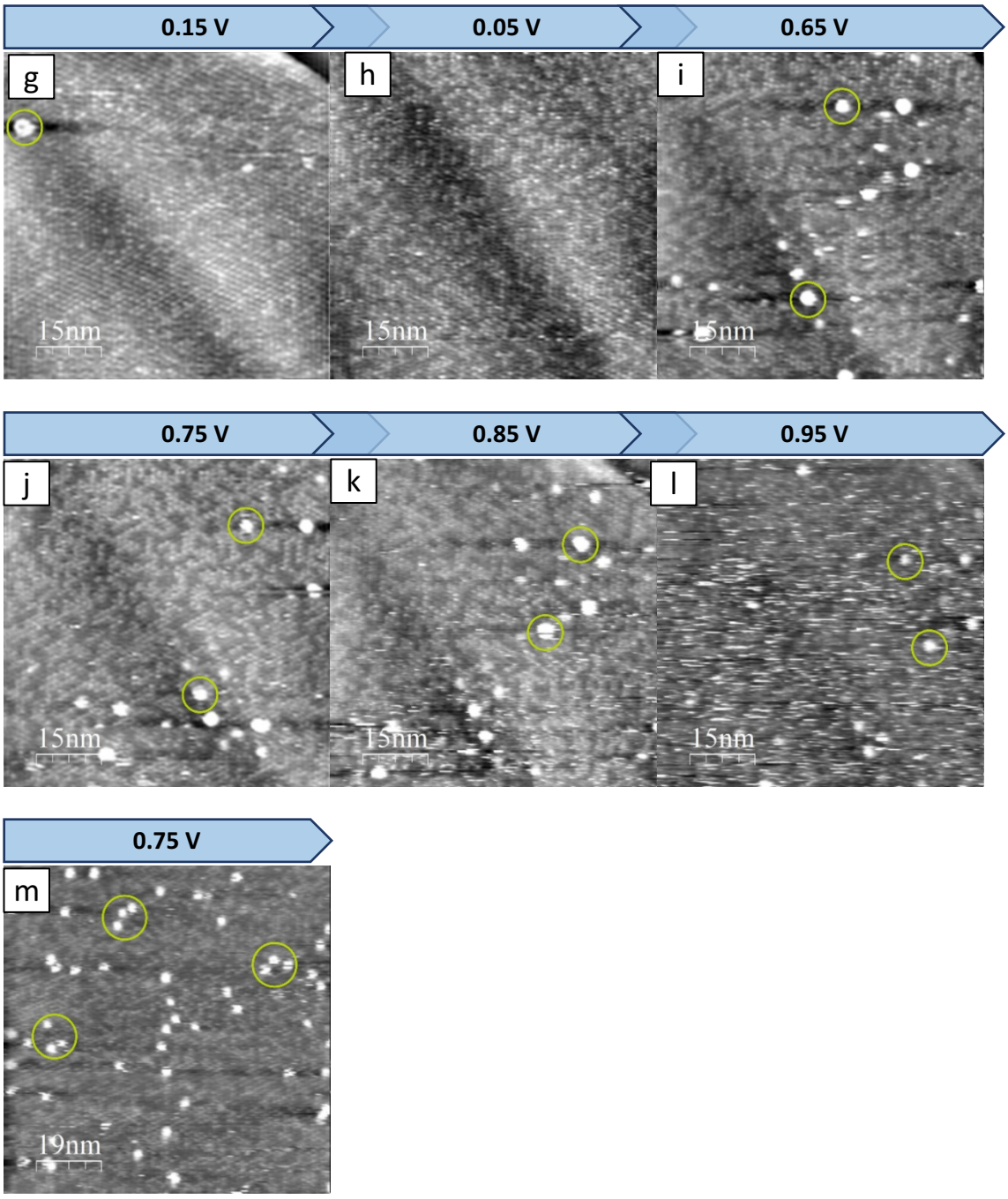

Figure 6.30. large scale potentiodynamic EC-STM images of mixed CuOEP / CoOEP adlayer on HOPG in the case of deaerated 0.1 M $HClO_4$. Tunnelling parameters for all images are: I_t = 0.58 nA, U_b = -150 mV vs RHE. The applied potential is: a) E_{app} = +0.75 V vs RHE; b) E_{app} = +0.65 V vs RHE; c) E_{app} = +0.55 V vs RHE; d) E_{app} = +0.45 V vs RHE; e) E_{app} = +0.35 V vs RHE; f) E_{app} = +0.25 V vs RHE; g) E_{app} = +0.15 V vs RHE; h) E_{app} = +0.05 V vs RHE; i) E_{app} = +0.65 V vs RHE; j) E_{app} = +0.75 V vs RHE; k) E_{app} = +0.85 V vs RHE; l) E_{app} = +0.95 V vs RHE; m) Eapp = +0.75 V vs RHE;

High resolution images in Ar purged electrolyte were also recorded. In this way, precise features at the single molecule level can be captured by STM and compared for the two

metal porphyrins. Three examples are reported in figure 6.31. Yellow dashed circles are employed for copper porphyrin, while red circles are assigned to cobalt porphyrin. One can clearly appreciate the contrast difference, with cobalt porphyrins appearing brighter, and copper porphyrins appearing darker. The topographic profile extracted along the yellow dashed line of figure 6.31b confirms that cobalt porphyrins retain a higher protrusion, in the order of ≈100 pm, comparable to the previously determined one for the pure CoOEP (section 6.1.4). CuOEP, as well, maintains a lower profile, without a clear protrusion, as already shown in section 6.1.5.

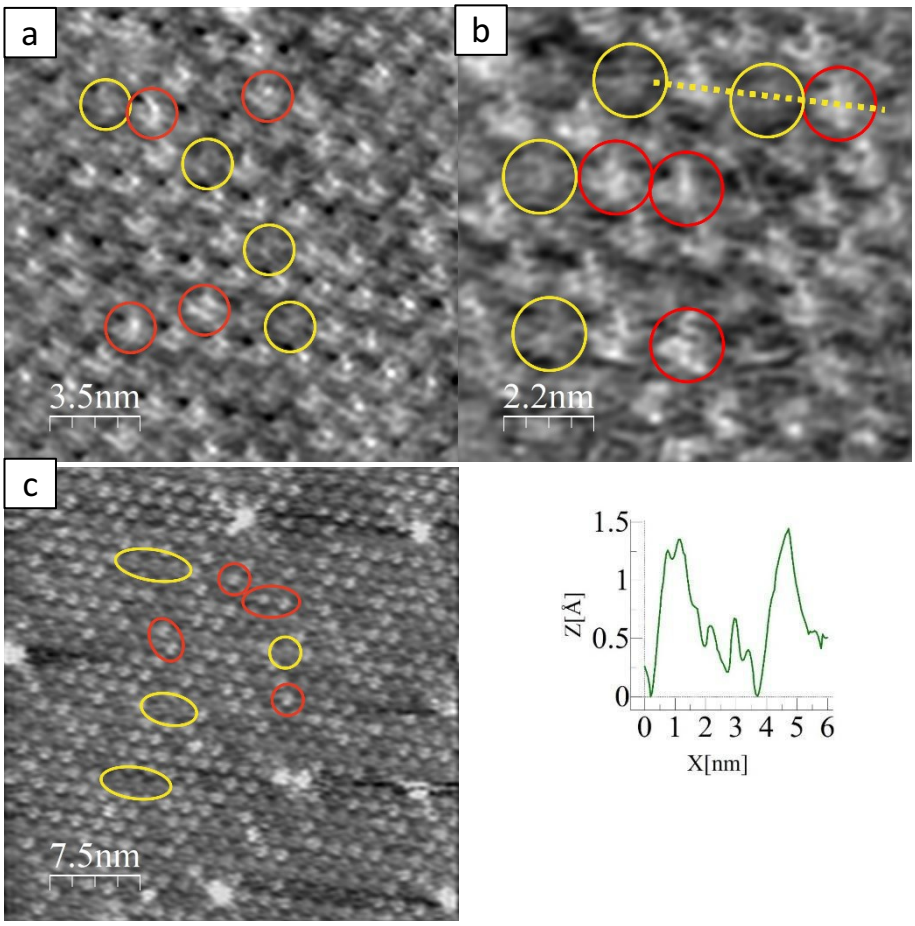

Figure 6.31. High-resolution EC-STM images of mixed CuOEP / CoOEP adsorbed on HOPG obtained in deaerated 0.1 M $HClO_4$. Tunnelling parameters are: I_t = 0.47 nA, U_b = - 250 mV vs RHE, E_{app} = +0.75 V vs RHE.

The mixed Co/Cu OEP adlayer was probed also in O_2 saturated electrolyte (figure 6.32), with the following unit cell parameters: $\overrightarrow{b_1} = (1.6 \pm 0.1)\ nm$ and $\overrightarrow{b_2} = (1.4 \pm 0.1)\ nm$, the measured angle between the two vectors is $\measuredangle = (102 \pm 2)°$. The surface concentration is $4.56 * 10^{13}\ molecules\ cm^{-2}$ and the corresponding surface coverage is $\theta = 0.012$. Contrary to the previously determined parameters in Ar purged electrolyte, in this case one unit cell vector is found to be slightly shorter and, above all, the measured angle is not close to 120° anymore, though being not close to 90° as well. Due to a fewer number collected in O_2 saturated electrolyte, it is possible that this image was depicting

one type of molecular domains, and that other domains with similar symmetry of the Ar case existed but were not successfully imaged.

Yellow and red circles were again used to indicate copper and cobalt porphyrins, respectively. The yellow dashed line features the extracted topographic profile, which confirms the higher protrusion for cobalt porphyrins and the low profile for copper porphyrins. Although the scan size of figure 6.32 was not as small as those obtained for other metal-porphyrins, two relevant features should be noticed. The first is the presence of an intense protrusion, with a height of ≈ 100 pm. This could be ascribed to an O2-binded Co centre, that was not possible to observe in pure CoOEP adlayer due to a higher instability of the molecule. The second is the detection of one dim molecule, ascribed to CuOEP, which had been demonstrated not to bind O_2.

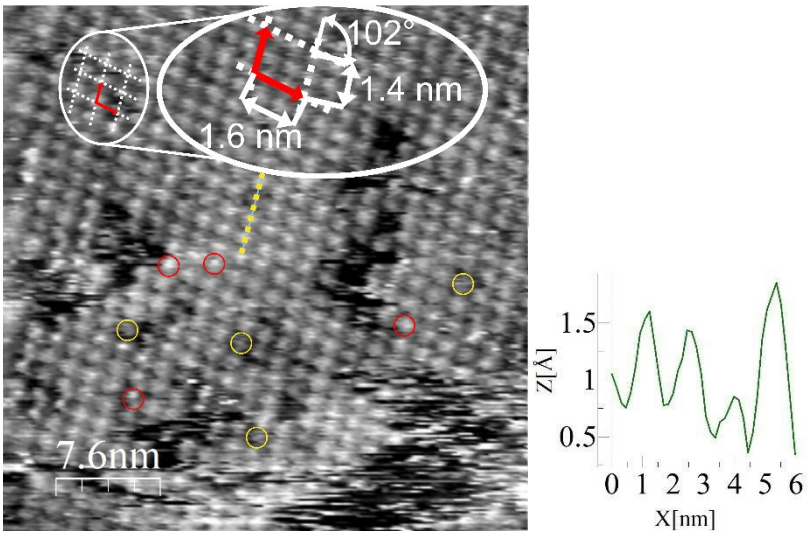

Figure 6.32. High resolution EC-STM image of a mixed CuOEP / CoOEP adlayer on HOPG in presence of O_2-saturated 0.1 M $HClO_4$. Tunnelling parameters are: I_t = 0.47 nA, U_b = - 350 mV vs RHE, E_{app} = +0.95 V vs RHE. Yellow and red circles indicate CoOEP and CuOEP, respectively

In summary, an intermixed layer consisting of CoOEP and CuOEP was realised, with the intent of exploiting CuOEP as a sort of internal reference, as previously done with H_2OEP and FeOEP. Actually, more extended monolayers were found with respect to the pure CoOEP system, and the two different components were clearly distinguishable in both large scale and high-resolution images. O_2 saturation was also pursued, with some insights on O_2 adsorption being gathered. It appeared that selective O_2 binding on Co centres led to an increase in the topographic profile. As in the case of the pure layer of CoOEP (section 6.1.4), additional investigations are needed to discriminate this selective O_2 adsorption process, especially because Co was already found to give apparently contradictory results in terms of STM contrast, with Co-O_2 adducts being imaged as darker or brighter spots [41,53,70].

6.1.7 EC-STM investigation of PtOEP at HOPG

A 0.1 mM platinum (II) octaethylporphyrin solution in DMF was drop-casted on the HOPG surface, letting it functionalise for 30 min and then dry under an argon stream, for a total process of about 60 minutes. Large and ordered domains were obtained, even if a full coverage was not always achieved, and various domains featuring a large number of molecules are separated by darker contrast areas attributed to an absent or weak HOPG coverage. The green arrows in figure 6.33.a indicate the portion of uncovered HOPG.

Focusing on an ordered domain, like figure 6.33.b and 6.33.c, the unit cell parameters can be extracted, as follows: vectors are $\overrightarrow{b_1} = (1.3 \pm 0.1)\ nm$ and $\overrightarrow{b_2} = (1.5 \pm 0.1)\ nm$, the measured angle between the two vectors is $\measuredangle = (110 \pm 2)°$. The surface concentration is $5.46 * 10^{13}\ molecules\ cm^{-2}$ and the corresponding surface coverage is $\theta = 0.014$. Figure 6.33c is an example of highly ordered defect-free PtOEP monolayer, and it can be appreciated the hexagonal disposition of molecules on the flat HOPG surface.

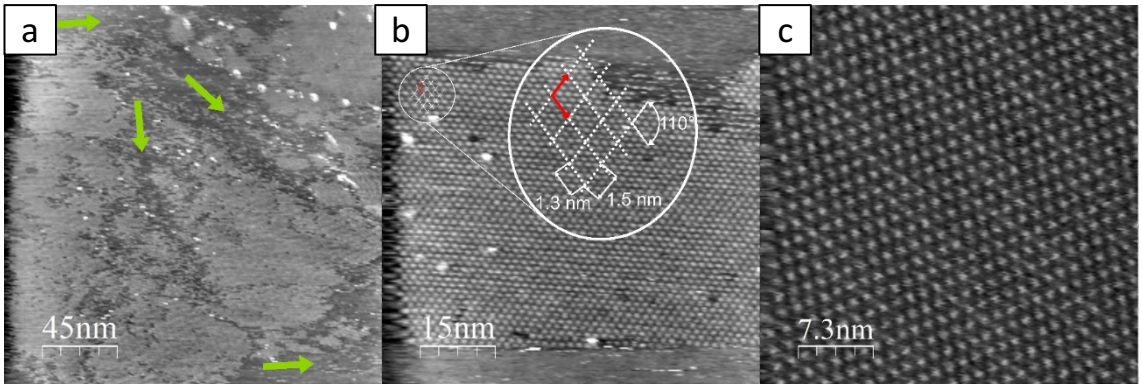

Figure 6.33. a,b) Large scale EC-STM image of a PtOEP adlayer on HOPG in the case of deaerated 0.1 M $HClO_4$. c) example of defect-free PtOEP adlayer region on HOPG. Tunnelling parameters for all images are: I_t = 0.47 nA, U_b = - 700 mV, E_{app} = OCP.

Small area images were collected to improve the resolution at single-molecule level, so that molecular features were more clearly discernible. Two sample images are reported in figure 6.34. In both cases, the traced yellow dashed line stands for the extracted topographic profile. Both profiles confirm that the brighter central part of each molecule entails a protrusion in the order of 40-60 pm. A caveat must be made regarding Pt electronic levels and its contrast in EC-STM pictures. Pt shares the same type of *d* orbital population of Ni, considering that two additional shells are completed, arriving to a low-spin $5d^8$ final orbital configuration. Platinum has a (II) oxidation state, and like Ni, its complexes possess square-planar symmetry, with a poor tendency to bind axial ligands [71]. The reason is readily explained: owing to the filled $5dz^2$ orbital, Pt(II) complexes repel axial ligands, with few exceptions under specific circumstances only for smaller atoms, like Ni [72]. It must be mentioned that Pt, notwithstanding the high atomic radius, is mostly coplanar with the porphyrin ring, and this is due to an effect of back-donation from Pt to the porphyrin ring, with electron density flowing away from the metal to the porphyrin d_π^* orbital [72,73].

Another consideration stems from the redox properties of Pt. Differently from other transition metal porphyrins, especially the first-raw transition metal series, Pt complexes like Pt(II)OEP possess a scarce redox activity, with few stable oxidation states being reached. Some Pt(IV) complexes were found to be stable [72] but they were obtained upon electrochemical oxidation in presence of chloride to satisfy the demand of two additional ligands to stabilise the Pt(IV) centre, so this effect can be discarded for the purpose of this work.

To sum up, there is an uncertainty regarding the STM contrast of PtOEP, which is expected to show a depression in the centre due to the filled $5dz^2$ orbital population of platinum. However, the unexpected protrusion was already visualised in a previous work [74], but its origin was wrongly attributed to a partially filled $5dz^2$ occupancy.

A final remark verts on the possibility of transition metal-atoms hosted in porphyrin cavities to couple with one or more substrate atoms, at a limit of generating new chemical bonds. However, this possibility appears unlikely to occur with HOPG, even if intermolecular charge transfer via noncovalent functionalization can be considered. Additional details will be provided in section 6.2.2. dealing with the same PtOEP in presence of Au(111) as substrate.

In conclusion, the only solid information to this point is that STM pictures still exhibit a protrusion in the centre, indicating a somewhat enhanced tunnelling phenomenon through the Pt centre.

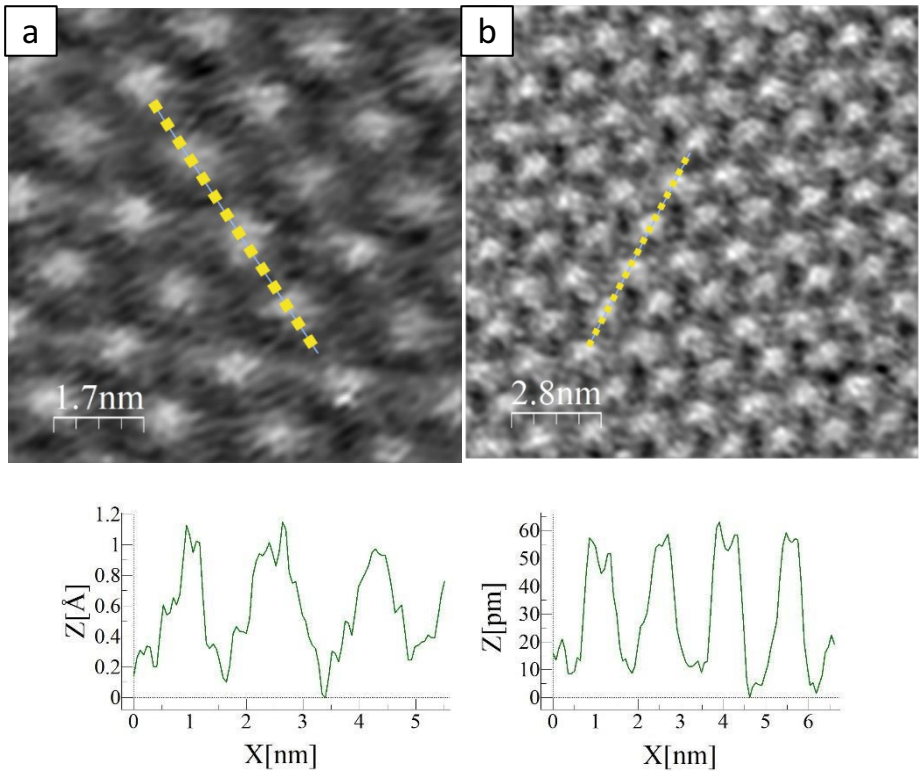

Figure 6.34. high-resolution EC-STM images of PtOEP adlayer on HOPG in the case of deaerated 0.1 M $HClO_4$. Tunnelling parameters are: a) I_t = 0.47 nA, U_b = - 700 mV, E_{app} = OCP; b) I_t = 0.47 nA, U_b = - 650 mV, E_{app} = OCP.

Potentiodynamic imaging was first performed in deaerated electrolyte (Ar purged) to reveal any STM contrast change in the further investigated potential window for ORR. In fact, the applied potential ranged from 0.35 V vs RHE mV to -0.45 mV, which is almost at the limit in the cathodic part of the corresponding cyclic voltammetry (section 5.1.6). At Eapp= 0.35 V vs RHE, the molecules show a protrusion of 50-65 pm, accordingly to the previously presented high-resolution pictures. It was not encountered a significant contrast change in the investigated scan range, and returning to a positive applied potential, Eapp=0.55 V vs RHE, the situation is unchanged. This is a sign of a remarkable stability of the PtOEP adlayer even if quite negative potential, close to HER, was achieved while scanning the surface.

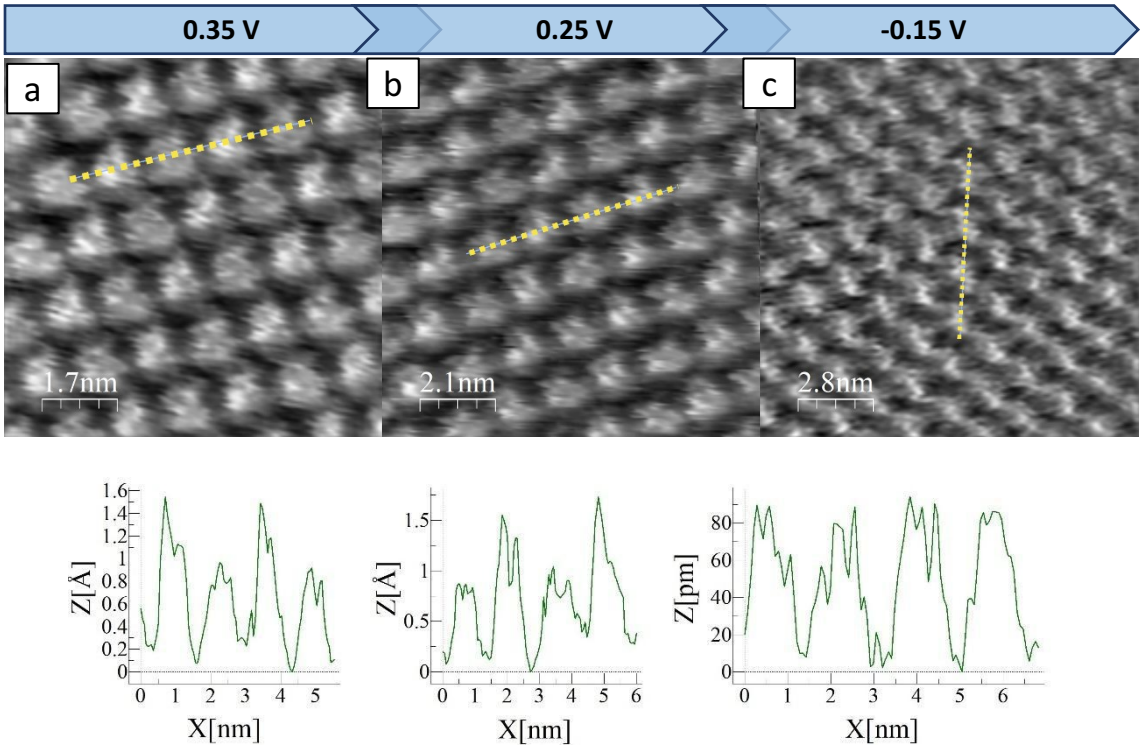

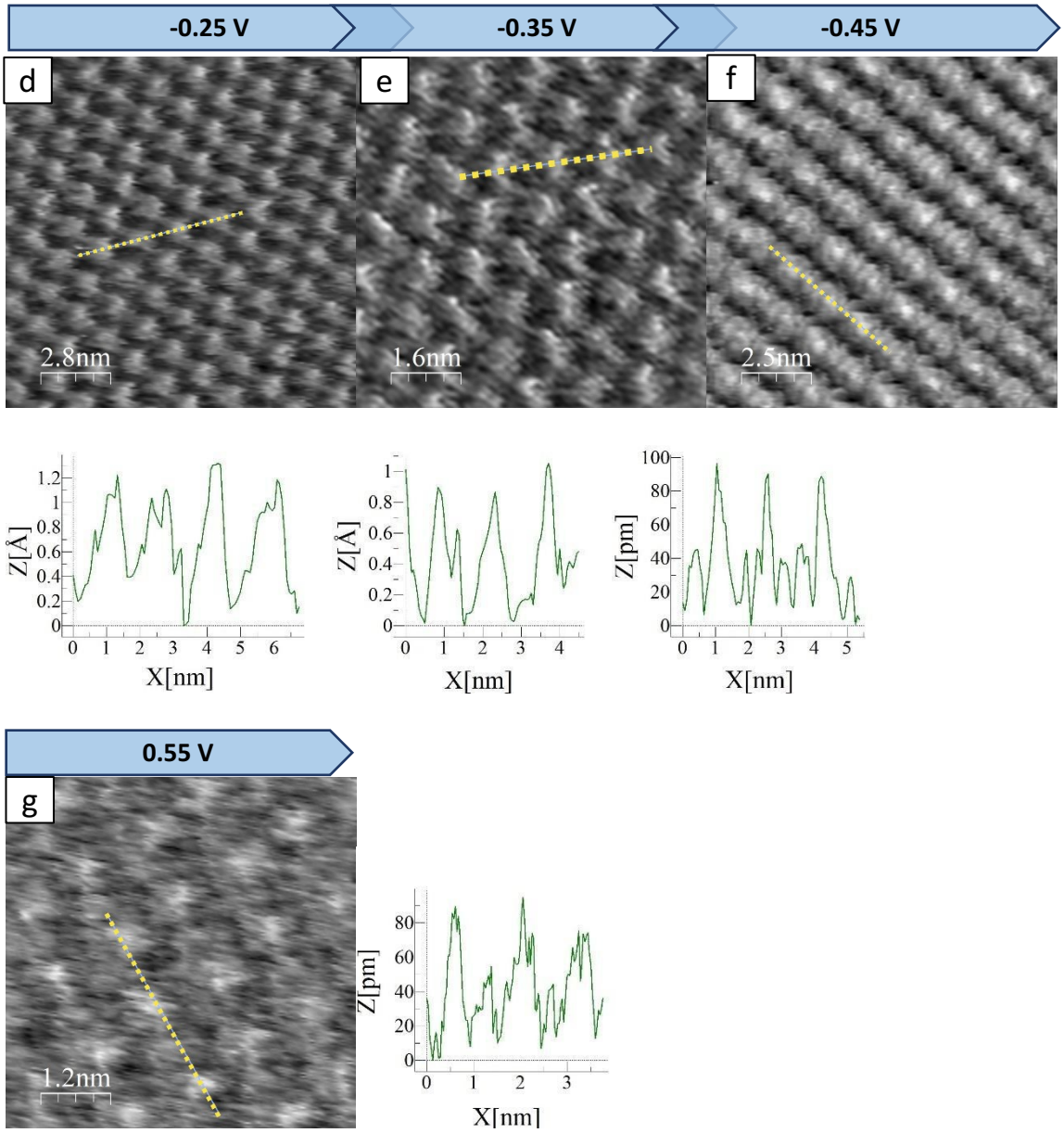

Figure 6.35. High-resolution EC-STM images collected under potential control of PtOEP adlayer on HOPG in the case of deaerated 0.1 M $HClO_4$. Tunnelling current for all images is: I_t = 0.47 nA. Other tunnelling parameters are: a) U_b = - 150 mV vs RHE, E_{app} = +0.35 V vs RHE; b) U_b = - 150 mV vs RHE, E_{app} = +0.25 V vs RHE; c) U_b = 250 mV vs RHE, E_{app} = -0.15 V vs RHE; d) U_b = 250 mV vs RHE, E_{app} = -0.25 V vs RHE; e) U_b = 250 mV vs RHE, E_{app} = -0.35 V vs RHE; f) U_b = 250 mV vs RHE, E_{app} = -0.45 V vs RHE; g) U_b = - 50 mV vs RHE, E_{app} = +0.55 V vs RHE.

An example of large size image featuring PtOEP adlayer in O_2 saturated electrolyte is reported in figure 6.36. As already noticed for the Ar-saturation case, the sample may present some uncovered or partially covered areas. In figure 6.36, a green dashed line is traced to distinguish a large ordered molecular domain (bottom and right part) from a

partially covered area (top and left part). Unit cell parameters are not reported due to complete correspondence with Ar saturation case.

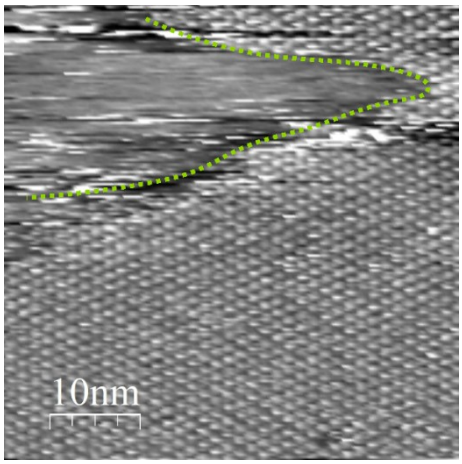

Figure 6.36. Large scale EC-STM image of a PtOEP adlayer on HOPG in the case of O_2 saturated 0.1 M $HClO_4$. Tunnelling parameters for all images are: I_t = 0.47 nA, U_b = -1000 mV, E_{app} = 0.55 V vs RHE.

High-resolution pictures were collected also in the case of O_2-saturated electrolyte, to eventually investigate the O_2 adsorption process onto the PtOEP units. The mean of comparison is the topographic profile, which was collected also for Ar purged electrolyte. In this case, the topographic profiles corresponding to the yellow dashed line of figure 6.37.a-c confirm that a higher protrusion was revealed, in the range 80-100 pm. This is taken as proof to assess the O_2 adsorption process occurring for the O_2 molecule at the Pt centre. Contrary to the previous observations made for FeOEP, and similarly to those made for MnOEP, it appears that for PtOEP the protrusion is not shifted from molecular centre, probably indicating a side-on O_2 adsorption geometry onto the Pt centre.

At this point, one could raise an objection to the just described O_2 adsorption ability by PtOEP, since in the description of Ar saturation case the poor tendency to bind axial ligands was brought forth as a characteristic of Pt(II)-based complexes. However, computational data seem to confirm both an almost complete filling of the $5dz^2$ orbital and the interaction between the O_2 molecule and the Pt centre. This is claimed to be possible thanks to an effect of electron back-donation from the occupied $5dz^2$ orbital on Pt to the 3p anti-bonding orbitals of O_2 [75].

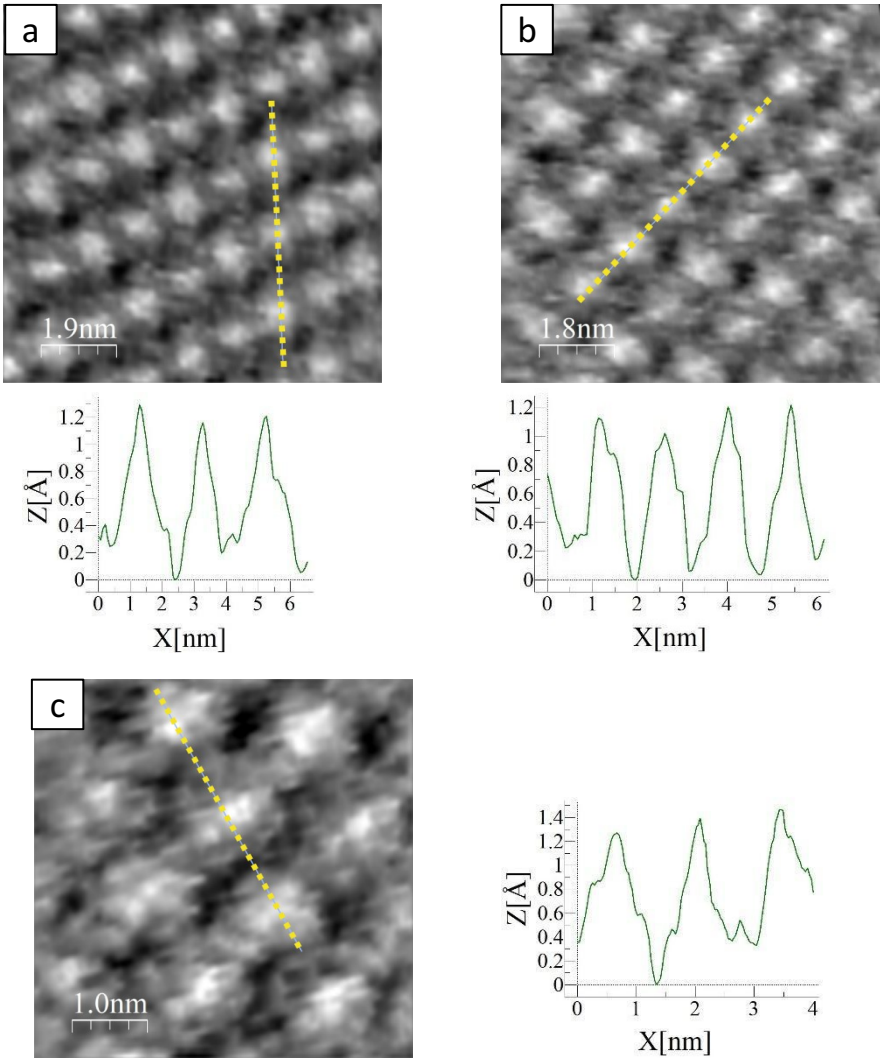

Figure 6.37. High-resolution EC-STM images collected for a PtOEP adlayer on HOPG in O_2 saturated 0.1 M $HClO_4$. Tunnelling parameters for all images a-c) are: I_t = 0.47 nA, U_b = - 50 mV vs RHE, E_{app} = +0.55 V vs RHE.

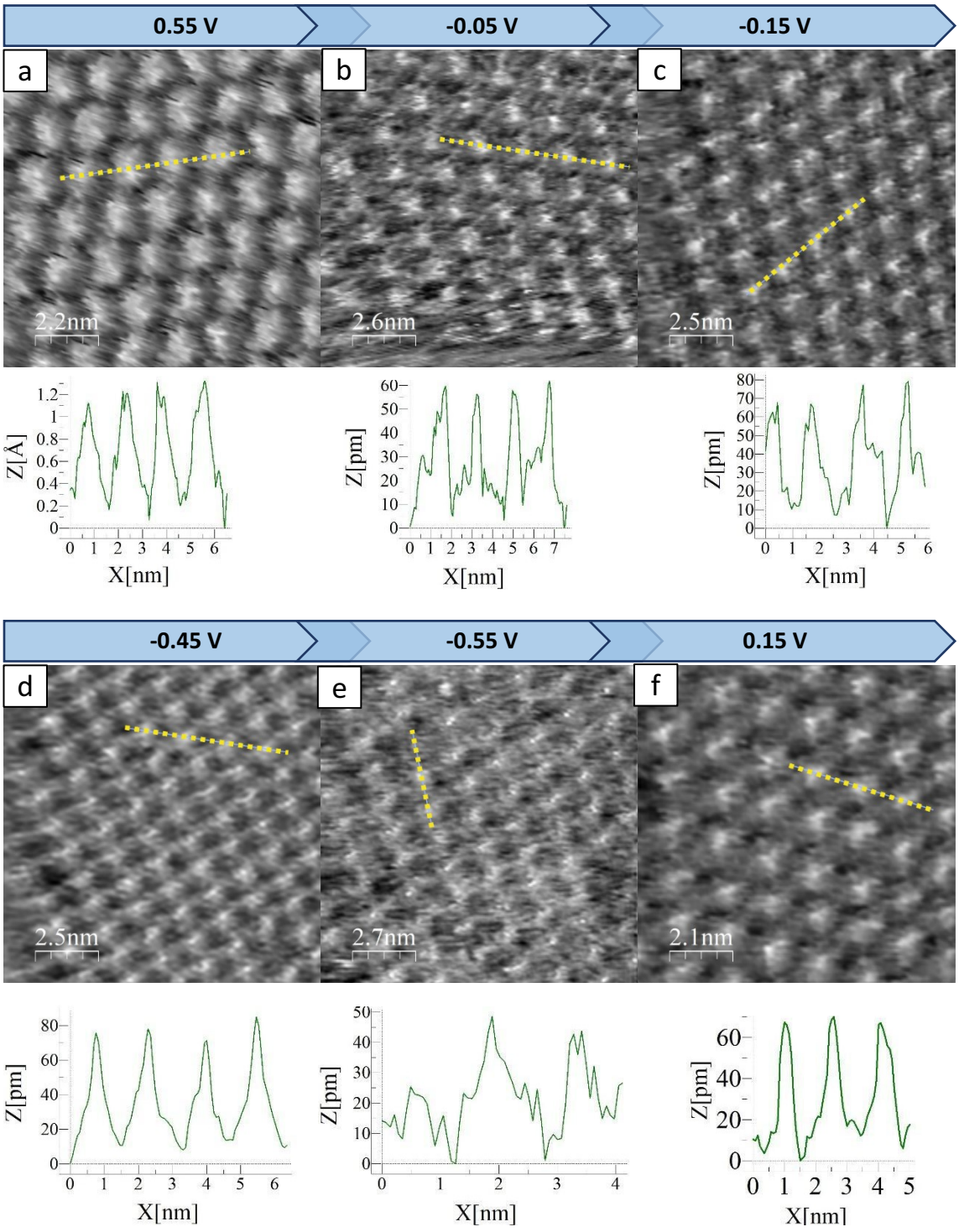
0.55 V
-0.05 V
-0.15 V
a
b
c
2.2nm
2.6nm
2.5nm
Z[Å]
Z[pm]
Z[pm]
X[nm]
X[nm]
X[nm]
-0.45 V
-0.55 V
0.15 V
d
e
f
2.5nm
2.7nm
2.1nm
Z[pm]
Z[pm]
Z[pm]
X[nm]
X[nm]
X[nm]

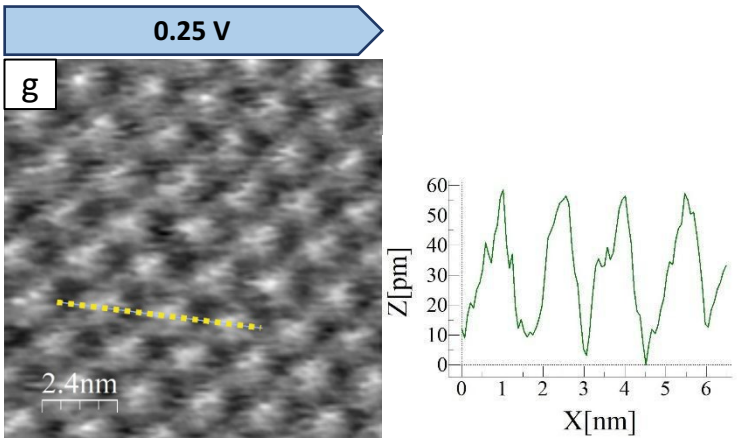

Figure 6.38. high-resolution EC-STM images collected under potential control of PtOEP adlayer on HOPG in the case of O_2 saturated 0.1 M $HClO_4$. Tunnelling current for all images is: I_t = 0.47 nA. Other tunnelling parameters are: a) U_b = - 150 mV vs RHE, E_{app} = +0.55 V vs RHE; b) U_b = +50 mV vs RHE, E_{app} = -0.05 V vs RHE; c) U_b = 50 mV vs RHE, E_{app} = -0.15 V vs RHE; d) U_b = - 150 mV vs RHE, E_{app} = -0.45 V vs RHE; e) U_b = - 50 mV vs RHE, E_{app} = -0.55 V vs RHE; f) U_b = -50 mV vs RHE, E_{app} = 0.15 V vs RHE; g) U_b = -50 mV vs RHE, E_{app} = 0.25 V vs RHE.

The PtOEP adlayer was finally subjected to potentiodynamic imaging in the case of O_2 saturated electrolyte (figure 6.38). At positive applied potential, E_{app} = 0.55 V vs RHE, the extracted topographic profile confirms the protrusion of 80-100 pm, while it reduces to 40-60 when lowering the potential to E_{app} =-0.05 V vs RHE. Despite the high current developed at the sample surface due to the concurrent oxygen reduction reaction, the adlayer remains stable, since molecules are regularly imaged even at E_{app}=-0.55 V vs RHE. Upon returning to positive potentials, the initial contrast is restored, even if a slightly small protrusion is measured (60 pm). This can be explained either with a small loss of resolution of the tip during potentiodynamic imaging or to a low O_2 adsorption rate at the Pt centres.

In conclusions, PtOEP was found to form a highly ordered monolayer on the surface of HOPG, but some uncovered patches of HOPG were also present. The adlayer in any case did not present defects like domain boundaries, bilayers or clusters. High resolution images in Ar purged electrolyte did exhibit a protrusion in correspondence of Pt, even if this sounded like a controversy when thinking of the fully occupied $5dz^2$ orbital. Different hypotheses were examined, but the further increase of the protrusion in the case of O_2 saturated electrolyte confirmed the possibility of Pt to bind O_2 as axial ligand, with computational data corroborating this observation.

6.1.8 EC-STM investigation of SnOEP at HOPG

A 0.1 mM Sn(IV) octaethylporphyrin dichloride solution in DMF was drop-casted on the freshly cleaved HOPG surface, and it was let functionalise for 30 min. After that, an Ar stream was directed on the sample to let the drop dry. The outcome of this

functionalisation procedure is displayed in figure 6.39, which features a large scale EC-STM image collected in Ar purged electrolyte. As visible from figure 6.39, the HOPG is not fully covered by the SnOEP molecules. In particular, the yellow circles indicate missing molecules defects, and the red ellipses stand for wider areas of missing molecules surrounded by ordered molecules. Finally, the yellow dashed curves delimit two different domains separated by an area of uncovered HOPG.

Different attempts were made to fine tune the adsorption process and obtain larger ordered domains, like longer functionalisation time, higher and lower molecule concentration, but none of these solutions led to appreciable results.

Figure 6.39 contains also a sketch for the unit cell parameters, which are, as follows: $\overrightarrow{b_1} = (1.5 \pm 0.1)\ nm$ and $\overrightarrow{b_2} = (1.5 \pm 0.1)\ nm$, the measured angle between the two vectors is $\measuredangle = (115 \pm 2)°$. The surface concentration is $4.90 * 10^{13}\ molecules\ cm^{-2}$ and the corresponding surface coverage is $\theta = 0.012$.

SnOEP shares similar unit cell shape and parameters compared to the previously analysed metal octaethylporphyrins, and the hexagonal HOPG surface dictates the symmetry of the molecular array, since the measured angle is close to 120°.

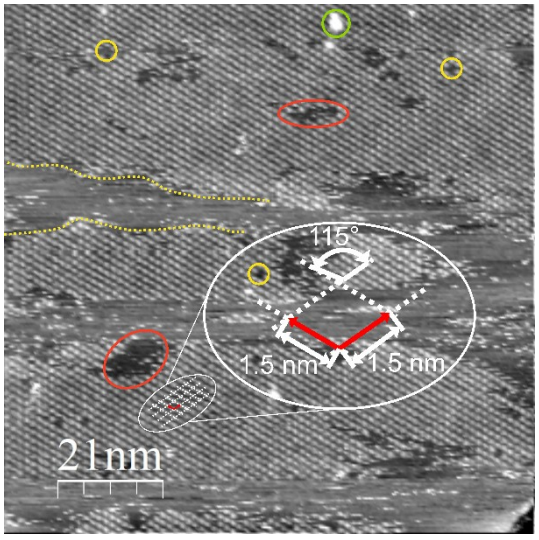

Figure 6.39. large scale EC-STM image of a SnOEP adlayer on HOPG in the case of deaerated 0.1 M $HClO_4$. Tunnelling parameters are: I_t = 0.47 nA, U_b = - 700 mV, E_{app} = OCP. Yellow and red circles indicate missing molecules defects wider areas of missing molecules, respectively.

Besides the inconvenience of getting narrow covered areas, a few ordered ones could be successfully imaged, the result being reported in figure 6.40.a and 6.40.b. In both figures, the solid circles indicate two different types of molecules based on their STM contrast. Yellow circles indicate molecules featuring a bright protrusion in their centre, whereas red circles stand for molecules with a depression in their centre. A very rough estimation could be made basing on these two images, and a population of ≈60% of bright molecules was found versus a remaining ≈40% of dark molecules. At a first glance, it appears that

dark molecules, showing a depression at the centre, should be addressed as demetalated molecules, which lost their metal centre during the functionalisation step and/or at the moment of adsorption onto the HOPG surface. Indeed, it had been pointed out in section 6.1.1 that H2OEP displays a dip at its centre, due to absence of the metal. However, previously published data seem to corroborate a different result. In fact, tin phthalocyanine was successfully imaged with these double types of contrasts, both on HOPG, Au(111), Au(100), Cu(111), Ag(100), Ag(111) and TiO2(110) [76–80]. For all these substrates, a similar behaviour was observed, namely the presence of bright or dark molecules. The final explanation is that tin, due to its considerable size, is not able to fully fit in the phthalocyanine cavity, and therefore protrudes of 1.1 Å [76]. Therefore, at the moment of deposition, some molecules will adsorb with the tin atom point toward the surface, some others outward the surface. Those molecules with the tin atom point to surface will appear with a protrusion, and the opposite occurs for molecules with tin atom pointing out of the surface. Therefore, in this case the STM contrast is not mediated, at least at this stage, by the orbital population, but rather simply by the geometry of the sample, namely the topography (topographical contrast).

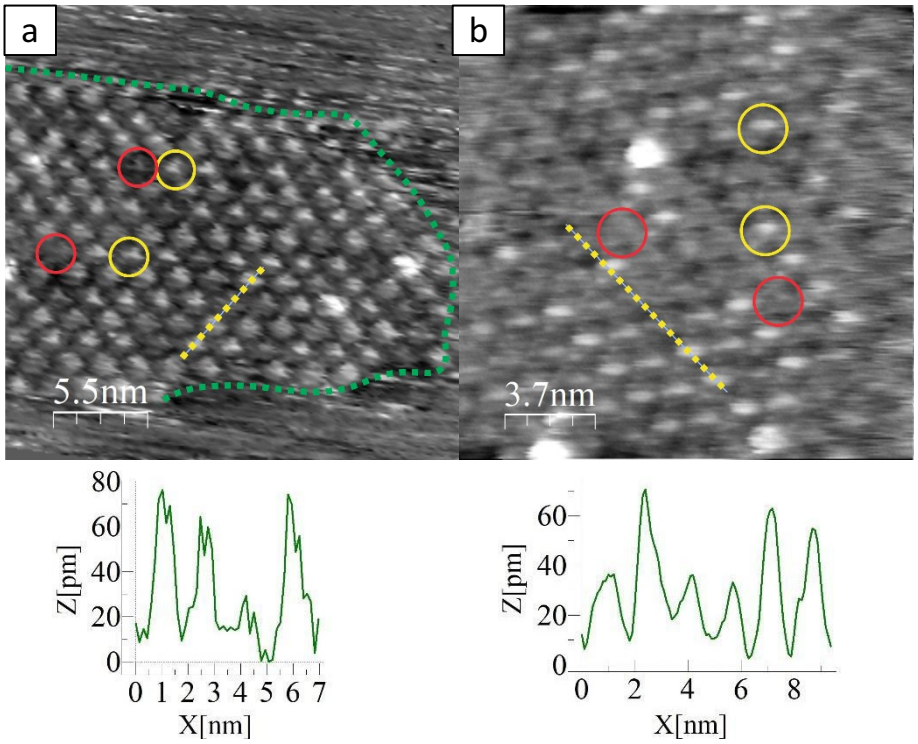

Figure 6.40. High-resolution EC-STM images of SnOEP on HOPG in the case of deaerated 0.1 M $HClO_4$. Tunnelling parameters are: a) I_t = 0.47 nA, U_b = - 900 mV, E_{app} = OCP; b) I_t = 0.47 nA, U_b = - 700 mV, E_{app} = OCP.

In O_2 saturated electrolyte, the contrast of individual SnOEP units seem to change in favour of a unique type, without a clear depression at the centre nor with a protrusion (see figure 6.41). This difference could be a harbinger of oxygen adsorption onto the Sn centre, since a certain electrochemical activity towards ORR was detected (section 5.1.8 Figure

5.22), but additional images with more careful observations are certainly necessary to assess this hypothesis.

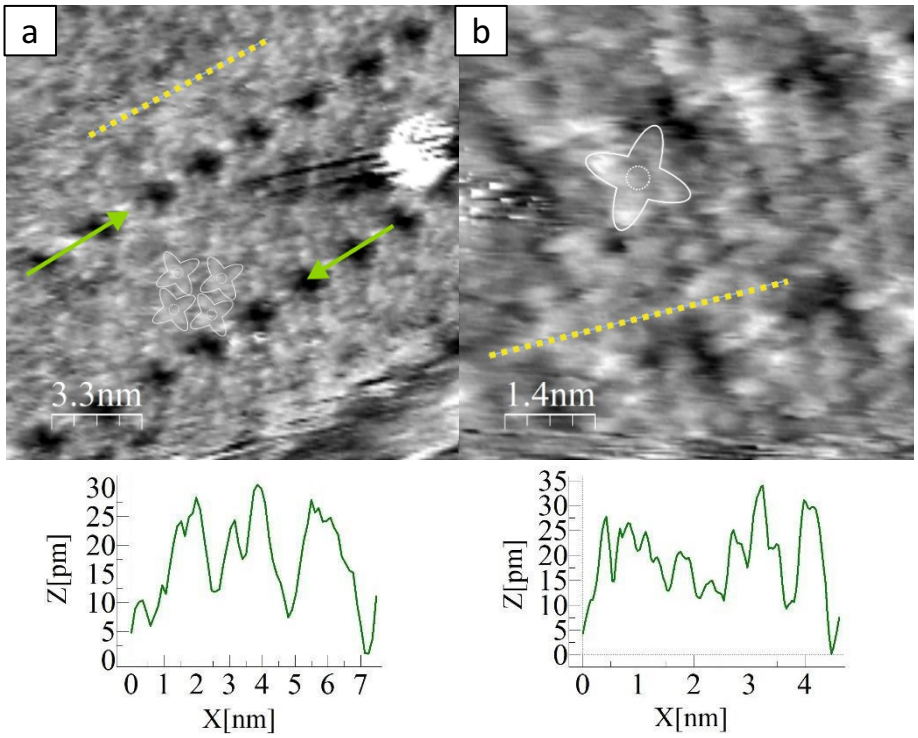

Figure 6.41. high-resolution EC-STM images of SnOEP on HOPG in the case of O_2 saturated 0.1 M $HClO_4$. Tunnelling parameters for both figures are: I_t = 0.47 nA, U_b = - 600 mV, E_{app} = OCP.

Few images of SnOEP on HOPG were collected, probably due to a non-suitable functionalisation procedure compared to the previous transition-metal octaethylporphyrin. Nonetheless, high resolution pictures allowed to notice a peculiar phenomenon, namely the presence of molecules with a protrusions and others with a depression. It was found that it is compatible with a Sn-up or Sn-down adsorption, respectively, due to a net non-planarity of Sn with the rest of the porphyrinato ligand. A contrast change was also revealed when passing to O_2 saturated electrolyte, even if the number of recorded images is insufficient to fully ascertain the O_2 binding behaviour of Sn.

6.1.9 EC-STM investigation of RuOEP at HOPG

A 0.1 mM Ru(II) carbonyl octaethylporphyrin solution in DMF was drop-casted onto the freshly cleaved HOPG surface. After 30 min, an Ar stream was directed over the sample surface, in order to dry the DMF droplet. The total functionalisation time required was about 60 minutes. Despite different trials based on longer/shorter functionalisation time and lower/higher molecule concentration, a non-uniform substrate functionalisation was revealed, with few ordered areas being imaged, moreover featuring a number of defects. These measurements were intentionally done with a metal centre "poisoned" with CO (the only one pucheasible) for a twofold reason. Firstly, to see how CO poisoning affects

oxygen reactivity and secondly, how the carbonylated adduct can act as an intermediate for the CO2 reduction reaction. In both cases we were unable to progress with the work, due to time constraints, but it remains a central research activity in the near future

The unit cell parameters are sketched in a large size images reported in figure 6.42 with $\overrightarrow{b_1} = (1.5 \pm 0.1)\, nm$ and $\overrightarrow{b_2} = (1.6 \pm 0.1)\, nm$, the measured angle between the two vectors is $\measuredangle = (121 \pm 2)°$. The surface concentration is $4.86 * 10^{13}\ molecules\ cm^{-2}$ and the corresponding surface coverage is $\theta = 0.013$.

Due to a trickier functionalisation procedure if compared to other metal-octaethylporphyrins, a low number of satisfactory EC-STM images was obtained, and they are limited to the Ar purged electrolyte experimental condition.

However, the image reported in figure 6.42 lets us notice that a great number of brighter spots is visible, and an example is indicated with a yellow circle. A first gross inspection of this large size image leads to think that bilayer molecules are present over the first molecular monolayer. Indeed, examples of this behaviour do exist [81–84], but in all cases the 2nd-layer molecules were shifted from the centre of the 1st layer-molecules, especially for an electrostatic reason. In fact, for an exactly on-top position of the 2nd layer with respect to the 1st layer, a great repulsion will manifest between the two metallic centres. In the case of figure 6.42, the "2nd-layer molecules" would find themselves in the same position of the "1st layer molecules", but this would signify a very unfavourable situation due to electrostatic repulsion. [85]

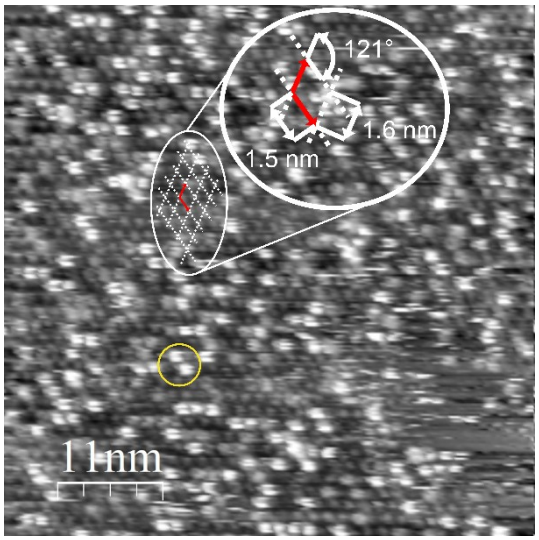

Figure 6.42. Large-scale EC-STM image of RuOEP on HOPG in the case of deaerated 0.1 M $HClO_4$. Tunnelling parameters are: I_t = 0.47 nA, U_b = - 250 mV vs RHE, E_{app} = 0.85 V vs RHE.

As a matter of fact, figures 6.43.a and 6.43.b are two examples of higher resolution EC-STM images obtained for the Ru-CO-OEP system, and the bright and dark features are better visible. Again, the suspected bilayer molecules seem to be placed exactly on-top of the first layer. At this point, an important literature comparison linked to the physical chemical nature of the investigated system goes against the previous bilayer hypothesis.

In this case, ruthenium centres feature a carbonyl ligand as fifth axial ligand. As already pointed out for FeOEP and MnOEP, their chloride axial ligands should be lost before or at the moment of the functionalisation, since no evidence of its presence came out when imaging the sample. In this case, the carbonyl ligand may determine a stronger binding with the ruthenium centre, making it harder from an energetic point of view to completely remove it directly in solution or on surface at the moment of functionalisation. In fact, a literature work reports the absence of carbonyl from a ruthenium (II) carbonyl tetraphynlporphyrin due to Ru-CO-TPP evaporation at 200°C. Upon evaporation of the ruthenium tetraphynlporphyrin with a co-dosage of CO, the Ru-CO adduct was restored [86]. It is interesting to compare the STM contrast of this Ru-CO-TPP due to its good similarity with our Ru-CO-OEP. In this sense, it is possible to imagine that CO molecules bridge between two Ru centres, inducing the formation of a second layer on-top of the 1st layer, that obviously cannot be accomplished on Ru center without the axial ligand. Furthermore, molecules featuring CO present in fact a definitely brighter protrusion at the centre of the molecule, whereas less bright molecules are ascribed to Ru-TPP molecules with the missing CO [86]. Being the contrast of figure 6.43.a and 6.43.b of the same type of the reference, it seems natural to conclude that also in the case of octaethylporphyrins on HOPG, both bare ruthenium centres and CO-adducts are present. Topographic profiles were also extracted, trying to include both bright and dark contrast molecules, and those molecules appearing brighter determine a higher protrusion, as expected. Due to the fact that other CO-binded metal-porphyrins caused a smaller topographic profile to manifest [86–88], we must conclude that the STM contrast is mainly driven by a modification of the LDOS when CO is present, and not by the simple topography of the sample. In other words, the presence of an additional feature on the Ru centres, in this case CO, does not automatically translate into an enhanced protrusion in the final STM image [86].

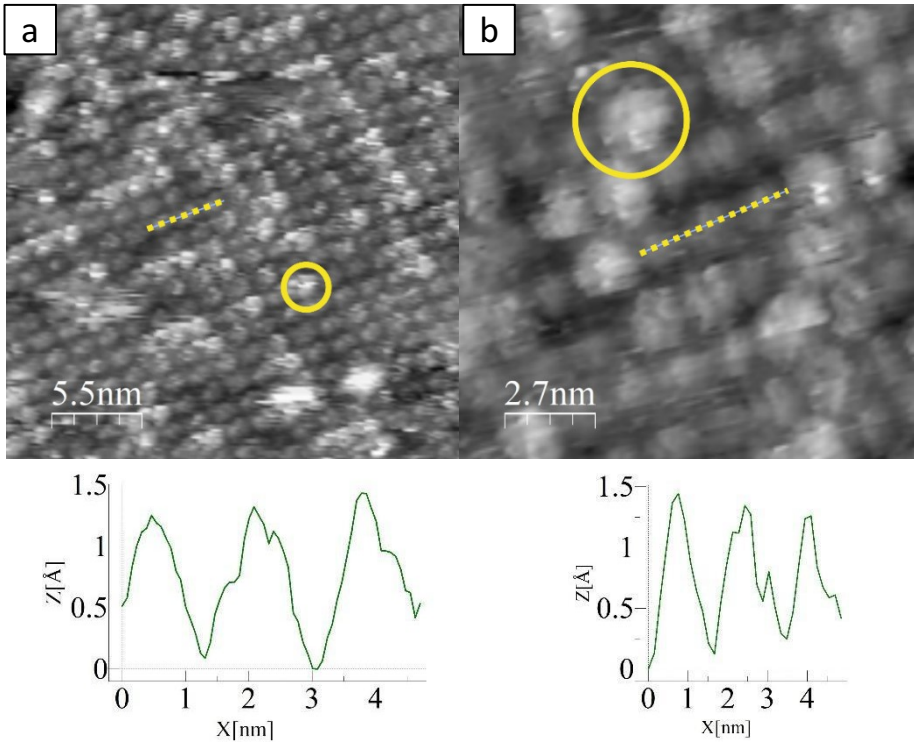

Figure 6.43. High-resolution EC-STM images of RuOEP on HOPG in the case of deaerated 0.1 M $HClO_4$. Tunnelling parameters are: a) I_t = 0.47 nA, U_b = - 150 mV vs RHE , E_{app} = 0.85 vs RHE; b) I_t = 0.47 nA, U_b = - 250 mV vs RHE, E_{app} = 0.85 V vs RHE.

A novel set of images will be in future required to extend the number of available images, especially those regarding the O_2 electrolyte saturation case, for which EC-STM images are not presented for the aforementioned reasons regarding the functionalisation procedure optimization. However, if our intuition were correct, we would expect oxygen functionalization of CO-free Ru centres only, at least not to induce CO stripping to promote oxygen adsorption or to check whether this equilibrium can still be shifted by the effect of potential. This would also allow a comparison of the behaviour of the two different adsorbates both in terms of tunnelling current and of electrochemical behaviour.

Summarizing, RuOEP did form few ordered domains onto the HOPG surface. Differently from PtOEP, their extent was far smaller, again addressing this result to the interplay of molecules-molecules and molecules-substrate interactions. Both large size and small size images evidenced the presence of very bright molecules, together with less bright ones. Their presence was roughly around 50%-50%, and at a first glance the very bright features were attributed to bilayer molecules. Remarking that ruthenium features a carbonyl as fifth axial ligand in its crystal form, it could be possible that this ligand was retained by nearly half of the molecules during the dissolution stage in DMF, and also during the functionalisation on HOPG. In fact, the loss of carbonyl from a Ru centre was reported to cause the passage from a bright spot to a dimmer one, exactly comparable to the situation imaged in this case.

6.1.10 EC-STM investigation of FeTPP at HOPG

A 0.1 mM Fe(III) tetraphenylporphyrin chloride solution in DMF was drop-casted on the freshly cleaved HOPG surface, letting it functionalise for 30 minutes and then it was dried under an Ar stream, for a total functionalisation time of about 60 minutes.

This molecule features a different ligand with respect to the other metal-octaethylporphyrins previously presented and in fact a different adsorption behaviour was encountered. In figure 6.44, two examples are provided. Figure 6.44 shows alternated domains, in which molecules assume an apparent brighter contrast with respect to adjacent darker ones. These domains are indicated with green and blue arrows. Yellow circles indicate single molecules appearing with a dark contrast, as if these molecules are "switched off". Due to the low number of switched off molecules, they are ascribed to free-base ,molecules, which could come directly from the molecular crystal form or they could be a consequence of demetallation processes occurred in solution phase before or at the moment of functionalisation.

The unit cell parameters are drawn in figure 6.44 and they are: $\overrightarrow{b_1} = (1.5 \pm 0.1)\ nm$ and $\overrightarrow{b_2} = (1.6 \pm 0.1)\ nm$, the measured angle between the two vectors is $\measuredangle = (106 \pm 2)°$. Unit cell parameters derived from figure 6.44.b slightly differ, especially in the measured angle. Further in-depth analysis and additional images will be in future required for a better assessment of the unit cell parameters. For the moment, a prudential explanation involves the drift issue, and since all metal-porphyrins, herein presented, showed almost exclusively a hexagonal array, it is likely that also FeTPP does. The surface concentration is $4.33 * 10^{13}\ molecules\ cm^{-2}$ and the corresponding surface coverage is $\theta = 0.011$.

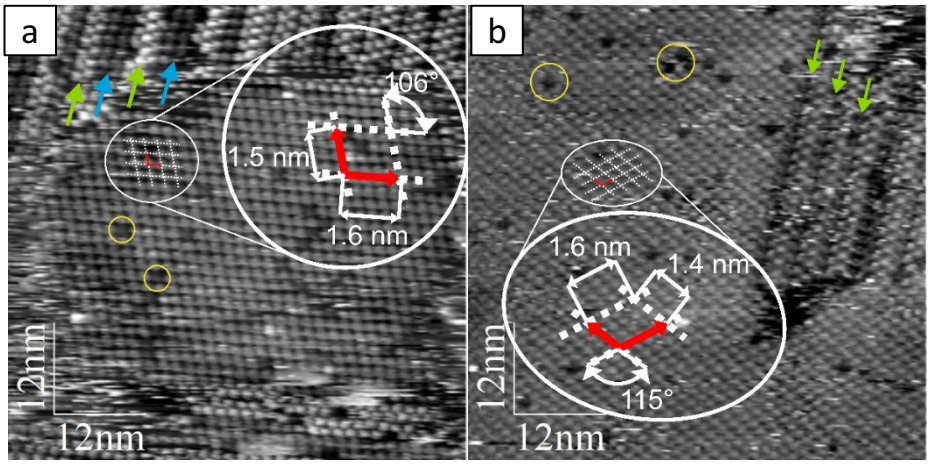

Figure 6.44. large-scale EC-STM image of FeTPP on HOPG in the case of deaerated 0.1 M $HClO_4$. Tunnelling parameters are: a) I_t = 0.47 nA, U_b = - 900 mV, E_{app} = OCP; b) I_t = 0.47 nA, U_b = - 700 mV, E_{app} = OCP.

A high-resolution image is brought forth for the FeTPP adlayer in contact with Ar purged electrolyte (figure 6.45). It must be mentioned the presence of defects (molecular clusters), as noticeable from the yellow circle. The yellow dashed line stands for the topographic profile hereafter reported, which shows that each FeTPP molecule features a

central protrusion of about 50 pm. Actually, this value is less than half compared to the parent FeOEP previously described, even if the two molecules differ only for the peripheral substituents. It is clear that this difference cannot arise from a difference in electron population of *d* orbitals, to the very same metallic centre, same oxidation state and same initial axial ligand (chloride). The part of ligand which is in direct contact with the Fe centre is also the same, namely the porphyrin ring. The only difference lies in the peripheral substituents, both in their number and in their position. In this case, the substituents are four, and they find themselves at the *meso* position of the porphyrin ring. Moreover, the phenyl substituents are certainly a more rigid system (sp^2 bonds) with respect to the alkyl one (ethyls, sp^3 bonds). The fact that octaethylporphyrin and tetraphenylporphyrin differ for just a handful of atoms should not be underestimated, because just one atom can lead to significantly different results in terms of unit cell parameters [58,89–93]. A further unneglectable example is given by adsorption of free-base tetraphenylporphyrin on Cu(111)[94]. Basically, it was revealed that a coordination occurs with the two iminic nitrogen atoms to the Cu(111) surface via their lone pairs, and this phenomenon leads to a decisively different STM contrast, which passes from a "saddle shape" to an "inverted shape"[94].

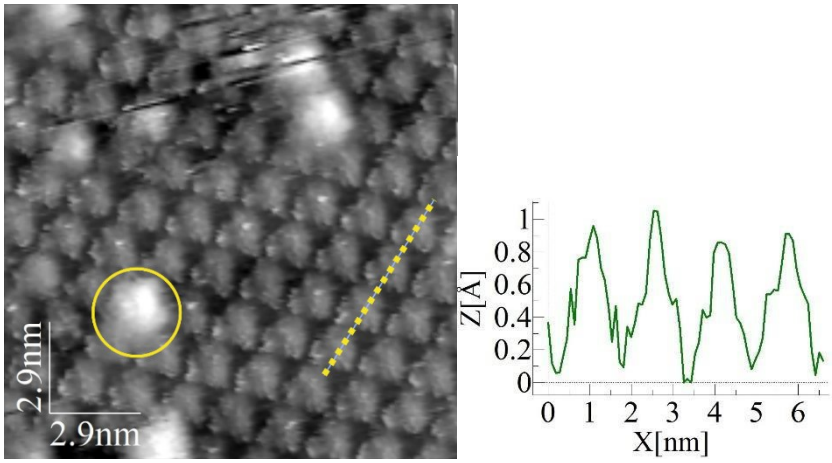

Figure 6.45. high-resolution EC-STM image of FeTPP on HOPG in the case of deaerated 0.1 M $HClO_4$. Tunnelling parameters are: I_t = 0.70 nA, U_b = - 200 mV, E_{app} = OCP.

Potentiodynamic imaging in deaerated electrolyte was conducted on the FeTPP adlayer (figure 6.46). Large size pictures were collected to better evidence a phenomenon of surface mobility. In fact, image 45.a was collected at E_{app} = 0.60 V vs RHE, and a unique defect consisting of alternated domains. For the sake of clarity, this portion is enclosed in a white dashed rectangle. Upon lowering the applied working electrode potential first to E_{app} = 0.50 V vs RHE and then to 0.45 V vs RHE, this portion of molecules undergoes significant changes. In particular, at E_{app}= 0.45 V vs RHE, this portion completely separates from the original large domain and starts to migrate outward. At this point part of the molecules desorb, also considering the disturbing effect of the tunnelling tip, and another part attaches to the external border of the domain. Anyway, a hole remains in lieu of the original alternating lines-domain.

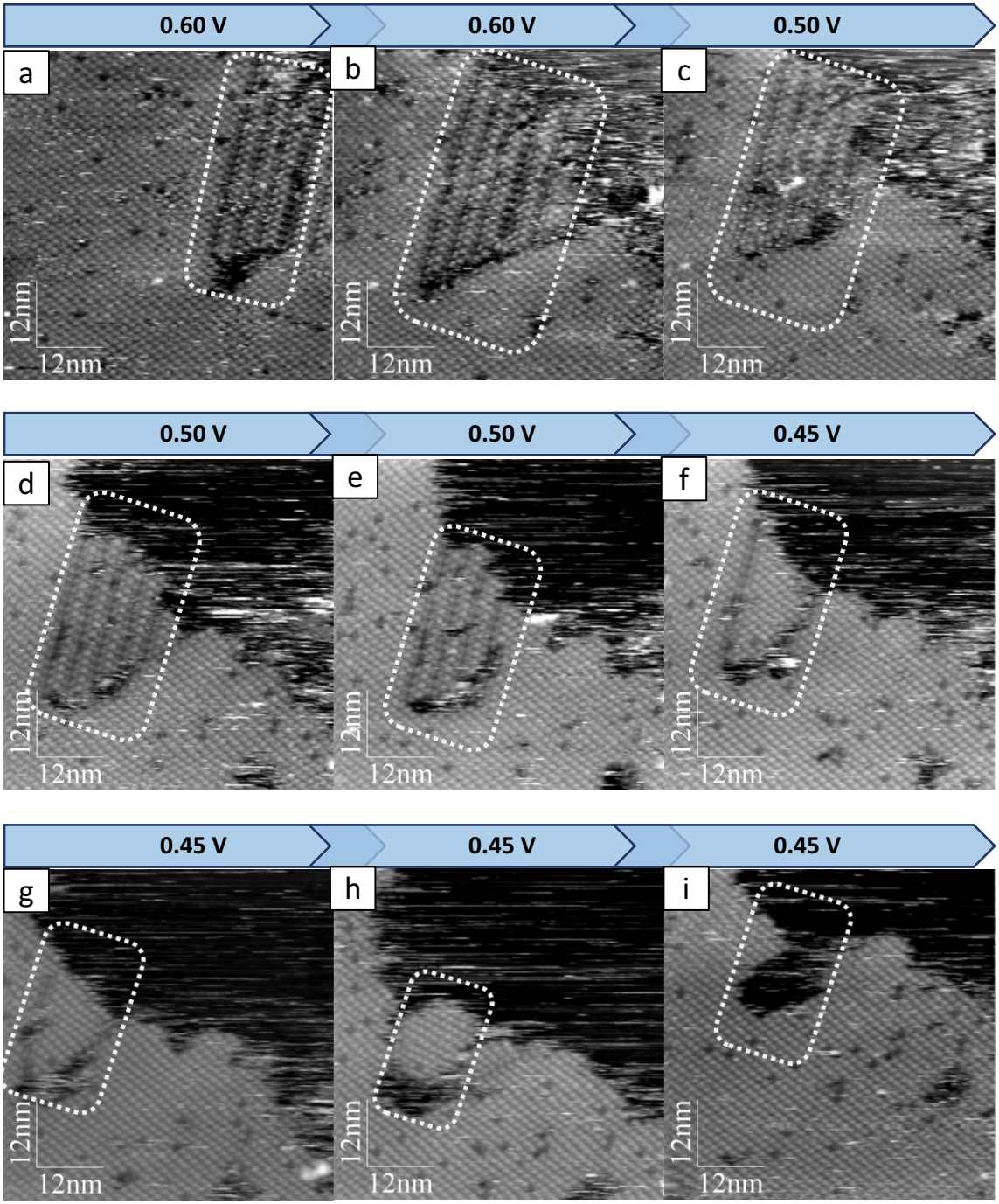

Figure 6.46. large-scale EC-STM images obtained under potential control for a FeTPP adlayer adsorbed on HOPG in the case of deaerated 0.1 M $HClO_4$. Tunnelling parameters for all images are: I_t = 0.47 nA, U_b = 150 mV vs RHE. The applied potential is: a) E_{app} = 0.60 vs RHE; b) E_{app} = 0.60 V vs RHE; c-e) E_{app} = 0.50 V vs RHE; f-i) E_{app} = 0.45 V vs RHE.

The tetraphenylporphyrin being a different ligand compared to octaethylporphyrin, and the multiple defects being detected in large scale images, made difficult to obtain satisfactory high-resolution images, both for Ar purged and O_2 saturated electrolyte. Therefore, pictures regarding the aforementioned cases are not presented, demanding their analysis in future publications.

In conclusion, FeTPP was successfully functionalised on a HOPG substrate, but incomplete monolayers were encountered. Large size STM images confirmed an evident effect of surface mobility mediated by the applied electrode potential. The high-resolution picture presented a clear difference with respect to FeOEP, although sharing the same metal centre within the same oxidation state and axial ligand (in crystal form), attesting a crucial role also of peripheral group in determining the tunnelling condition at the metal center. The change of contrast was probably mediated by a rather different external ligand, namely the tetraphenylporphyrin.

6.1.11 EC-STM investigation of a mixed FeOEP / FeTPP adlayer at HOPG

Despite an incomplete study of the pure FeTPP adlayer, tentative experiments on an intermixed layer consisting of FeOEP and FeTPP were conducted. The results, although far from being exhaustive and complete, are anyway worth to be presented.

A mixture of FeOEP and FeTPP solutions was then realised, in order to obtain a final metal porphyrin solution with 0.1 mM concentration. The so-obtained mixed solution was drop-casted on the freshly cleaved HOPG surface, and the sample was let rest for 30 min. After that, an Ar flux was placed over the surface to make the DMF droplet dry. This functionalised HOPG specimen was probed by EC-STM, with the aim to reveal differences with respect to the pure FeOEP and FeTPP systems. This experiment also allows to evaluate, at least from a qualitative point of view, the effect of the ligand onto the physisorption process. It also allows us to understand the role of molecule-molecule interactions, considering that in this case these interactions are asymmetric due to the different ligands.

Due to these new aspects to be taken into account, the analysis of the obtained STM images must be conducted with additional care, and a higher number of images is required to obtain trustworthy results. For this reason, the images hereafter reported are meant to give a first and partial presentation of this complex system, and additional experiments will be conducted to complete the information, especially concerning the O_2 electrolyte saturation case, which is excluded from the following description.

A large-scale image is reported in figure 6.47a, together with sketched unit cell parameters, which are: $\overrightarrow{b_1} = (1.5 \pm 0.1)\, nm$ and $\overrightarrow{b_2} = (1.6 \pm 0.1)\, nm$, the measured angle between the two vectors is $\measuredangle = (113 \pm 2)°$. The surface concentration is $4.53 * 10^{13}\ molecules\ cm^{-2}$ and the corresponding surface coverage is $\theta = 0.012$.

As visible from figure 6.47a, the adlayer is almost fully covering the HOPG surface, and a peculiar contrast is evident. Namely, some molecules appear bright, some others appear dark. At a first glance, it seems easy to associate bright molecules to FeOEP and dark molecules to FeTPP, since the corresponding single component adlayers were exhibiting a similar contrast (bright for FeOEP and darker for FeTPP), but a more quantitative analysis through topographic profile comparison is needed. Therefore, a topographic profile was extracted from a high resolution STM image, shown in figure 6.47.b. The contrast difference is very sharp, and the extracted topographic profile is in accordance

with those of the single component adlayers. FeOEP shows a protrusion of about 150 pm, whereas FeTPP protrudes of only 50 pm. At a first impact, it appears strange that two very similar systems, both featuring a Fe(III) centre and a porphyrin ring (with different peripheral substituents), give such a different STM contrast. However, in the previous section 6.1.10, it had been pointed out that a handful of atoms could imply an impacting difference on the final STM contrast. Therefore, it appears that the two different components do not directly interact and try to maintain their characteristic at the single molecular levels, confirmed by the topographic profiles comparable to the pure systems.

Both figure 6.47.a and 6.47.b show that the population of the two porphyrins is similar. Indeed, the intermixed solution was formed by equal parts of FeOEP and FeTPP. In figure 6.47.a, a particularly extended FeOEP domain can be found on the right portion of the image, but also the corresponding FeTPP counterparts were found on other HOPG areas, as a confirmation of an almost 50/50 population.

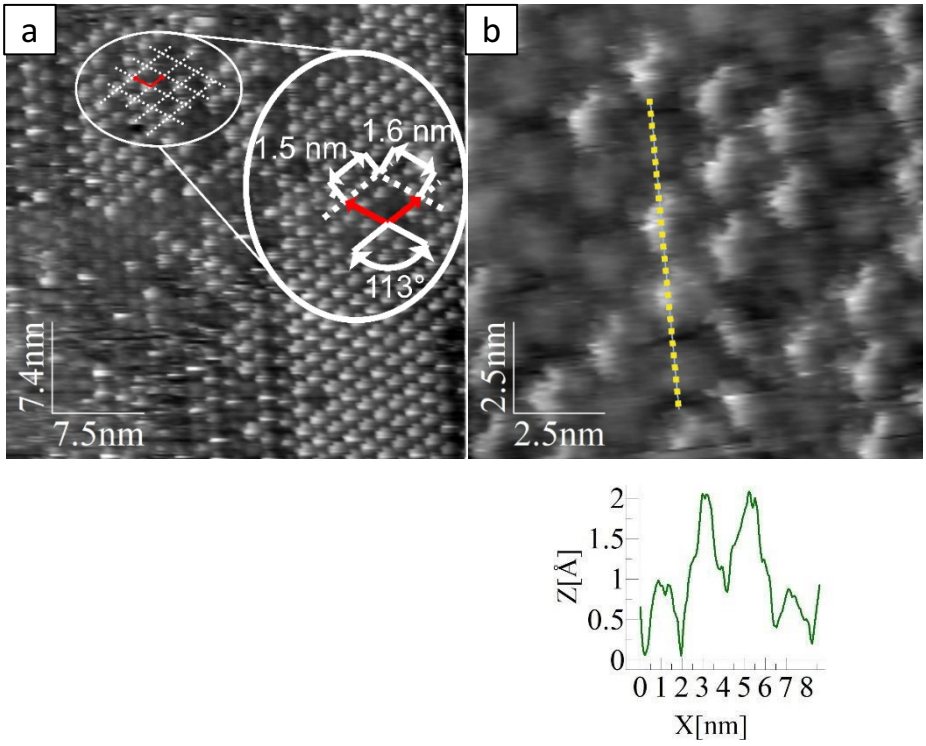

Figure 6.47. a) large-scale EC-STM image of a mixed FeOEP / FeTPP adlayer on HOPG in the case of deaerated 0.1 M $HClO_4$. Tunnelling parameters are: I_t = 0.47 nA, U_b = - 700 mV, E_{app}= OCP; b) high-resolution EC-STM image of a mixed FeOEP / FeTPP on HOPG in the case of deaerated 0.1 M $HClO_4$. Tunnelling parameters are: I_t = 0.47 nA, U_b = - 700 mV, E_{app} = OCP. The topographic profile corresponding to the yellow dashed line is reported below in the insert.

The intermixed adlayer consisting of FeOEP and FeTPP enables to directly compare two porphyrins featuring the same metal centre (Fe). The pure components were previously analysed, and differences emerged both for the molecular ordering and for the high-resolution features. The intermixed layer seemed to preserve these differences, but this analysis still lacks of O_2 saturated electrolyte characterisation.

6.1.12 Final considerations

This section summarises the main observations from in situ STM measurements on different porphyry systems. In particular, it was observed that:

- Porphyrins having an active redox metal centre are visualised with different contrast depending on the redox state of the metal.
- Porphyrins with a metal centre capable of adsorption of oxygen and carbon monoxide, or more generally of a ligand in an axial position, are visualised with different contrasts.
- The condition of having an active redox metal centre is sufficient but not necessary for observing oxygen adsorption. It is also essential to have a charge backdonation from the metal center to the π* of the axial ligand. This was well observed when comparing FeOEP with CuOEP and then PtOEP with CuOEP.
- The peripheral ligands of the porphyrin ring influence the tunnelling process and thus also the contrast at the metal centre, since the local density of the energy states is varied, but passing from TPP to OEP the difference in minimal
- The potential can change the surface arrangement of molecules e.g., from hexagonal to tetragonal as observed in particular with CoOEP.
- When the electrode potential is sufficient for triggering ORR, the metal center is visualized as free of oxygen. Being the process that fast, the image acquisition is not sufficiently fast to freeze the cyclical O_2 adsorption, reduction and modification of the redox state of the metal centre.

6.2 EC-STM investigation at Au(111) single crystal

6.2.1 EC-STM investigation of H_2OEP at Au(111)

The free-base octaethyl porphyrin is herein employed as a means of reference for the later presented metal-octaethylporphyrins, even if their number is lower if compared to HOPG substrate.

A free-base octaethyl porphyrin 0.1 mM solution in DMF was prepared and the newly flame-annealed Au(111) surface was placed in contact with this solution via the hanging meniscus method, leaving the surface to functionalise for 1 minute. After that, the surface was rinsed with ultrapure water and the sample was placed in the dedicated cell for EC-STM experiments.

An ordered self-assembled monolayer was obtained, as shown in figure 6.48. The unit cell parameters are also sketched, and they are: $\overrightarrow{b_1} = (1.6 \pm 0.1)\, nm$ and $\overrightarrow{b_2} = (1.4 \pm 0.1)\, nm$, the measured angle between the two vectors is $\measuredangle = (119 \pm 2)°$. The surface concentration is $5.10 * 10^{13}\, molecules\, cm^{-2}$ and the corresponding surface coverage is $\theta = 0.037$.

The monolayer is covering the entire Au(111) surface, without significant defects to be mentioned. The herringbone reconstruction is maintained under the molecular adlayer, pointing out the electrondonating effect of the octaethylporphyrin ligand. More in details, it is claimed that metal-octaethylporphyrins (and -tetraphenylporphyrins) are able to stabilise herringbone reconstruction pattern even at potentials more positive than expected, and this is possible thanks to an electron density donation from the porphyrin molecules to the Au(111) substrate. This effect has to be reconducted first of all to the ligand itself, being a large conjugated macrocyclic molecule. The metal centre also plays its role, as it will be further elucidated with PtOEP and FeOEP [37,59,85,95–99].

The hexagonal symmetry of the (111) facet is reflected also by the H_2OEP layer, whose unit cell presents an angle very close to 120°, therefore confirming a role of structure directing agent of the Au surface.

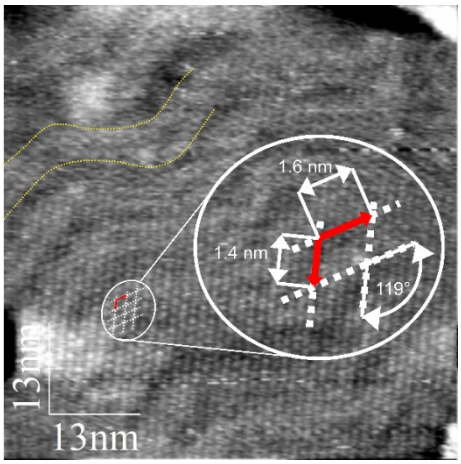

Figure 6.48. Large scale EC-STM image of H_2OEP on Au(111) in the case of deaerated 0.1 M $HClO_4$. Tunnelling parameters are: I_t = 1.54 nA, U_b = - 700 mV, E_{app} = OCP.

Smaller size images were collected with the aim to increase the STM resolution at the single molecule level. Moreover, the applied potential was varied and potentiodynamic imaging was therefore performed (figure 6.49). At an applied potential of E_{app} = 0.45 V vs RHE, the molecules show a dark spot in their centre, and the topographic profiles confirms the presence of a dip of 10-20 pm. Upon lowering the applied potential up to E_{app}= 0.25V vs RHE, no significant phenomenon occurs, the herringbone reconstruction remains visible beneath the molecular adlayer and the molecules continue to exhibit the dark spot in their centre. This to conclude that the free-base molecule is not going through any significant phenomenon on the Au(111) surface, even under potential control. Therefore, the hereafter presented metal-octaethylporphyrins owe their electrocatalytic activity almost exclusively to their specific central metal.

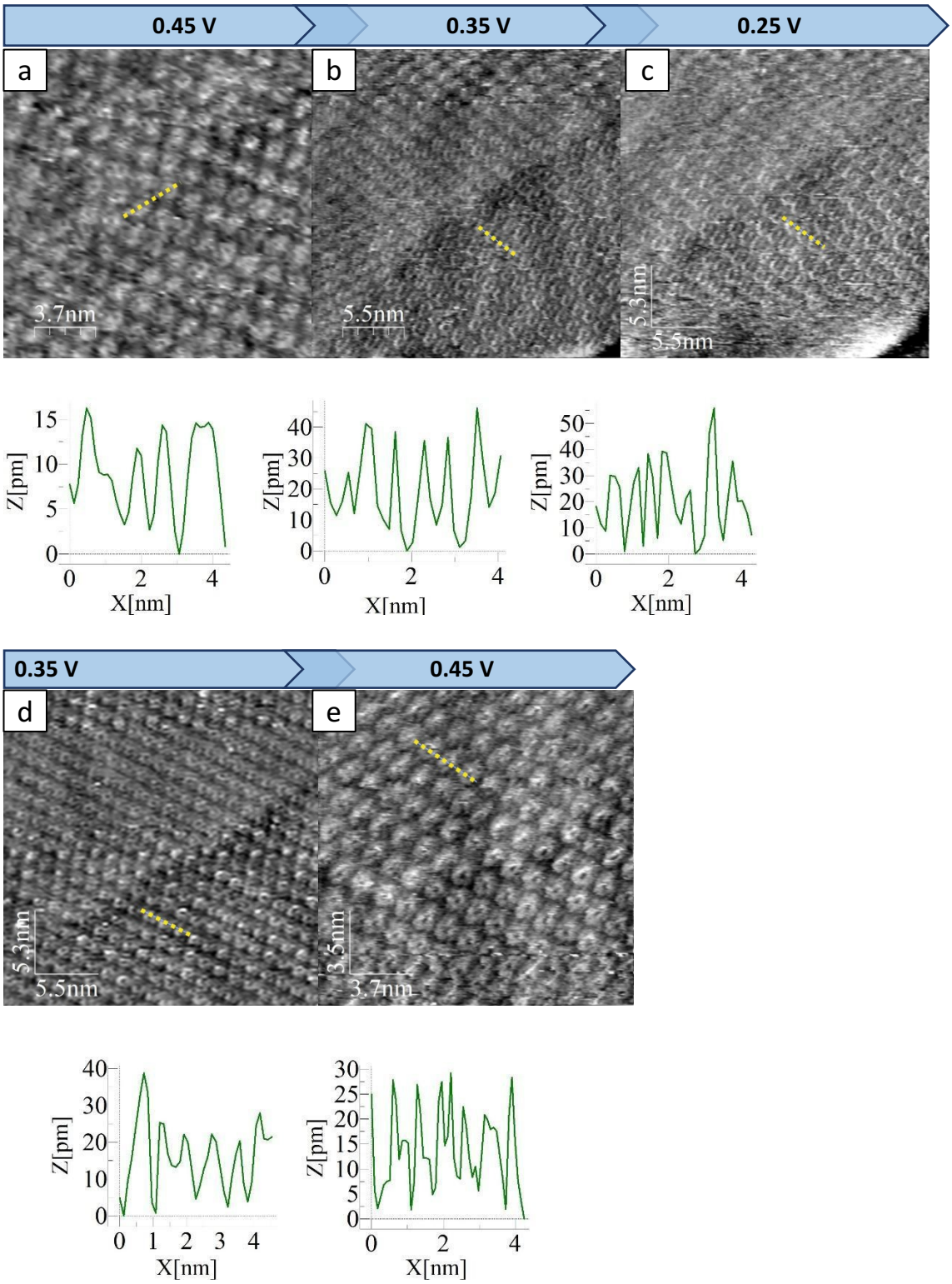

Figure 6.49. High-resolution EC-STM images under potential control of H_2OEP on Au(111) in the case of deaerated 0.1 M $HClO_4$. Tunnelling parameters are: I_t = 2.28 nA, U_b = + 300 mV vs RHE. Applied potential is: a) E_{app} = 0.45 V vs RHE; b) E_{app} = 0.35 V vs RHE; c) E_{app} = 0.25 V vs RHE; d) E_{app} = 0.35 V vs RHE; e) E_{app} = 0.45 V vs RHE.

H_2OEP was successfully functionalised on the (111) facet of gold single crystal. Molecules fully covered the Au(111) terraces, and herringbone reconstruction pattern was maintained under the adlayer, demonstrating the electron-donating effect of free-base octaethylporphyrin. High resolution images confirmed the absence of a metal centre thanks to the imaged black depression.

6.2.2 EC-STM investigation at PtOEP on Au(111)

A 0.1 mM Pt(II) octaethylporphyrin solution in DMF was used to immerse the newly flame-annealed Au(111) surface by a hanging meniscus method. After 1 minute of functionalisation, the surface was rinsed and the sample was inserted in the dedicated cell for EC-STM characterisation.

Wide and highly ordered self-assembled monolayers were found on the Au(111) surface, as visible from figure 6.50. In both images, the herringbone reconstruction is well perceivable beneath the PtOEP adlayer. Stabilisation of herringbone reconstruction had been already observed [95]. Compared to the previously analysed free-base octaethylporphyrin, herringbone lines are far more evident and sharper. This is not surprising: having already stated that herringbone presence depends on the electron donation ability of the porphyrin, it is clear that the presence of Pt, with its additional filled *5f* orbital, adds a significant contribution to the donated electron density [95].

Almost no defects were encountered, even domain boundaries were hardly discovered. This is a common point for PtOEP deposited on HOPG and it can be explained with a stronger molecule-molecule interaction rather than molecule-substrate one, as previous works also demonstrate [74,95].

The unit cell parameters are sketched in both figure 6.50.a and 6.50.b. The two images gave slightly different values for the unit cell vector, even if they were in the uncertainty interval of the measurement. Hence, it is prudential to ascribe it to a drift-related effect, and not to a really different adlayer geometry. Therefore, the unit cell parameters are: $\overrightarrow{b_1} = (1.6 \pm 0.1)\, nm$ and $\overrightarrow{b_2} = (1.7 \pm 0.1)\, nm$, the measured angle between the two vectors is $\measuredangle = (62 \pm 2)°$. The surface concentration is $4.16 * 10^{13}\ molecules\ cm^{-2}$ and the corresponding surface coverage is $\theta = 0.030$.

The (111) facet exerts a structure directing effect on the molecular layer, which maintains the hexagonal symmetry, with a unit cell vector very close to 60°. The yellow dashed lines are meant to follow one herringbone reconstruction ridge.

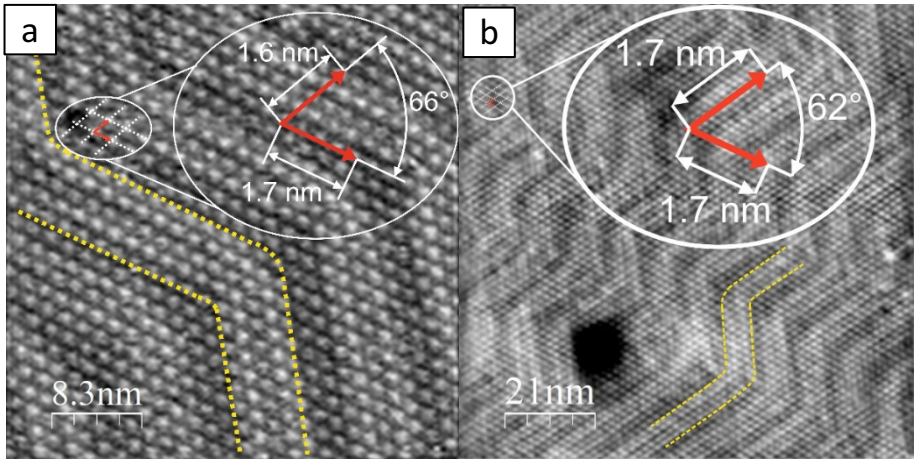

Figure 6.50. Large scale EC-STM image of PtOEP on Au(111) in the case of deaerated 0.1 M $HClO_4$. Tunnelling parameters are: a,b) I_t = 0.70 nA, U_b = - 50 mV vs RHE, E_{app} = 0.55 V vs RHE.

High resolution EC-STM pictures were collected under potential control (figure 6.51). At Eapp = 0.55 V vs RHE, molecules appear as bright circles, without a significant feature. The extracted topographic profile, indeed, indicates the presence of protrusion of just 20-30 pm, which remains so up to Eapp = 0.05 V vs RHE. The presence of a protrusion instead of a depression had been already elucidated in section 6.1.7.

At Eapp = 0.05 V vs RHE, the layer remains stable on the Au(111) surface, but the contrast changes, showing rather flat molecules without any height feature. Upon increasing the potential to 0.55 mV, the initial contrast is restored, with the 20-30 pm protrusion, too.

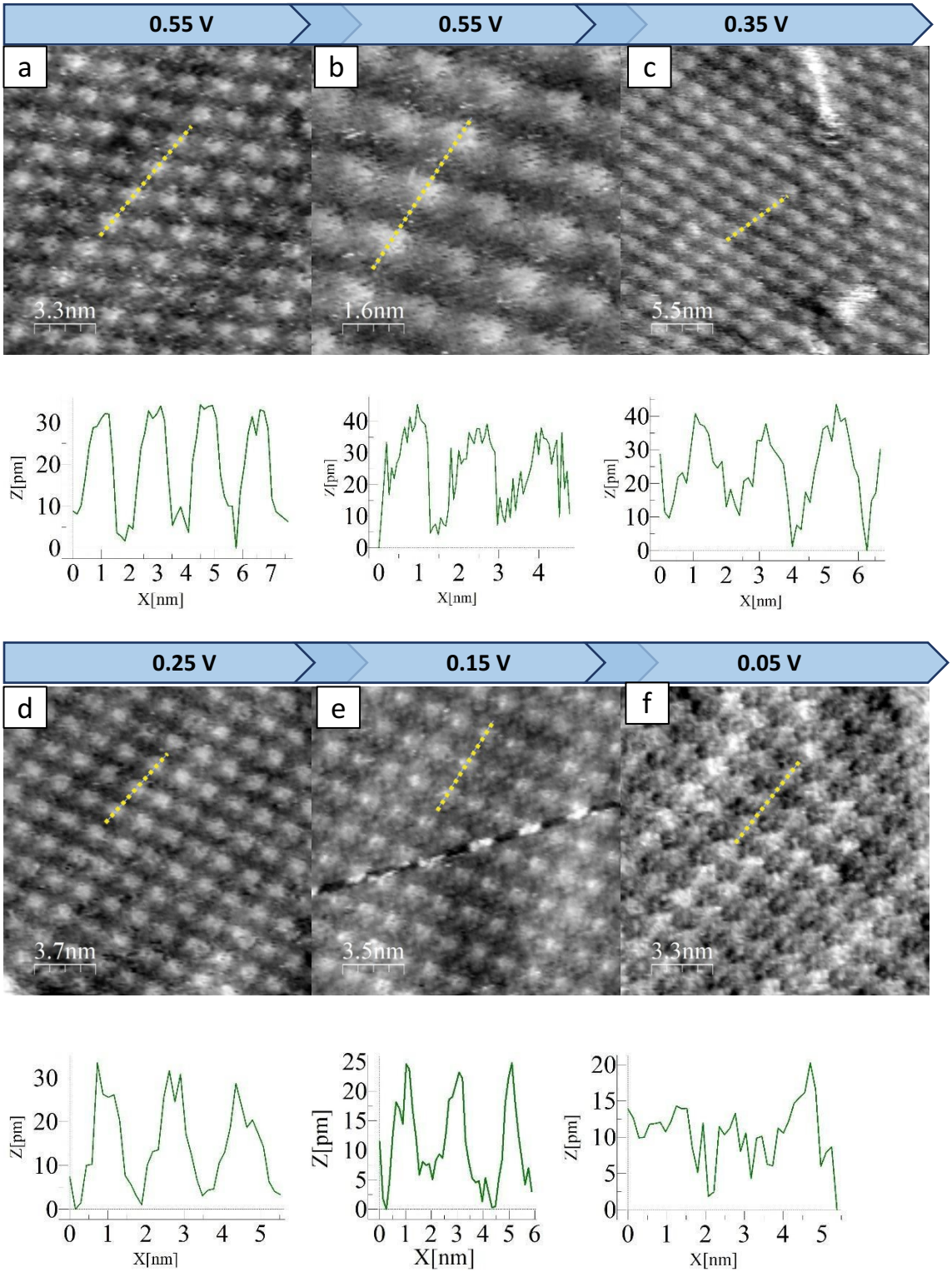
0.55 V
0.55 V
0.35 V
a
b
c
3.3nm
1.6nm
5.5nm
Z[pm]
X[nm]
0.25 V
0.15 V
0.05 V
d
e
f
3.7nm
3.5nm
3.3nm

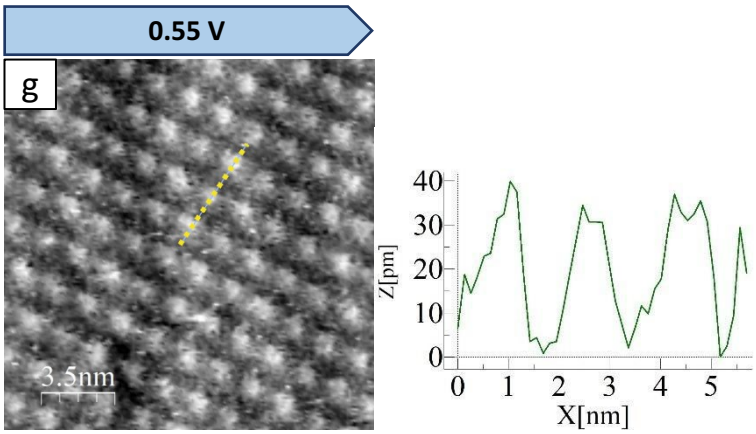

Figure 6.51. Large scale EC-STM images obtained under potential control of a PtOEP adlayer adsorbed on Au(111) in deaerated 0.1 M $HClO_4$. Tunnelling parameters are: I_t = 0.7 nA, U_b = - 50 mV vs RHE. Applied potential is: a-b) E_{app} = 0.55 V vs RHE; c) E_{app} = 0.35 V vs RHE; d) E_{app} = 0.25 V vs RHE; e) E_{app} = 0.15 V vs RHE; f) E_{app} = 0.05 V vs RHE; g) E_{app} = 0.55 V vs RHE.

A high-resolution picture is now presented for the PtOEP adlayer in contact with O_2 saturated electrolyte (figure 6.52). The central spot appears brighter, and the extracted topographic profile confirms a higher profile, in the range of 50-60 pm.

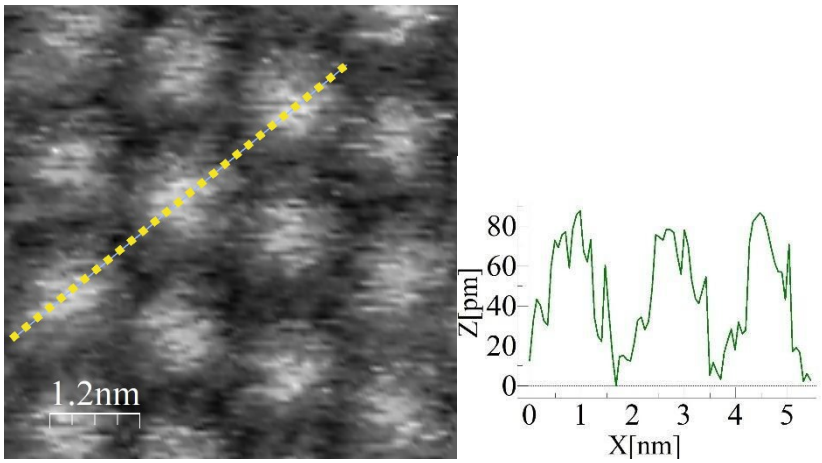

Figure 6.52. high-resolution EC-STM image of PtOEP on Au(111) in O_2 saturated 0.1 M $HClO_4$. Tunnelling parameters are: I_t = 0.7 nA, U_b = - 50 mV vs RHE, E_{app} = 0.55 V vs RHE.

Upon recording high resolution pictures at different applied potentials, potentiodynamic images were obtained (figure 6.53). At E_{app} = 0.55 V vs RHE molecules present the aforementioned protrusion of 50-60 pm, which should be an indication of O_2 adsorption. This bright spot, and subsequently the associated protrusion, are maintained up to Eapp = 0.05 V vs RHE, at which the layer is still stable but the contrast changes on the single molecules, with an associated rather flat topographic profile.

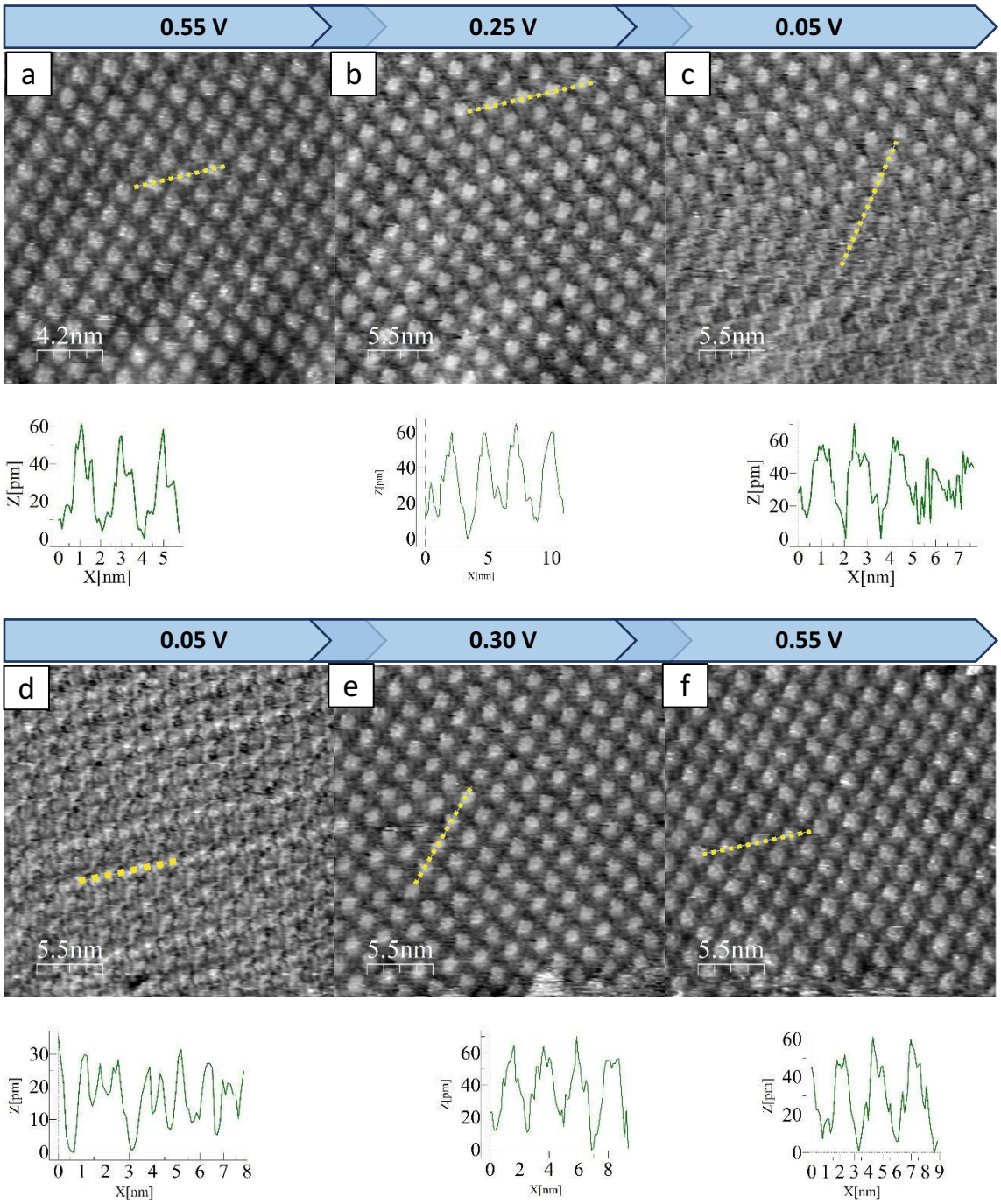

Figure 6.53. High-resolution EC-STM images obtained under potential control of a PtOEP adlayer adsorbed on Au(111) in the case of deaerated 0.1 M $HClO_4$. Tunnelling parameters are: I_t = 5 nA, U_b = 0 mV vs RHE. Applied potential is: a) E_{app} = 0.55 V vs RHE; b) E_{app} = 0.25 V vs RHE; c,d) E_{app} = 0.05 V vs RHE; e) E_{app} = 0.30 V vs RHE; f) E_{app} = 0.55 V vs RHE.

Very extended PtOEP monolayers were observed on the Au(111) substrate. The almost total absence of domain boundaries indicated a stronger role of molecules-molecules interactions at the expense of molecules-substrate interactions. As already discussed for PtOEP-functionalised HOPG, the manifestation of a protrusion for Pt centres represents an apparent contradiction if one reminds of the fully occupied $5dz^2$ orbital.

High resolution pictures in O_2 saturated electrolyte confirmed the tendency to bind O_2 due to an enhanced protrusion with respect to the Ar case.

To have a more complete overview of PtOEP behaviour, a simple scheme showing the modulation of the topographic protrusion upon variation of the applied electrode potential is shown in figure 6.54. Both O_2-free and O_2-saturated experimental results were reported, indicated with black and red symbols, respectively. From each image collected at a certain potential, two to four values of protrusion were measured, so that the data points are presented as averages with an associated confidence interval calculated as maximum semidispersion. What is immediately visible is that PtOEP molecules in deaerated electrolyte exhibit slight topographic profile variations, while in presence of O_2 the protrusion is not only significantly higher, but it undergoes a considerable drop in correspondence of the ORR peak potential. This enables to highlight the dynamic nature of O_2 adsorption and reduction, which EC-STM aims and succeeds in characterising.

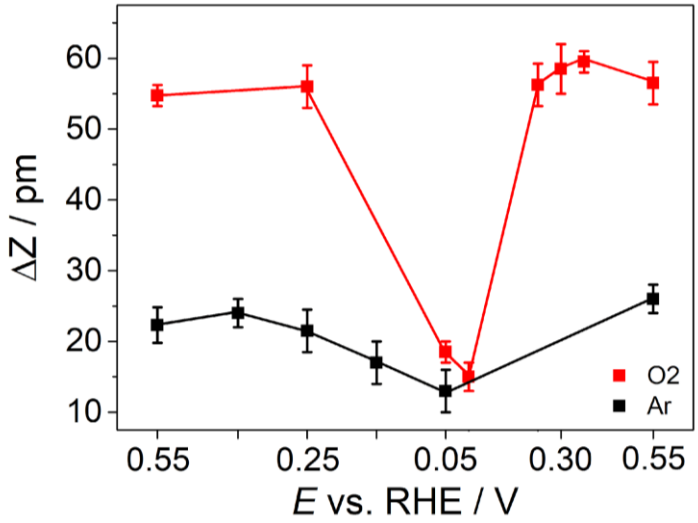

Figure 6.54. Scheme of the measured topographic profile protrusion of PtOEP adlayer adsorbed on Au(111). Black symbols refer to deaerated electrolyte cse, whereas red ones refer to O_2 electrolyte saturation case.

6.2.3 EC-STM investigation of FeOEP at Au(111)

A 0.1 mM Fe(III) octaethylporphyrin chloride solution in DMF was put in contact by hanging meniscus with the newly flame-annealed Au(111) surface. This functionalisation lasted 60 seconds, and the result is shown in figure 6.55.

Figure 6.55 shows that FeOEP builds up large ordered domains, but a higher number of defects can be perceived with respect to PtOEP. Herringbone reconstruction is still present under the molecular layer. The unit cell parameters, as sketched in figure 6.55, are: $\overrightarrow{b_1} = (1.7 \pm 0.1)\ nm$ and $\overrightarrow{b_2} = (1.7 \pm 0.1)\ nm$, the measured angle between the two vectors is $\measuredangle = (118 \pm 2)°$. The angle is close to 120°, again confirming the templating effect of the hexagonally arranged (111) facet. The surface concentration is $3.92 * 10^{13}\ molecules\ cm^{-2}$ and the corresponding surface coverage is $\theta = 0.028$.

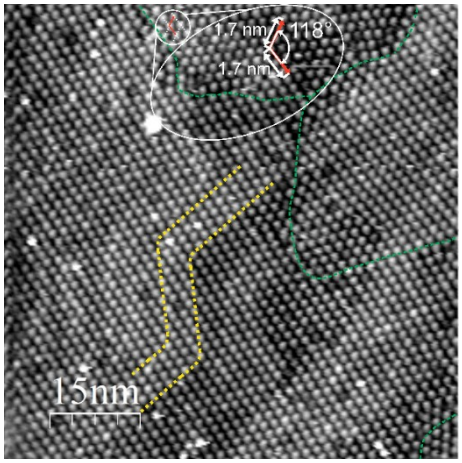

Figure 6.55. large scale EC-STM image of FeOEP on Au(111) in the case of deaerated 0.1 M $HClO_4$. Tunnelling parameters are: a) I_t = 1 nA, U_b = - 650 mV, E_{app} = OCP.

A closer view to the single molecule level shows that the Fe centre appears with a protrusion in the range of 40-60 pm, as confirmed by the topographic profiles extracted by figure 6.56.a and 6.56.b.

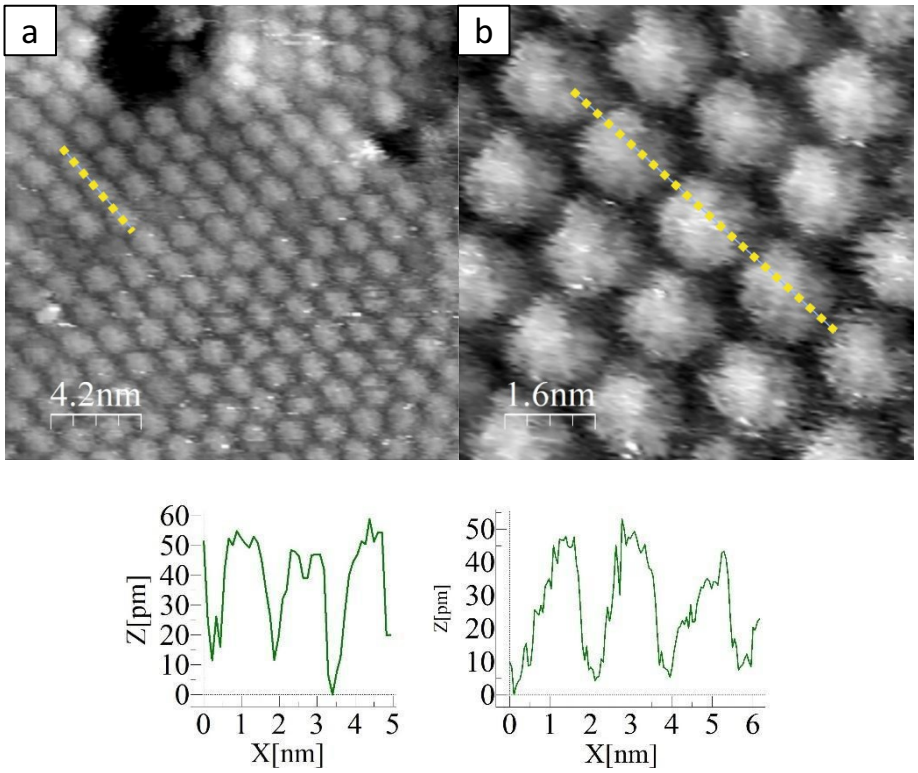

Figure 6.56. high resolution EC-STM image of FeOEP on Au(111) in the case of deaerated 0.1 M $HClO_4$. Tunnelling parameters are: a) I_t = 1.54 nA, U_b = - 650 mV vs RHE, E_{app} = 0.65 V vs RHE; b) I_t = 2.28 nA, U_b = - 650 mV, E_{app} = OCP.

The FeOEP@Au(111) adlayer was subjected to potentiodynamic imaging in deaerated electrolyte. Multiple potential sweeps were accomplished, since a peculiar STM contrast variation with the applied potential was noticed. Namely, a compresence of brighter and

darker molecules was present at E_{app} =0.65 V vs RHE. The brighter features possessed a protrusion of 50-60 pm, ascribable to previously determined Fe species. When the potential was made more negative, the number of bright molecules decrease in favour of the number of dark molecules, which increased. At E_{app} =0.25 V, almost all molecules appeared dark. Then, returning to a more positive potential up to E_{app} =0.85 V vs RHE, the bright/dark population dynamically changed, passing from completely dark molecules to almost completely bright ones. Topographic profiles, reported under each respective image, obviously confirmed the visual data evaluation. To properly interpret this series of images, it is necessary to recall the cyclic voltammogram recorded for FeOEP@Au(111) adlayer in deaerated electrolyte (figure 5.26a). EC-STM images were collected in the same potential range of CV, and a reduction peak could be noticed commencing at Eon≈0.20 V vs RHE, with a peak potential at EFe,Ar,red = 0.36 V vs RHE. the presence of a corresponding oxidation peak led to assess this CV features to the redox behaviour of the Fe centre. In light of this, the STM contrast can now be more safely interpreted. It is believed that the bright features, mostly present at positive potential, should be associated to oxidised Fe centres, i.e. Fe(III), while darker features should be addressed as reduced Fe centres, i.e Fe(II). The gain/loss of one electron by Fe centres therefore determines a different orbital population, and tunnelling is consequently affected. This bright/dark contrast was quantified in a histogram reported in figure 6.58: for each image of figure 6.57, the number of bright and dark molecules was manually counted. Each image may differ in the total number of molecules due to slightly shifted scan area or to unclear portions. Indeed, a small substrate hole was used as reference point to obtain consecutive images in the very same area, but small drift at the nanometric level should be in any case taken into account.

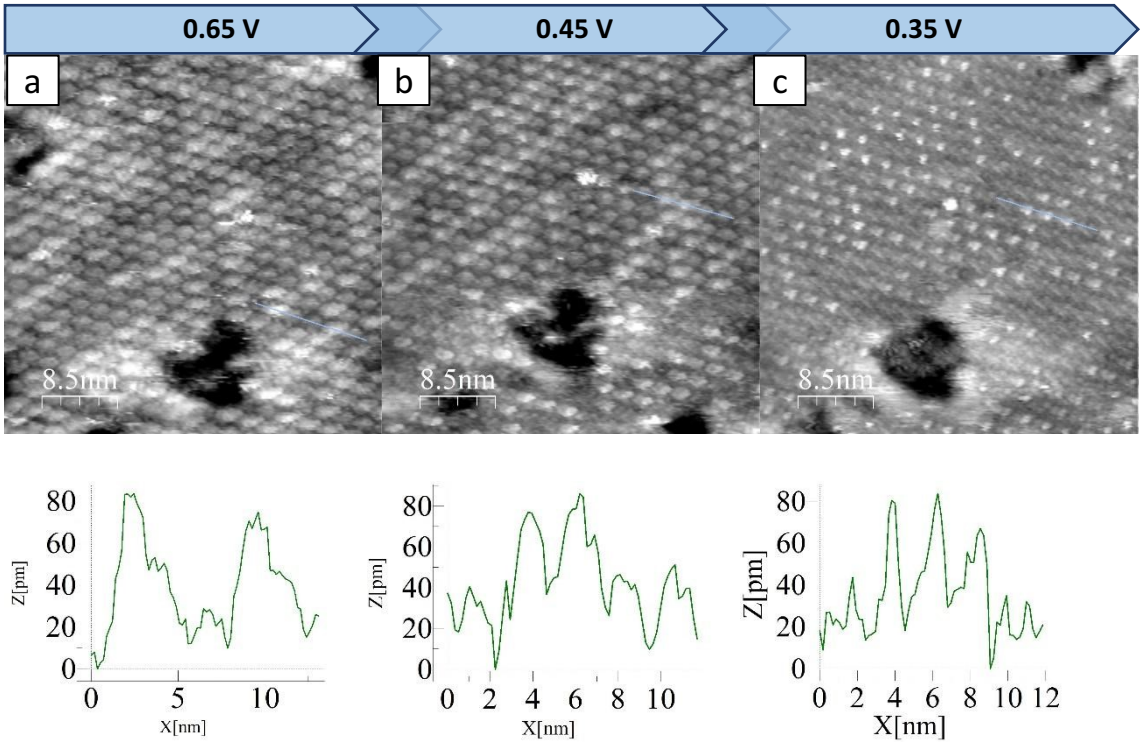

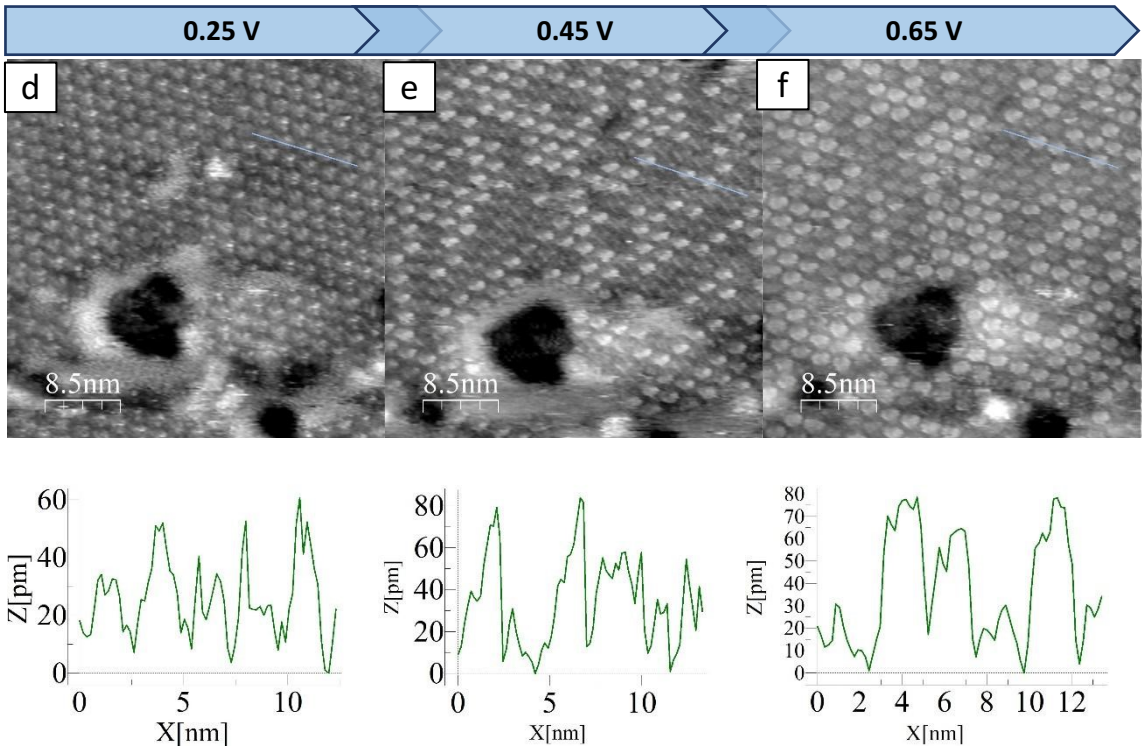
0.25 V
0.45 V
0.65 V
d
e
f
8.5nm
8.5nm
8.5nm
Z[pm]
X[nm]

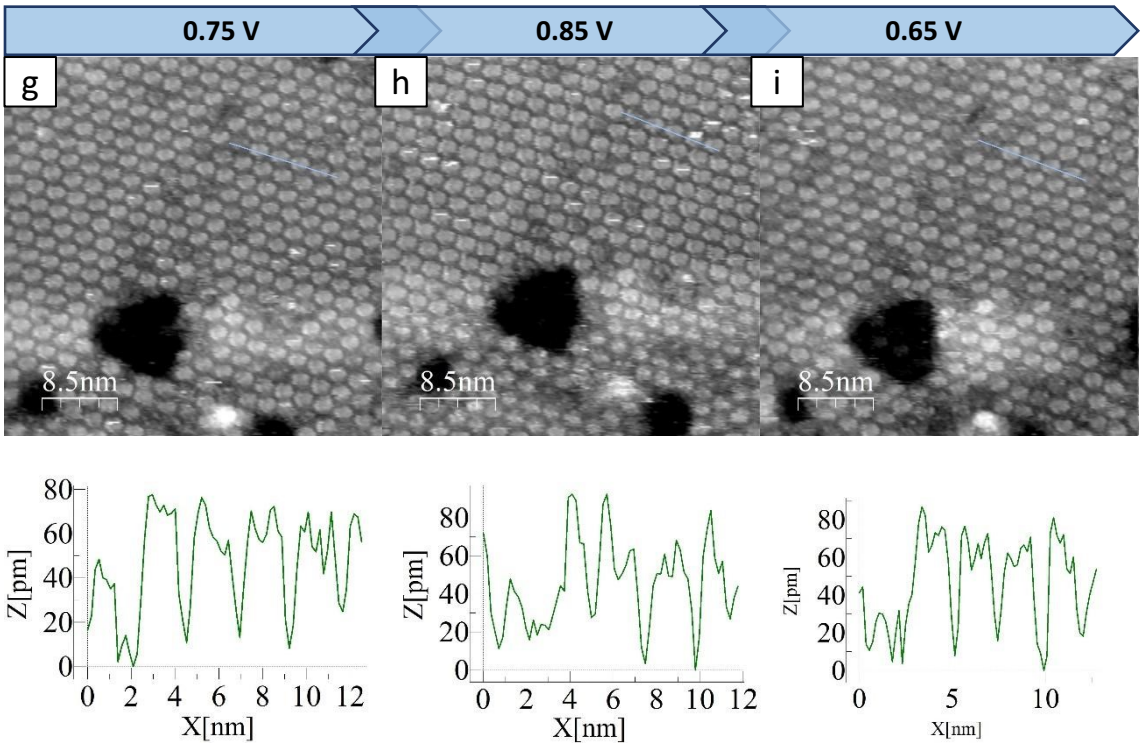
0.75 V
0.85 V
0.65 V
g
h
i
8.5nm
8.5nm
8.5nm
Z[pm]
X[nm]

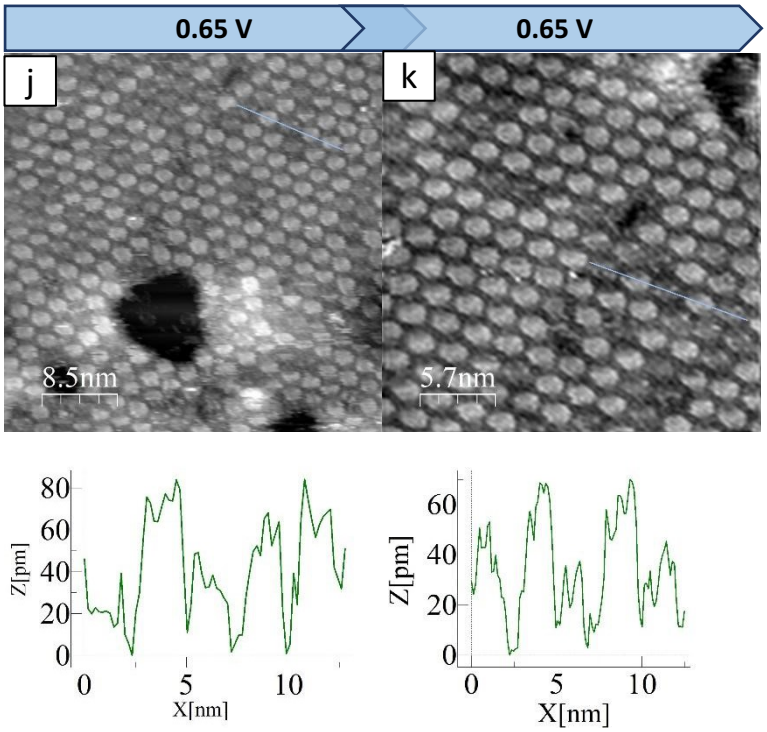

Figure 6.57. EC-STM images of FeOEP@Au(111) collected under potential control, whose variation is indicated by superimposed blue arrows. For all images, the tunnelling parameters are: I_t = 5 nA, U_b = +150 mV vs RHE. Applied potential is: a) E_{app} = 0.65 V vs RHE; b) E_{app} = 0.45 V vs RHE; c) E_{app} = 0.35 V vs RHE; d) E_{app} = 0.25 V vs RHE; e) E_{app} = 0.45 V vs RHE; f) E_{app} = 0.65 V vs RHE; g) E_{app} = 0.75 V vs RHE; h) E_{app} = 0 V vs RHE; i-k) E_{app} = 0.65 V vs RHE.

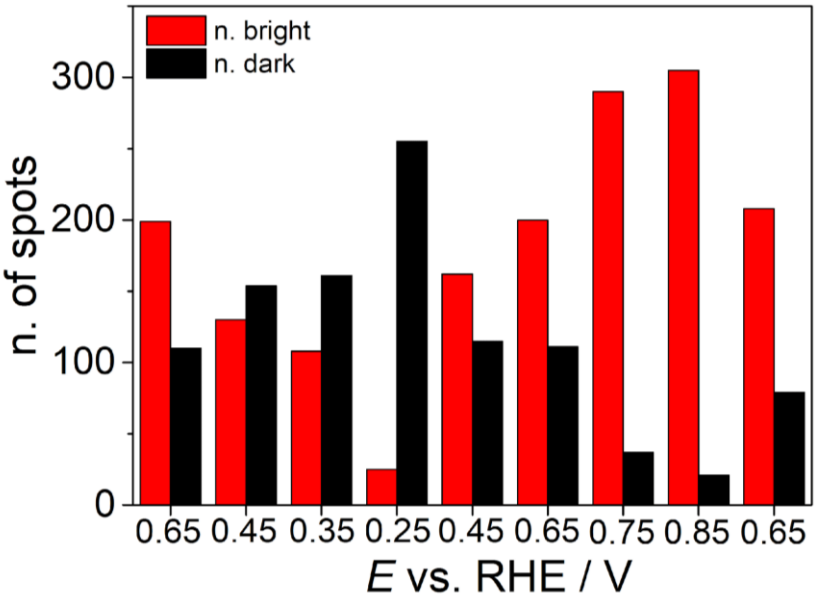

Figure 6.58. histogram of the bright/dark molecular population. The number of bright and dark molecules are reported for each measured potential, and it was obtained upon manual counting.

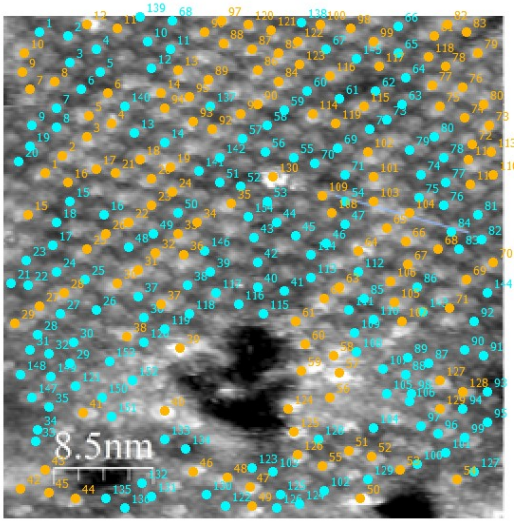

Figure 6.59. Example of one-by-one counting for one STM image of figure 56. In each figure two populations of molecules were counted, indicating in blue the dark-contrast molecules and in orange the bright-contrast ones. This counting procedure was conducted on each image of figure 6.57, leading to the histogram of figure 6.58.

The high-resolution image of FeOEP adlayer in O_2 saturated electrolyte is reported in figure 6.60. This image was recorded after a partial saturation with O_2 of the electrolyte. In fact, an O_2 stream was introduced in the STM chamber, letting it partially saturate the electrolyte for at least 30 minutes. After that, EC-STM images were collected, and an example is shown in figure 6.60. In this figure, at a first glance two different kinds of molecules can be identified. Most of the molecules appear with a bright protrusion, shifted from the molecular centre. These protrusions are associated with the presence of an oxygen molecule bonded with an iron centre, therefore constituting the first step of the ORR electrocatalysis. Another part of the molecule appears darker, and a topographic profile was extracted trying to include both bright and dark molecules. The outcome is shown on the right part of figure 6.60, noticing high protrusions of 80-100 pm, and lower protrusions of 30-50 pm. The lower protrusions correspond to the previously characterised FeOEP layer in Ar saturated electrolyte, so the higher profile herein determined can be ascribed to the O_2 presence onto the catalytic site.

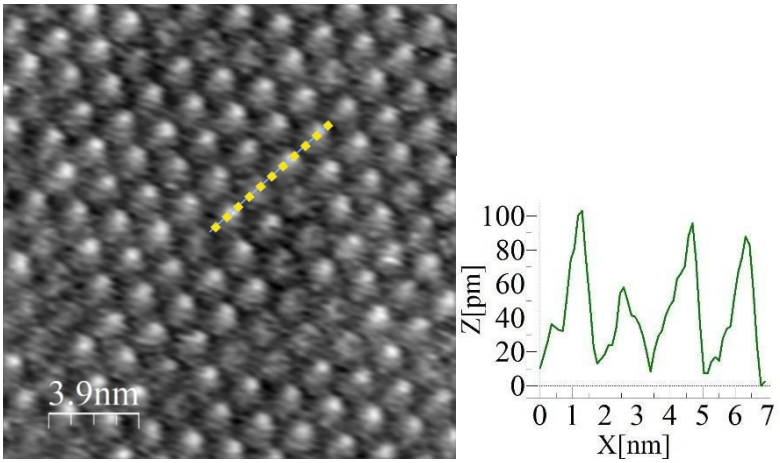

Figure 6.60. High-resolution EC-STM image of FeOEP on Au(111) in the case of O_2 saturated 0.1 M $HClO_4$. Tunnelling parameters are: a) I_t = 3.38 nA, U_b = - 700 mV, E_{app} = 0.65 V vs RHE.

A set of potentiodynamic images collected in O_2 saturated electrolyte is now presented in figure 6.61. At Eapp=0.65 V vs RHE mV, the molecules are imaged with the bright spot associated with the presence of O_2. Upon lowering the potential to 0.35 V vs RHE, the Faradaic current increases due to the incoming ORR peak, and the STM contrast changes, with a certain number of molecules becoming darker. At Eapp=0.25 V vs RHE (fig 57.c) and even further at Eapp=0.15 V vs RHE, the contrast completely changes, with some molecules featuring a hole in their centre, as confirmed by the extracted topographic profile. This is compatible with the absence of O_2 molecules from the Fe centre and also with the subsequent reduction of Fe(III) to Fe(II) [50,100].

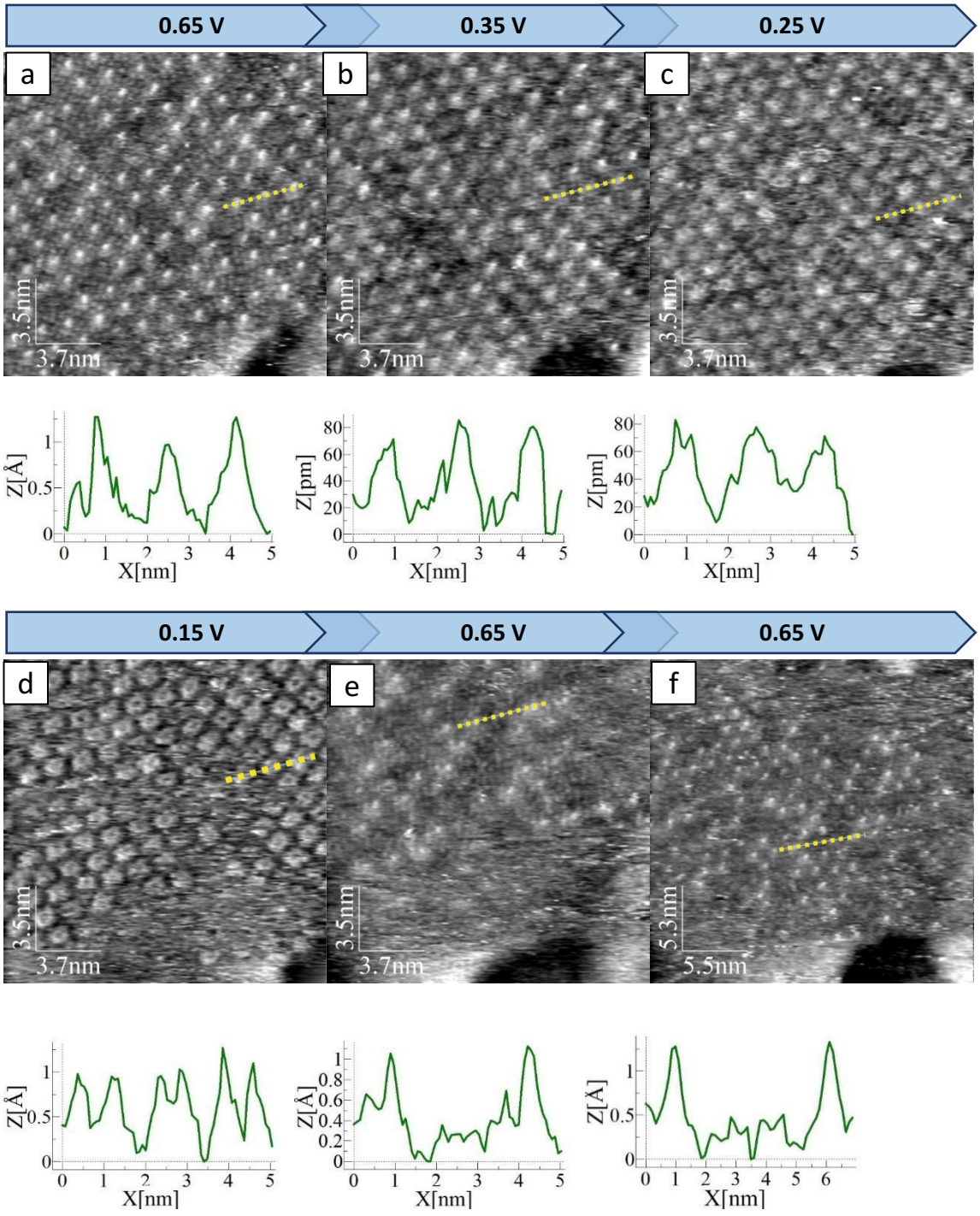

Figure 6.61. high resolution EC-STM images collected under potential control of a FeOEP on Au(111) in the case of O_2 saturated 0.1 M $HClO_4$. Tunnelling parameters are: I_t = 5 nA, U_b = 50 mV vs RHE. The applied potential is: a) E_{app} = 0.65 V vs RHE; b) E_{app} = 0.35 V vs RHE; c) E_{app} = 0.25 V vs RHE; d) E_{app} = 0.15 V vs RHE; e) E_{app} = 0.65 V vs RHE; f) E_{app} = 0.65 V vs RHE.

FeOEP successful physisorbed on Au(111). Herringbone ridges were still present beneath the molecular layer (electron-donation). However, domain boundaries also rises (stronger molecules-substrate interactions). The extremely high resolution attained for FeOEP allowed to perceive a sharp protrusion in the case of O_2 saturated electrolyte, with a

consequently higher topographic profile being detected with respect to the Ar purged case. O_2 binding properties of Fe centres were therefore confirmed.

As already done with PtOEP@Au(111), to have a more complete overview of FeOEP behaviour, a simple scheme showing the modulation of the topographic protrusion upon variation of the applied electrode potential is shown in figure 6.62. Both O_2-free and O_2-saturated experimental results were reported. From each image collected at a certain potential, two to four values of protrusion were measured, so that the data points are presented as averages with an associated confidence interval calculated as maximum semidispersion. Recalling that FeOEP was exhibiting a bright and dark contrast in O_2-free electrolyte, in this case both protrusion values observed in Ar purged electrolyte were here reported, as black circles for brighter molecules and blue circles for darker ones. The O_2 saturation case is presented with red circles. In presence of O_2 the protrusion is not only significantly higher, but it undergoes a considerable drop in correspondence of the ORR peak potential. This enables to highlight the dynamic nature of O_2 adsorption and reduction, which EC-STM aims and succeeds in characterising.

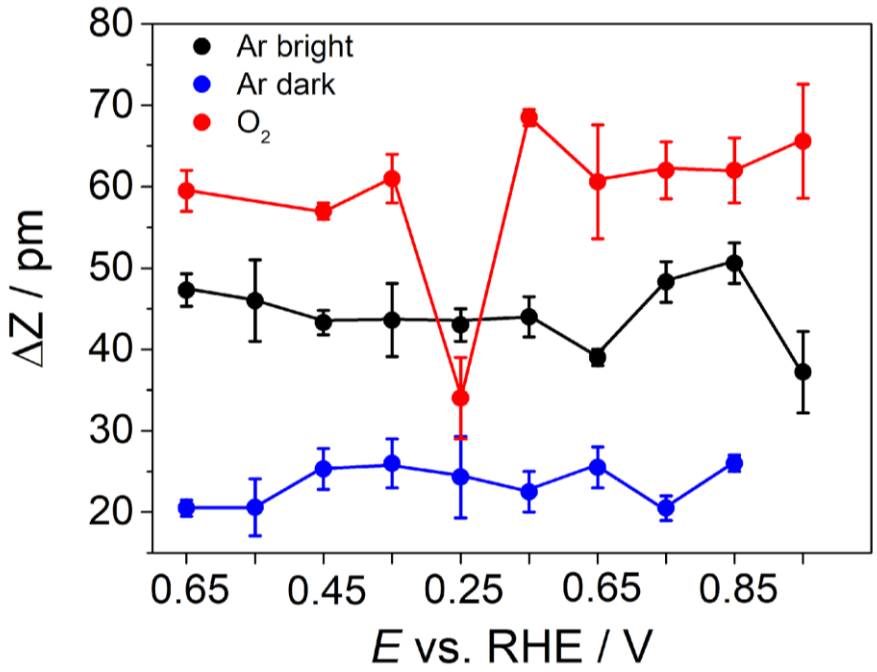

Figure 6.62. topographic protrusion variations of FeOEP@HOPG in absence (black, blue) or presence (red) of O_2 saturated electrolyte.

6.2.4 EC-STM investigation of Sn naphthalocyanine at Au(111)

The unique contrast features observed for Sn(IV)octaethylporphyrin dichloride on HOPG convinced us to conduct a similar experiment with tin naphthalocyanine on Au(111) as substrate. Since the Sn-up and Sn-down observed contrast on HOPG was directly comparable with results obtained for Sn phthalocyanine on a number of metal substrates, the same results were expected also for Au(111). However, the functionalisation

procedure caused almost to fail any attempt of imaging this molecule by STM. It is true that also SnOEP gave functionalisation issues and just a few ordered domains were revealed. For tin naphthalocyanine on Au(111), the number of imaged ordered domains was further reduced. Two images are reported in figure 6.63.a and 6.63.b. The unit cell parameters, as sketched in figure 6.63.a, are: $\overrightarrow{b_1} = (2.2 \pm 0.1)\, nm$ and $\overrightarrow{b_2} = (2.6 \pm 0.1)\, nm$, the measured angle between the two vectors is $\measuredangle = (88 \pm 2)°$. The surface concentration is $1.75 * 10^{13}\ molecules\ cm^{-2}$ and the corresponding surface coverage is $\theta = 0.013$.

The obtained resolution is quite satisfactory, but the revealed contrast does not meet the expectancies, with almost all molecules showing a dark depression at their centre. Based on the previously obtained results and considerations (section 6.1.8), this means that all the imaged SNPc molecules are adsorbed within the Sn-down geometry. Although statistically unlikely, this hypothesis cannot be *a priori* discarded to the very low number of collected images and to the very limited extent of ordered molecules detected. A more aware statement is that the limited number of imaged molecules does not constitute a statistically relevant measurement, and additional thorough inspections are needed to confirm or discard the "all Sn-down" hypothesis.

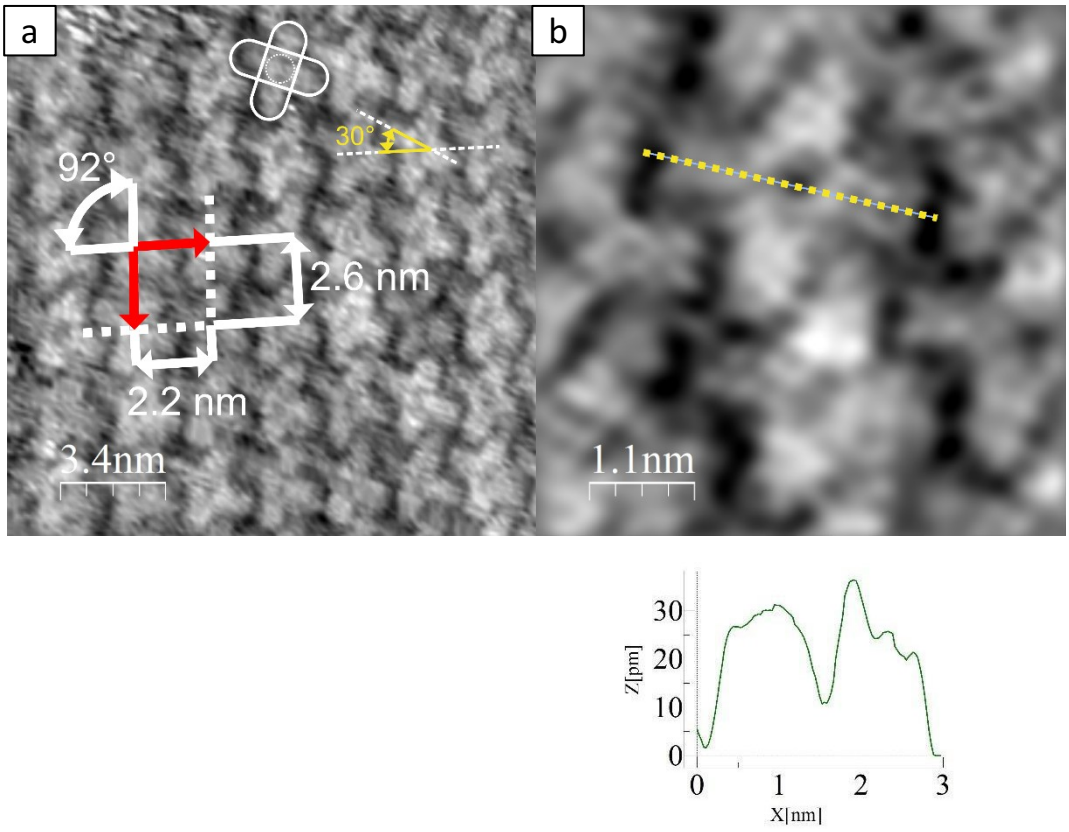

Figure 6.63. High-resolution EC-STM images of SnNpc on Au(111) in the case of deaerated 0.1 M $HClO_4$. Tunnelling parameters are: I_t = 0.58 nA, U_b = -650 mV, E_{app} = 0.50 V vs RHE.

6.2.5 Final considerations

For the Au(111) supported metal porphyrin systems, similar consideration can be drawn as done for >HOPG case. In particular, it was observed that:

- Porphyrins having an active redox metal centre are visualised with different contrast depending on the redox state of the metal.
- Porphyrins with a metal centre capable of adsorption of oxygen are visualised with different contrasts.
- The condition of having an active redox metal centre is sufficient but not necessary for observing oxygen adsorption.
- For PtOEP intermolecular charge transfer via noncovalent functionalization with Au(111) was considered to be responsible for the huge increase of the metal center protrusion upon O_2 adsorption.
- When the electrode potential is sufficient for triggering ORR, the metal center is visualized as free of oxygen. Being the process that fast, the image acquisition in not sufficiently fast to freeze the cyclical O_2 adsorption, reduction and modification of the redox state of the metal centre.
- Different supports (Au(111) and HOPG) exert different molecule-support electronic interaction so that a different metal center protrusion upon O_2 adsorption can be observed, that in turn can be associated with a different interaction (different adsorption strength) between the metal centre and the O_2 molecule.

References

[1] M. Grzeszczuk, Polymer electrodes: Preparation, properties, and applications, Elsevier, 2018.

[2] G. Bussetti, L. Duò, Anion intercalation in graphite studied by electrochemical-scanning probe microscopy: State of the art and perspectives, Encyclopedia of Interfacial Chemistry: Surface Science and Electrochemistry. (2018) 27–37.

[3] J. Kunze-Liebhäuser, Electrochemical scanning tunneling microscopy studies of copper oxide formation-A review, Encyclopedia of Interfacial Chemistry: Surface Science and Electrochemistry. (2018) 107–120.

[4] B. Madry, M. Nowicki, K. Wandelt, Sulfate adsorption on copper: From upd to bulk copper on Au(111), Elsevier, 2018.

[5] P. Marcus, V. Maurice, Scanning probe microscopies. (2010) 1430–1442.

[6] V. Maurice, P. Marcus, Adsorption layers and passive oxide films on metals, Tribocorrosion of Passive Metals and Coatings. (2011) 29–64.

[7] V. Maurice, P. Marcus, Surface Reactivity and Corrosion Mechanisms of Metal Surfaces Studied by Scanning Tunneling Microscopy (STM), Elsevier Ltd., 2016.

[8] F.U. Renner, M. Oezaslan, Dealloying on the atomic scale, Elsevier, 2018.

[9] M.P. Soriaga, J.H. Baricuatro, A.C. Javier, Y.G. Kim, K.D. Cummins, C.F. Tsang, J.C. Hemminger, N.N. Bui, J.L. Stickney, Electrochemical surface science of CO_2 reduction at well-defined cu electrodes: Surface characterization by emersion, ex situ, in situ, and operando methods, Elsevier, 2018.

[10] M.E. Davis, R.J. Davis, Fundamentals of Chemical Reaction Engineering, 2003..

[11] T. Bligaard, J.K. Norskov, Heterogeneous catalysis, in: A. Nilsson, L.G.M. Petterson, J.K. Norskov (Eds.), Chemical Bonding at Surfaces and Interfaces, Elsevier B.V, 2008: pp. 255–321.

[12] L. Smykalla, P. Shukrynau, C. Mende, T. Rüffer, H. Lang, M. Hietschold, Interplay of hydrogen bonding and molecule-substrate interaction in self-assembled adlayer structures of a hydroxyphenyl-substituted porphyrin, Surface Science. 628 (2014) 132–140.

[13] M. Roos, B. Uhl, D. Künzel, H.E. Hoster, A. Groß, R.J. Behm, Intermolecular vs molecule-substrate interactions: A combined STM and theoretical study of supramolecular phases on graphene/Ru(0001), Beilstein Journal of Nanotechnology. 2 (2011) 365–373.

[14] J. Schnadt, W. Xu, R.T. Vang, J. Knudsen, Z. Li, E. Lægsgaard, F. Besenbacher, Interplay of adsorbate-adsorbate and adsorbate-substrate interactions in self-assembled molecular surface nanostructures, Nano Research. 3 (2010) 459–471.

[15] Y. fang Geng, P. Li, J. zhen Li, X. mei Zhang, Q. dao Zeng, C. Wang, STM probing the supramolecular coordination chemistry on solid surface: Structure, dynamic, and reactivity, Coordination Chemistry Reviews. 337 (2017) 145–177.

[16] C.G. Claessens, J.F. Stoddart, π-π interactions in self-assembly, Journal of Physical Organic Chemistry, 10 (1997) 254–272.

[17] P.A. Gale, E.N.W. Howe, X. Wu, M.J. Spooner, Anion receptor chemistry: Highlights from 2016, Coordination Chemistry Reviews. 375 (2018) 333–372.

[18] P.A. Gale, Anion and ion-pair receptor chemistry: Highlights from 2000 and 2001, Coordination Chemistry Reviews. 240 (2003) 191–221.

[19] P.A. Gale, R. Quesada, Anion coordination and anion-templated assembly: Highlights from 2002 to 2004, Coordination Chemistry Reviews. 250 (2006) 3219–3244.

[20] P.A. Gale, Anion coordination and anion-directed assembly: Highlights from 1997 and 1998, Coordination Chemistry Reviews. 199 (2000) 181–233.

[21] L.J. Prins, D.N. Reinhoudt, P. Timmerman, The Cooperativity Concept, Angewandte Chemie International Edition. 40 (2001) 2382–2426.

[22] F. Würthner, C.C. You, C.R. Saha-Möller, Metallosupramolecular squares: from structure to function, Chemical Society Reviews. 33 (2004) 133–146.

[23] D.W. Zhang, X. Zhao, J.L. Hou, Z.T. Li, Aromatic amide foldamers: Structures, properties, and functions, Chemical Reviews. 112 (2012) 5271–5316.

[24] G. Berghäuser, E. Malić, Molecule-substrate interaction in functionalized graphene, Carbon. 69 (2014) 536–542.

[25] J. D. Fuhr, A. Carrera, N. Murillo-Quirós, L. J. Cristina, A. Cossaro, A. Verdini, L. Floreano, J. E. Gayone, and H. Ascolani, Interplay between Hydrogen Bonding and Molecule−Substrate Interactions in the Case of Terephthalic Acid Molecules on Cu(001) Surfaces, J. Phys. Chem. C, 2013, 117, 1287-1296.

[26] T.W. White, N. Martsinovich, A. Troisi, G. Costantini, Quantifying the "subtle Interplay" between Intermolecular and Molecule-Substrate Interactions in Molecular Assembly on Surfaces, Journal of Physical Chemistry C. 122 (2018) 17954–17962.

[27] X. Qiu, C. Wang, Q. Zeng, B. Xu, S. Yin, H. Wang, S. Xu, C. Bai, Alkane-assisted adsorption and assembly of phthalocyanines and porphyrins, Journal of the American Chemical Society. 122 (2000) 5550–5556.

[28] Y. Shen, K. Deng, M. Li, X. Zhang, G. Zhou, K. Müllen, Q. Zeng, C. Wang, Self-assembling in fabrication of ordered porphyrins and phthalocyanines hybrid nano-arrays on HOPG, CrystEngComm. 15 (2013) 5526–5531.

[29] J.P.D.C. Calupitan, O. Galangau, O. Guillermet, R. Coratger, T. Nakashima, G. Rapenne, T. Kawai, Scanning Tunneling Microscope Tip-Induced Formation of a Supramolecular Network of Terarylene Molecules on Cu(111), Journal of Physical Chemistry C. 121 (2017) 25384–25389.

[30] D. Wang, L.J. Wan, Electrochemical scanning tunneling microscopy: Adlayer structure and reaction at solid/liquid interface, Journal of Physical Chemistry C. 111 (2007) 16109–16130.

[31] M. Stark, J. Träg, S. Ditze, W. Brenner, N. Jux, H.P. Steinrück, H. Marbach, Supramolecular order and structural dynamics: A STM study of 2H-tetraphenylporphycene on Cu(111), Journal of Chemical Physics. 142 (2015).

[32] H. Marbach, H.P. Steinrücka, Studying the dynamic behaviour of porphyrins as prototype functional molecules by scanning tunnelling microscopy close to room temperature, Chemical Communications. 50 (2014) 9034–9048.

[33] W. Auwärter, A. Weber-Bargioni, S. Brink, A. Riemann, A. Schiffrin, M. Ruben, J. v. Barth, Controlled metalation of self-assembled porphyrin nanoarrays in two dimensions, ChemPhysChem. 8 (2007) 250–254.

[34] F. Buchner, V. Schwald, K. Comanici, H.P. Steinrück, H. Marbach, Microscopic evidence of the metalation of a free-base porphyrin monolayer with iron, ChemPhysChem. 8 (2007) 241–243.

[35] T.E. Shubina, H. Marbach, K. Flechtner, A. Kretschmann, N. Jux, F. Buchner, H.P. Steinrück, T. Clark, J.M. Gottfried, Principle and mechanism of direct porphyrin metalation: Joint experimental and theoretical investigation, Journal of the American Chemical Society. 129 (2007) 9476–9483.

[36] T. Kosmala, M. Blanco, G. Granozzi, K. Wandelt, Potential Driven Non-Reactive Phase Transitions of Ordered Porphyrin Molecules on Iodine-Modified Au(100): An Electrochemical Scanning Tunneling Microscopy (EC-STM) Study, Surfaces. 1 (2018) 12–28.

[37] S. Yoshimoto, A. Tada, K. Itaya, In Situ Scanning Tunneling Microscopy Study of the Effect of Iron Octaethylporphyrin Adlayer on the Electrocatalytic Reduction of O2 on Au(111), Journal of Physical Chemistry B. 108 (2004) 5171–5174.

[38] J.Y. Gu, Z.F. Cai, D. Wang, L.J. Wan, Single Molecular Imaging of Iron-Phthalocyanine Catalyzed Oxygen Reduction Reaction by in situ Scanning Tunneling Microscopy, ACS Nano. (2016) 1–10.

[39] W. Hieringer, K. Flechtner, A. Kretschmann, K. Seufert, W. Auwärter, J. v. Barth, A. Görling, H.P. Steinrück, J.M. Gottfried, The surface trans effect: Influence of axial ligands on the surface chemical bonds of adsorbed metalloporphyrins, Journal of the American Chemical Society. 133 (2011) 6206–6222.

[40] P.S. Deimel, R.M. Bababrik, B. Wang, P.J. Blowey, L.A. Rochford, P.K. Thakur, T.L. Lee, M.L. Bocquet, J. v. Barth, D.P. Woodruff, D.A. Duncan, F. Allegretti, Direct quantitative identification of the surface: Trans -effect, Chemical Science. 7 (2016) 5647–5656.

[41] B.A. Friesen, A. Bhattarai, U. Mazur, K.W. Hipps, Single molecule imaging of oxygenation of cobalt octaethylporphyrin at the solution/solid interface: Thermodynamics from microscopy, Journal of the American Chemical Society. 134 (2012) 14897–14904.

[42] G. Nandi, B. Chilukuri, K.W. Hipps, U. Mazur, Surface directed reversible imidazole ligation to nickel(II) octaethylporphyrin at the solution/solid interface: A single molecule level study, Physical Chemistry Chemical Physics. 18 (2016) 20819–20829.

[43] D.E. Barlow, L. Scudiero, K.W. Hipps, Scanning tunneling microscopy study of the structure and orbital-mediated tunneling spectra of cobalt(II) phthalocyanine

and cobalt(II) tetraphenylporphyrin on Au(111): Mixed composition films, Langmuir. 20 (2004) 4413–4421.

[44] L. Scudiero, D.E. Barlow, K.W. Hipps, Physical Properties and Metal Ion Specific Scanning Tunneling Microscopy Images of Metal(II) Tetraphenylporphyrins Deposited from Vapor onto Gold (111), Journal of Physical Chemistry B. 104 (2000) 11899–11905.

[45] F. Buchner, K.G. Warnick, T. Wölfle, A. Görling, H.P. Steinrück, W. Hieringer, H. Marbach, Chemical fingerprints of large organic molecules in scanning tunneling microscopy: Imaging adsorbate-substrate coupling of metalloporphyrins, Journal of Physical Chemistry C. 113 (2009) 16450–16457.

[46] K. Comanici, F. Buchner, K. Flechtner, T. Lukasczyk, J.M. Gottfried, H.P. Steinrück, H. Marbach, Understanding the contrast mechanism in Scanning Tunneling Microscopy (STM) images of an intermixed tetraphenylporphyrin layer on Ag(111), Langmuir. 24 (2008) 1897–1901.

[47] S. Müllegger, W. Schöfberger, M. Rashidi, L.M. Reith, R. Koch, Spectroscopic STM studies of single gold(III) porphyrin molecules, Journal of the American Chemical Society. 131 (2009) 17740–17741.

[48] K.W. Hipps, X. Lu, X.D. Wang, U. Mazur, Metal d-orbital occupation-dependent images in the scanning tunneling microscopy of metal phthalocyanines, Journal of Physical Chemistry. 100 (1996) 11207–11210.

[49] S. Yoshimoto, N. Higa, K. Itaya, Two-dimensional supramolecular organization of copper octaethylporphyrin and cobalt phthalocyanine on Au(111): Molecular assembly control at an electrochemical interface, Journal of the American Chemical Society. 126 (2004) 8540–8545.

[50] A. Facchin, M. Zerbetto, A. Gennaro, A. Vittadini, D. Forrer, C. Durante, Oxygen Reduction Reaction at Single Site Catalysts : A combined Electrochemical Scanning Tunnelling Microscope and DFT investigation of Iron Octaethylporphyrin Chloride on HOPG, ChemElectroChem. (2021), 8, 2825-2835.

[51] M.J.J. Coenen, M. Cremers, D. den Boer, F.J. van den Bruele, T. Khoury, M. Sintic, M.J. Crossley, W.J.P. van Enckevort, B.L.M. Hendriksen, J.A.A.W. Elemans, S. Speller, Little exchange at the liquid/solid interface: Defect-mediated equilibration of physisorbed porphyrin monolayers, Chemical Communications. 47 (2011) 9666–9668.

[52] Y. Kim, W.H. Doh, J. Kim, J.Y. Park, In Situ Observations of UV-Induced Restructuring of Self-Assembled Porphyrin Monolayer on Liquid/Au(111) Interface at Molecular Level, Langmuir. 34 (2018) 6003–6009.

[53] D. Hötger, M. Etzkorn, C. Morchutt, B. Wurster, J. Dreiser, S. Stepanow, D. Grumelli, R. Gutzler, K. Kern, Stability of metallo-porphyrin networks under oxygen reduction and evolution conditions in alkaline media, Physical Chemistry Chemical Physics. 21 (2019) 2587–2594.

[54] B.E. Murphy, S.A. Krasnikov, N.N. Sergeeva, A.A. Cafolla, A.B. Preobrajenski, A.N. Chaika, O. Lübben, I. v. Shvets, Homolytic cleavage of molecular oxygen by manganese porphyrins supported on Ag(111), ACS Nano. 8 (2014) 5190–5198.

[55] B. Hulsken, R. van Hameren, J.W. Gerritsen, T. Khoury, P. Thordarson, M.J. Crossley, A.E. Rowan, R.J.M. Nolte, J.A.A.W. Elemans, S. Speller, Real-time single-molecule imaging of oxidation catalysis at a liquid-solid interface, Nature Nanotechnology. 2 (2007) 285–289.

[56] D. den Boer, M. Li, T. Habets, P. Iavicoli, A.E. Rowan, R.J.M. Nolte, S. Speller, D.B. Amabilino, S. de Feyter, J.A.A.W. Elemans, Detection of different oxidation states of individual manganese porphyrins during their reaction with oxygen at a solid/liquid interface, Nature Chemistry. 5 (2013) 621–627.

[57] A.T. Gallagher, J.Y. Lee, V. Kathiresan, J.S. Anderson, B.M. Hoffman, T.D. Harris, A structurally-characterized peroxomanganese(IV) porphyrin from reversible O2 binding within a metal-organic framework, Chemical Science. 9 (2018) 1596–1603.

[58] J.M. Gottfried, H. Marbach, Surface-confined coordination chemistry with porphyrins and phthalocyanines: Aspects of formation, electronic structure, and reactivity, Zeitschrift Fur Physikalische Chemie. 223 (2009) 53–74.

[59] S. Sadegh Hassani, Y.G. Kim, E. Borguet, Self-assembly of insoluble porphyrins on Au(111) under aqueous electrochemical control, Langmuir. 27 (2011) 14828–14833.

[60] M. Kunitake, U. Akiba, N. Batina, K. Itaya, Structures and dynamic formation processes of porphyrin adlayers on iodine-modified Au(111) in solution: In situ STM study, Langmuir. 13 (1997) 1607–1615.

[61] B. Madry, I. Morawski, T. Kosmala, K. Wandelt, M. Nowicki, Porphyrin Layers at Cu/Au(111)–Electrolyte Interfaces: In Situ EC-STM Study, Topics in Catalysis. 61 (2018) 1335–1349.

[62] S. Uemura, R. Tanoue, N. Yilmaz, A. Ohira, M. Kunitake, Molecular dynamics in two-dimensional supramolecular systems observed by STM, Materials. 3 (2010) 4252–4276.

[63] T. Ye, Y. He, E. Borguet, Adsorption and electrochemical activity: An in situ electrochemical scanning tunneling microscopy study of electrode reactions and potential-induced adsorption of porphyrins, Journal of Physical Chemistry B. 110 (2006) 6141–6147.

[64] X. Lu, K.W. Hipps, Scanning tunneling microscopy of metal phthalocyanines: d6 and d8 cases, Journal of Physical Chemistry B. 101 (1997) 5391–5396.

[65] X. Lu, K.W. Hipps, X.D. Wang, U. Mazur, Scanning tunneling microscopy of metal phthalocyanines: d7 and d9 cases, Journal of the American Chemical Society. 118 (1996) 7197–7202.

[66] K.W. Hipps, U. Mazur, Kinetic and Thermodynamic Control in Porphyrin and Phthalocyanine Self-Assembled Monolayers, Langmuir. 34 (2018) 3–17.

[67] I. Ponce, J.F. Silva, R. Oñate, M.C. Rezende, M.A. Páez, J. Pavez, J.H. Zagal, Enhanced catalytic activity of Fe phthalocyanines linked to Au(111) via conjugated self-assembled monolayers of aromatic thiols for O2reduction, Electrochemistry Communications. 13 (2011) 1182–1185.

[68] K. Liu, J. Masa, Electrochemistry of N4 Macrocyclic Metal Complexes, 2016.

[69] J.H. Zagal, S. Griveau, J.F. Silva, T. Nyokong, F. Bedioui, Metallophthalocyanine-based molecular materials as catalysts for electrochemical reactions, Coordination Chemistry Reviews. 254 (2010) 2755–2791.

[70] J.W. Buchler, C. Dreher, F.M. Kunzel, Structure and Bonding, Springer, 1995.

[71] L.M. Mink, M.L. Neitzel, L.M. Bellomy, R.E. Falvo, R.K. Boggess, B.T. Trainum, P. Yeaman, Platinum(II) and platinum(IV) porphyrin complexes: Synthesis, characterization, and electrochemistry, Polyhedron. 16 (1997) 2809–2817.

[72] David Dolphin, The Porphyrins, volume I, 1978.

[73] N. Oncel, S.L. Bernasek, The effect of molecule-molecule and molecule-substrate interaction in the formation of Pt-octaethyl porphyrin self-assembled monolayers, Applied Physics Letters. 92 (2008).

[74] E.S. Dy, H. Kasai, Characterization of Platinum Porphyrins and its interaction with oxygen by density functional theory, E-Journal of Surface Science and Nanotechnology. 3 (2005) 473–475.

[75] K. Walzer, M. Hietschold, STM and STS investigation of ultrathin tin phthalocyanine layers adsorbed on HOPG(0 0 0 1) and Au(1 1 1), Surface Science. 471 (2001) 1–10.

[76] M. Lackinger, M. Hietschold, Determining adsorption geometry of individual tin – phthalocyanine molecules on Ag (1 1 1)— a STM study at submonolayer coverage, 520 (2002).

[77] L. Bodek, M. Engelund, A. Cebrat, B. Such, Adsorption behavior of tin phthalocyanine onto the (110) face of rutile TiO 2, (2020) 821–828.

[78] N. Tao, Pushing the right button, 1 (2009) 108–109.

[79] A.Y. Zhang, Y. Wang, J. Lü, M. Brandbyge, Mechanochemistry induced with a robust functionalized tip, Angewandte Chemie - International Edition. 2017, 56(39):11769-11773

[80] X. Zhu, S. Zhang, H. Xiao, C. Li, W. Huang, Q. Fang, X. Li, M. Zhang, F. Cheng, B. Tu, Y. Geng, J. Song, Q. Zeng, Bilayer Adsorption of Porphyrin Molecules Substituted with Carboxylic Acid atop the NN4A Network Revealed by STM and DFT, Langmuir. 35 (2019) 4428–4434.

[81] D. Lensen, T. Habets, J.A.A.W. Elemans, Dynamic rearrangement of bilayers of porphyrin hetero-dimers at a solid/liquid interface, Chemical Communications. 50 (2014) 7291–7294.

[82] T. Habets, D. Lensen, S. Speller, J.A.A.W. Elemans, Self-assembly of covalently linked porphyrin dimers at the solid-liquid interface, Molecules. 24 (2019).

[83] Z.Q. Zou, L. Wei, F. Chen, Z. Liu, P. Thamyongkit, R.S. Loewe, J.S. Lindsey, U. Mohideen, D.F. Bocian, Solution STM images of porphyrins on HOPG reveal that subtle differences in molecular structure dramatically alter packing geometry, Journal of Porphyrins and Phthalocyanines. 9 (2005) 387–392.

[84] S. Yoshimoto, E. Tsutsumi, K. Suto, Y. Honda, K. Itaya, Molecular assemblies and redox reactions of zinc(II) tetraphenylporphyrin and zinc(II) phthalocyanine on Au(1 1 1) single crystal surface at electrochemical interface, Chemical Physics. 319 (2005) 147–158.

[85] T. Omiya, P. Poli, H. Arnolds, R. Raval, M. Persson, Y. Kim, Desorption of CO from individual ruthenium porphyrin molecules on a copper surface: Via an inelastic tunnelling process, Chemical Communications. 53 (2017) 6148–6151.

[86] N. Tsukahara, E. Minamitani, Y. Kim, M. Kawai, N. Takagi, Controlling orbital-selective Kondo effects in a single molecule through coordination chemistry, Journal of Chemical Physics. 141 (2014).

[87] W. Auwärter, F. Klappenberger, A. Weber-Bargioni, A. Schiffrin, T. Strunskus, C. Wöll, Y. Pennec, A. Riemann, J. v. Barth, Conformational adaptation and selective adatom capturing of tetrapyridyl-porphyrin molecules on a copper (111) surface, Journal of the American Chemical Society. 129 (2007) 11279–11285.

[88] W. Auwärter, A. Weber-Bargioni, S. Brink, A. Riemann, A. Schiffrin, M. Ruben, J. v. Barth, Controlled metalation of self-assembled porphyrin nanoarrays in two dimensions, ChemPhysChem. 8 (2007) 250–254.

[89] F. Buchner, V. Schwald, K. Comanici, H.P. Steinrück, H. Marbach, Microscopic evidence of the metalation of a free-base porphyrin monolayer with iron, ChemPhysChem. 8 (2007) 241–243.

[90] A. Weber-Bargioni, W. Auwärter, F. Klappenberger, J. Reichert, S. Lefrançois, T. Strunskus, C. Wöll, A. Schiffrin, Y. Pennec, J. v. Barth, Visualizing the frontier

orbitals of a conformationally adapted metalloporphyrin, ChemPhysChem. 9 (2008) 89–94.

[91] L. Scudiero, D.E. Barlow, K.W. Hipps, Physical Properties and Metal Ion Specific Scanning Tunneling Microscopy Images of Metal(II) Tetraphenylporphyrins Deposited from Vapor onto Gold (111), Journal of Physical Chemistry B. 104 (2000) 11899–11905.

[92] A. Weber-Bargioni, J. Reichert, A.P. Seitsonen, W. Auwärter, A. Schiffrin, J. v. Barth, Interaction of cerium atoms with surface-anchored porphyrin molecules, Journal of Physical Chemistry C. 112 (2008) 3453–3455.

[93] M. Lepper, J. Köbl, T. Schmitt, M. Gurrath, A. de Siervo, M.A. Schneider, H.P. Steinrück, B. Meyer, H. Marbach, W. Hieringer, "inverted" porphyrins: A distorted adsorption geometry of free-base porphyrins on Cu(111), Chemical Communications. 53 (2017) 8207–8210.

[94] S. Yoshimoto, S. Yasunishi, T. Kawamoto, Effect of the formation of highly ordered platinum(II) octaethylporphyrin adlayer on the surface reconstruction of gold and supramolecular assembly of fullerenes, Journal of Physical Chemistry C. 118 (2014) 29880–29886.

[95] K. Suto, S. Yoshimoto, K. Itaya, Electrochemical control of the structure of two-dimensional supramolecular organization consisting of phthalocyanine and porphyrin on a gold single-crystal surface, Langmuir. 22 (2006) 10766–10776.

[96] S. Yoshimoto, Y. Honda, O. Ito, K. Itaya, Supramolecular pattern of fullerene on 2D bimolecular " chessboard" consisting of bottom-up assembly of porphyrin and phthalocyanine molecules, Journal of the American Chemical Society. 130 (2008) 1085–1092.

[97] S. Yoshimoto, A. Tada, K. Suto, R. Narita, K. Itaya, Adlayer Structure and Electrochemical Reduction of O 2 on Self-Organized Arrays of Cobalt and Copper Tetraphenyl Porphines on a Au (111) Surface, Langmuir. 19 (2003) 672–677.

[98] S. Yoshimoto, J. Inukai, A. Tada, T. Abe, T. Morimoto, A. Osuka, H. Furuta, K. Itaya, Adlayer Structure of and Electrochemical O_2 Reduction on Cobalt Porphine-Modified and Cobalt Octaethylporphyrin-Modified Au(111) in HClO 4, Journal of Physical Chemistry B. 108 (2004) 1948–1954.

[99] A. Facchin, T. Kosmala, A. Gennaro, C. Durante, Electrochemical Scanning Tunnelling Microscopy Investigations of FeN4-Based Macrocyclic Molecules Adsorbed on Au(111) and Their Implications in the Oxygen Reduction Reaction, ChemElectroChem. 7 (2020) 1431–1437.

Chapter 7

Graphene nanoribbons and nanowires

The growth of epitaxial graphene and the production of surface covalent organic framework has an increasing research interest in the field of surface science [1–8]. However, focusing on possible applications as field-effect transistors, graphene presents a major drawback, namely the absence of a band gap. A way to "open" a band gap is represented by confinement of charge carriers within nanoribbons and nanodots [9–11].

Graphene nanoribbons are planar and finite graphene structures. They are nearly one-dimensional structures, since their length is much higher than their thickness. Their long edges can present an armchair, a zig-zag or an intermediate character, and depending on the long edge structure the band-gap can undergo modifications [12]. In fact, zig-zag nanoribbons have a metallic character, while armchair can be either metallic or semiconducting [13].

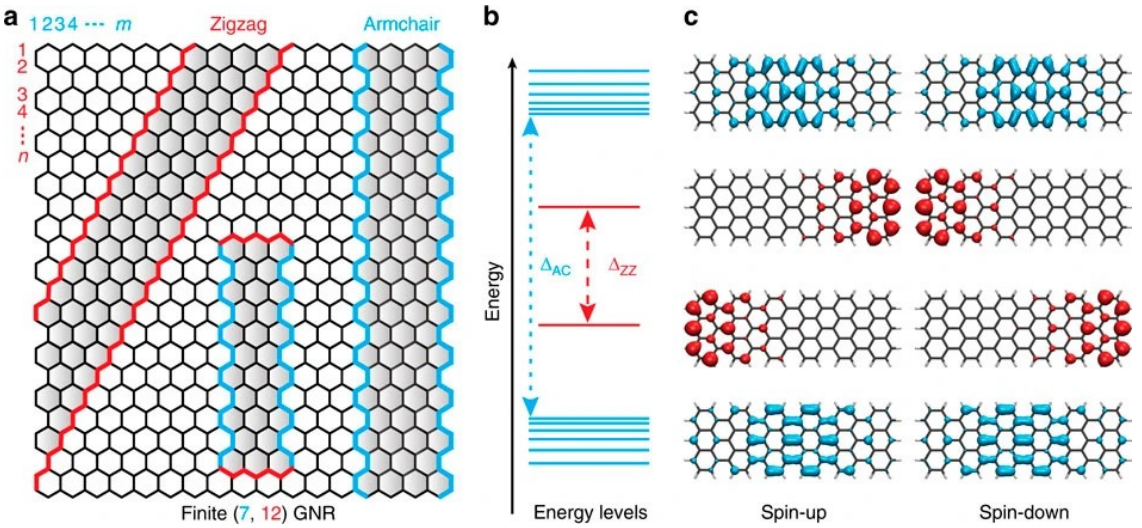

Figure 7.1. Visual representation of zig-zag and armchair graphene nanoribbons. Figure from reference [14].

Therefore, the synthesis of graphene nanoribbons on the (111) facet of an Au single crystal is now presented, remarking that all the samples prepared and described in this section were produced by the group of prof. M. Sambi, University of Padova, Department of Chemical Sciences.

The first step of the on-surface synthesis is the Ullmann coupling between brominated precursor units, in this case 4,4"-dibromo-*p*-terphenyl (DBTP). This step is accomplished by annealing on the DBTP-functionalised Au(111) surface. once the sample is subjected to annealing, the DBTP molecules start to form oligomolecular units, and once temperature is in the range 360-390 K, bromine molecules start to be ejected and C-C bonds are formed. Over 400 K, an almost complete network of poly-para-phenylene (PPP) is formed. When temperature reaches 520 K, these molecular wires acquire a more confused pattern, and more corrugations on the surface can be observed.

Finally, at 650 K, wider nanostructures without a preferential orientation are obtained: it is the case of graphene nanoribbons. The further increasing of the temperature leads to wider nanoribbons, but in this case the reaction is limited by diffusion, and the result is a highly defective nanoribbons mesh.

An example of graphene nanoribbons network imaged by UHV-STM is reported in figure 7.2.

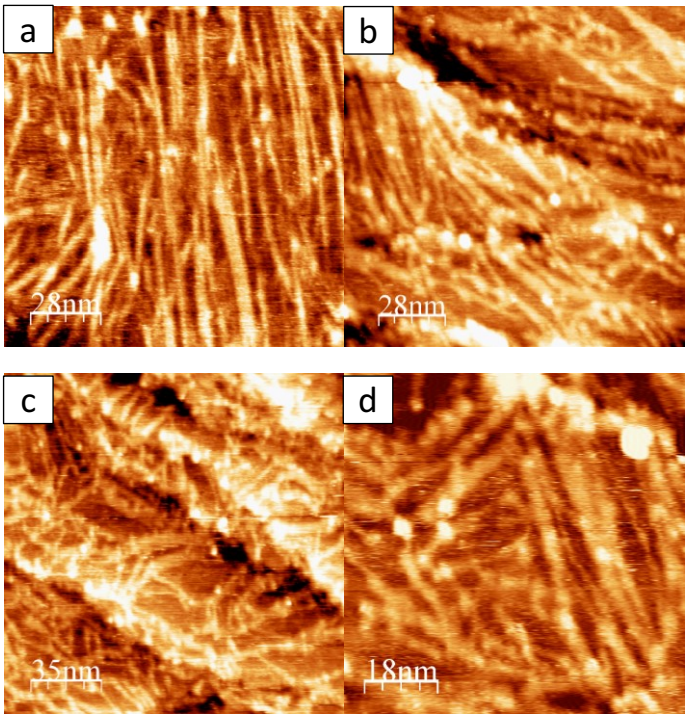

Figure 7.2. UHV-STM images of an Au(111) substrate covered with graphene nanoribbons. Tunnelling parameters are: I_t = 1.00 nA, U_b = -800 mV.

The surface coverage is almost complete (around 95%), with mainly 6- and 9- GNR being present with a small amount of single PPP wires. The ribbons have an average length equal to 65 nm, but a great variability is present, with much longer and shorter ribbons. In fact, a real long-range order is missing and many areas with strong lateral ramification can be found. This is a consequence of bromine desorption, which makes the ribbons more mobile on the Au(111) surface. XPS measurements confirm the complete bromine elimination and the final carbonaceous nature of the nanoribbons. Brighter spots can be distinguished, but they are usually ascribed to junctions among ribbons. In case of a faulty tip, these spots can appear larger and brighter, inhibiting a proper STM image interpretation.

The Au(111) surface functionalised with GNR in UHV chamber can be brought to ambient condition and mounted in the PEEK electrochemical cell for EC-STM characterisation. Although graphene-functionalised surfaces can be sensitive to airborne molecules, the images obtained at the solid/electrolyte interface after exposure to ambient pressure from UHV do not present significant differences [15]. In any case, this passage is delicate and can potentially lead to worsening of the sample quality.

Once mounted, the electrolyte is added and an example of EC-STM images featuring the graphene nanoribbons network is reported in figure 7.3. Figures 7.3a-b refer to a graphene nanoribbon sample measured in Ar purged electrolyte, whereas figure 7.3c was collected with O_2 saturated electrolyte. Although graphene nanoribbons have already been characterised with various techniques, like UHV-STM, LEED, Raman, XPS, there is not any report yet featuring their characterisation under *in operando* conditions. In fact, EC-STM allows to explore their behaviour at the solid/electrolyte interface, with potentially new features to be pointed out. First of all, obtaining consecutive and reproducible EC-STM pictures of the GNR-Au(111) sample to test and prove the stability of this system. Stability was proved by collecting images of the same sample for several days, finding out that no significant differences arise upon ageing of the sample.

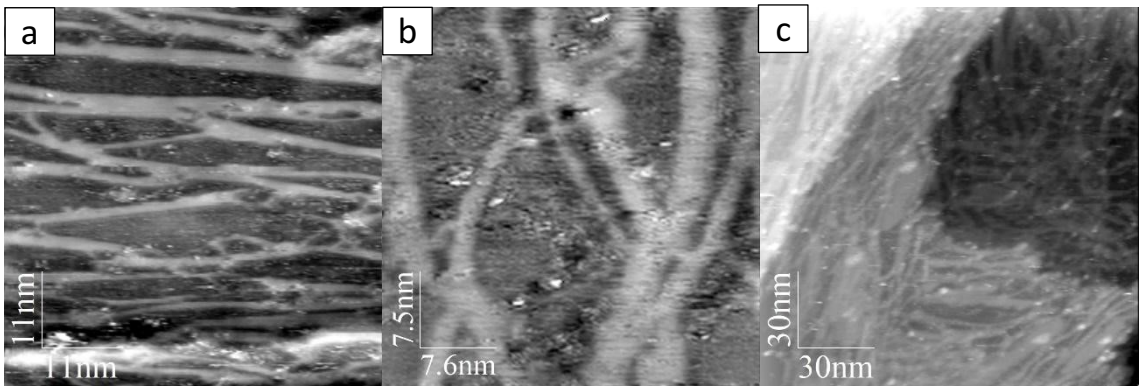

Figure 7.3. EC-STM images of graphene nanoribbons grown on Au(111) and in contact with a,b) Ar purged and c) O_2 saturated 0.1 M $HClO_4$. Tunnelling parameters are: a) I_t = 0.47 nA, U_b = -300 mV, E_{app} = OCP; b) I_t = 0.32 nA, U_b = -300 mV, E_{app} = OCP; c) I_t = 0.39 nA, U_b = -400 mV, E_{app} = OCP.

The absence/presence of oxygen does not bring any difference of contrast in the final STM image, but a non-negligible current culminating with a peak is observable by the corresponding cyclic voltammogram of figure 7.4. In figure 7.4, cyclic voltammograms are reported for GRN and PPP on Au(111), in both cases collected either in Ar and O_2 saturated electrolyte. The two systems are rather similar, with an almost featureless CV in Ar purged electrolyte. This is compatible with the electrochemical behaviour of graphene on Au(111) [15]. In presence of O_2, both carbon structures present a cathodic peak at $E_{app}\approx$ -900 mV vs Pt, indicating that an electrocatalytic activity towards ORR is present though not ground-breaking.

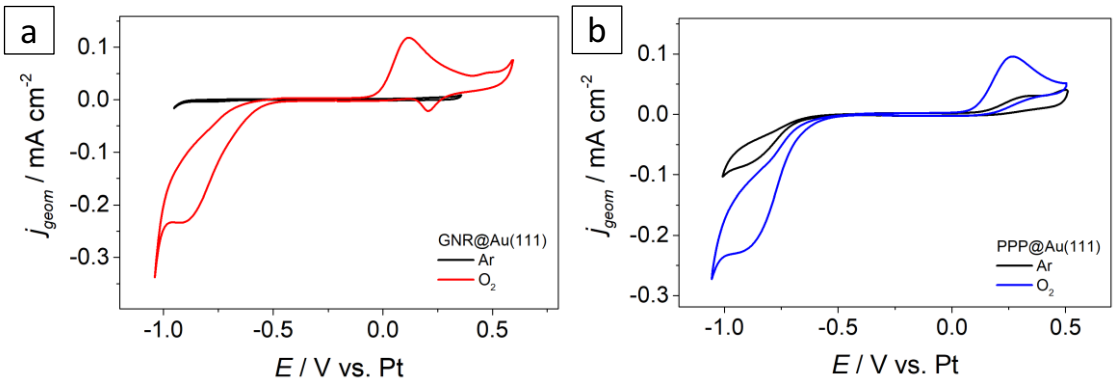

Figure 7.4. Cyclic voltammograms obtained in Ar or O_2 saturated 0.1 M $HClO_4$ for: a) graphene nanoribbons; b) poly-para-phenylene wires.

Since the stability of the graphene nanoribbons network has been ascertained, it is now worth to take into exam the previous step in the synthetic path to graphene nanoribbons, namely the poly-para-phenylene wires network. These samples can be attained upon heating the DBTP adlayer at a temperature of at least 400 K, but lower than 520 K. In this way, the temperature is sufficiently high to promote the elimination of bromine molecules and the formation of new C-C bonds, resulting in the formation of long poly-para-phenylene wires, also referred as nanowires. The temperature is at the same time sufficiently low to avoid side coupling among nanowires, which would lead to the nanoribbon formation. An example of PPP framework is reported in figure 7.5. Single wires can be clearly distinguished, indicating that the synthesis did result in the formation of wires, without making them join together, except in a few cases of closer wires, for which it is difficult to state whether they are connected or not.

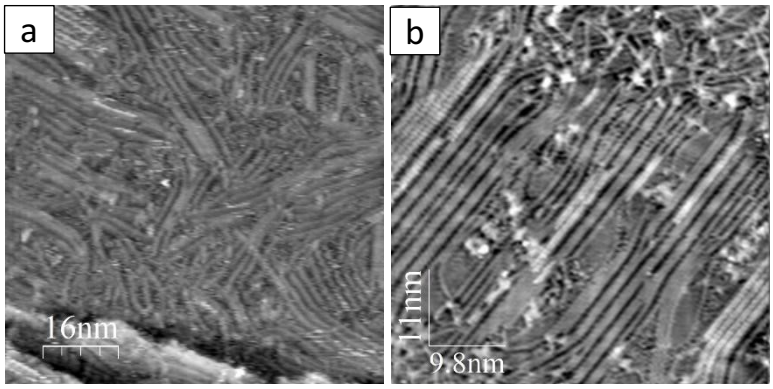

Figure 7.5. Examples of EC-STM images obtained for PPP wires in deaerated 0.1 M $HClO_4$. In b) herringbone reconstruction is visible beneath the PPP framework, in accordance with [16]. Tunnelling parameters are: a) I_t = 0.47 nA, U_b = -500 mV, E_{app} = 0.55 V vs RHE; b) I_t = 1.00 nA, U_b = -500 mV, E_{app} = OCP.

The electrochemical stability of the PPP sample was tested for few days, and the same behaviour of graphene nanoribbons was evidenced, indicating that both systems are equally stable in a strong acidic environment.

EC-STM instrumentation is capable to probe a sample *in operando* conditions, therefore the possibility to apply a variable working electrode potential was exploited also for the nanoribbons/nanowires-functionalised Au(111) crystal. The aim is to probe their stability also under potentiodynamic conditions, in order to fill a knowledge lack in this scientific field.

Four significant EC-STM pictures collected under potential control for a graphene nanoribbons sample are reported in figure 7.6. The explored potential window is quite large, ranging from -300 mV, which is close to OCP, to -800 mV, which is close to HER. In fact, further reducing the potential would imply a huge current to develop at the Au(111) surface due to hydrogen evolution, that might lead to the surface ruining. Additionally, images of figure 7.6 were recorded in O_2 saturated electrolyte, and the corresponding voltammetric behaviour was already shown in figure 7.4. This means that figure 7.6.c was collected along with a concurrent oxygen reduction reaction. Anyway, all STM images of figure 7.6 show that the sample does not undergo significant changes upon lowering the applied potential, even in O_2 saturated electrolyte.

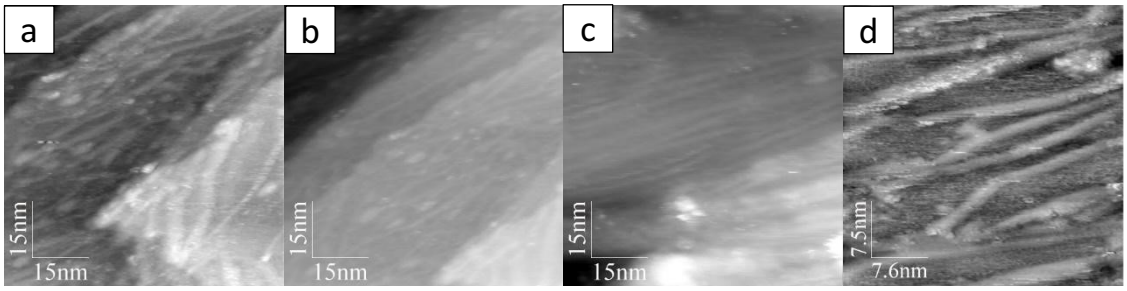

Figure 7.6. EC-STM images of graphene nanoribbons grown on Au(111) in contact with O_2 saturated 0.1 M $HClO_4$. Tunnelling parameters are: I_t = 0.22 nA, U_b = -200 mV. Applied potential is: a) E_{app} = 0.55 V vs RHE; b) Eapp = 0.25 V vs RHE; c) Eapp = 0.05 V vs RHE; d) Eapp = 0.55 V vs RHE.

The same experiment for potentiodynamic stability was conducted on the PPP nanowires-functionalised sample, as reported in figure 7.7. However, in this case a substantial difference arises with respect to graphene nanoribbons. The sample is found to be stable at Eapp=-300 mV, but when the applied potential is cathodically swept at -400 mV, a fuzzy contrast starts to appear. Further lowering the applied potential makes the fuzzy regions appear larger. When the potential is swept back to its original value of -300 mV, the fuzzy contrast completely disappears, but the surface appears changed. Thanks to the fact that EC-STM pictures were collected almost on the same spot, it is easy to notice that the central portion, initially featuring a large array of nanowires, is showing at the end a different nanowires organisation. Indeed, the most part of the wires now seem to be joined together.

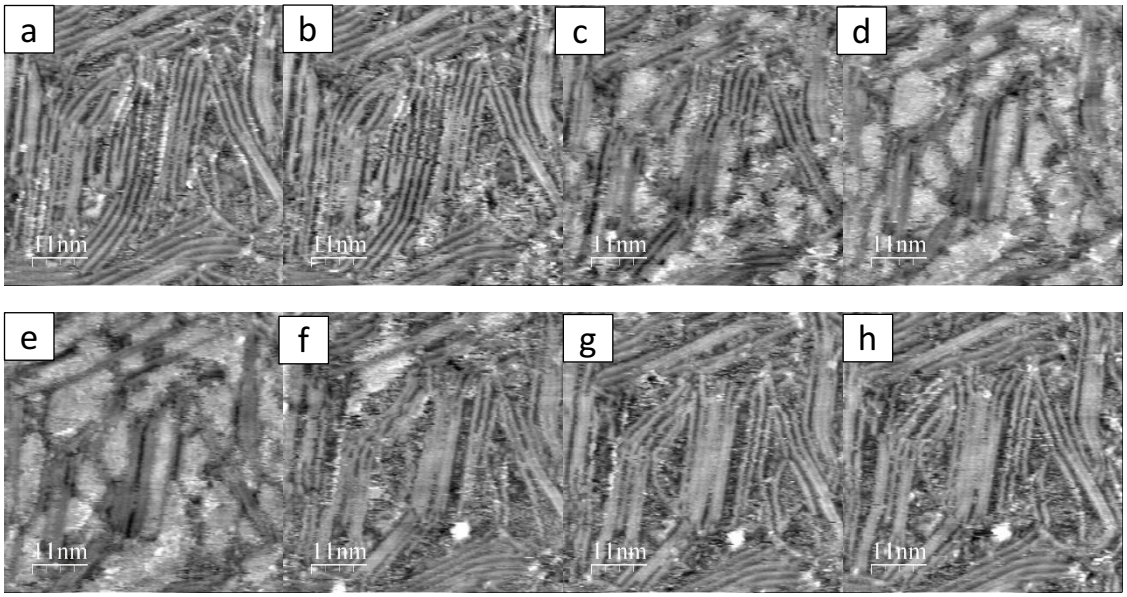

Figure 7.7. EC-STM images showing a PPP framework on Au(111) in contact with deaerated 0.1 M $HClO_4$. Tunnelling parameters are: I_t = 0.47 nA, U_b = +50 mV vs RHE. Applied potential is: a) E_{app} = 0.55 V vs RHE; b) Eapp = 0.45 V vs RHE; c,d) Eapp = 0.35 V vs RHE; e-h) Eapp = 0.55 V vs RHE.

The reason behind this behaviour remains unclear, even if some hypothesis may be brought forth. One first possibility is that the PPP nanowires sample was still carrying a consistent amount of bromine, whose desorption induced by negative applied potential manifests with the fuzzy contrast appearing at Eapp < -400 mV. As a result, nanowires become more mobile during the concurrent bromine removal, leading to their approach, even without a real chemical bonding. Bromide is known to adsorb and undergo order/disorder transitions in the potential window [+200; +600 mV vs RHE][17], and the potentiodynamic EC-STM images shown in figure 7.7 are contained in this potential range. It must be considered that bromide concentration would be in any case very small, and this is expected to lower the potential of characteristic features in the cyclic voltammograms.

An additional consideration concerns the effect of the tunnelling tip, which with its probing action could enhance the nanowires framework mobility. This argument focuses on the disturbing nature of the tunnelling phenomenon, which is known to exert a major role in the field of scanning tunnelling microscopy, both in UHV [18] [19] and at the solid/liquid interface [20].

Another hypothesis is verting on the capability of water molecules or perchlorate anions to intercalate beneath the PPP framework. Indeed, it must be considered that, despite the high PPP nanowires coverage on the Au(111) surface, their framework is not regular, featuring portions of long and aligned wires but also patches of irregular and short wires with higher ramification. In fact, for a graphene layer on Au(111) the interface is formed at the graphene moiety [15]. Since in some higher resolution images herringbone reconstruction was noticed beneath the PPP nanowires framework (figure 7.5.b), it can

be stated that the peculiar Au(111) reconstruction is stabilised by the presence of the carbon network, and the surface excess charge of the electrode is located onto the carbonaceous matrix, rather than on Au(111) [15].

These can be thought as defects were the most abundant species (water and perchlorate) can penetrate, preventing a more stable nanowire immobilisation on the Au surface. In this case, the fuzzy contrast and the consequent nanowires approaching would be represented by the removal of perchlorate from its residing state under the nanowires due to stronger electrostatic repulsion subsequent to a reduction of applied potential, similar to the case of bromine elimination.

Nevertheless, it must be excluded that the joining of nanowires upon variation of potential is actually caused or enhanced by other effects, in particular by the tunnelling phenomena. For this reason, holding the applied potential constant, the tunnelling parameters (tunnelling current, voltage bias) were alternatively varied. Figure 7.8 contains EC-STM pictures at different applied voltage bias, whereas figure 7.9 contains EC-STM pictures collected at a different tunnelling current.

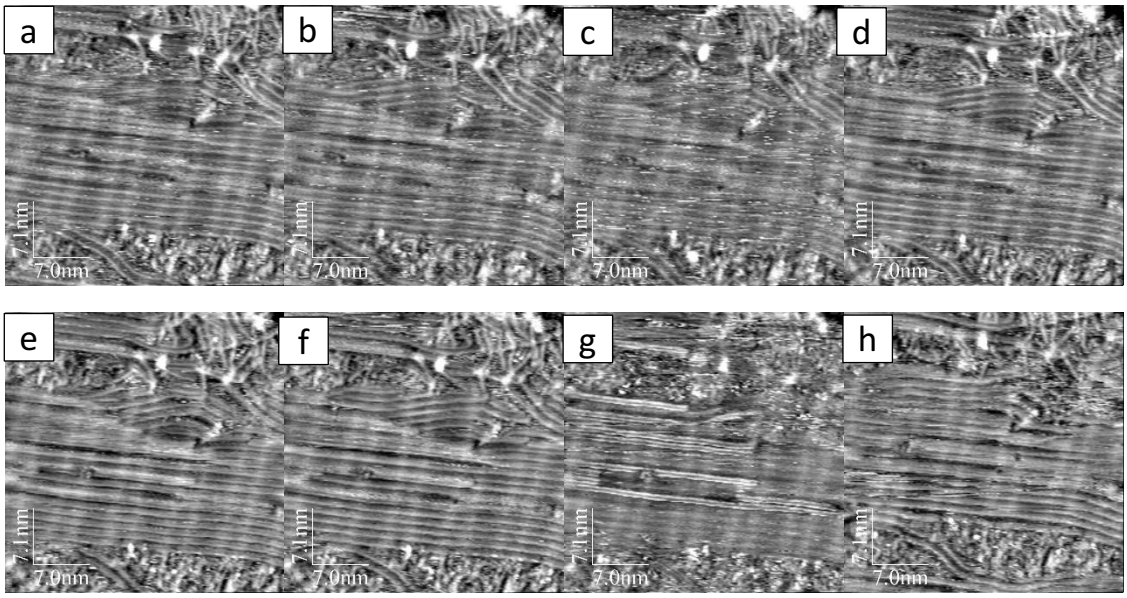

Figure 7.8. EC-STM images showing a PPP framework on Au(111) in contact with deaerated 0.1 M $HClO_4$. Tunnelling parameters are: I_t = 0.47 nA, E_{app} = OCP. Bias voltage is: a) U_b = -400 mV; b) U_b = -500 mV; c) Ub = -600 mV; d) Ub = -400 mV; e) Ub = -300 mV; f) Ub = -400 mV; g) Ub = -250 mV; h) Ub = -400 mV.

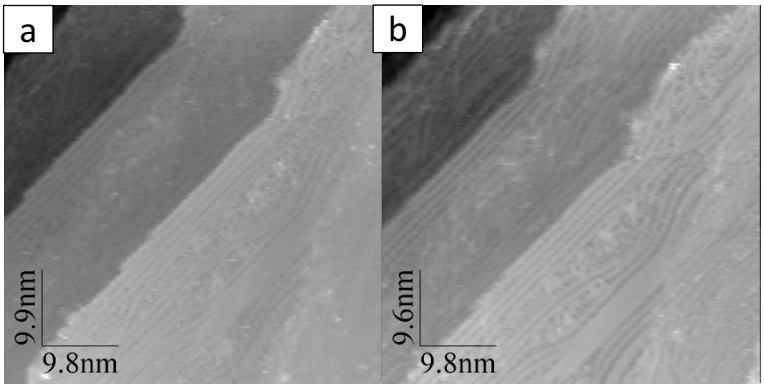

Figure 7.9. EC-STM images showing a PPP framework on Au(111) in contact with deaerated 0.1 M $HClO_4$. Tunnelling parameters are: Ub = -400 mV, E_{app} = OCP. Tunnelling current is: a) I_t = 4.7 nA; b) I_t = 0.47 nA.

7.1 Di-bromo-terphenyl intermediate step

An attempt to image one of the early stages of graphene nanoribbons formation is now presented. A satisfactory number of images was collected, and three examples at different scan sizes are shown in figure 7.10.

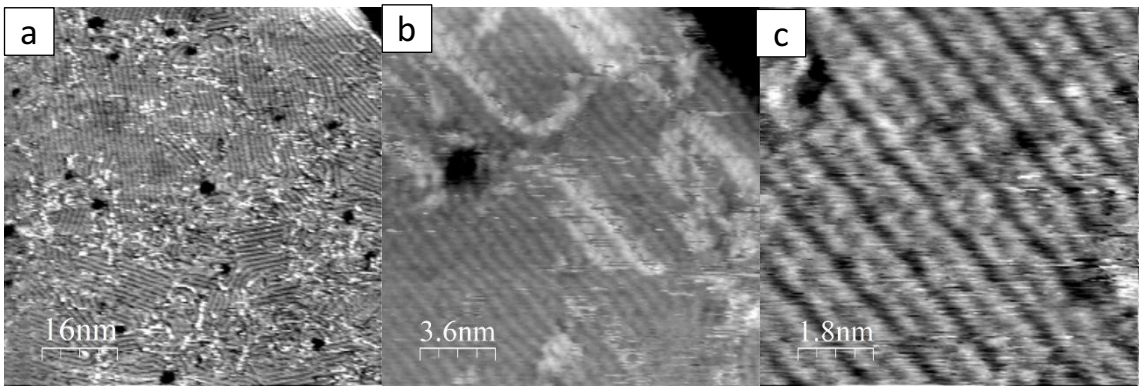

Figure 7.10. EC-STM images showing a DBTP oligomeric layer on Au(111) in deaerated 0.1 M $HClO_4$. Tunnelling parameters are: a) I_t = 1.00 nA, U_b = -300 mV; b,c) I_t = 1.00 nA, U_b = -400 mV. Applied potential is: E_{app} = OCP.

This synthesis was so conducted in order to reach a maximum heating temperature of 360-390 K in UHV, which should guarantee an extended oligomerisation of the precursor molecules (DBTP) without forming the complete network of poly-para-phenylene wires. At first glance, figure 7.10.a resembles quite well the image of figure 7.5, giving the idea that the two kinds of samples are impossible to distinguish or that the lower heating temperature was unsuccessful in preventing the phenylene framework formation. However, upon examining more carefully figures 7.10.b and 7.10.c, which enable a higher resolution, one can appreciate certain differences in terms of STM contrast. In this case, single units are more clearly distinguishable, giving a first signal that the aligned wire is actually constituted by single molecules and not by fused monomers. A further indication stems from figure 7.10.b, where bilayer portions are noticeable. Bright stripes are in fact present above the underlying aligned stripes, and also in this case single units

can be fairly perceived, confirming the hypothesis that the sample is actually characterised by the oligomeric units. A more careful inspection to the high-resolution image of figure 7.10.c recall the idea that two DBTP units are laterally paired to form one stripe, as a first result of the moderate heat treatment to which they were subjected. This finding are consistent with previously published results conducted in UHV [16].

Graphene nanoribbons are an intermediate system between a monolayer made of single molecules and large area films. Therefore, for the purpose of this work, they should be intended as a starting point towards a complete and more accurate realisation of a model system for FeN_x sites embedded in a carbonaceous matrix. In fact, a further step on this regard will account for the doping of the graphene nanoribbons framework with heteroatoms, in particular nitrogen. It is known that doping with heteroatoms changes the electronic structure and therefore the band-gap of pristine graphene nanoribbons. In this case, the heteroatom doping should be meant to introduce macromolecules like porphyrins, which also offer the possibility to insert a metal in their internal cavity. This system featuring metal porphyrins embedded in the graphene nanoribbon framework would constitute a real joining link between the metal porphyrin monolayers, presented in this thesis, and the MN_x compounds employed nowadays as non-PGM catalysts.

References

[1] J.W. Colson, W.R. Dichtel, Rationally synthesized two-dimensional polymers, Nature Chemistry. 5 (2013) 453–465.

[2] L. Lafferentz, V. Eberhardt, C. Dri, C. Africh, G. Comelli, F. Esch, S. Hecht, L. Grill, Controlling on-surface polymerization by hierarchical and substrate-directed growth, Nature Chemistry. 4 (2012) 215–220.

[3] J. Sakamoto, J. van Heijst, O. Lukin, A.D. Schlüter, Two-dimensional polymers: Just a dream of synthetic chemists?, Angewandte Chemie - International Edition. 48 (2009) 1030–1069.

[4] L. Grill, M. Dyer, L. Lafferentz, M. Persson, M. v. Peters, S. Hecht, Nano-architectures by covalent assembly of molecular building blocks, Nature Nanotechnology. 2 (2007) 687–691.

[5] R. Mas-Ballesté, C. Gómez-Navarro, J. Gómez-Herrero, F. Zamora, 2D materials: To graphene and beyond, Nanoscale. 3 (2011) 20–30.

[6] J.M. Wofford, E. Starodub, A.L. Walter, S. Nie, A. Bostwick, N.C. Bartelt, K. Thürmer, E. Rotenberg, K.F. McCarty, O.D. Dubon, Extraordinary epitaxial alignment of graphene islands on Au(111), New Journal of Physics. 14 (2012).

[7] A.K. Geim, K.S. Novoselov, The rise of graphene, Nature Materials. 6 (2007) 183–191.

[8] T. Seyller, A. Bostwick, K. v. Emtsev, K. Horn, L. Ley, J.L. McChesney, T. Ohta, J.D. Riley, E. Rotenberg, F. Speck, Epitaxial graphene: A new material, Physica Status Solidi (B) Basic Research. 245 (2008) 1436–1446.

[9] X. Wang, Y. Ouyang, X. Li, H. Wang, J. Guo, H. Dai, Room-temperature all-semiconducting sub-10-nm graphene nanoribbon field-effect transistors, Physical Review Letters. 100 (2008) 100–103.

[10] Q. Yan, B. Huang, J. Yu, F. Zheng, J. Zang, J. Wu, B.L. Gu, F. Liu, W. Duan, Intrinsic current-voltage characteristics of graphene nanoribbon transistors and effect of edge doping, Nano Letters. 7 (2007) 1469–1473.

[11] J. Lee, K. Kim, W.I. Park, B.H. Kim, J.H. Park, T.H. Kim, S. Bong, C.H. Kim, G. Chae, M. Jun, Y. Hwang, Y.S. Jung, S. Jeon, Uniform graphene quantum dots patterned from self-assembled silica nanodots, Nano Letters. 12 (2012) 6078–6083.

[12] C. Bronner, Bottom-up synthesis and electronic structure of graphene nanoribbons on surfaces, Elsevier, 2018.

[13] Y. Hernandez, S. Pang, X. Feng, K. Müllen, Graphene and Its Synthesis, Elsevier B.V., 2012.

[14] S. Wang, L. Talirz, C.A. Pignedoli, X. Feng, K. Müllen, R. Fasel, P. Ruffieux, Giant edge state splitting at atomically precise graphene zigzag edges, Nature Communications. 7 (2016) 3–8.

[15] S. Yasuda, R. Kumagai, K. Nakashima, K. Murakoshi, Electrochemical potential stabilization of reconstructed Au(111) structure by monolayer coverage with graphene, Journal of Physical Chemistry Letters. 6 (2015) 3403–3409.

[16] A. Basagni, F. Sedona, C.A. Pignedoli, M. Cattelan, L. Nicolas, M. Casarin, M. Sambi, Molecules-oligomers-nanowires-graphene nanoribbons: A bottom-up stepwise on-surface covalent synthesis preserving long-range order, Journal of the American Chemical Society. 137 (2015) 1802–1808.

[17] S.N. Thorgaard, P. Bühlmann, Bromine-passivated Au(111) as a platform for the formation of organic self-assembled monolayers under electrochemical conditions, Langmuir. 26 (2010) 7133–7137.

[18] J. van der Lit, P.H. Jacobse, D. Vanmaekelbergh, I. Swart, Bending and buckling of narrow armchair graphene nanoribbons via STM manipulation, New Journal of Physics. 17 (2015) 3–8.

[19] W. Ko, C. Ma, G.D. Nguyen, M. Kolmer, A.P. Li, Atomic-Scale Manipulation and In Situ Characterization with Scanning Tunnelling Microscopy, Advanced Functional Materials. 29 (2019) 1–24.

[20] J.A.A.W. Elemans, Externally Applied Manipulation of Molecular Assemblies at Solid-Liquid Interfaces Revealed by Scanning Tunnelling Microscopy, Advanced Functional Materials. 26 (2016) 8932–8951.

Chapter 8

Conclusions and perspectives

In Chapter 5 it was introduced a thorough elucidation of metal-porphyrin reactivity descriptors, pointing out in particular the role of number of *d* electrons and redox potential in the ORR mechanism. Examples of correlation between these parameters and the electrochemical activity towards ORR do already exist and were in part shown in chapter 5. Similar types of correlations, even if from a different point of view, were also produced with collected data of this work, especially considering the various metal-octaethylporphyrins functionalised on HOPG in O_2 saturated electrolyte.

For all the following considerations and comparisons, two important electrochemical parameters were employed, namely the half-peak current and the half-peak potential. The two parameters were adopted as kinetic parameters to describe aggregated data in an organic way. The half-peak current ($i_{p/2}$) was obtained by halving the peak current after capacitive current correction, and the decision to consider $i_{p/2}$ instead of i_p is that $i_{p/2}$ falls in a purely kinetic zone whereas i_p is also affected by the mass transfer to the electrode surface. The corresponding potential value is the half-peak potential, $E_{p/2}$, and it is a convenient kinetic parameter expression, especially when peak potential is difficult to assess due to a broad shape [1].

Figure 5.2 shows a volcano-like trend for various metal-centred macrocycles when the electrocatalytic activity towards ORR was plotted against the number of *d* electrons, with iron culminating at the top of the plot. A similar correlation was brought forth in figure 8.1.a with four first-raw transition metal octaethylporphyrins, the iron octaethylporphyrin being located almost on top of the volcano, with cobalt also maintaining a high position. These two metal porphyrins are then recognised as the most active molecular catalysts towards oxygen reduction reaction. This partially differs from previously published articles, in which Fe macrocycles were found to be located on top [2,3] or on intermediate positions of the volcano [4]. However, it must be considered that these previously reported volcano-like correlations were often obtained in alkaline electrolyte. Conversely, in this work strongly acidic conditions were realised, constituting an unprecedented case study though still at a first stage, with the ambition to further extend the number of characterised metal macrocycles, trying to complete the first-raw transition metal series. Indeed, also MnOEP exhibits an interesting performance, confirming the positive role of partially filled *d* orbitals in catalysing ORR. As an additional evidence, copper octaethylporphyrin has a poor catalytic behaviour, therefore locating at the bottom of the volcano. In fact, copper is known to energetically prefer a complete 3*d* shell occupancy, leaving an unpaired electron in the 4*s* orbital. Contrasting computational result emerged [5] and more specific computational investigation should be run on this specific adsorbed CuOEP@HOPG system to attribute the real molecular orbital occupancy. CuOEP performance in any case denotes its scarce binding ability towards O_2.

Only metals belonging to the same periodic table raw were compared in figure 8.1.a, since heavier transition metals can lead to different or additional type of interaction with substrate and reactant molecule. In fact, Ru and Pt octaethylporphyrins were also characterised, but their performance is far from first-raw transition metal porphyrins, and they were inserted in a different correlation graph, presented in figure 8.1.b. RuOEP retains the best performance, while Pt retains the worst. It is not surprising that Ru complexes exert a definite activity towards O_2 reduction, and its redox properties had been in the past stated [6], but in this case the carbonyl ligand presence, also confirmed by EC-STM, should be taken into account. It is claimed that CO can exert a poisoning effect onto the metal active centre, inhibiting or retarding its catalytic effects towards ORR. For this reason, other carbonyl-free Ru-macrocycles were planned to be tested. Platinum, like copper, is not believed to properly interact with O_2 molecule due to the filled $5dz^2$ orbital which should repel axial coordination, but O_2 adsorption was theoretically computed [7] and experimentally perceived by EC-STM, see section 6.1.7. The final catalytic performance is in any case poor. Moreover, SnOEP was also included in figure 8.1b, although actually belonging to the *p*-block metals but possessing in any case a complete 4d shell. In section 5.1.8, the catalytic properties of novel Sn-N-C materials were pointed out, demonstrating that an electrocatalytic effect outside of a classical redox catalysis can attain desirable performances [8], but SnOEP was also figured out to not represent a performing molecular catalyst towards ORR.

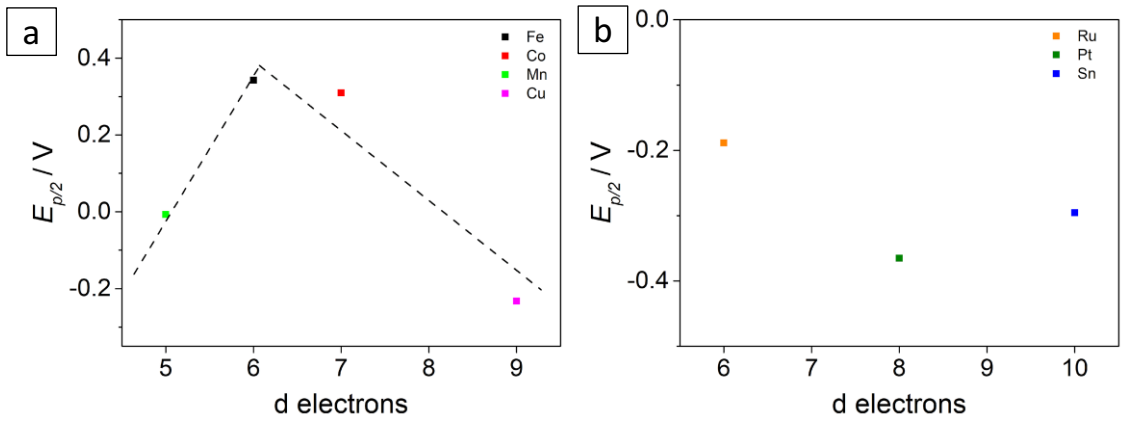

Figure 8.1. a) plot of half-peak potential versus the number of *d* electrons. Only first-raw transition metal porphyrins were included; b) plot of half-peak potential versus the number of *d* electrons. Only high atomic number metal porphyrins were included.

A similar correlation with the number of *d* electrons was conducted also with the half-peak current, as reported in figure 8.2. At a first glance, figure 8.2 appears complementary to figure 8.1, since the same reduction wave is exploited in the electrochemical performance comparison. This time the half-peak current is plotted against the number of *d* electrons. From figure 8.2a is meant to compare only first-raw transition metal octaethylporphyrin, whereas figure 8.2b contains heavier metals. Figure 8.2a differs from figure 8.1a since only iron is emerging as more active with respect to the other metals. In particular, cobalt and manganese now exhibit very similar results, displaying once more

the promising catalytic effect of manganese porphyrins. Indeed, upon suitable ring substitution, a series of manganese porphyrins were examined in their ORR activity by M[illegible]a and Schuhmann [4] and a clear enhanc[illegible]nt of Mn(III)/Mn(II) redox potential (and consequently of ORR peak potential and current) was ascertained.

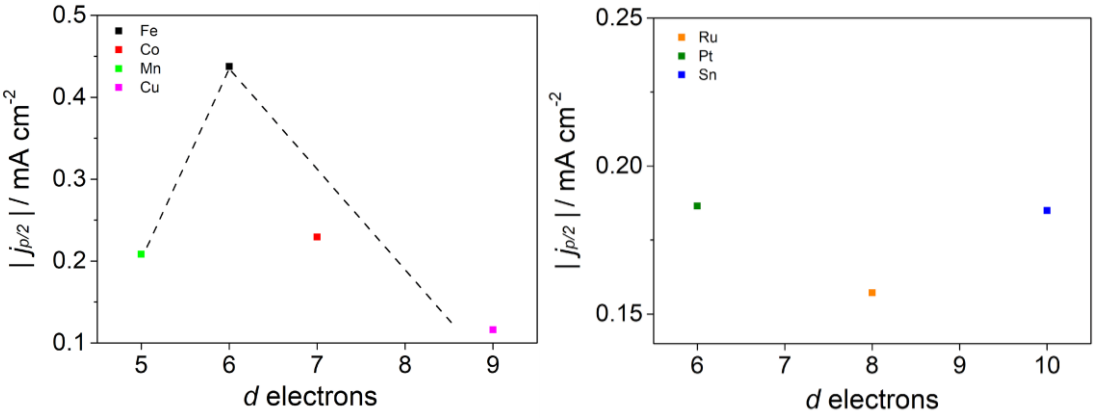

Figure 8.2. a) plot of half-peak current versus the number of *d* electrons. Only first-raw transition metal porphyrins were included; b) plot of half-peak potential versus the number of *d* electrons. Only high atomic number metal porphyrins were included.

A really innovative approach is now presented to associate electrochemical and scanning tunnelling microscopy data. This statement may seem controversial or inappropriate, because two very different data sources are now tentatively joint together in a unique relationship. Cyclic voltammetry is in fact expected to return a macroscopic information of the electrochemical response of an electrode towards a certain reaction, i.e. oxygen. On the other side, STM provides a "photograph" of a very tiny portion of the sample surface, which one could claim not to be representative of the total substrate. However, if the tiny portion of the sample surface coincides with the active site involved in the ORR process, then we can infer that the macroscopically information from cyclic voltammetry and that from STM are expected to correlate. On this regard, it must be recalled that this work is based on the EC-STM technique, which combines the imaging ability of STM to an electrochemical instrumentation, so that *in situ* or *in operando* imaging is performed on a sample, which at the same time acts as working electrode surface at the solid/electrolyte interface. This first point moves the imaging output closer to electrochemical data, since the imaged system is exactly the same that undergoes macroscopic electrochemical characterisation. Moreover, the characterised samples are in this case well known in all their components. First of all, the substrates were thoroughly characterised both by EC-STM and by cyclic voltammetry, see chapter 4. Secondly, the probed metal macrocycles were properly selected. The same porphyrinato ligand was kept constant for all the analysed metal porphyrin, thereby rejecting any possible ligand influence in the determined STM contrast in the following presented correlation. Additionally, the free-base porphyrinato ligand was also characterised, so that the ligand STM contrast was fully elucidated prior to analyse that of the metal-octaethylporphyrins. Finally, an extremely large number of STM images were collected for each sample, and thanks to the employed instrumentation different sample areas were characterised. A

significant part of them must be discarded due to absence of resolution or electronic noise covering the real surface features. Anyway, though rough and simple, this actually stands for an averaging of the obtained images, also considering that STM technique is often interpreted in a qualitative way, rather than quantitatively. So, it is safe to state that EC-STM pictures of each metal-octaethylporphyrin presented in chapter 6 are representative of the fully functionalised electrode surface. In this work, one step further in STM images comes in the analysis of topographic features to compare them with electrochemical data. The idea is to associate the main characteristic of a CV, i.e. the ORR peak, to the STM topographic protrusion (if present). This approach allows to consider all the investigated system in the very same plot, that was not possible considering the sole rule of d-electron occupation.

In figure 8.3a, the topographic protrusion is plotted against the half-peak potential, and a volcano-like shape is obtained. In this case, all metal porphyrins investigated in O_2 saturated electrolyte were reported: Ru is absent due to unsuccessful EC-STM imaging in O_2 saturated electrolyte (see section 6.1.9). The use of $E_{p/2}$ as ORR parameter sees the presence of iron and cobalt in the upper part of the volcano plot, corresponding to an intermediate value of the protrusion. Interestingly, both Co and Fe underwent a halving of the protrusion when passing from deaerated to O_2 saturated electrolyte, and both possess a singly occupied $3dz^2$ orbital, which was claimed to be the major responsible of the STM contrast in deaerated electrolyte. It appears straightforward that an implication could be envisaged also for O_2 adsorption and further reaction, thus explaining the STM contrast variation between O_2-free and O_2-saturated electrolyte. Manganese and platinum are located in the right part of the volcano, where high protrusion values were determined in presence of O_2 in the electrolyte solution. Tin and copper share the left part of the plot, since low or no protrusions were determined. Actually, copper was described as incapable of successfully binding O_2, but a certain catalytic activity eventually appeared. Platinum, as well, was indicated as the worst performing metal porphyrin, but shares the same protrusion height of manganese in STM images. One could wonder what the physical interpretation of the measured protrusion is, and an answer without claiming to be a confirmation could come from the bond strength of the metal-O_2 adduct. According to the simple Sabatier's principle of catalysis, a good catalyst should bind reactants neither too strongly nor too weakly, and the same is valid for reaction products. Transferring this concept to the volcano-plot of figure 8.3a, Co and Fe could be related to an intermediate binding strength, while Pt and Mn could be associated to strongly binded O_2. However, an apparent contradiction may arise for the fact that Mn and Pt share the same protrusion height but significantly different catalytic activity ($E_{p/2}$). Two arguments must be considered. The first is that the protrusion determination is susceptible of an error which will be object of investigation in future experiments. The second is that Mn and Pt were determined to catalyse ORR within different mechanisms: in particular, Mn takes part to the redox-like catalysis, from which Pt was a priori excluded. The final result is therefore not contradictory, because O_2 adsorption strength can be in both cases quite strong, simultaneously explaining why Mn is performing worse than other first-raw transition metals and Pt retains the worst activity towards ORR than any other tested metals. The

left part of the volcano sees the presence of Cu and Sn. According to the O_2 binding energy correlation with the measured protrusion, these two metals are expected to bind O_2 too weekly. Indeed, the electrochemical performance towards ORR sees quite negative $E_{p/2}$ values, thus explaining in first approximation the poor catalytic effect. Again, it should be pointed out that the orbital population of Cu and Sn is significantly different, being copper a first-raw transition metal and tin a *p*-block metal. Moreover, for the sake of completeness, in section 5.1.8 an article was reported in which O_2 adsorption energy calculation onto a Sn(IV) porphyrinic moiety resulted in a too strong binding, leading to an unfavourable electrocatalytic behaviour. As already stated for figure 8.1, additional characterisations for Ru and other transition metal porphyrins will in the future allow a more complete and robust data interpretation, allowing to confirm the volcano-like data trend and the STM protrusion association with O_2 binding strength. Finally, figure 8.3b reports the correlation of $j_{p/2}$ and the STM revealed protrusion. The result substantially agrees with the consideration exposed for figure 8.3a, with iron being at the top of a volcano plot and cobalt still retaining a suitable position for ORR electrocatalysis. Manganese and platinum are on the right part, whilst cupper and tin are on the left one. The association of the STM protrusion with O_2 binding energy again sees Fe and Co as the best metal, owing to an intermediate binding strength. The remaining metals seem to bind too strongly or too weekly the O_2 molecule, thus leading to worse electrochemical performances.

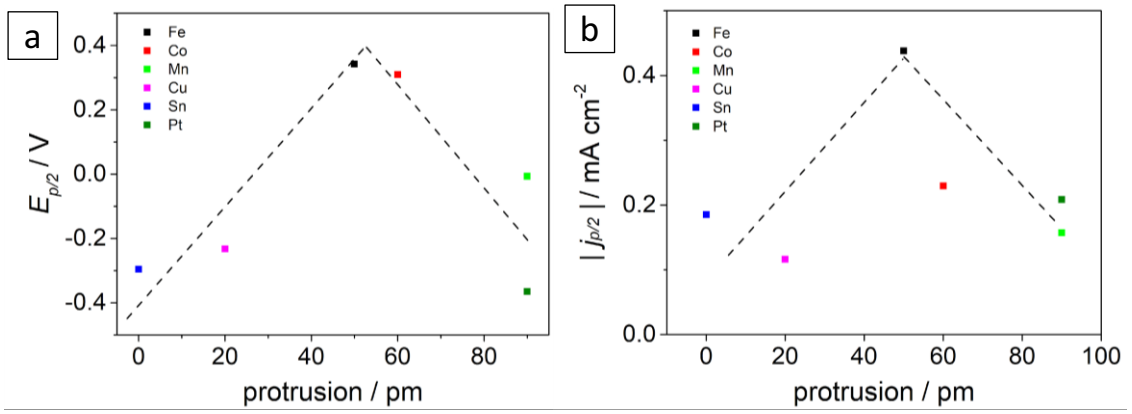

Figure 8.3 a) Correlation of the STM revealed protrusion and the half-peak potential for all the investigated metal porphyrins; b) correlation of the STM revealed protrusion and the half-peak current for all the investigated metal porphyrins.

In figure 8.4 a different comparison is brought forth. Cyclic voltammograms recorded for PtOEP and FeOEP on both substrates, Au(111) and HOPG, are reported together. In addition, CV of FeTPP@HOPG is featured. One can immediately appreciate the best performance of Fe porphyrins, both for FeOEP and FeTPP, compared to PtOEP. Actually, the most striking result is the large difference of ORR activity of PtOEP depending on the substrate. PtOEP@Au(111) ORR peak lies in fact almost 0.7 V more positive than PtOEP@HOPG, indicating that some kind of synergetic effect between Pt and Au(111) surface atoms should occur to provide such a significant impact on the ORR electrocatalysis. Contrary, FeOEP shares the same ORR peak potential considering both

Au(111) and HOPG substrates. What still remains unclear is why Fe porphyrins on HOPG substrates exhibit such an intense ORR peak current, while on Au(111) this effect is modest. The two substrates are actually extremely different at the microscopic scale, in the sense that Au(111) always presents a rougher surface compared to HOPG, and this is verified by STM imaging. Additionally, Au(111) always presents a significantly higher defects number, like hole and cracks which surely interfere with molecular adsorption. CVs were in fact normalised by the geometric surface area, but on this regard a more proper active surface area determination method should be addressed within future characterisations to overcome this unclear point.

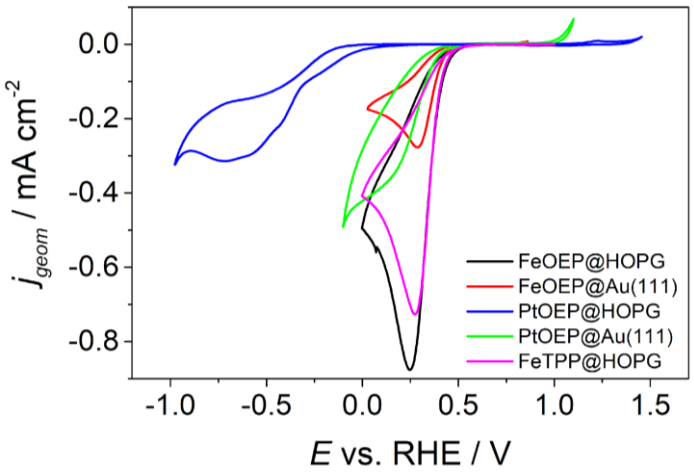

Figure 8.4. Superimposition of cyclic voltammograms recorded at 50 mV s^{-1} scan rate in O_2 saturated electrolyte. CV of PtOEP and FeOEP functionalised on both Au(111) and HOPG are featured. CV of FeTPP functionalised on HOPG is Also included.

A general overview is now worth to be presented as final summary of the collected data, highlighting the obtained results, the achieved goals, and the required improvement steps. First of all, STM technique was introduced starting from its early invention days, describing its evolution and extension to many fields of surface science. It was then associated with ambient experimental condition, ultimately arriving to the main characterisation technique exploited in this work, electrochemical scanning tunnelling microscopy (EC-STM). The high versatility of this microscopy technique was evidenced with different application examples, always showing riveting results.

STM technique was then examined in its theoretical details, presenting the most relevant mathematical passages that describe and quantify the tunnelling phenomenon, which must be treated in a quantum mechanical framework. Additional theoretical aspects were explored when passing from UHV to *in situ* STM, in particular in the case of aqueous electrolyte. Different approaches were examined, arriving to the conclusion that a unique model for tunnelling through an aqueous medium has not been developed yet.

The adopted experimental procedure was described in all its details. More specifically, the electrochemical setup used for cyclic voltammetric investigation was presented, followed by an extensive description of EC-STM investigation. Samples preparation and

procedures were ruled out for both the employed substrates, Au(111) and HOPG. Lastly, two extremely essential components of EC-STM instrumentation were presented and rebuilt, namely the STM scanners and the preamplifier electronic circuit. New home-made tools were in fact designed at this specific purpose, and the aim is to further improve these instrumental features to obtain a more performing imaging hardware. Both HOPG and Au(111) substrate were characterised in their electrochemical and imaging properties, and a specific section was dedicated to the instrumental calibration, needed each time a new piezoelectric scanner is mounted on the EC-STM instrumentation.

Then, experimental data were presented, dividing them into macroscopic electrochemical techniques, namely cyclic voltammetry and linear sweep voltammetry with RRDE electrode, and microscopic imaging technique, namely EC-STM. A number of different macrocyclic compounds were analysed, due to their implication in oxygen reduction reaction thanks to the presence of MN_4 sites. The aim of this work was to characterise this type of catalytic sites with the use of metal octaethylporphyrins. The studied metals on HOPG substrate are iron, cobalt, copper, manganese, ruthenium, platinum and tin. The metal-free porphyrin adlayer was also investigated. Each metal macrocycle revealed its own electrochemical response, both in deaerated and O_2 saturated electrolyte. Indeed, redox properties at the metal centre were revealed for iron, cobalt and manganese porphyrins, for which a redox catalysis mechanism was then recognised to be involved in ORR. Ru was also expected to show a similar response, but the presence of carbonyl seemed to hinder this phenomenon. Platinum, copper and tin were excluded from this redox behaviour, and they were also showing worse catalytic properties towards ORR. Free-base, iron and platinum octaethylporphyrins were investigated also on Au(111) substrate. In this case, PtOEP presented a significantly better catalytic activity towards ORR with respect to the HOPG case, though still worse compared to iron porphyrin on Au(111). Anyway, it is clear that a substrate effect should be taken into account when dealing with molecular electrocatalysis, especially when a scanning probe technique, like EC-STM, is also available and provides a direct visualisation tool at single site level. Furthermore, the effect of peripheral substituents was also explored, even if at an early stage, and it emerged that passing from ethyl to phenyl substituents determine slight variations in terms of electrochemical response. This was somehow predictable, because ring substitution changed from eight ethyl groups to four phenyl groups, so that a substantial electron-donating or electron-withdrawing effect was not actually realised. A more significant difference arose when comparing STM images of the two molecular systems on HOPG, but this is not surprising because small changes at the submolecular level can potentially lead to dramatic consequences in the physisorption process.

EC-STM data were then presented. Large scale images were collected for each analysed molecule, and they were exploited to calculate unit cell parameters. Then, smaller size images were collected, in order to attain a high-resolution level. This allowed to rule out aspects like number of *d* electrons and orbital population. Subsequently, high-resolution images were collected on the same metal porphyrins but in contact with oxygen saturated electrolyte. O_2 adsorption was successfully visualised for some of the analysed metal

porphyrins, included some porphyrins which then resulted in a poor electrocatalysis. This indicates that reactant adsorption is the fundamental first step of the electrocatalytic reduction, but additional factors should be considered when characterising the full ORR process. At this purpose, correlations of electrochemical and imaging data were brought forth. First, ORR activity was associated to the number of *d* electrons of the metal porphyrins, finding that half-filled populations of Fe and Co produced the best results. Then, it was correlated with the protrusion revealed by STM, and a tentative linkage with O_2 binding energy was proposed, again finding Fe and Co at the top of a volcano-like plot for catalytic activity. It was clearly pointed out that the redox behaviour of the metal center allows an improved catalytic activity in what can be defined as "redox-like catalysis" since the metal center mediates the reduction of the oxygen molecule, recovering its original oxidation state by reduction at the electrode. However, this is not the typical redox catalysis since it is not limited by the diffusion of the redox molecule to/from the electrode surface since the molecule itself is stuck on the electrode by weak interaction forces. However, even if to a lower extent, a certain catalysis was observed also at non-redox active metal centres, such as Pt or Cu, where intermolecular charge transfer via non-covalent functionalization was considered to impart ORR electrocatalytic activities to the exposed sites of the support or of the molecule [9]. This is a curious effect since the support itself is not active, nor is the molecule, but the ensemble of both let arising new properties and new catalytic activity. In fact, we assert that metal redox inactive octaethylporphyrins or the octaethylporphyrins itself can adsorb on the single crystal (HOPG or Au(111)) and electrons can be transferred from or to the support, depending on the HOMO or LUMO energy of the molecule and on the local density of state at the Fermi level of the electrode support. For example, upon the adsorption of octaethylporphyrins on HOPG it is expected that electrons are transferred from HOPG to the porphyrinato ring, resulting in a net positive charge on HOPG surface. In this case it would be the exposed edge sites, positively charged, of HOPG to be the active sites for ORR, on the other hand we already pointed out in Chapter 5 that carbon atoms nearby the nitrogen functional group of porphyrinato ligand can play as active sites. In both cases, the effect is similar to that obtained by the chemical doping of a graphene layer, or more in general of a carbon material, with a heteroatom element such as Nitrogen, Sulphur or Phosphorous. Conversely when Pt octaethylporphyrin is adsorbed on HOPG we may infer that charge density is transferred from the Pt metal center to the HOPG support, making the metal center, *de facto,* able to adsorb O_2 and catalyse the ORR process, even in the absence of a redox catalysis. Clearly, the capability to transfer charge density to the support critically depends on the support itself, therefore we may infer that the catalytic activity can be tuned by tuning the molecule/support interaction. This can explain the huge effect exerted on the catalytic activity of PtOEP with respect FeOEP, which follows a completely different catalytic mechanism. A simple sketch of the ORR process occurring on PtOEP and FeOEP functionalised on the Au(111) surface is reported in figure 8.5. In both cases O_2 comes in close proximity to the metal centre at the point of complete the adsorption process. Then it reduced, but the final products can be different,

and only Fe is participating in the ORR within a redox-like electroctalysis thanks to the Fe(III)/Fe(II) redox couple.

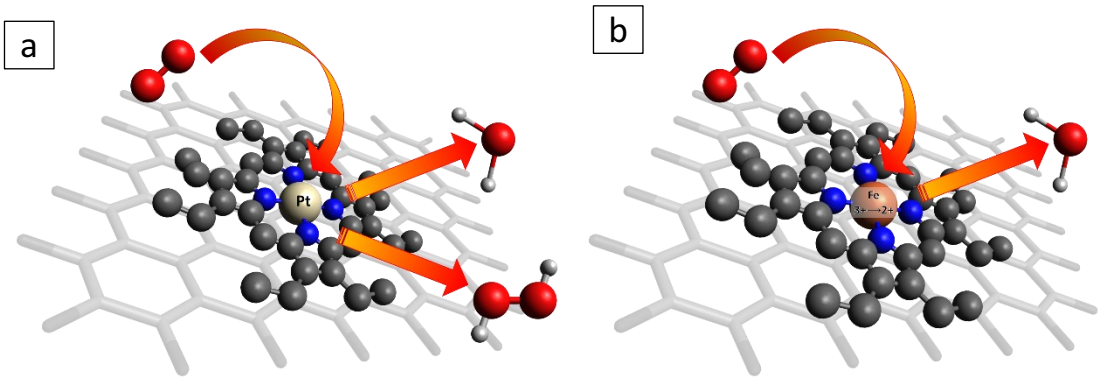

Figure 8.5. a) O_2 adsorption onto PtOEP, H_2O and H_2O_2 can be in principle formed; b) O_2 adsorption and further reduction onto FeOEP, H_2O is almost exclusively produced.

Despite the interesting and promising data collected by electrochemical and EC-STM experimental activity, additional characterisations performed on other metal-centred macrocycles will be needed to provide a full insight of molecular electrocatalysis of ORR. Many different routes can be followed, starting by the comparison of a huge number of metals that can be incorporated in the porphyrin cavity, passing to an insightful ring substitution, and ultimately studying the effect that the substrate exerts on O_2 adsorption onto the metal centre. The present work is therefore considered successful in studying O_2 reduction at single site metal-porphyrins adsorbed on solid substrates, intended that future work will further enhance the knowledge of these systems, allowing the achievement of more enticing catalytic properties.

References

[1] A.J. Bard, L.R. Faulkner, Electrochemical Methods: Fundamentals and Applications, 2nd Edition, Wiley, New York, 2001.

[2] J.H. Zagal, Metallophthalocyanines as catalysts in electrochemical reactions, Coordination Chemistry Reviews. 119 (1992) 89–136.

[3] J.H. Zagal, M.A. Paez, A.A. Tanaka, J.R.Jr. dos Santos, C.A. Linkous, Electrocatalytic activity of metal phthalocyanines for oxygen reduction, Journal of Electroanalytical Chemistry. 339 (1992) 13–30.

[4] J. Masa, W. Schuhmann, Systematic selection of metalloporphyrin-based catalysts for oxygen reduction by modulation of the donor-acceptor intermolecular hardness, Chemistry - A European Journal. 19 (2013) 9644–9654.

[5] M.S. Liao, S. Scheiner, Electronic structure and bonding in metal phthalocyanines, metal=Fe, Co, Ni, Cu, Zn, Mg, Journal of Chemical Physics. 114 (2001) 9780–9791.

[6] J.H. Zagal, M.T.M. Koper, Reactivity Descriptors for the Activity of Molecular MN4 Catalysts for the Oxygen Reduction Reaction, Angewandte Chemie - International Edition. 55 (2016) 14510–14521.

[7] E.S. Dy, H. Kasai, Characterization of Platinum Porphyrins and its interaction with oxygen by density functional theory, E-Journal of Surface Science and Nanotechnology. 3 (2005) 473–475.

[8] F. Luo, A. Roy, L. Silvioli, D.A. Cullen, A. Zitolo, M.T. Sougrati, I.C. Oguz, T. Mineva, D. Teschner, S. Wagner, J. Wen, F. Dionigi, U.I. Kramm, J. Rossmeisl, F. Jaouen, P. Strasser, P-block single-metal-site tin/nitrogen-doped carbon fuel cell cathode catalyst for oxygen reduction reaction, Nature Materials. 19 (2020) 1215–1223.

[9] Z. Zhao, L. Zhang, Z. Xia, Electron Transfer and Catalytic Mechanism of Organic Molecule-Adsorbed Graphene Nanoribbons as Efficient Catalysts for Oxygen Reduction and Evolution Reactions, J. Phys. Chem. C 2016, 120, 4, 2166–2175.

Conferences

Electrochemical Discussions: latest insights on PGM-free catalysts for Energy Systems and Fuel Cells, Torino, February 8, 2019. EC-STM Investigations on Iron-based Macrocycles SAMs as Sources of Fe-N active centres towards ORR, A. Facchin, C. Durante, Poster presentation

Materials for Today's energy Challenges, Padova, June 3-4, 2019, Iron-based macrocycles SAMs probed by EC-STM towards oxygen reduction reaction (ORR), A. Facchin, G. Daniel, M. Mazzucato, C. Durante, Poster presentation

XLVII Congresso Nazionale di Chimica Fisica, Roma, July 1-4, 2019, Electrochemical Scanning Tunnelling Microscopy investigations of Fe(III)- and H2-octaethyl porphyrin adlayers on HOPG towards ORR, A. Facchin and C. Durante, Oral presentation

XLVII Congresso Nazionale di Chimica Fisica, Roma, July 1-4, 2019, Effect of substituents on MN4 macrocycles adsorbed on HOPG towards ORR, A. Facchin and C. Durante, Poster presentation

Photo and ElectroCatalysis at the Atomic Scale (PECAS 2019), Donostia-San Sebastián, Basque Country (Spain), August 27-30, 2019, Effect of substituents on MN4 macrocycles adsorbed on HOPG towards ORR, A. Facchin and C. Durante, Oral presentation

Photo and ElectroCatalysis at the Atomic Scale (PECAS 2019), Donostia-San Sebastián, Basque Country (Spain), August 27-30, 2019, Electrochemical scanning tunnelling microscopy of Fe(III) tetrakismethoxyphenyl porphyrin chloride on Au(111), A. Facchin and C. Durante, Poster presentation

Giornate dell'Elettrochimica Italiana - GEI 2019, Padova, September 8-12, 2019, Electrochemical scanning tunneling microscopy of Fe(III tetrakismethoxyphenyl porphyrin chloride on Au(111), A. Facchin, A. Gennaro and C. Durante, Poster presentation

Giornate dell'Elettrochimica Italiana - GEI 2019, Padova, September 8-12, 2019, Behavior of Fe(III)-octaethylporphyrin adsorbed on HOPG towards ORR probed by electrochemical scanning tunneling microscopy, A. Facchin, A. Gennaro and C. Durante, Poster presentation

29th Topical Meeting of the International Society of Electrochemistry, Mikulov, Czech Republic, April 18-21, 2021, Oxygen Reduction Reaction at Single Site Catalysts: A combined Electrochemical Scanning Tunnelling Microscope and DFT investigation of Iron Octaethylporphyrin Chloride on HOPG, A. Facchin, M. Zerbetto, D. Forrer and C. Durante, Oral presentation

29th Topical Meeting of the International Society of Electrochemistry, Mikulov, Czech Republic, April 18-21, 2021 Pt versus Fe single site catalyst models for oxygen reduction reaction: and EC-STM investigation on metal octaethylporphyrins, A. Facchin and C. Durante, Poster presentation

New Trends in Materials Science and Engineering, 1st International Virtual Conference, June 14-18, 2021, Oxygen Reduction Reaction monitoring at Iron Single Site Catalyst: Electrochemical Scanning Tunnelling Microscopy of Iron Octaethylporphyrin, A. Facchin, M. Zerbetto, A. Vittadinini, D. Forrer and C. Durante

New Trends in Materials Science and Engineering, 1st International Virtual Conference, June 14-18, 2021, Pt versus Fe single site catalyst models for oxygen reduction reaction: an EC-STM investigation on metal octaethylporphyrins, A. Facchin and C. Durante

XXVII congresso Nazionale della Società Chimica Italiana, September 14-23, 2021, Oxygen Reduction Reaction monitoring at Iron Single Site Catalyst: Electrochemical Scanning Tunnelling Microscopy of Iron Octaethylporphyrin, A. Facchin, M. Zerbetto, A. Vittadini, D. Forrer and C. Durante

XXVII congresso Nazionale della Società Chimica Italiana, September 14-23, 2021, From Redox-like to Heterogeneous Electrocatalysis at Metal-Octaethylporphyrins@HOPG investigated by EC-STM, A. Facchin and C. Durante

Papers

A. Facchin, T. Kosmala, A. Gennaro, C. Durante, Electrochemical Scanning Tunnelling Microscopy Investigations of FeN4-Based Macrocyclic Molecules Adsorbed on Au(111) and Their Implications in the Oxygen Reduction Reaction, ChemElectroChem. 2020, 7 (6), 1431-1437.

A. Facchin, M. Zerbetto, A. Gennaro, A. Vittadini, D. Forrer and C. Durante, Oxygen Reduction Reaction at Single-Site Catalysts: A Combined Electrochemical Scanning Tunnelling Microscopy and DFT Investigation on Iron Octaethylporphyrin Chloride on HOPG, ChemElectroChem 2021, 8, 2825–2835.

G. Daniel, T. Kosmala, F. Brombin, M. Mazzucato, A. Facchin, M. C. Dalconi, D. Badocco, P. Pastore, G. Granozzi and C. Durante, Highly Graphitized Fe-N-C Electrocatalysts Prepared from Chitosan Hydrogel Frameworks, Catalysts 2021, 11, 390.

Y. Zhang, G. Daniel, S. Lanzalaco, A. A. Isse, A. Facchin, A. Wang, E. Brillas, C. Durante, I. Sirés, H2O2 Production at Gas-diffusion Cathodes Made from Agarose-Derived Carbons with Different Textural Properties for Acebutolol Degradation in Chloride Media, Journal of Hazardous Materials, 2021, 127005.